Spin Interactions in Graphene-Single Molecule Magnets Hybrid Materials

Von der Fakultät Mathematik und Physik der Universität Stuttgart
zur Erlangung der Würde eines Doktors der Naturwissenschaften
(Dr. rer. nat.) genehmigte Abhandlung

vorgelegt von

Christian Cervetti

aus Modena (Italien)

Hauptberichter: Dr. Lapo Bogani
Mitberichter: Prof. Dr. Jörg Wrachtrup

Tag der mündlichen Prüfung: 04.09.2015

1. Physikalisches Institut der Universität Stuttgart
2015

Dedicated to Laura

"Progress is what the hard worker is looking for"

– Tony Allen

Contents

Zusammenfassung

Die Möglichkeiten immer mehr Informationen zu speichern und zu verarbeiten hat in den letzten Jahrzehnten stetig zugenommen. Treibender Motor dieser Entwicklung ist die immer fortschreitender Miniaturisierung elektronischer Bauteile, so wurden im Jahr 2014, Speicherdichten von 1.3 Gbit/mm^2 erreicht (Seagate 2014 [1]) . Im selben Zeitraum lag die Transistordichte pro mm^2 bei 16 Millionen, wobei die Größe einzelner Komponenten lediglich 8 nm betrug (Intel 14 nm technology [2, 3]), was der Ausdehnung eines einzelnen Moleküls entspricht. In solch mesoskopischen Skalen spielen bisher vernachlässigbar kleine Quanteneffekte, wie das Quantentunneln und Quanteninterferenzen eine prägende Rolle und können die Leistung eines Bauelementes limitieren. Um diese neuen Hindernisse zu überwinden wird eine zukünftige Technologie auf anderen physikalischen Grundlagen und neuartigen Materialien begründen müssen. Einen vielversprechenden Ansatz hierfür stellt das Gebiet der Spintronik (alias Spin-Elektronik) dar. Dabei werden die Spin Eigenschaften der Elektronen nutzbar gemacht, um damit Informationen zu verschlüsseln und zu verarbeiten [4–7]. In diesen Rahmen kann Graphen [8, 9], ein kürzlich entdecktes Material, die Spin-Informationen über Rekordweiten von über $\lambda_s = 100\,\mu$m transportieren. Weiterhin stellt Graphen ein "reines Oberflächen-Material" dar, dessen spintronische Eigenschaften durch die maßgeschneiderte Einbringung externer Einflüsse, wie der Kombination mit magnetischen Molekülen, genau kontrolliert werden können.

Die Kopplung von Graphen zu solch mesoskopischen magnetischen Systemen bietet neue Wege Spin-Zustände elektronisch zu manipulieren. Gleichwohl stellt es eine ungeheure Herausforderung dar solche Spin-Systeme in reale Bauelemente zu integrieren, da die Wechselwirkungen der Spins mit in einer komplexen Umgebung nur schwer zu verstehen oder gar handzuhaben sind. Zwei wichtige Größen die Kopplungseigenschaften zu charakterisieren sind zum einen die Spin-Relaxationszeit T_1 (auch indiziert mit τ) und die Spin-Dephasierungs Zeit T_2. Erstere beschreibt die Lebenszeit eines "klassischen Bits", in welchem die Informationen in "up" und "down" Zuständen kodiert sind. Im Gegensatz dazu beschreibt T_2 die kohärente Lebenszeit eines "Quantenbits" wobei die Informationen durch die Phase der Spin-Wellenfunktion verschlüsselt werden.

Im Zuge dieser Arbeit werden magnetische Moleküle aus der Familie der "Single Molecule Magnets" als Modellsysteme verwendet, um die Relaxationsprozesse solch mesoskopischer Spins in Verbindung mit Graphen und ihren Einfluss auf die Ladungsträger innerhalb realer Bauelemente zu untersuchen. Dabei werden zwei unterschiedliche Ansätze verfolgt. Im ersteren werden die Single Molecule Magnets (SMMs) als Modellsysteme genutzt um

die komplexen Wechselwirkungs-Mechanismen zwischen Spin und Umgebung zu entwirren. Dahingehend kombinieren wir Graphen mit dem SMM [Fe$_4$(L)$_2$(dpm)$_6$], wobei dpm^- für deprotonated dipivaloylmethane steht. Als Ligande L, fungiert triply deprotonated H$_3$L=2-hydroxymethyl-2-(4-(pyren-1-yl)butoxy)methylpropane-1,3-diol, welcher eine Pyrengruppe enthält welche eine nichtkovalente Bindung an die Graphenoberfläche via π-stacking ermöglicht.

Diese Funktionalisierung der exfolierten Graphenschichten findet in Lösung statt, was es ermöglicht sowohl Substrat-unterstützte als auch "bulk"-Material Proben herzustellen. Die erzeugten Hybridsysteme werden dann durch mehrere Techniken charakterisiert. Matrix-unterstützte-Desorption-Ionisations-Time of Flight Massen Spektroskopie wird dabei genutzt um die strukturelle Stabilität der Moleküle nach der Dispersions-Deponierung sicherzustellen. Röntgen-Strahlen Photo-elektron Spektroskopie zeigt dabei, dass der Oxidationszustand der magnetischen Kern-Ionen unverändert bleibt.

Das neuartige Hybridsystem zeigt vernachlässigbaren Ladungsaustausch zwischen dem SMM und dem Graphen, welcher mittels elektronischen Messungen und Raman-Spektroskopie an einen Graphen-basierten Feld-Effekt Transistor nachgewiesen wurde. Um die Details der Selbstassemblierung von die SMMs auf Graphen zu untersuchen wurde die Hybrid-Oberflächen-topographie mit Hilfe von hochaufgelöster Raster Kraft Mikroskopie gemessen. Durch Variierung der Lösungskonzentration C von die SMMs wurde eine präzise statistische Analyse ermöglicht, welche eine beträchtliche Diffusion der Molekül-Entitäten auf der Graphenoberfläche aufzeigte. Dynamische Skalierungsanalysen erlaubten es zwischen verschiedenen Anordnungsverläufen, wie *Nukleation*, *Aggregierung* und *Koaleszenz* zu unterscheiden. Zurückbleibende Oberflächen-Cluster Diffusion eröffnet hierbei neue Strategien zur Herstellung von ausgedehnten supermolekularen Strukturen auf Graphen. Durch die Bestrahlung mit Laserlicht kann ein Reorganisierung der molekularen Adsorbate induziert werden, was eine zufällige zweidimensionale Netzwerkausbildung auf dem Graphen zur Folge hat.

Die statisch magnetischen Eigenschaften von die SMMs innerhalb der Graphenumgebung wurden in Abhängigkeit von Temperatur und Magnetfeld bestimmt und mit der Kristallmessung von SMM verglichen. Die Temperaturabhängigkeit des Produktes $\chi_\mathrm{m}T$, aus molarer Suszeptibiltät $\chi_\mathrm{m} = M_\mathrm{m}/H$ (wobei M_m für die molare Magnetisierung, H für das externe magnetische Feld stehen) und der Temperatur T, bestätigt dabei den $S = 5$ Grundzustand von SMM und zeigt dabei eine perfekte Übereinstimmung zwischen Hybrid und Kristall. Die Isothermischen Magnetisierugnskurven können sehr gut über den Giant Spin Hamiltonian modelliert werden:

$$\mathcal{H} = D\hat{S}_z^2 + g\mu_\mathrm{B}\hat{\mathbf{S}} \cdot \hat{\mathbf{H}} \tag{1}$$

Während der erste Term die uniaxiale magnetische Anisotropie des SMMs beschreibt, definiert der zweite Teil des Hamiltonians den Effekt des angelegten externen Magnetfeldes. Der uniaxial Ansiotropy Parameter D und die z-Komponente des Spinoperatoren S_z, bestimmen die resultierende Energiebarriere welche die $(2S + 1)$ entarteten Grundmultiplietts $|m\rangle$ and $|-m\rangle$ voneinander trennt. Die Gegenwart der Energiebarriere bes-

timmt die Relaxation des molekularen Spins, wobei zwei Hauptrelaxationsmechanismen möglich sind. Der klassische Mechanismus basiert auf der Absorption von Phononen aus der äußeren Umgebung, während der quantenmechanische Prozess durch Quantentunnel-Eigenschaften des Spins definiert ist. Das Tunneln des Spins durch die Energiebarriere wird durch zusätzliche transversale Terme im Kristallfeldhamiltonian ermöglicht. Mittels dynamischer Suszeptibilität Messungen können diese Prozesse durch die Extrahierung der Relaxationszeit t in Abhängigkeit von der Temperatur beobachtet werden. Im Vergleich zum Kristall zeigen die SMM-Graphen Hybriden in beiden Prozessen ein signifikant unterschiedliches Relaxationsverhalten. So wurde zum Beispiel ein extrem verstärktes Quantentunneln bei tiefen Temperaturen festgestellt. Dahingehend wurde ein neues theoretisches Modell entwickelt in welchem alle fundamentalen Wechselwirkungen in Betracht gezogen werden die zu Spin-Relaxation in einer Graphenumgebung beitragen können. Während der Unterschied in der thermischen Relaxation von der zwei-dimensionalen Natur der Graphen-Phononen herrührt, kann die hohe Tunnelrate bei tieferen Temperaturen nur durch eine Wechselwirkung zwischen Spin und den Graphenladungen erklärt werden. Diese zusätzliche Wechselwirkung wurde im Rahmen des Stevensformalismus dargestellt und zeigt das sie vollständig kohärentes Tunneln ermöglicht, wie bereits vor über einer Dekade von Villains vorhergesagt. Dies eröffnet neue Möglichkeiten die Kohärenz eines Spin-Zustande elektronisch anzusteuern.

Der zweite Teil dieser Arbeit beschäftigt sich mit der Fabrikation und Optimierung von Graphen basierten Spinvalve-Bauelementen und deren Charakterisierung bei tiefen Temperaturen. Ferromagnetische Kobaltkontakte werden hierfür mit Graphen verbunden und fungieren als Quelle für Spin-polarisierte Ladungsträger. Über eine nicht lokale Messungsgeometrie kann der Spin-Transport von Ladungstransport und weiteren magnetoresisitiven Mechanismen getrennt werden. Die Spininjektionseffizienz ist limitiert durch den Leitungsunterschied am Übergang zwischen Ferromagnet und Graphen (FM/G), was zu einem erheblich schwächeren Spin-Signal führt. Um diesen Umstand zu umgehen muss der Widerstand des Spin-abhängigen Überganges angepasst werden. Die kann durch die Implementierung von Tunnelkontakten oder durch eine Größenreduzierung der Kontaktstelle erreicht werden. In dieser Arbeit werden beide Strategien getestet, wobei der erste Ansatz sehr herausfordernd ist, daher die Kreation von ultra-dünnen Tunnelbarrieren erfordert. Diese wurden aus Al_2O_3 gefertigt und haben eine dicke von < 2 nm. In Kombination mit aus Titankeimen basierten Inseln und Dünnfilmdeponierung wurden hochhomogene Filme geschaffen. Die Injektion Effizienz ist sehr sensitiv was die chemische Zusammensetzung der Barriere betrifft, nur eine vollständig oxidierte Keimung erlaubt einen effizienten Spin Transport zusammen mit einer hohen Entkopplung zwischen den ferromagnetischen Kontakten und dem Graphenleitungskanal. Im zweiten Ansatz wurde versucht die Kontaktstelle durch die Herstellung von dünnen Graphenstreifen zu minimieren. Die Strukturierung dieser von 200 - 300 nm breiten Streifen erfolgte durch Elektronenstrahllithographie und reaktive Ionen Ätzung. Diese bieten des Weiteren eine passendere Grundlage für die folgende Funktionalisierung mit SMMs. Hanle Spin Prezession Messungen reiner Graphen-Spinvalves zeigten Relaxatzionzeiten von $\tau \approx 10^{-11}$ s. Vorläufige Messungen an den SMM funionalisierten Spinvalves weisen auf einen hohen Spin-Transport hin. Obwohl

das Spinsignal nach der Funktionalisierung stark reduziert war konnte ein deutlicher Einfluss der magnetischen Adsorbate festegestellt werden. Insbesondere die Hanle-Kurven bei 300 mK zeigen dabei ein Hystereseverhalten welches von den molekularen Spins herrührt. Weitere Experimente und detaillierte Modellierung können diese Beobachtungen und die Gate-Abhängigkeit der Spinrelaxation erklären.

Chapter 1

Introduction

The world's technological capacity to store and compute information has grown rapidly and steadily over the past few decades [10]. The major driving force of this performance increase has been *device scaling*. In 2014 the information storage density in magnetic hard disc drives touched 1.3 Gbit/mm^2 (Seagate 2014) [1]. At the same time, transistor count in consumer microprocessors reached 16 Million transistors/mm^2, pushing the dimension of the smallest feature down to only 8 nm (Intel 14 nm technology) [2, 3], the size of a single molecule. This length lies already at the *mesoscopic scale*, where quantum phenomena, such as tunneling and interference, start to limit the device performance. To cross this hurdle, and further increase computational and storage capacities, future computer technology will need to rely on different physical principles and novel materials.

A promising approach, called *spintronics* (aka *spin-electronics*), is to use the spin degree of freedom to encode and process information [4–7]. In this context, *graphene* [8, 9], a recently discovered material, exhibits an unprecedented ability to transport spin information over a record length scale of $\lambda_s = 100\,\mu\text{m}$ at room temperature[1] [11]. Moreover, being graphene an all-surface materials, its spintronic properties can be tailored by external means, e.g by combining it with different materials or by decorating its surface with magnetic molecules or atoms [12].

Coupling magnetic systems to graphene charge carriers can offer new ways to electrically manipulate spin-states. Nevertheless, integrating mesoscopic spin-systems in real devices is a challenging task, since the interaction of a spin with a complex environment is difficult to control, and, in general difficult to understand. Two important quantities that characterize the coupling to the surroundings are[2] the *spin relaxation time* T_1 (also indicated with τ) and the *spin coherence time* T_2. The former measures the life time of a classical bit, where the information is encoded in the up- and down spin states, while the latter measures the coherence lifetime of a quantum bit where the information is encoded in the phase of the spin-wavefunction.

This thesis work employs magnetic molecules, belonging to the family of *single molecule*

---

[1]For a given material, the *spin diffusion length* λ_s represents the maximum distance covered by a spin-polarized electron without losing its spin orientation.

[2]T_1 and T_2 are also called *spin population relaxation time* and *phase memory time* respectively

magnets (SMMs) [13], as model systems to study the relaxation of mesoscopic spins on graphene, and their interaction with graphene charge carriers in real devices. Their large uniaxial anisotropy makes SMMs behave like giant spins[3], with relaxation times τ of years at low temperatures [14–16]. Their spin dynamics combines a classical and a quantum relaxation mechanism, that can be selectively switched on and off by either applying an external magnetic field or by varying the temperature [17].

The work is organized as follows. The first part presents a thorough structural characterization of the SMMs-graphene hybrid materials via multiple techniques, including atomic force microscopy, x-ray photoelectrons spectroscopy, mass spectrometry, Raman spectroscopy, and electronic transport measurements on graphene-based field-effect transistors. The analysis of the dynamical arrangement of molecular adsorbates on graphene reveals new opportunities to control the supramolecular surface arrangement. A comprehensive study of the magnetization dynamics of SMMs on graphene is carried out by means of ac-susceptibility techniques in a broad temperature range ($T = 4K$ - 13 mK). The details of the complex spin-graphene interaction are unraveled in the framework of a newly developed theoretical model that accounts for all the possible fundamental contributions and the two-dimensional nature of graphene. The focus of the second part is the design, fabrication and characterization of graphene-based spintronic devices. Different strategies for the injection of spin-polarized carriers in graphene are implemented and tested down to very low temperatures ($T = 300$ mK). To conclude the first spin-transport and spin-relaxation measurements in SMMs-graphene devices are presented.

---

[3]Typically the magnetic moment of their ground state equals several Bohr magnetons.

Bibliography

[1] Seagate Technology. Archive HDD Data Sheet (2014). URL `http://www.seagate.com`.

[2] Bohr, M. 14 nm Process Technology: Opening New Horizons (2014). URL `http://www.intel.com`.

[3] Natarajan, S. *et al.* A 14nm logic technology featuring 2nd-generation FinFET interconnects, self-aligned double Patterning and a 0.0588 μm^2 SRAM cell size. *IEEE International Electron Devices Meeting (IEDM)* 3.7.1–3.7.3 (2014).

[4] Datta, S. & Das, B. Electronic analog of the electrooptic modulator. *Applied Physics Letters* **665**, 10–13 (1990).

[5] Behin-Aein, B., Datta, D., Salahuddin, S. & Datta, S. Proposal for an all-spin logic device with built-in memory. *Nature nanotechnology* **5**, 266–270 (2010).

[6] Datta, S., Salahuddin, S. & Behin-Aein, B. Non-volatile spin switch for Boolean and non-Boolean logic. *Applied Physics Letters* **101**, 252411 (2012).

[7] Zutic, I., Fabian, J., Das Sarma, S. & Sarma, S. D. Spintronics: Fundamentals and applications. *Rev. Mod. Phys.* **76**, 323–410 (2004).

[8] Novoselov, K. S. *et al.* Electric field effect in atomically thin carbon films. *Science* **306**, 666–669 (2004).

[9] Geim, A. K. & Novoselov, K. S. The rise of graphene. *Nat. Mater.* **6**, 183–191 (2007).

[10] Hilbert, M. & Lopez, P. The World's Technological Capacity to Store, Communicate, and Compute Information. *Science* **332**, 60–65 (2011).

[11] Han, W., Kawakami, R. K., Gmitra, M. & Fabian, J. Graphene spintronics. *Nature nanotechnology* **9**, 794–807 (2014).

[12] Geim, a. K. & Grigorieva, I. V. Van der Waals heterostructures. *Nature* **499**, 419–25 (2013).

[13] Gatteschi, D., Sessoli, R. & Villain, J. *Molecular Nanomagnets*. Mesoscopic Physics and Nanotechnology (OUP, Oxford, 2006).

[14] Caneschi, A., Gatteschi, D. & Sessoli, R. Alternating Current Susceptibility, High Field Magnetization and Millimeter Band EPR Evidence for a Ground S=10 State in $[Mn_{12}0_{12}(CH_3COO)_{16}(H_2O)_4)_2CH_3COOH\ 4H_2O$. *Journal of the American Chemical Society* **113**, 5873–5874 (1991).

[15] Barra, A. L. *et al.* Single-Molecule Magnet Behavior of a Tetranuclear Iron(III) Complex. The Origin of Slow Magnetic Relaxation in Iron(III) Clusters. *Journal of the American Chemical Society* **121**, 5302–5310 (1999).

[16] Gatteschi, D., Sessoli, R. & Cornia, A. Single-molecule magnets based on iron(iii) oxo clusters. *Chemical Communications* 725–732 (2000).

[17] Bogani, L. & Wernsdorfer, W. L. Molecular spintronics using single-molecule magnets. *Nat. Mater.* **7**, 179–186 (2008).

Chapter 2

Background Concepts

This thesis work establishes the connection between three fundamental fields, *spintronics*, *molecular magnetism* and *graphene*, that are currently the focus of the scientific community worldwide. In this chapter the main concepts and the unsolved challenges of each topic are introduced together with the basic modeling for the main characteristic phenomena.

2.1 Spintronics

Spin-electronics, aka *spintronics*, aims at using spins to store and compute information [1, 2]. Spintronics finds its roots in a set of fundamental effects involving spin-polarized currents and their interaction with electric charges.

2.1.1 Giant magneto-resistance

The discovery that triggered the development of spintronics is the *giant magneto-resistance* (GMR) effect [3, 4], observable in *all-metallic spin-valve* devices [5–7]. Figure 2.1 shows a current-perpendicular-to-plane spin-valve (CPP-SV) consisting in a non-ferromagnetic metallic thin film (NM) sandwiched between two ferromagnetic electrodes (FM1 and FM2). The thickness L of NM is chosen to be smaller than the electron mean free path λ_e^{NM} of the metal (typically $\lambda_e^{\mathrm{NM}} = 8$ - 30 Å) so that no scattering is expected in NM, and the trilayer resistance R originates uniquely from scattering of carriers in the two ferromagnetic films. R shows a large change, depending on whether the magnetic moments of the two ferromagnetic layers are aligned antiparallel (AP) or parallel (P) by an external magnetic field H. This large magnetoresistance (MR), defined as the maximum change in resistance over the magnetic field range of interest divided by the high field resistance:

$$\mathrm{MR} = \frac{\Delta R}{R} = \frac{(R_{\mathrm{AP}} - R_{\mathrm{P}})}{R_{\mathrm{P}}} \tag{2.1}$$

is a direct evidence of *spin-dependent scattering* in the ferromagnetic layers [8, 9]. Con-

duction electrons in ferromagnetic materials "naturally" exhibit a certain degree of spin-polarization as consequence of exchange-split bands [10–14]. In the following the prefixes *up* and *down* indicate that the electron spin is oriented parallel or antiparallel to the magnetic moment of the ferromagnetic layer respectively.
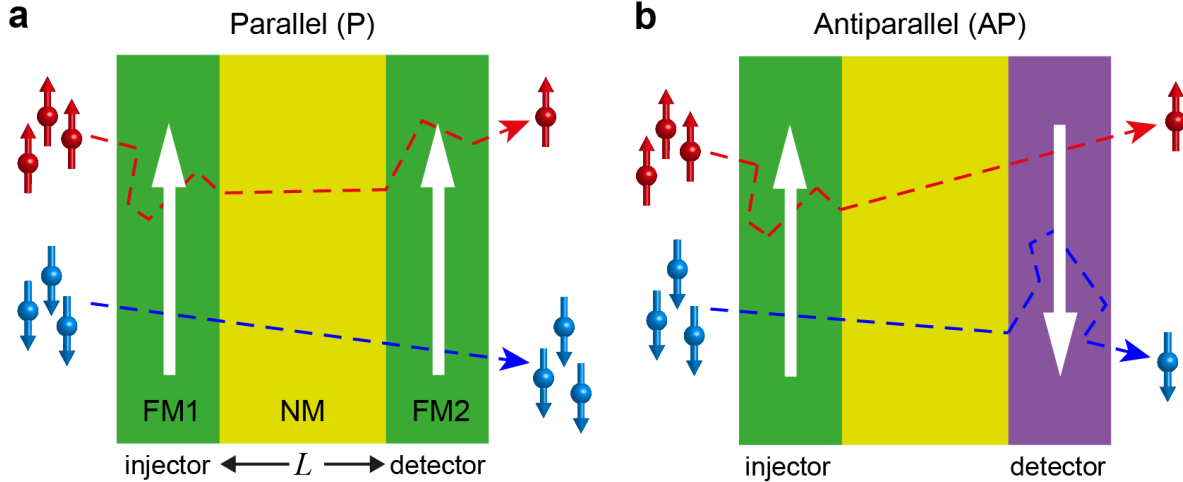
Figure 2.1: Schematic representation of a Current-perpendicular-to-plane *"vertical"* spin-valve, comprising a trilayer film with two identical ferromagnetic layers FM1 and FM2 sandwiching a non-magnetic layer NM. a) Parallel configuration b) Antiparallel configuration.

Assuming $\lambda_{up}^{\text{FM}} << \lambda_{down}^{\text{FM}}$, spin-up electrons have higher probability to experience scattering events than spin-down one. When the two FM contacts are magnetized parallel (P), down-spins move through the sandwich nearly unscattered, as a consequence, a large number of electrons makes it through the trilayer leading to low resistance R_{P} (Figure 2.1a). For antiparallel alignment (AP), both up and down spins experience scattering at either one or the other FM, resulting in a higher device resistance R_{AP} (Figure 2.1b). In other words, the relative alignment of the magnetic moments of the two electrodes affects the flow of spin-polarized currents by altering the overall mean free path of the conduction electrons [15].

An external magnetic field H can be used to control the relative alignment of the FM layers and thus change the resistance of the trilayer, resulting in the *valve-like* behavior shown in Figure 2.2a. At $H = 0$ the FM1 and FM2 magnetic moments are antiferromagnetically coupled to each other by *indirect exchange coupling* J_{12} via the nonmagnetic metal [16–24], Figure 2.2a. The external H-field has to overcome this coupling in order to drive the magnetic moments to parallel alignment. During the magnetization process ($H \neq 0$), R decreases and saturates to a constant value when parallel alignment is reached at $H = H_S$. Magnitude [18, 23] and sign [20] (i.e. ferro/antiferro) of J_{12}, and consequently $\Delta R/R$, are found to oscillate on varying the thickness of the NM interlayer following a RKKY-like function [24, 25] (Figure 2.2b).

CPP-SVs can be used to build very sensitive magnetic field sensors, and find application as
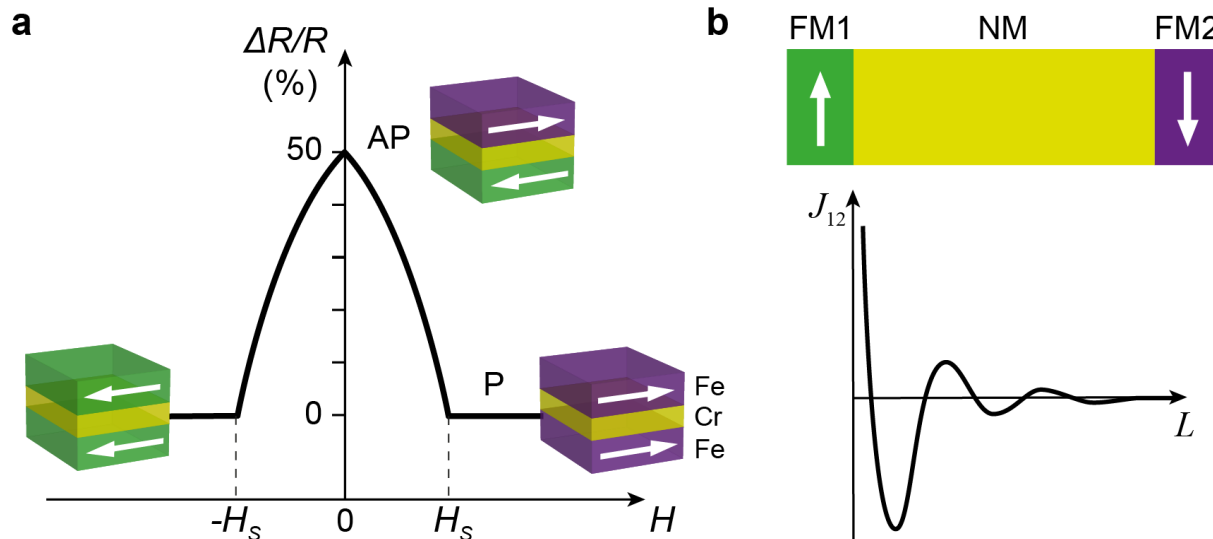
Figure 2.2: a) Typical *"spin-valve"* behavior. Parallel (P) and antiparallel (AP) magnetizations configurations correspond to different resistance levels R_P and R_{AP}. b) Oscillating variation of interlayer exchange coupling J_i with thickness L of the non magnetic layer.

reading elements in the magnetic disc drive (HDD) heads [26–28]. The characteristic quantity which determines the "sensitivity" of the CPP-SV to an external field is the *saturation field H_S*. The larger $\Delta R/R$ and the smaller H_S, the more sensitive the sensor is. A way to increase the sensitivity is to arrange several FM/NM stacks in a multilayer structure, so as to increase the scattering for the up-spins and $\Delta R/R$, Figure 2.3a. Nevertheless, this method is not very effective since also H_S increases accordingly. A more sensitive GMR-sensor can be built by *pinning* the magnetic moment of one FM electrode by placing it in contact with a antiferromagnetic layer, e.g. FeMn , (AF in Figure 2.3b) [20]. The exchange-bias field caused by AF layer induces a uniaxial anisotropy in FM2 that constrains its magnetic moment in the direction perpendicular to the layer plane. As a consequence, the hysteresis loop of FM2 is centered at $B \neq 0$, while the magnetic moment of FM1 is free to move under the influence of the external H-field.

The latter configuration enabled a more detailed understanding of the GMR effect and revealed the different factors controlling $\Delta R/R$. Importantly, further studies demonstrated that spin-dependent scattering occurs mainly at the FM/NM interface, where magnetic states are predominantly localized [29]. Inserting different magnetic atoms at the FM/NM interface enhances the spin-polarization of carriers injected in NM, thus increasing $\Delta R/R$ significantly (Figure 2.3b) [19]. GMR effects are thus largely determined by the details of the ferromagnetic/non-magnetic interface, which extends over a maximum lateral size of only 2 - 3Å [30].
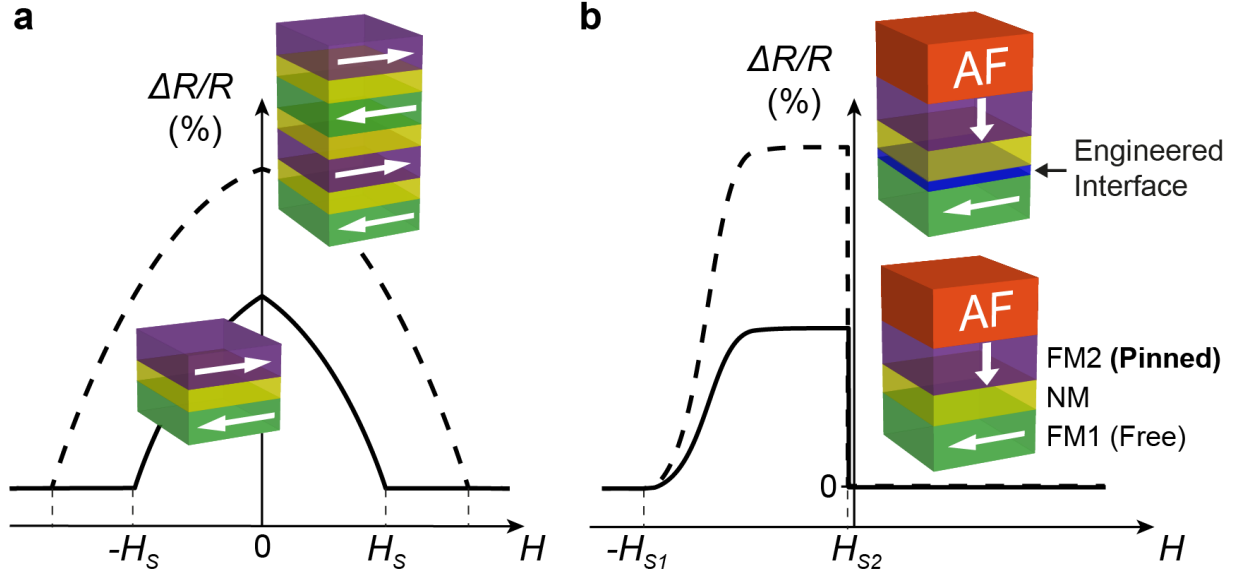
Figure 2.3: Structures with increased $\Delta R/R$. a) Comparison between trilayer and multilayer CPP-SV b) *Uncoupled* SV: the magnetic moment of FM2 is pinned by the exchange bias field induced by the nearby antiferromagnetic layer, while FM1 magnetic moment respond freely to the external H-field. The MR can be enhanced by proper *interface engineering*.

2.1.2 Tunneling magneto-resistance

The interface structure plays an even more important role in the *tunneling magneto-resistance* (TMR) effect in *magnetic tunnel junction* devices (MTJ) [31–35]. MTJs are trilayer CPP-SVs, where a thin insulating (I) barrier replaces the metallic NM interlayer. Similar to all-metallic CPP-SV, the relative orientation of the electrodes magnetic moments controls the flow of spin-polarized carriers, but $\Delta R/R$ reaches much higher values ($\sim 220\%$ for MgO barriers at room temperature) [36, 37]. This large TMR arises from the *spin-dependent tunneling* mechanism. In contrast to all-metallic CPP-SV, in MTJs spin polarized electrons have to tunnel through the insulating barrier. Within the barrier, the electrons wave functions decay evanescently with a *decay length* λ_α, that depends on the wave function symmetry Δ_α [38–41]. Given a certain insulator thickness L, only electron having $\lambda_\alpha > L$ will make it through the barrier, while the others, being strongly attenuated, are filtered out, Figure 2.4a. This mechanism provides the FM/I interface with a *spin-filtering* capability. Indeed, in the bulk ferromagnet, majority and minority spins originate from conduction states with different symmetries Δ_α. A certain spin species will then be more strongly suppressed, leading to an very high spin-polarization:

$$P = \frac{\rho_\uparrow - \rho_\downarrow}{\rho_\uparrow + \rho_\downarrow} \sim 85\% \tag{2.2}$$

where $\rho_\uparrow$ and $\rho_\downarrow$ are the number density of up and down spins respectively.
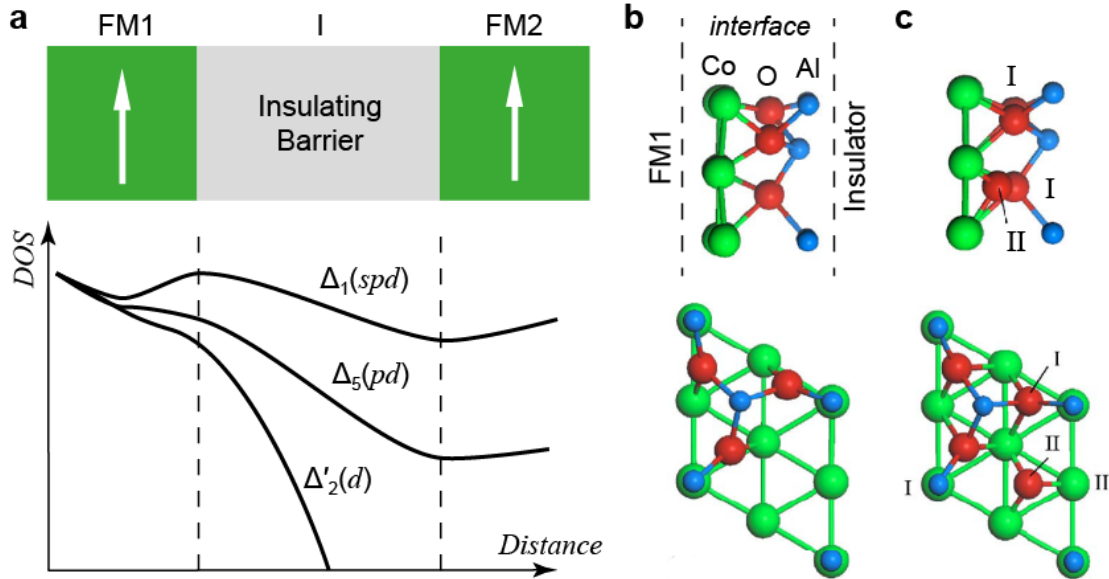
Figure 2.4: Spin-filtering in MTJs. a)Example of density of states for different Bloch-states symmetries decaying at different rates inside the barrier. b) Co-O bonds at the origin of spin-filtering effect in Co/Al$_2$O$_3$ interface. c) Different adsorption geometry of oxygen atoms at the interface (II) have show enhanced spin-polarization. From: [41, 42]

Spin-dependent tunneling varies appreciably at the atomic scale, even for highly metallic surfaces where the electron wave functions are delocalized [43, 44]. A fundamental point is that the tunnel matrix elements that couple the ferromagnet Bloch-states and the insulator evanescent states are modulated by the *chemistry* of the ferromagnet/insulator interface [45–47]. For example, the Co-O covalent bonds in Co/Al$_2$O$_3$/Co MTJs, Figure 2.4b are found to strongly attenuate the transmission of minority spins [42]. Moreover, varying the Co-O bond-strength, by changing the adsorption geometry (Figure Figure 2.4c), is seen to enhance the spin-polarization of the tunneling current, and even change its sign (Figure 2.4c). Therefore, the potential for controlling spintronic effects, such as the interaction between magnetic elements (i.e.*indirect exchange*) and the polarization of spin-currents (i.e.*spin-filtering* effect), relies on the ability to *engineer* the properties of the interface at the nanoscale.

2.1.3   Towards molecular-spintronics

In this regard, the possibility of using *magnetic molecules* to tailor the interface properties is attracting increasing interest [48]. For istance, hybridization of the molecular orbitals with the spin-polarized bands of a ferromagnetic surface creates new interface states that increase the spin-dependent interface resistance in MJTs, i.e. *interface magnetoresistance* (IMR) effect [49–52]. The tools of *molecular synthesis* provide new ways to control spin-

tronic effects down to the single molecule level, and the opportunity to build spintronic nanodevices where the central active element is a single molecule is now the focus of many research groups worldwide.
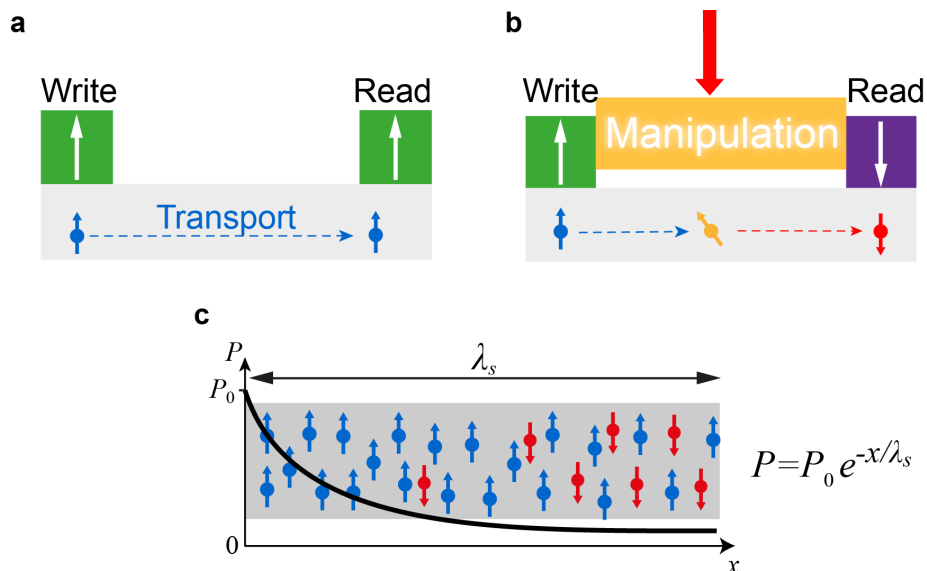
Figure 2.5: Spin relaxation and manipulation. a) Spin transport, the spin has to travel with unaltered polarization over a distance λ_s sufficient to reach the reading element. b) Spin manipulation enabling spin-logic applications. c) The *spin diffusion length* λ_s is limited by spin-flip mechanisms that bring an unbalanced spin population (left) back into equilibrium (right).

2.1.4   Spin relaxation of conduction electrons

Spintronic phenomena are yet used to store and read information in magnetic storage devices. Nevertheless, their application may not be limited to this, as they can bring some notable advantages also for logic applications [53–56]. For instance, electrons have a relatively large *spin memory*, that is conduction electrons retain their spin state much longer than their momentum. In a typical metal, momentum coherence is lost after about ten femtoseconds, while spin coherence can survive for more than a nanosecond [57]. This means that the length λ_s, called *spin diffusion length*, over which electrons conserve their spin-polarization is much longer than the mean free path l_e, over which they conserve their momentum. Intuitively, devices based on diffusion of spins may thus require less power than devices based on charge drift [58].

As seen in CPP-SVs, the information (*up* or *down* magnetization) stored in a magnetic layer can be encoded, via *spin-injection*, in the spin of conduction electrons flowing in the NM channel (Figure 2.5a). Once the spins have reached the other side of NM, a second ferromagnetic element "reads" the information (*spin-detection*), translating it into two

resistance values R_P and R_{AP}. In order to perform logic operations, the spin information needs to be manipulated in its way towards the reading element (Figure 2.5b) [59]. It is therefore essential to find materials in which spins can retain their polarization over a length λ_s sufficiently large to allow their manipulation. λ_s is an intrinsic property of the channel material, describing the *spin-relaxation* (*spin-flip*) mechanisms that cause loss of spin-polarization, thus bringing the unbalanced spin population back into equilibrium $(\rho_\uparrow \neq \rho_\downarrow, P \neq 0) \rightarrow (\rho_\uparrow = \rho_\downarrow, P = 0)$, Figure 2.5c [2, 57]. Equivalently, spin-flip processes can be described by a *spin-relaxation time τ*, that corresponds to the spin-lattice relaxation time $T_1 = \tau$ [2].

The major cause of spin-relaxation in metals and semiconductors is spin-orbit coupling (SOC), a phenomenon originating from the relativistic transformation of electric and magnetic fields for a moving electron and from the Thomas precession [60]. In the reference frame of an electron moving in a crystal, the lattice electric potential acts as an effective magnetic field B_{eff}. The latter couples to the electron spin via the Zeeman interaction, thus coupling the spin to the electron orbital motion [61]. Depending on the symmetry properties of the crystal, SOC can give rise to different spin-relaxation mechanisms [57]:

- *D'yakonov-Perel' mechanism* [62, 63]. For bulk crystals lacking inversion symmetry, the SOC assumes the *Dresselhaus form* [64] and lifts the spin-degeneracy of electrons states $E_\uparrow(\mathbf{k}) \neq E_\downarrow(\mathbf{k})$, i.e. spin-up and spin-down electrons have different energies even if they are in the same momentum state $\mathbf{k}$. This can be pictured as an internal *momentum-dependent* magnetic field $\mathbf{B}(\mathbf{k})$ that induces precession of spins with momentum $\mathbf{k}$ along a direction perpendicular to the electron trajectory and the crystal electric field. As a consequence, a momentum scattering event $\mathbf{k} \rightarrow \mathbf{k}'$ cause the spin to change its precession axis $\mathbf{B}(\mathbf{k}) \rightarrow \mathbf{B}(\mathbf{k}')$, with back-scattering events causing a complete spin-flip. Since the spin relaxation happens *between* two scattering events, the spin relaxation time T_1 is inversely proportional to the momentum scattering time:

$$T_1 \propto 1/\tau_e \tag{2.3}$$

meaning that the more the electron is scattered the less its spin flips on average. The application of an external magnetic field reduces the effect of the D'yakonov - Perel' mechanism.

- *Elliott-Yafet relaxation* [65, 66]. In crystals with inversion symmetry, SOC does not remove the spin-degeneracy $E_\uparrow(\mathbf{k}) = E_\downarrow(\mathbf{k})$, but still affects the electron wavefunctions introducing mixing of spin-up and spin-down Bloch states. As a consequence, the Bloch states are not pure spin-eigenstates, but linear combinations of spin-up and spin-down components. The interaction with lattice ions (i.e. lattice vibrations [67–69], magnetic and non-magnetic impurities [69] and other electrons [70]) modulates this mixing, inducing a complete spin-flip after several ($\approx 10^5$) scattering events. T_1 is then proportional to the momentum scattering time:

$$T_1 \propto \tau_e \tag{2.4}$$

Other relaxation mechanisms involve the *electron-hole exchange interaction* (Bir-Aronov-Pikus mechanism) [71]or the nuclear *hyperfine field* [72],

For systems with spatial confinement, such as a two-dimensional electron gas (2DEG), the confinement potential induces an additional SOC term of *Rashba type* [73, 74]. The Rashba and Dresselhaus SOCs can be tuned by an external electric field [75] thus giving the possibility of electrically manipulate the spin-state and opening the way to spintronic logic architectures [53].

2.2   Single Molecule Magnets

Single molecule magnets (SMMs) [76, 77] are nano-sized magnetic molecules whose magnetic behavior exhibits both classical [78] and quantum features [79–81]. At low temperatures, they behave like non-interacting *giant spins* (i.e. super-paramagnetic particles) with long magnetic relaxation times at low temperature ($\sim$ 2 months at $T = 2K$).
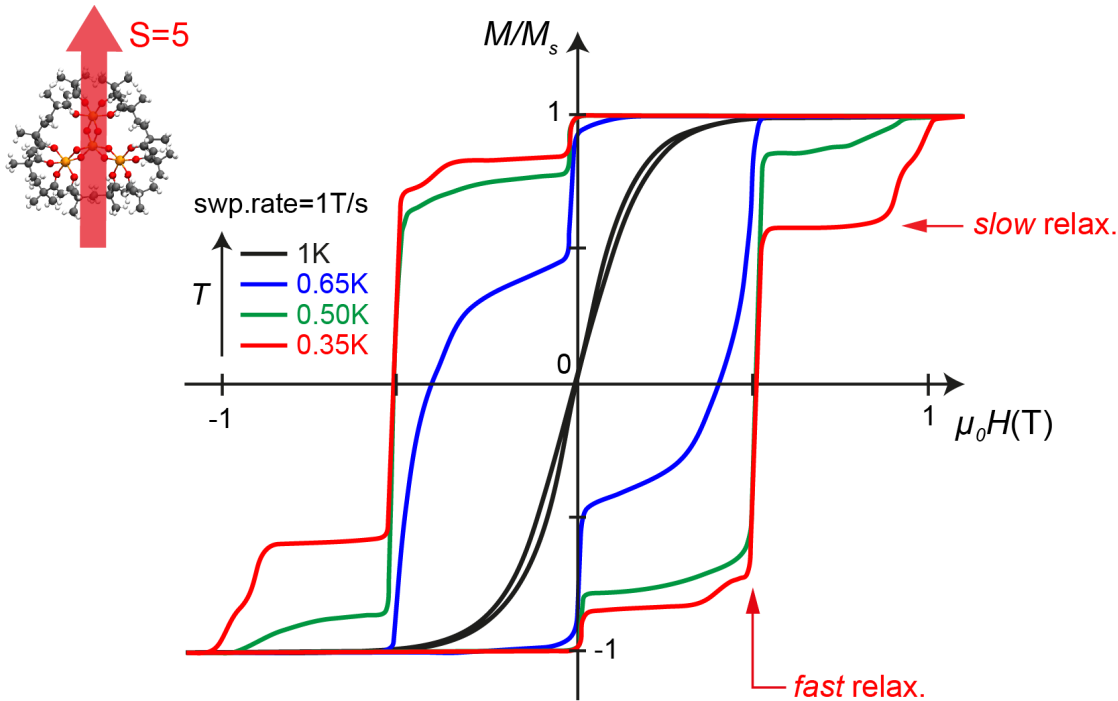
Figure 2.6: Dynamic hysteresis loop of a Fe_4 SMM single crystal for different temperatures [82]. The hysteresis loop opens at about 1K. Step-like features are due to quantum tunneling of the magnetization. Flat regions indicate slow relaxation of the magnetization, while vertical steps correspond to faster relaxation enhanced by resonant quantum tunneling. Inset: Structure of the Fe_4 SMM that behave as a giant spin $S = 5$.

Their Ising-like magnetic anisotropy stems from the *intra*molecular ligand field and gives rise to a dynamic hysteresis loop [78] that bears clear evidence of resonant quantum tun-

neling (QT) [80], Figure 2.6. The latter is enabled by both *intrinsic* (e.g. distortion of the molecular structure) [83, 84] and *extrinsic* (e.g. interaction with the surrounding) factors [85–89].

The way the interaction with the surrounding influences quantum tunneling is one of this thesis main focuses.

2.2.1 Bottom-up vs. top-down nanomagnets

Being bottom-up objects, SMMs possess some fundamental advantages compared to other top-down nano-objects (e.g. magnetic nanoparticles). First of all, they are *monodispersed* and can be arranged in large single crystals. This affords exceptionally clean magnetic properties, without any broadening due to size dispersion and offers the unique opportunity to study quantum phenomena in very high detail in macroscopic samples. For instance, quantum interference and Berry phase phenomena were reported [79, 81] and considered as milestone in spin physics.

The other important advantage is the opportunity to design and add new functionalities at will [92–94]. For example, the molecular structure can be equipped with different functional groups to integrate the SMM in an new environment (e.g. gold surfaces [95], carbon-based materials [82, 93] or single-molecule junctions [96] or to couple two or more SMMs to each other [97, 98]). Adjusting the linking groups is found to control the coupling to the environment both electrically and magnetically, with important effects on the molecular quantum features [99, 100].

An outstanding example of the high level of control achievable on both structural and magnetic features and the role played by quantum properties is that of Cr_7Ni dimers of general formula $[\{Cr_7NiF_3(Etglu)(O_2CtBu)_16\}_2L]$, where the Ni site allows changing the linking group L systematically [91, 97]. These dimers included different hetero-aromatic linkers, such as pyrazine (*pyr* in short), bidimethylpyrazolyl (*bipz*), 4,4'-bipyridyl (*bipy*), trans-1,2-bipyridylethene (*bipyet*) and bipyridyltetrazine (*bipytz*), as in Figure 2.7b. These groups differ primarily in: (1) length (ranging from 7 Å for *pyr* to 15 Å of *bipytz*), (2) dihedral (torsional) angle between the aromatic cycles (from 28° in *bipytz* to 56° in *bipz*), and (3) number of simple covalent σ bonds between the hetero-aromatic groups.

DFT calculations [91, 101] revealed that, in general, the magnetic interaction is maximum when the overlap (both spatial and in energy) between the spin-polarized orbitals of the Ni site and the orbitals of the N linker atoms is maximized. Moreover, the π orbitals propagate the spin-polarization along the linker group more effectively than σ orbitals. Comparing the different linkers evinced that the spin polarization propagates through them following a few general criteria. First of all, the spin polarization alternates moving from each atom to the next along the linker. This implies that it is possible to impose either ferromagnetic (FM) or antiferromagnetic (AFM) coupling between the two molecular spins by choosing a linker structure which enables bond pathways containing either an odd or even number of atoms respectively. Furthermore, when the linker structure (e.g. *bipz*) supports both even and odd numbered pathways, imparting AFM and FM coupling simultaneously, destructive
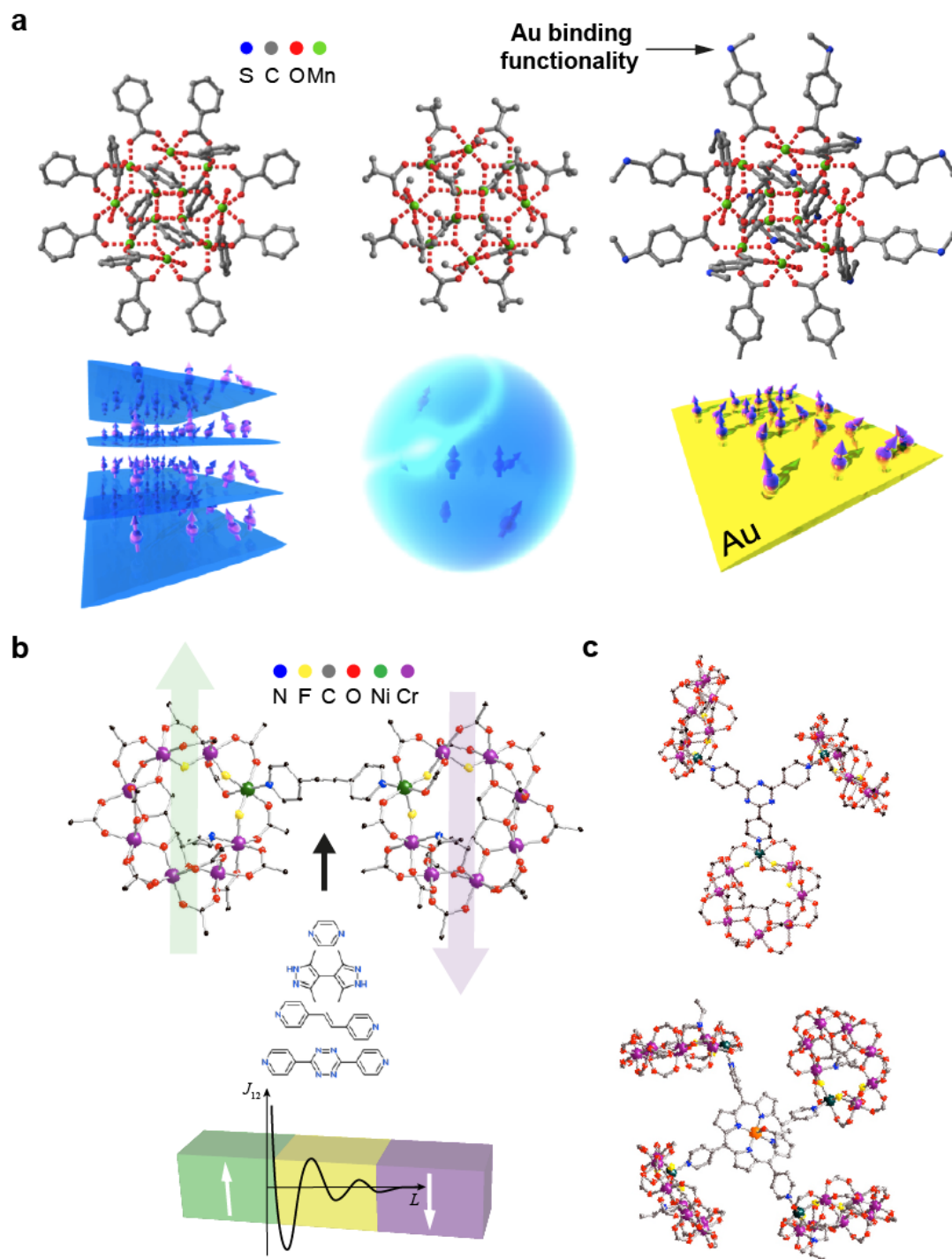
Figure 2.7: Chemical tailoring of SMMs. a) Mn_{12} SMM functionalized for different environments , *from left to right*: Langmuir-Blodgett films, polymers and Au surface *From*: [88]. b) Substituting the linker in a Cr_7Ni dimer tunes the exchange coupling. *From*: [90, 91]. c) *top*: trimer of Cr_7Ni clusters *bottom*: four Cr_7Ni clusters linked via a group sporting a Cu center.

interference between the two paths reduces considerably the spin polarization in the middle of the linker. This explains why the cross-talking between the two molecular spins is weaker for *bipz*, despite it being shortest. In the case of linkers containing more than one aromatic ring, the dihedral angle θ_d between the conjugated rings is found to play an important role in tuning the spin coupling [102]. The exchange coupling constant between two molecular spins is found to obey a $\cos^2(\theta_d)$ trend, reaching the maximum value for coplanar rings. Importantly, the electrical conductance of *biphenyl* junctions was found to follow the same angular behaviour, [103] establishing a fundamental parallel between electron transfer mechanisms and magnetic coupling.

2.2.2   Static properties and the spin Hamiltonian of SMMs

Figure 2.8 shows the molecular structure of the $[Fe_4(OMe)_6(dpm)_6]$ SMM, (shortly:Fe$_4$) [104, 105], sporting a magnetic core of four Fe^{3+} ions arranged in a triangular structure, and surrounded by a shell of *dpm* ligands (*dpm*= deprotonated dipivaloylmethane).
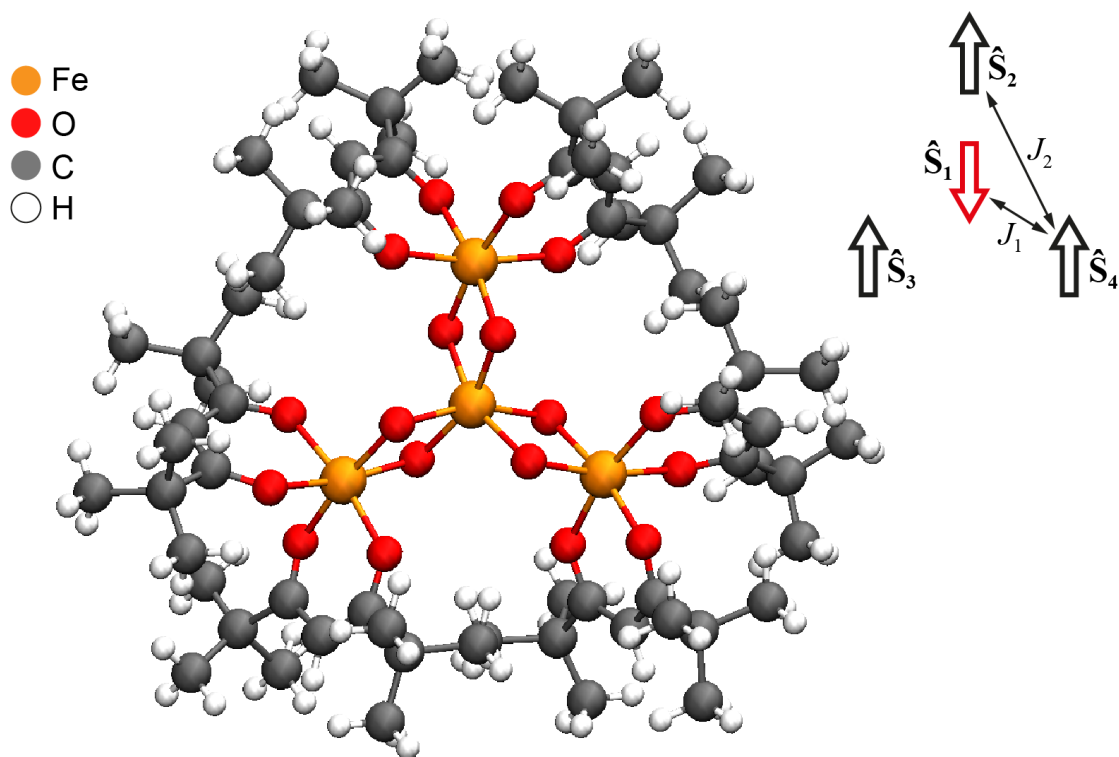
Figure 2.8: Molecular structure of $[Fe_4(OMe)_6(dpm)_6]$ single molecule magnet (hydrogens in OMe have been omitted for clarity). The four Fe^{3+} ions are coordinated with Oxygen in a propeller-like structure. The structure is stabilized by dpm$^-$ ligands. Inset: the magnetic ground state resulting from the interplay between the antiferromagnetic J_1 and the ferromagnetic J_2.

The temperature dependence of the product $\chi_{\mathrm{m}}T$ (where $\chi_{\mathrm{m}} = M_{\mathrm{m}}/H$ is the molar magnetic susceptibility, M_{m} is the molar magnetization, H is the external magnetic field and T the sample temperature) is characteristic of antiferromagnetically coupled systems in which the spin topology does not allow full compensation of the magnetic moments [104, 106]. Indeed by lowering the temperature, the product $\chi_{\mathrm{m}}T$ shows a decreasing trend down to 100 K indicative of antiferromagnetic coupling [107], after which $\chi_{\mathrm{m}}T$ increases reaching a maximum value of about 15 emu K mol^{-1} at 10 K, matching the Curie constant of a spin state $S = 5$.

This behavior indicates that below 100 K the excited magnetic states are gradually emptied till only the ground state remains populated at about 10 K, meaning that below this temperature the Fe$_4$ molecule behaves like a single giant spin with $S = 5$.

The above picture is also confirmed by the isothermal molar magnetization M_{m} at low temperatures (inset of Figure 2.9), which approaches the saturation value $M_{\mathrm{m}} = 10N_{\mathrm{A}}\mu_B$ at fields > 4 T, matching the expected value for a spin $S = 5$.
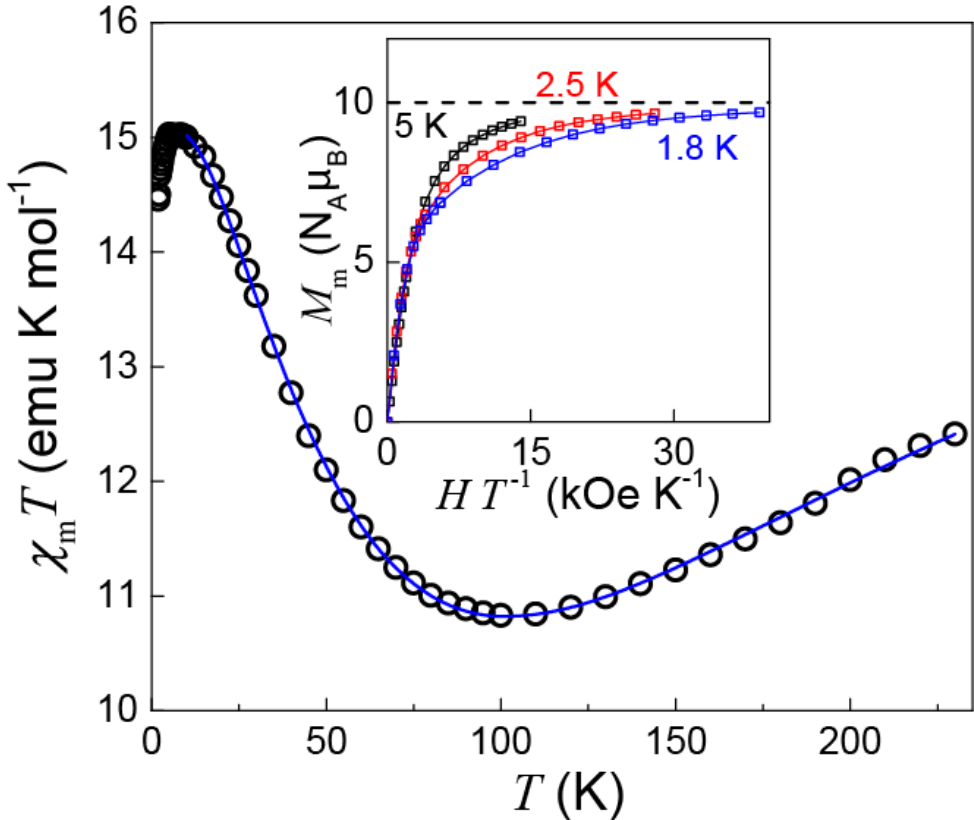
Figure 2.9: Temperature dependence of the product $\chi_{\mathrm{m}}T$ for a Fe$_4$ powder sample, measured at $H = 1$kOe. The blue line is a fitting with the Heisenberg Hamiltonian (2.5) comprising two exchange constants. Inset: isothermal molar magnetization M_{m} of the same sample at three different temperatures, 1.8K, 2.5K and 5K, lines are fit with Equation (2.6).

Modeling of the above static response helps understanding the magnetic structure of the cluster. The core magnetic ions are magnetically super-exchange coupled via the methoxo ligands. Since each Fe^{3+} ion bears a spin $s = 5/2$, the observed $S = 5$ suggests that the central Fe^{3+} ion is antiferromagnetically coupled to the peripheral ones, while the latter are ferromagnetically coupled to each other, see inset Figure 2.8. Fitting of $\chi_m T$ vs. T curve allows quantifying the intra-molecular magnetic interactions, blue line in Figure 2.9. It can be analyzed considering a Heisenberg Hamiltonian comprising four spins coupled by two exchange interactions [76, 92]:

$$\mathcal{H} = J_1 \left(\hat{\mathbf{S}}_1 \cdot \hat{\mathbf{S}}_2 + \hat{\mathbf{S}}_1 \cdot \hat{\mathbf{S}}_3 + \hat{\mathbf{S}}_1 \cdot \hat{\mathbf{S}}_4 \right) + J_2 \left(\hat{\mathbf{S}}_2 \cdot \hat{\mathbf{S}}_3 + \hat{\mathbf{S}}_3 \cdot \hat{\mathbf{S}}_4 + \hat{\mathbf{S}}_2 \cdot \hat{\mathbf{S}}_4 \right) + g\mu_B \hat{\mathbf{S}} \cdot \hat{\mathbf{H}} \quad (2.5)$$

where $\hat{\mathbf{S}}_1$ is the spin operator for the central spin interacting via J_1 with the peripheral $\hat{\mathbf{S}}_2$, $\hat{\mathbf{S}}_3$, $\hat{\mathbf{S}}_4$ spins while the latter are coupled to each other via J_2. The third term in (2.5) takes into account the Zeeman interaction between the fixed external magnetic field $\hat{\mathbf{H}}$ and the spin total spin $\hat{\mathbf{S}}$, where the g stands for the Landé g-factor and μ_B is the Bohr magneton. Best fit procedure gives $J_1 = 14.84(3)$ cm^{-1} and $J_2 = 0.088(18)$ cm^{-1} with $g = 2.0037(7)$, revealing the dominance of the antiferromagnetic nearest-neighbor interaction J_1.

Even though below 10 K the system behaves like a single giant integer spin, the M_m vs. H characteristic cannot be fitted with a single paramagnetic Brillouin function, suggesting the existence of *magnetic anisotropy*. Given the D_3 symmetry of the Fe$_4$, the magnetic anisotropy can be described by a *spin Hamiltonian* (see the next paragraph or further details) that models the crystal field acting on the core magnetic ions by a uniaxial anisotropy term [76]:

$$\mathcal{H} = D\hat{S}_z^2 \quad (2.6)$$

where $\hat{S}_z$ is the z component of the spin operator and D is the uniaxial anisotropy constant[1]. By including the effect of an external magnetic field in the model:

$$\mathcal{H} = D\hat{S}_z^2 + g\mu_B \hat{\mathbf{S}} \cdot \hat{\mathbf{H}} \quad (2.7)$$

and averaging over all possible crystal orientations (being the above measurements for a polycrystalline sample), best fit to M_m vs. H affords:

$$D = -0.350(5)\,\text{cm}^{-1} \quad g = 2.004(3)$$

The above observations, show that the low-temperature magnetic properties of SMMs are dominated by the presence of a large *Ising-type* uniaxial magnetic anisotropy, which, by

---

[1]An equivalent version [76] of equation 2.6 is :

$$\mathcal{H} = D\left[\hat{S}_z^2 - \frac{1}{3}S(S+1) \right] + g\mu_B \hat{\mathbf{S}} \cdot \hat{\mathbf{H}}$$

In this form the D tensor is diagonal in the basis of the eigenvalues $|m\rangle$ of the operator $\hat{S}_z$
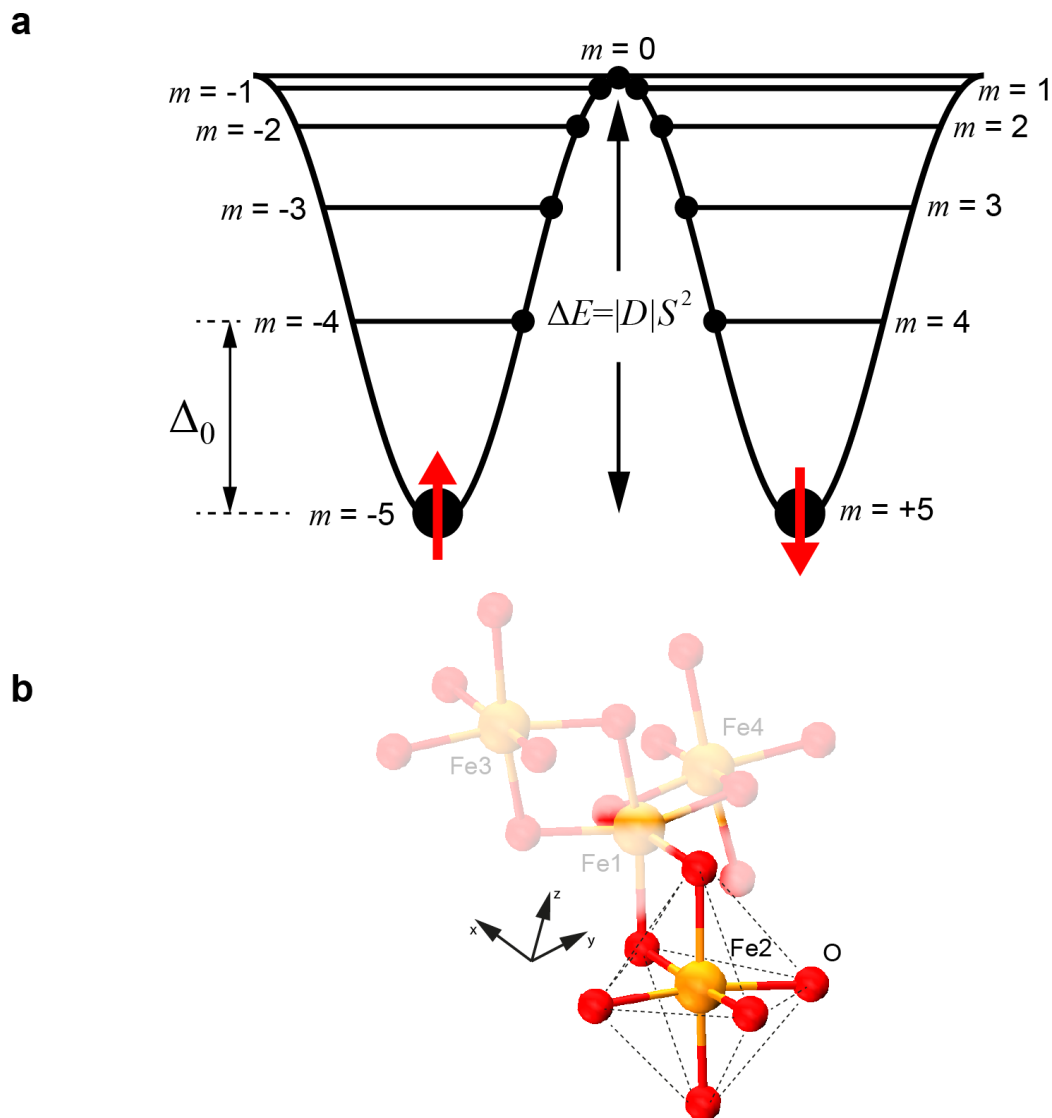
Figure 2.10: a) Parabolic energy barrier $\Delta E = |D|S^2$ for the lowest lying spin multiplet $S = 5$. The different $(2S+1)$ m spin levels are distributed in energy according to the zero-field splitting and form a *double-well potential* landscape. Here $\Delta_0 = (2S - 1)D$ indicates the ZFS between the lowest two-fold degenerate levels $m = \pm 5$ and the levels $m = \pm 4$. b) The distorted octahedral environment around one of the Fe^{3+} ions.

breaking the rotational symmetry, partially lifts the $2S + 1$ degeneracy of the ground multiplet S and creates an energy barrier:

$$\Delta E = |D|S^2 \tag{2.8}$$

that separates $|m\rangle$ and $|-m\rangle$ sublevels, Figure 2.10a.

This *zero-field splitting* (ZFS) provides a beautiful example of how the surroundings of an atom profoundly affect its magnetic state and determines its actual magnetic response. In the Fe_4 core for instance, each Fe^{3+} ion is coordinated with six Oxygen atoms in a distorted octahedral environment, Figure 2.10b. The crystal-field of the latter partially removes the degeneracy of the Fe^{3+} d orbitals, splitting them in the two subsets e_g and t_{2g} by Δ_0. The resulting zero-field splitting Δ_0, gives rise to the so-called *single-ion anisotropy*. Having Fe^{3+} a $3d^5$ electronic configuration, the t_{2g} orbital is half-filled imposing quenching of the angular momentum. In the next paragraphs, we will see that quenching of the angular momentum enables a detailed modelling of the spin anisotropy based on the *spin Hamiltonian* approach.

2.2.3 Modeling the anisotropy

In the SMM core, the electronic density distribution ρ_e surrounding the magnetic ions creates a local electric field of given symmetry. This field acts on the orbital component of the magnetic ions (the d electrons of the Fe ions, in the Fe_4 case), giving rise to the magnetic anisotropy. The crystal field potential can be expressed as a sum of spherical harmonics of progressively higher symmetry[2] [108–111]:

$$\mathcal{H}_{sp} = \sum_{i,j} B_i^j \hat{O}_i^j \tag{2.9}$$

with the indexes:

$$i = 2, 4, ..., 2S$$
$$\tag{2.10}$$
$$-i \leq j \leq +i$$

where S is the molecular spin.

The $\hat{O}_i^j$ terms, called Stevens operator equivalents, represent the spherical harmonics as a sum of equivalent angular momentum operators, Figure 2.11.

They contain the jth power of the spin ladder operators $\hat{S}_\pm = \hat{S}_x \pm i\hat{S}_y$ and the $(i-j)^{th}$ power of the spin operator $\hat{S}_z$, which effect on the eigenvectors $|m\rangle$ is:

$$\hat{S}_z|m\rangle = m|m\rangle \tag{2.11}$$

---

[2]Equation (2.9) is a generalization of Equations (2.6). In particular: $D = 3B_2^0$ [76]
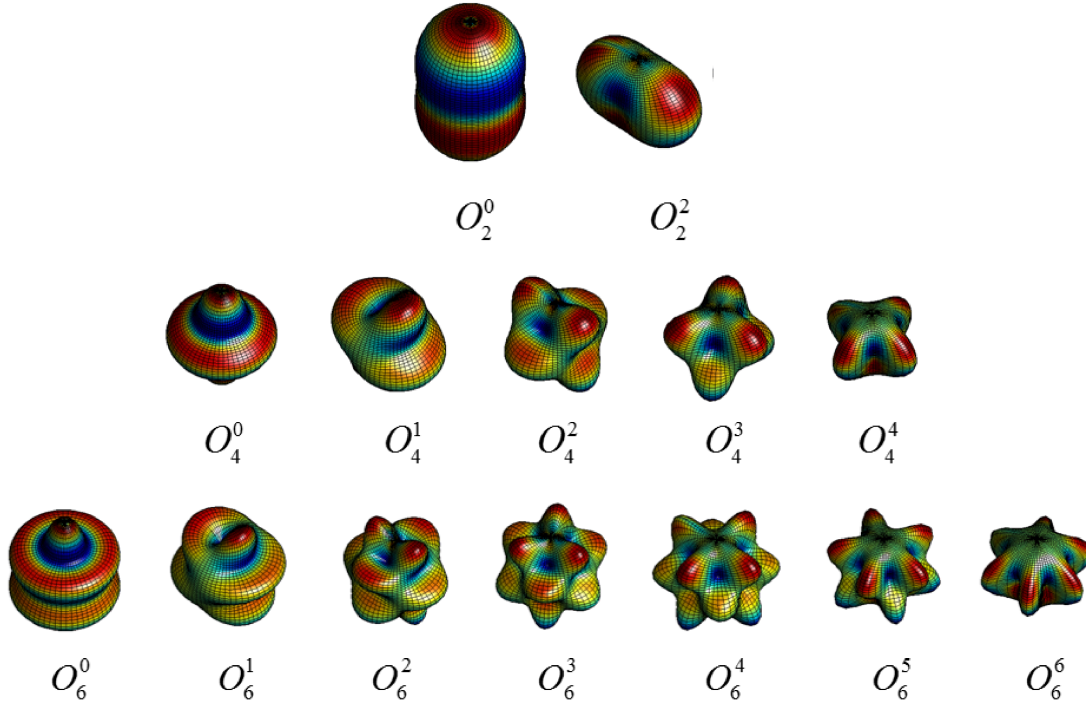
Figure 2.11: The shape of the spherical harmonics associated to each of the Stevens operators, up to the sixth order.

$$\hat{S}_{\pm}|m\rangle = \sqrt{S(S+1) - m(m \pm 1)}|m \pm 1\rangle \qquad (2.12)$$

Each $\hat{O}_i^j$ term is weighted by a coefficient B_i^j that vanishes for the $\hat{O}_i^j$'s not belonging to the point group of the molecular structure.

Equation (2.9) subdivides the spin anisotropy into different contributions, each having the symmetry of a corresponding spherical (tesseral) harmonic. Terms with $j = 0$ contain powers of $\hat{S}_z$ only and contribute to the energy barrier ΔE separating $|m\rangle$ states of opposite magnetic moment, but do not mix the $|m\rangle$ eigenstates [76], Figure 2.12a. On the contrary, terms with $j \neq 0$, containing the jth power of the ladder operators, mix $|m\rangle$ states differing in m by a multiple of j, and enable the quantum tunneling (QT) mechanism [83, 87] for spin-relaxation discussed in the next section. Examples of $\hat{O}_i^j$ operators with associated spherical harmonics are reported in Table 2.1.

Important note: Stevens' formalism non only provide an effective framework to model the magnetic anisotropy, but it also allows to model the effect of any external electric field, including that of the electron density in an underlying substrate, on the spin anisotropy, As discussed in Chapter 6, the effect of graphene charge density on the spin anisotropy will be modeled by introducing $B_i^j \hat{O}_i^j$ terms of corresponding symmetry in the sum (2.9), and discarding all terms not belonging to the point group of the spin environment.

The core of the tetrairon cluster Fe_4 is a model spin with $S = 5$, whose crystal field reflects the equilateral triangle D_3 symmetry, for which Equation 2.9 reads:

$$Y_2^0 = \frac{1}{4}\sqrt{\frac{5}{\pi}}\frac{3z^2 - r^2}{r^2}$$

$$\hat{O}_2^0 = 3\hat{S}_z^2 - S(S+1)$$

$$Y_4^0 = \frac{3}{16}\sqrt{\frac{1}{\pi}}\frac{35z^4 - 30z^2 r^2 + 3r^4}{r^4}$$

$$\hat{O}_4^0 = 35\hat{S}_z^4 - [30S(S+1) - 25]\hat{S}_z^2 - 6S(S+1) + 3[S(S+1)]^2$$

$$Y_2^{\pm 2} = \frac{1}{4}\sqrt{\frac{15}{2\pi}}\frac{(x \pm iy)^2}{r^2}$$

$$O_2^2 = \frac{1}{2}(\hat{S}_+^2 + \hat{S}_-^2)$$

$$Y_4^{\pm 3} = \mp\frac{3}{8}\sqrt{\frac{35}{\pi}}\frac{(x \pm iy)^3 z}{r^4}$$

$$\hat{O}_4^3 = \frac{1}{4}[\hat{S}_z(\hat{S}_+^3 + \hat{S}_-^3) + (\hat{S}_+^3 + \hat{S}_-^3)\hat{S}_z]$$

Table 2.1: Spherical harmonics and associated operator equivalents describing the spatial distribution of the crystal field around each Fe^{3+} site in the Fe_4 core.

$$\mathcal{H}_{\mathrm{sp}} = B_2^0\hat{O}_2^0 + B_4^0\hat{O}_4^0 + B_2^2\hat{O}_2^2 + B_4^3\hat{O}_4^3. \tag{2.13}$$

The higher order terms, $B_4^0\hat{O}_4^0$ and $B_4^3\hat{O}_4^3$, belong to the D_3 point group while the term $B_2^2\hat{O}_2^2$ does not belong to D_3 point group symmetry but it is necessary for a correct interpretation of neutron scattering data [112], and it may be due to distortions of the equilateral triangle in close packed single crystals [113, 114]

For Fe_4Py, used later in this work, electron paramagnetic resonance (EPR) studies yield [82]:

$$\begin{aligned}
B_2^0 &= -0.194\,\mathrm{K} \\
B_4^0 &= 3.45 \times 10^{-5}\,\mathrm{K} \\
B_2^2 &= 0.016\,K \\
B_4^3 &< 6.9 \times 10^{-5}\,\mathrm{K}
\end{aligned} \tag{2.14}$$

The dominant $j = 0$ term $B_2^0 \hat{O}_2^0$ affords the barrier:

$$\Delta E \simeq 3B_2^0 \cdot S^2 = 3B_2^0 \cdot 25 = 14.55\,\text{K} \tag{2.15}$$

2.2.4 Spin relaxation: master equation

The above picture opens up two possible paths for the relaxation of molecular spins [76, 83, 115, 116]:

- *Classical relaxation mechanism*: to reverse its direction, the molecular spin has to overcome the anisotropy barrier by interacting with the surrounding, e.g. absorbing or emitting phonons, Figure 2.12b.

- *Quantum relaxation mechanism*: the molecule reverses its spin via tunneling transition $|m\rangle \rightarrow |-m\rangle$ through the barrier, Figure 2.12c . The finite tunnel probability between degenerate states at opposite sides of the barrier is due to transverse ($j \neq 0$) Stevens terms which mix $|m\rangle$ and $|-m\rangle$ states differing in m by a multiple of j.
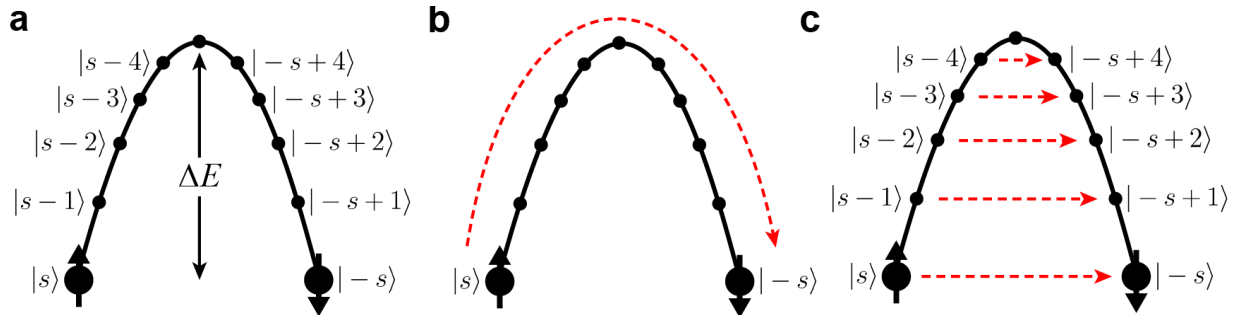
Figure 2.12: Spin relaxation mechanisms for molecular spins. a) Anisotropy barrier originating from crystal field. b) Thermal relaxation machanism. c) Resonant quantum tunneling between degenerate magnetic levels enabled by terms with $j \neq 0$.

The dynamics of a molecular spin can be modeled via the *master equation* [76, 115, 117]:

$$\frac{d}{dt}N_m(t) = \sum_{m'} [W_{m',m}N_{m'}(t) - W_{m,m'}N_m(t)] \tag{2.16}$$

that describes how the probability $N_m(t)$ of being in the state $|m\rangle$ evolves in time due to the above relaxation mechanisms.

$W_{m,m'}$ is the *transition probability* from state $|m\rangle$ to another state $|m'\rangle$ per unit time and it has to be calculated taking into account all the relaxation paths that connect $|m\rangle$ to $|m'\rangle$.

2.2.5 Effect of an external magnetic field

The effect of an external magnetic field applied along the easy axis z is to shift in energy the states $|m\rangle$ and $|-m\rangle$ at the opposite sides of the barrier, Figure 2.13.
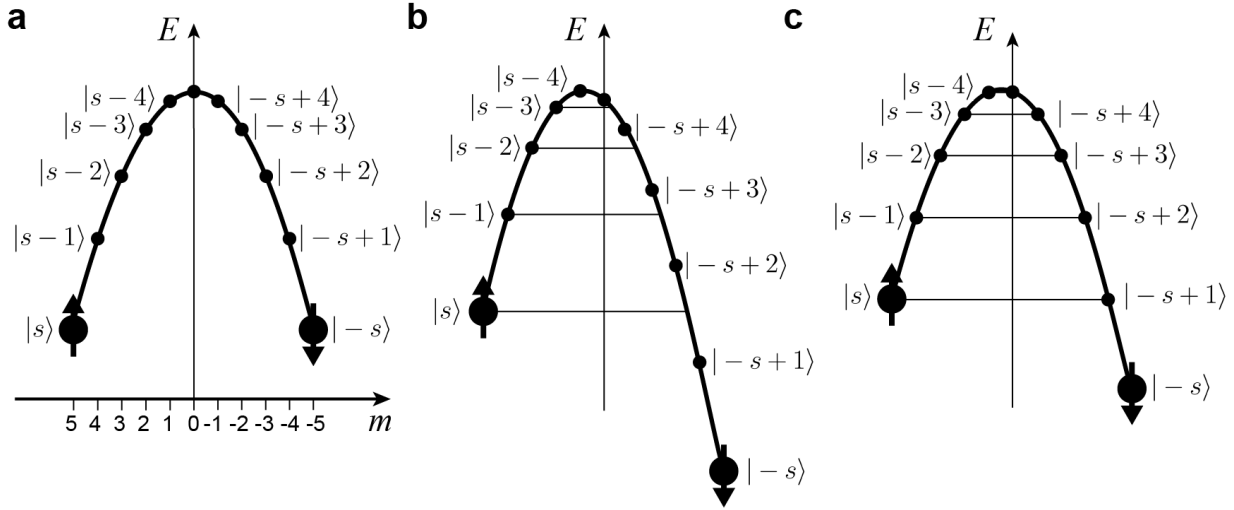
Figure 2.13: Effect of an external magnetic field on the eigenvalues of (2.6). a) For $H_z = 0$, states at the opposite sides of the barrier are degenerate. b) An external field $H_z \neq 0$ removes the degeneracy between the levels. c) For certain field values $H_z = H^{m,m'}$ the degeneracy between some levels is reestablished.

For $H_z \neq 0$, two given eigenvectors $|m\rangle$ and $|m'\rangle$ of the Hamiltonian:

$$\mathcal{H} = D\hat{S}_z^2 + g\mu_B \hat{S}_z H_z \tag{2.17}$$

are degenerate for certain field values $H_z = H^{m,m'}$ called *crossing fields*, Figure 2.13c, for which:

$$g\mu_B H^{m,m'} = D(m + m') \tag{2.18}$$

2.2.6 Thermal relaxation: Arrhenius

The energy barrier ΔE is at the origin of the slow relaxation of the magnetization in SMMs at low temperatures. In order to invert the orientation of its spin, a SMM has to overcome ΔE by exchanging energy with the surroundings, for example via spin-phonon interaction [115] or by hyperfine coupling to the nuclear spins [76]. Lowering the temperature decreases the density of phonons available to the system and the relaxation of the molecule slows down.

The spin dynamics can be explored by measuring the frequency and temperature dependence of the magnetic *ac*-susceptibility:
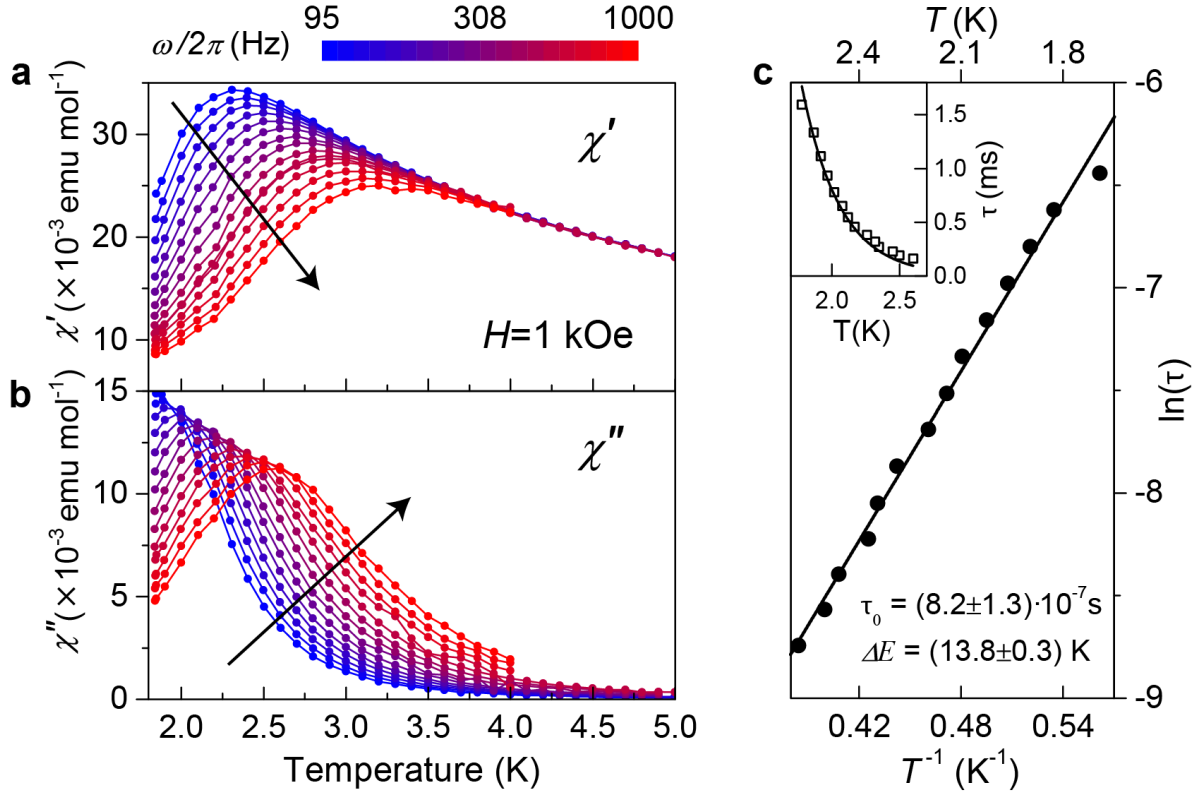
Figure 2.14: Temperature dependence of the dynamic molar susceptibility of Fe_4Py molecule in the T range 1.8 - 5 K, measured at different frequencies at $H = 1$kOe. a) In-phase component of the magnetic susceptibility χ'. b) Out-of-phase component of the magnetic susceptibility χ''. c) Arrhenius plot of the $\ln(\tau)$ vs. temperature reciprocal. Linear fit affords $\tau_0 = (8.2 \pm 1.3) \cdot 10^{-7}$ s and $\Delta E = 13.8 \pm 0.3$ K. Inset: temperature dependence of the relaxation time, line is a single exponential fit.

$$\chi(\nu, T) = \chi'(\nu, T) + i\chi''(\nu, T) \tag{2.19}$$

in response to an oscillating magnetic field with frequency ν. Figure 2.14 shows the real and imaginary components measured on the crystalline Fe_4Py. In order to reveal the pure thermal relaxation mechanism, a small external magnetic field $H = 1$ kOe was applied so as to lift the degeneracy of states at the opposite sides of the barrier and thus suppressing the quantum relaxation channel.

While the *ac*-susceptibility of simple paramagnets do not show any imaginary component χ'', on the contrary, SMMs are characterized by the *slow relaxation of the magnetization* and the appearance of a nonzero χ'' (Figure 2.14b). When the relaxation time τ of the giant spin equals the ac-field period $(2\pi\nu)^{-1}$, a maximum in χ'' is observed. The temperature dependence of τ is then determined by measuring $\tau(T_{\max}) = (2\pi\nu)^{-1}$ at different frequencies, where $T_{\max}$ indicates the temperature value at which the resonance (maximum in χ'')

occurs. In the temperature range 1.5 - 2.6K, Figure 2.14c, the relaxation time increases exponentially on decreasing temperature as for a typical thermally activated relaxation process. This can be described by the Arrhenius law [76, 104]:

$$\tau = \tau_0 \exp\left(\Delta E / k_{\mathrm{B}} T\right) \tag{2.20}$$

which provides the value:

$$\Delta E = 3|B_2^0|S^2 = 13.8 \pm 0.3\mathrm{K}$$

in $H = 1$ kOe in agreement with the teoretical value found above.

The prefactor τ_0 in Equation (2.20) contains information about the specific mechanisms coupling the molecular spins to the environment for which the transition probabilities $W_{m,m'}$ of Equation (2.16) have to be explicitly calculated [104, 115]. A detailed modeling of the spin-phonon interaction will be provided in the Section 6.8.

2.2.7   Cole-Cole model

ac-susceptibility measurements probe the population p_m of the different m levels by measuring the sample's magnetic moment directly:

$$\langle M \rangle = \sum_m p_m M_m \tag{2.21}$$

where p_m is given by the Boltzmann distribution $p_m = \dfrac{1}{Z}\exp\left(-\dfrac{E_m}{k_{\mathrm{B}}T}\right)$ and Z is the system partition function. Under the influence of the ac-magnetic field at frequency ω, the population of of the m states oscillates in time. To reach dynamical equilibrium, the system needs the time τ. Two different regimes are identified. When the H-field oscillation period is much larger than the system relaxation time ($\omega\tau \ll 1$), the measured susceptibility tend to that of a molecule in perfect thermal equilibrium $\chi = \chi_{\mathrm{T}}$, aslo called *isothermal susceptibility*. On the other hand, when the field is faster that the relaxation time ($\omega\tau \gg 1$), equilibrium cannot be reached and susceptibility approaches that of a perfectly isolated spin with no interaction with the surroundings $\chi = \chi_{\mathrm{S}}$, i.e. *adiabatic susceptibility*. In the frequency range between these two regimes, the susceptibility can be modeled by the *Cole-Cole model* [118]:

$$\chi(\omega, T) = \chi'(\omega, T) + i\chi''(\omega, T) = \chi_{\mathrm{S}} + \frac{\chi_{\mathrm{T}} - \chi_{\mathrm{S}}}{1 + (i\omega\tau)} \tag{2.22a}$$

The real and imaginary components are explicitly written:

$$\chi' = \chi_{\mathrm{S}} + \frac{\chi_{\mathrm{T}} - \chi_{\mathrm{S}}}{1 + \omega^2\tau^2} \quad \chi'' = \frac{(\chi_{\mathrm{T}} - \chi_{\mathrm{S}})\omega\tau}{1 + \omega^2\tau^2} \tag{2.22b}$$

The relaxation time of the system can then be extracted from the frequency dependence of χ measured at constant T, Figure 2.15.
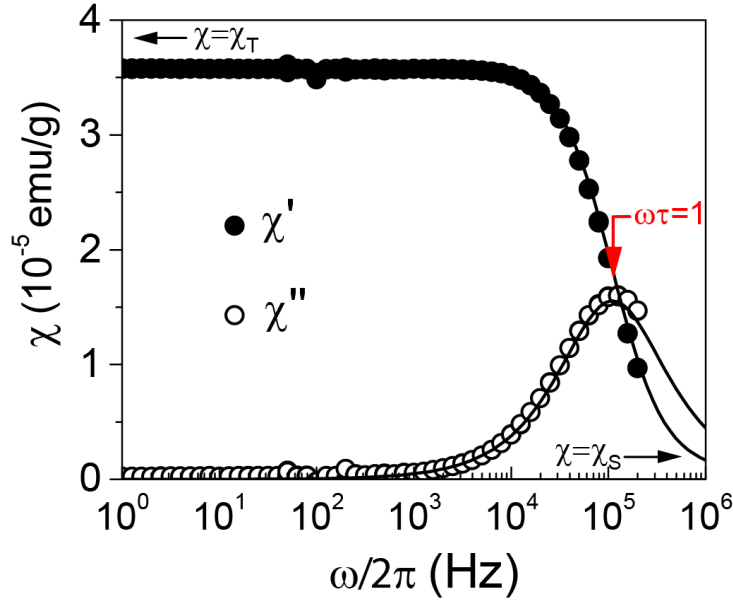
Figure 2.15: Frequency dependence of Fe_4Py dynamic susceptibility, measured at $H = 0$. Solid circles indicate the in-phase component χ', while open circles represent the out-of-phase part χ''. Lines are fit with Equations 2.22

In case the relaxation process, rather than being characterized by a single relaxation time τ, is characterized by a distribution of relaxation times, the Cole-Cole model can be extended as follows:

$$\chi = \chi_S + \frac{\chi_T - \chi_S}{1 + (i\omega\tau)^{1-\alpha}} \tag{2.23}$$

with α representing the broadening of the relaxation time distribution. The real and imaginary components become:

$$\chi'(\omega) = \chi_S + (\chi_T - \chi_S)\frac{1 + (\omega\tau)^{1-\alpha}\sin(\alpha\pi/2)}{1 + 2(\omega\tau)^{1-\alpha}\sin(\alpha\pi/2) + (\omega\tau)^{2-2\alpha}}$$

$$\tag{2.24}$$

$$\chi''(\omega) = (\chi_T - \chi_S)\frac{1 + (\omega\tau)^{1-\alpha}\cos(\alpha\pi/2)}{1 + 2(\omega\tau)^{1-\alpha}\sin(\alpha\pi/2) + (\omega\tau)^{2-2\alpha}}$$

A distribution of relaxation times is associated with the presence of different molecular species (with different ΔE values) in the specimen and it can be used to reveal if a fraction of molecules undergo some structural changes.

2.2.8 Quantum tunneling of the magnetization

The phenomenon of quantum tunneling (QT) of the magnetization is one of the prominent characteristics of single-molecule magnets [77, 119–121]As the temperature is decreased below 0.8 K, the relaxation time τ deviates from the Arrhenius exponential law and becomes temperature independent, indicating that at very low temperatures $T < 0.8K$, thermal relaxation is suppressed and quantum tunneling dominates the relaxation (Figure 2.16a).
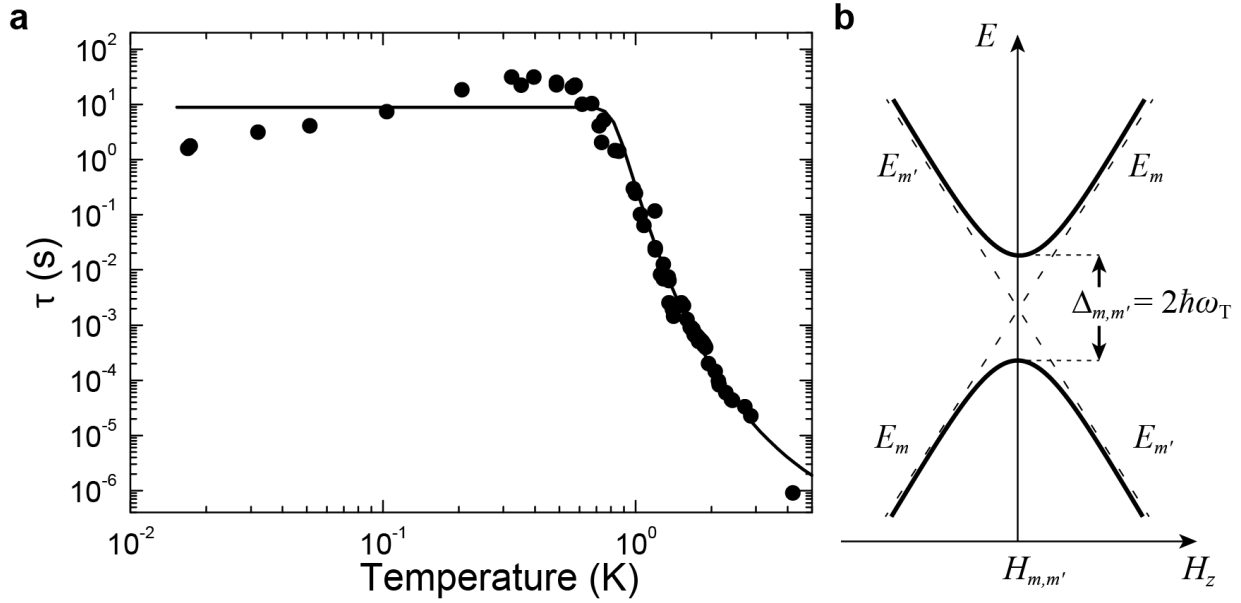
Figure 2.16: Quantum tunneling of spin states. a) Temperature dependence of relaxation time for the Fe_4Py molecule, in $H = 0$. At $T < 0.8$ K quantum tunneling becomes the dominant relaxation mechanism and τ saturates to a constant value. b) Level anticrossing due to mixing of $|m\rangle$ and $|m'\rangle$ states at the opposite sides of the energy barrier.

As anticipated above, *quantum tunneling* between spin states is enabled by transverse fields and transverse terms ($j \neq 0$) in Equation 2.9. In particular, these terms remove the degeneracy of $|m\rangle$ and $|m'\rangle$ at the level crossing fields $H_z = H^{m,m'}$. Thus at $H^{m,m'}$, the spin of the molecule is described by the superposition of the spin states $|m\rangle$ coupled by the anisotropy. This phenomenon is called *mixing of quantum states* and is associated with the so created *level anticrossing* [77, 79, 115, 117]. The degeneracy is lifted by the quantity $\Delta_{m,m'}$ called *tunnel splitting*, Figure 2.16b. The absence of actual crossing causes the spin wavefunction φ to *delocalize* over the two sides of the barrier (i.e. the modulus $|\varphi|$ has two maxima at $m < 0$ and $m' > 0$), in other words the spin *tunnels* through the barrier.

At level anticrossings $H^{m,m'}$ the spin oscillates between the left and right sides of the energy barrier and exhibits a much faster relaxation rate which reveals itself as vertical steps in the hysteresis loop, Figure 2.6. The *tunneling frequency* $\omega_T^{m,m'}$ is related to the magnitude of the tunnel splitting via:

$$\Delta_{m,m'} = 2\hbar\omega_{\text{T}m,m'} \tag{2.25}$$

2.2.9 Selection rules for tunneling

As seen above, level anticrossing originate from transverse anisotropy terms which mix states with different m. However, the symmetry of such terms imposes a selection rule on which states $|m\rangle$ are mixed and which not (thus forming anticrossings and true crossings respectively). As a consequence, tunneling does not occur for any field values satisfying Equation (2.18), but it occurs only between the states linked by the transverse anisotropy terms.

For instance the biaxial anisotropy:

$$O_2^2 = \frac{1}{2}(\hat{S}_+^2 + \hat{S}_-^2) \tag{2.26}$$

links states $|m\rangle$ and $|m'\rangle$, which magnetic quantum numbers differ by a multiple of two:

$$|m - m'| = 2k \tag{2.27}$$

where k is an integer. In the Fe_4 cluster, this second order term enables tunneling between the lowest lying states $|5\rangle$ and $|-5\rangle$ at $H = 0$.

The presence of the third order term:

$$\hat{O}_4^3 = \frac{1}{4}[\hat{S}_z(\hat{S}_+^3 + \hat{S}_-^3) + (\hat{S}_+^3 + \hat{S}_-^3)\hat{S}_z] \tag{2.28}$$

mixes states for which:

$$|m - m'| = 3k \tag{2.29}$$

For Fe$_4$ in zero field this term enhances the tunneling probability between the $|3\rangle$ and $|-3\rangle$ states.

In this work SMMs will be combined with graphene in order to create novel hybrid materials and devices with interesting spintronic properties. In these hybrids, molecular spins interact with a surrounding (i.e. graphene) that differs substantially from the crystal, and has an appreciable influence on their magnetic relaxation. The SMM-graphene interaction will be investigated in detail in the next chapters and it will be shown that a third order term (2.28) is essential to explain the effect of graphene charge carriers on the dynamics of molecular spins.

2.3 Graphene

In this section, the fundamental properties of graphene are presented. Special emphasis is given to the factors influencing graphene's electronic respons, while graphene spintronic properties are the focus of Chapter 7.
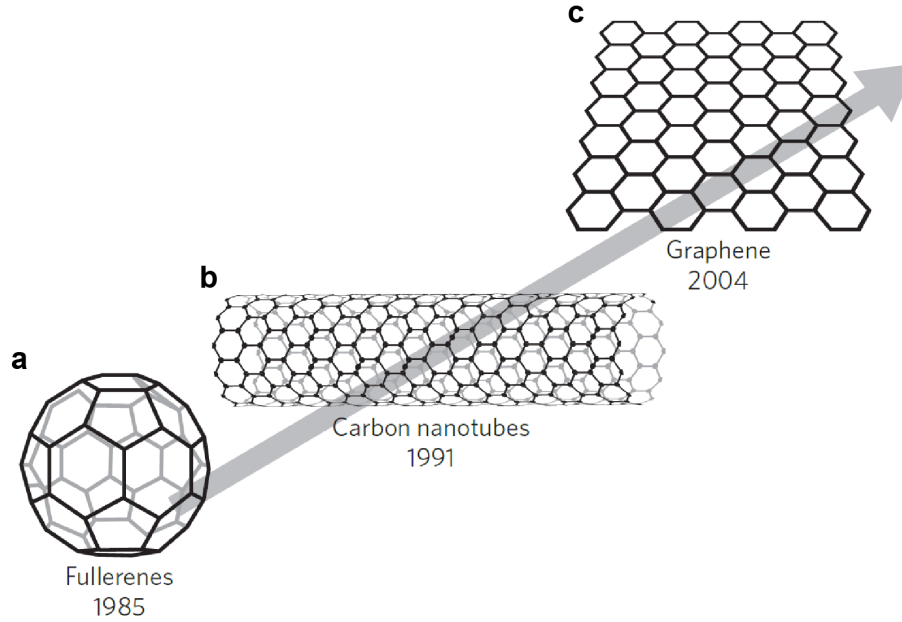
Figure 2.17: Carbon-based materials, a) C_{60} molecule, b) Single-walled carbon nanotube, c) Monolayer graphene (From: [122]).

2.3.1 Crystal structure and symmetry properties

Graphene, a single layer of Carbon atoms arranged in an hexagonal lattice, is the last discovered member of the carbon-based nanomaterials family (Figure 2.17 and 2.18a) [122, 123]. Of the four valence states of Carbon, three sp^2 orbitals form σ states with three nearest neighbor atoms, while the remaining p_z orbitals develop into delocalized π and π^* states, forming the highest occupied valence band (VB) and the lowest unoccupied conduction band (CB), respectively (Figure 2.18c) [124–127]. The σ bonds are mainly responsible for the mechanical strength of graphene[3] [128], whereas the delocalized π (π^*) electrons create a two-dimensional electron gas (2DEG) at the surface [129].

---

[3]The study of individual graphene membranes by nanoindentation gives a graphene *Young-Riccati's modulus* $E = 1.0$ terapascals and a *third-order elastic stifness* $D = -2.0$ terapascals, making graphene the strongest material ever measured. E and D are the coefficient in the extended Hooke's law:

$$\sigma = E\epsilon + D\epsilon^2 \qquad (2.30)$$
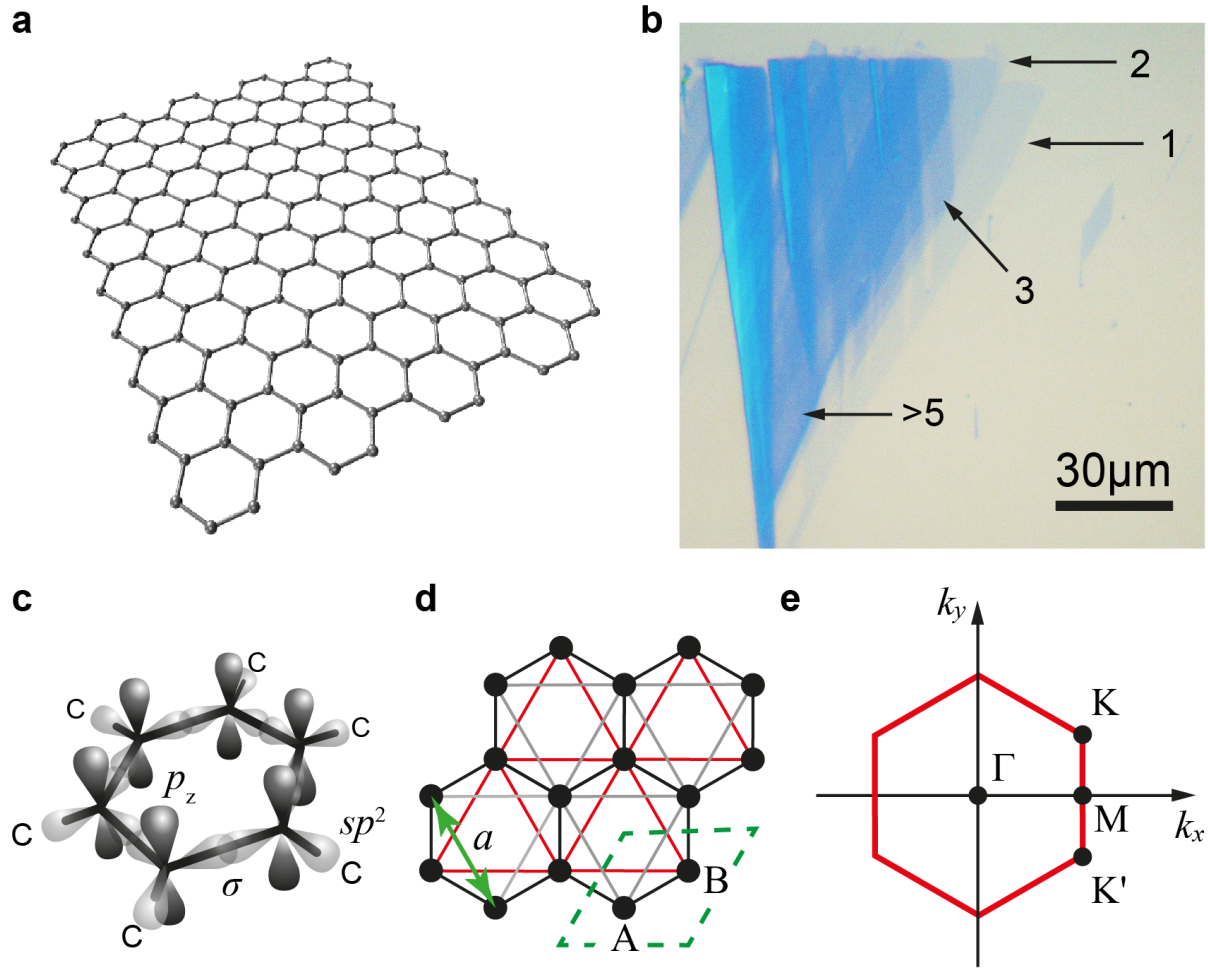
Figure 2.18: a) Crystal structure of single-layer graphene. b) Optical picture of graphene extracted from graphite (Arrows: number of layers). c) sp^2 orbitals form σ bonds while p_z orbitals delocalize in π and π^* bands. d) Two identical triangular sublattices A and B form the honeycomb lattice (green dashed line: graphene unit cell). e) Graphene First Brillouin Zone.

The graphene unit cell contains two carbon atoms, A and B in Figure 2.18d, that define two identical interwoven triangular sublattices with lattice constant $a = 2.46$ Å. This translates in two *inequivalent* points, K and K', at the Brillouin zone (BZ) boundary corners, each equivalent, through translational symmetry in the reciprocal lattice, to two of the others (Figure 2.18e). K and K' label two inequivalent *valleys* in k-space.

Importantly, CB and VB touch one another at K and K', where the π and π^* states are thus degenerate with energy E_D, Figure 2.19. For undoped graphene, one primitive cell contributes two electrons, thus at $T \approx 0$ the valence band is fully occupied while

---

with ϵ and σ indicating the uniaxial strain and stress respectively.

the conduction band is completely unoccupied, resulting in a point-like Fermi surface $(E_\mathrm{F} = E_\mathrm{D})$ [130].

2.3.2 Band Structure

The graphene peculiar electronic properties stem from the nature of the electron states in the neighbouroods of the K and K' points, where VB and CB dispersions are approximately linear, Figure 2.19b [124, 129, 131, 132].
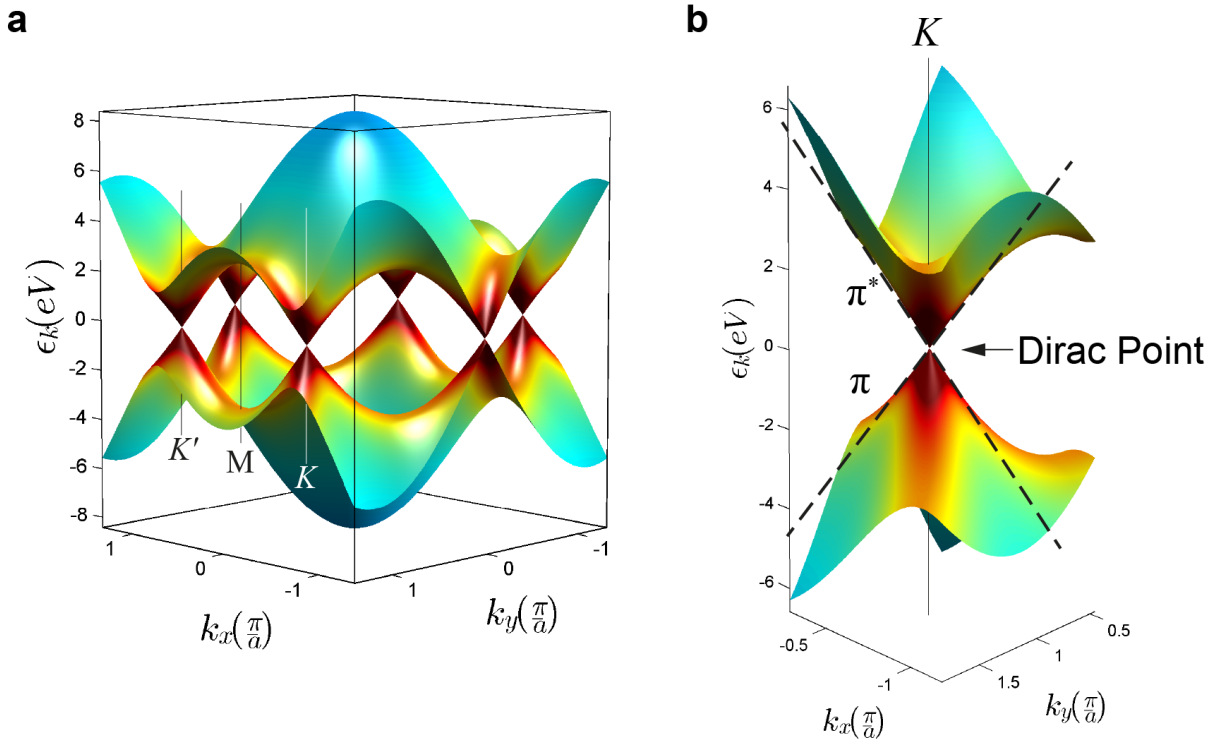
Figure 2.19: Graphene band dispersion. a) Graphene band structure in the first Brilluoin zone. b) Detail of the linear band dispersion in the vicinity of the K point.

The linearity comes from the fact that, in the framework of effective-mass aproximation and the tight-binding model , quasiparticle states in the vicinity of K are described by a Dirac Hamiltonian formally equivalent to that used to describe relativistic fermionic particles [124, 129, 132–134]:

$$\mathcal{H} = \hbar v_\mathrm{F} \boldsymbol{\sigma} \cdot \boldsymbol{k} \tag{2.31a}$$

where $\boldsymbol{k}$ is measured relative to the K point and the speed of light c is replaced by the carrier velocity at the Fermi level v_F. Because of this, the charge neutrality point is also called *Dirac point*.
Equivalenty, states in the vicinity of K' are described by:

$$\mathcal{H} = \hbar v_\text{F} \boldsymbol{\sigma}^* \cdot \boldsymbol{k} \tag{2.31b}$$

The terms $\boldsymbol{\sigma} = (\sigma_x \ \sigma_y)$ and $\boldsymbol{\sigma}^* = (\sigma_x \ -\sigma_y)$ are vectors of Pauli matrices:

$$\sigma_x = \begin{pmatrix} 0 & 1 \\ 1 & 0 \end{pmatrix} \quad \sigma_y = \begin{pmatrix} 0 & -i \\ i & 0 \end{pmatrix} \tag{2.32}$$

describing the *pseudospin* property [124, 133, 135] of the graphene wave functions, that will be discussed in the next paragraph.

The complete Hamiltonian reads:

$$\mathcal{H} = \begin{pmatrix} 0 & \gamma(k_x - ik_y) & 0 & 0 \\ \gamma(k_x + ik_y) & 0 & 0 & 0 \\ 0 & 0 & 0 & \gamma(k_x + ik_y) \\ 0 & 0 & \gamma(k_x - ik_y) & 0 \end{pmatrix} \tag{2.33}$$

where[4] $\gamma = \hbar v_\text{F}$.

The Hamiltonian (2.33) does not contain elements that mix different valleys [136] so that the problem becomes completely decoupled into that of K and K' equations (2.31).

Considering nearest neighbors-interactions only, the eigenvalues of (2.31) are [124, 133, 135, 136]:

$$\epsilon_b(\boldsymbol{k}) \approx b\hbar v_\text{F}|\boldsymbol{k}| \tag{2.34}$$

Equation (2.34) describes a linear band dispersion close to E_D and implies a vanishing effective mass $m^* = 0$ for the graphene carriers. $b = \pm 1$ imparts positive and negative energies to π^* and π states respectively, that hence are particles and antiparticles of each other.

The main consequence of this peculiar band dispersion, compared to the well known parabolic dispersion $\epsilon(\boldsymbol{k}) = \hbar^2 k^2/2m$, is that the Fermi velocity is constant ($v_\text{F} \approx 1 \times 10^6$ m/s) and does not depend on energy or momentum. So charge carriers in graphene move at constant velocity whatever their energy, much like photons.

2.3.3 Pseudospin, Isospin: absence of back-scattering

The linear dispersion (2.34) and the massless nature of the π carriers emerge directly from symmetry reasons. The structure of the Dirac Hamiltonians (2.33) imposes to the electron wavefunctions a four-components spinor structure [124, 133, 134, 136, 137]:

---

[4]The row-column product is here used:

$$\boldsymbol{\sigma} \cdot \boldsymbol{k} = \begin{pmatrix} \sigma_x & \sigma_y \end{pmatrix} \begin{pmatrix} k_x \\ k_y \end{pmatrix} = \begin{pmatrix} 0 & k_x \\ k_y & 0 \end{pmatrix} + \begin{pmatrix} 0 & -ik_y \\ ik_y & 0 \end{pmatrix} = \begin{pmatrix} 0 & \gamma(k_x - ik_y) \\ \gamma(k_x + ik_y) & 0 \end{pmatrix}$$

$$\mathbf{\Psi} = \begin{pmatrix} \psi_{\mathrm{A}}^{K} \\ \psi_{\mathrm{B}}^{K} \\ \psi_{\mathrm{A}}^{K'} \\ \psi_{\mathrm{B}}^{K'} \end{pmatrix} \tag{2.35}$$

where ψ_{A}^{K}, $\psi_{\mathrm{A}}^{K'}$, ψ_{B}^{K}, $\psi_{\mathrm{B}}^{K'}$ are the slowly-varying envelope functions describing the effect of the sublattice periodic potential on the π (π^*) wavefunctions at K and K'.

From (2.35) follows that a graphene π (π^*) electron, in addition to its physical spin and momentum, carries two additional degrees of freedom. One, called *sublattice pseudospin* index, labels the sublattice state (A or B), while the other, called *valley isospin* index, labels the two independent Dirac points K and K' [124, 133, 138]. In analogy to the two-components spinor describing the usual spin, the pseudospin ($\boldsymbol{\sigma}$ in (2.31)) is a vector with two components, each describing the amplitude of the envelope functions on one sublattice. The direction of the pseudospin reflects the character (bonding or antibonding) of the underling molecular orbital [133].

The eigenvectors of (2.31) are the two-components wave functions:

$$\psi_{\boldsymbol{k},\pm}^{K}(\boldsymbol{r}) = \begin{pmatrix} \psi_A^K \\ \psi_B^K \end{pmatrix} = \frac{1}{\sqrt{2}} e^{i\boldsymbol{k}\cdot\boldsymbol{r}} \begin{pmatrix} \mp i e^{-i\theta_{\boldsymbol{k}}/2} \\ e^{i\theta_{\boldsymbol{k}}/2} \end{pmatrix} \tag{2.36a}$$

$$\psi_{\boldsymbol{k},\pm}^{K'}(\boldsymbol{r}) = \begin{pmatrix} \psi_A^{K'} \\ \psi_B^{K'} \end{pmatrix} = \frac{1}{\sqrt{2}} e^{i\boldsymbol{k}\cdot\boldsymbol{r}} \begin{pmatrix} \mp i e^{i\theta_{\boldsymbol{k}}/2} \\ e^{-i\theta_{\boldsymbol{k}}/2} \end{pmatrix} \tag{2.36b}$$

where $\theta_{\boldsymbol{k}} = \arctan(k_x/k_y)$ indicates the direction of $\boldsymbol{k}$ with respect to k_y, i.e. $k_x + ik_y = i|\boldsymbol{k}|e^{i\theta_{\boldsymbol{k}}}$ and the terms in brackets on the right side describe a rotation of the pseudospin with respect to $\boldsymbol{k}$.

The pseudospin is locked to the $\boldsymbol{k}$ direction and points either parallel or antiparallel to it. In fact, $\psi_{\pm}^{K}(\boldsymbol{r})$ and $\psi_{\pm}^{K'}(\boldsymbol{r})$ are eigenvectors of the helicity operator $\boldsymbol{\Sigma} = \frac{1}{2}\boldsymbol{\sigma} \cdot \frac{\boldsymbol{p}}{|\boldsymbol{p}|}$ describing the projection of the momentum operator along the pseudospin direction:

$$\boldsymbol{\Sigma}\psi_{\pm}^{K}(\boldsymbol{r}) = \pm\frac{1}{2}\psi_{\pm}^{K}(\boldsymbol{r}) \tag{2.37a}$$

$$\boldsymbol{\Sigma}\psi_{\pm}^{K'}(\boldsymbol{r}) = \mp\frac{1}{2}\psi_{\pm}^{K'}(\boldsymbol{r}) \tag{2.37b}$$

Thus in analogy with the physics of massless neutrinos, charge carriers in graphene have a well defined *chirality*, i.e. states around K are right-handed (pseudospin parallel to $\boldsymbol{k}$) while states close to K' are left-handed (pseudospin antiparallel to $\boldsymbol{k}$). For the antiparticles in the valence band, the situation is reversed. Physically, this means that the character (bonding or antibonding) of the wavefunction depends on the propagation direction, a valence state close to K with a positive k_x is decribed by a linear combination of antibonding orbitals while a state with $-k_x$ is decribed by a linear combination of bonding orbitals [133].

The chiral nature of the graphene wavefunctions and the conservation of pseudospin in long-wavelength scattering processes influence the graphene transport properties profoundly. In single-layer graphene in particular the conservation of pseudospin inhibits backscattering [133, 137] and gives rise to Klein tunneling [139], reducing considerably the effect of disorder and impurities.
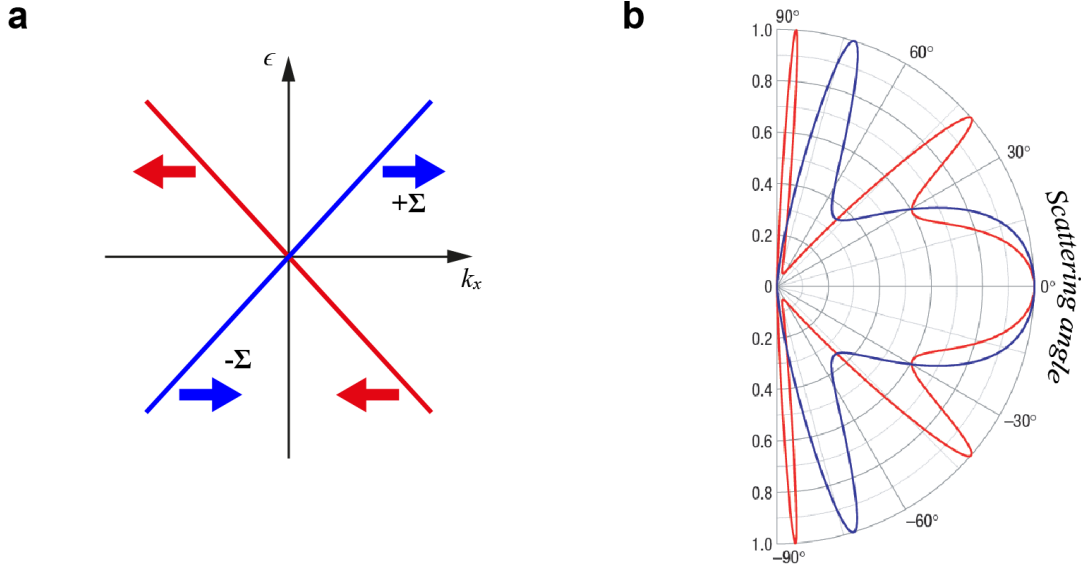
Figure 2.20: Chiral massless Dirac particles a) Carriers in the conduction and valence band have positive and negative chiralities respectively. b) Enhanced forward scattering (From: [139]).

2.3.4 Density of states

The shape of graphene density of states (DOS) reflects the linear band dispersion and the symmetric π - π^* spectrum [124, 134]. Figure 2.21a, shows the graphene DOS as derived from (2.34):

$$D(\epsilon) = \frac{1}{S} \sum_{b,\boldsymbol{k}} \delta[\epsilon - \epsilon_b(\boldsymbol{k})] = g_v g_s \frac{|\epsilon|}{2\pi\gamma^2} \tag{2.38}$$

where $g_v = 2$ is the valley degeneracy, $g_s = 2$ is the spin degeneracy, S is the volume of the primite cell and γ is given by:

$$\gamma = \frac{\sqrt{3}at}{2} = \frac{v_F}{\sqrt{3}} \tag{2.39}$$

with t indicating the nearest neighbour transfer integral of the tight-binding model. As seen in Figure 2.21, unlike the constant DOS of other 2D systems with parabolic bands,

graphene DOS varies linearly with energy and it is symmetric with respect the K point energy $\epsilon = E_D$ where, importantly, it vanishes [124].
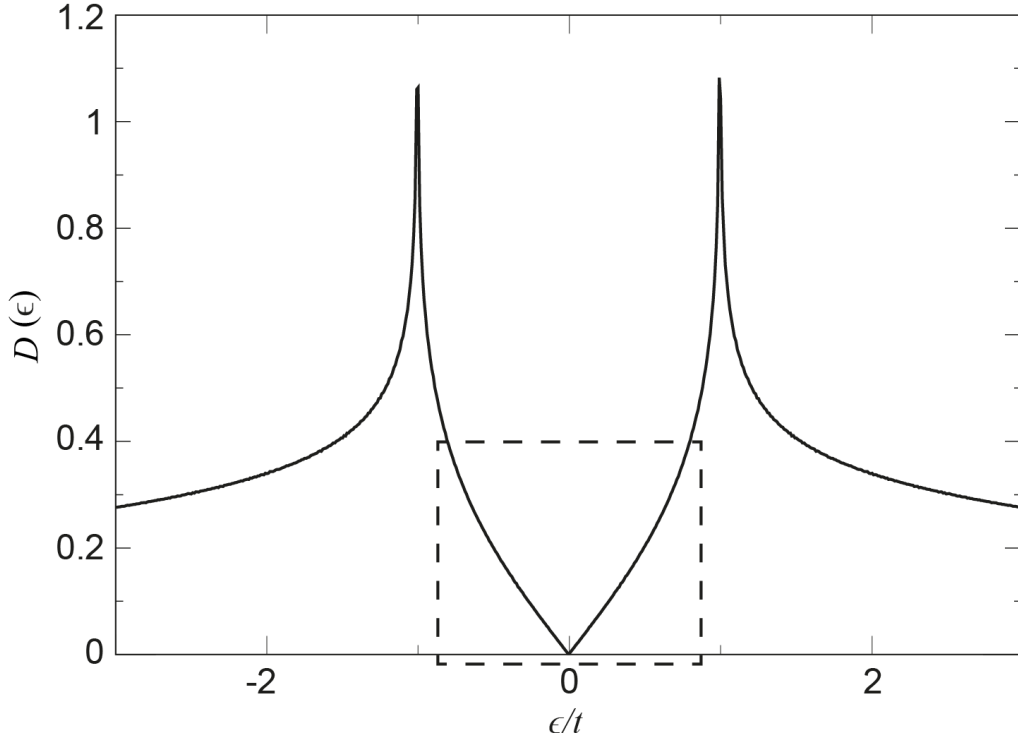
Figure 2.21: Graphene density of states plotted over a wide range of nearest neighbor hopping parameter t, showing pronounced van Hove singularities for $\epsilon \sim \pm t$ [124]. The dashed rectangle indicates the almost linear low energy DOS normally spanned in back-gated transport measurements.

2.3.5 Electronic transport: ambipolar field-effect

The above distinctive features are at the origin of the *ambipolar field effect* [124, 131, 140] observable in graphene-based field effect transistor (FET) and give rise to a characteristic transfer curve (σ vs. V_{gate}).

Being an all-surface material, graphene proves extremely sensitive to external electric fields (e.g. either produced by an external gate or by the dipoles of molecules in contact with it). Figure 2.22a,b shows a typical graphene FET in 5-terminal configuration. The device has been fabricated by transfering a single-layer graphene flake onto a Si substrate with a 300nm-thick SiO_2 upperlayer and contacting it using standard electron beam lithography. The Si/SiO_2 stack works as a global electrostatic gate for the device. The 5-terminal configuration is chosen in order to extract the intrinsic graphene conductivity, minimizing the contribution from the contact resistance R_C. A modest electric field < 0.3 V/nm
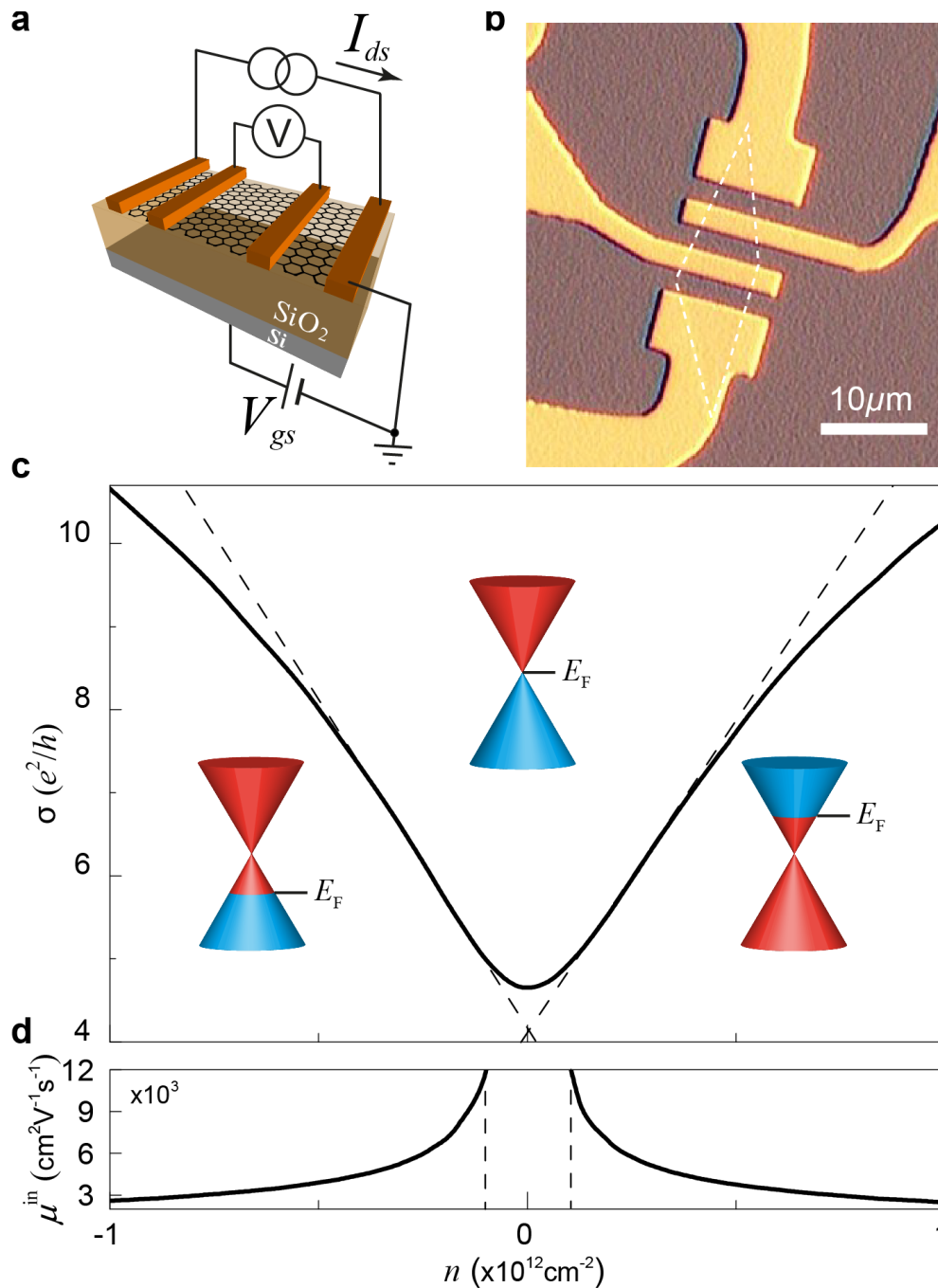
Figure 2.22: Ambipolar field effect in graphene at room temperature. a) Scheme of the 5 terminals graphene device with the Si/SiO_2 back-gate stack. b) Optical picture of the actual device. The dashed line highlights the graphene flake. c) σ vs. n, dashed lines highlight the linear behavior. d) Intrinsic mobility μ^{in} extracted from c) using the semiclassical Drude model, dashed lines indicate the range where μ^{in} starts diverging and the Drude model stops to be valid.

induced by the gate-source voltage V_{gs} produces an appreciable variation in the device conductivity $\sigma = 1/\rho$, Figure 2.22c. Sweeping V_{gs} shifts the Fermi level E_{F} around the Dirac point, tuning the graphene carrier density n. A positive V_{gs} shifts E_{F} into the conduction band so that the *electrons* become the majority carriers, whereas a negative V_{gs} induces *hole* transport being the E_{F} pushed into the valence band. This is known as the ambipolar field effect: *an external electric field tunes the conductivity of the material and induces a transition between electron and hole conduction*. The field effect in graphene can be described using a parallel plate capacitor model [140] expressing the relation between a change in the sheet carrier density n due to a variation in V_{gs}:

$$n = \frac{\epsilon_0 \kappa}{ed} V_{\mathrm{gs}} \tag{2.40}$$

ϵ_0 is the vacuum permittivity, κ and d are the relative permittivity (for $\mathrm{SiO_2}$, $\kappa = 3.9$) and the thickness of the gate oxide, and e is the absolute value of the electron charge.
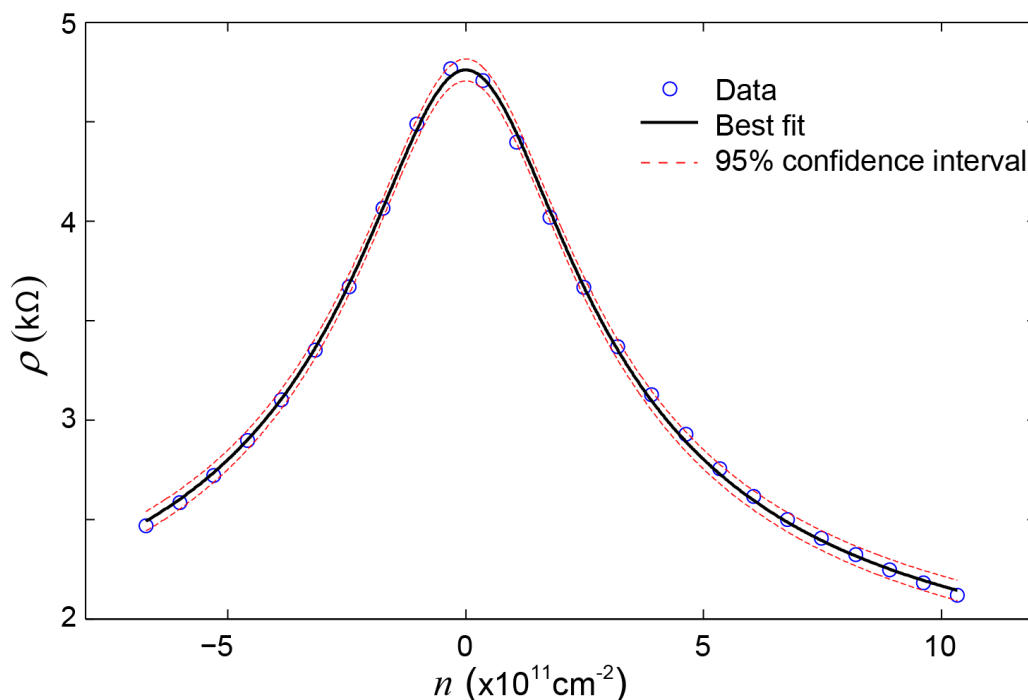
Figure 2.23: Fitting of the graphene tranfer curve. Best fit to equation (2.43) gives $\rho_S = (1.43 \pm 0.04) \cdot 10^3$ Ohms, $\mu^{\mathrm{int}} = (8.3 \pm 0.3) \cdot 10^3$ cm^2 V^{-1} s^{-1} and $n_0 = (2.25 \pm 0.07) \cdot 10^{11}$ cm^{-2}.

The above model can be expanded [141–143] in order to estimate the *residual carrier concentration* n_0 at the charge neutrality point and take into account the *quantum capacitance* [144, 145] of the 2DEG :

$$n = \sqrt{n_0^2 + n(V_{\mathrm{gs}})^2} \tag{2.41}$$

where $n(V_{gs})$ is extracted from:

$$\frac{e}{C_e}n + \frac{\hbar v_{\mathrm{F}}\sqrt{\pi n}}{e} = V_{\mathrm{gs}} - V_{\mathrm{min}} \tag{2.42}$$

The total gate capacitance $C_{\mathrm{gate}} = \frac{C_e C_q}{C_e + C_q}$ is the series capacitance of the electrostatic capacitance $C_{\mathrm{e}} = \frac{\epsilon_0 \kappa}{d}$ and $C_{\mathrm{q}} = \frac{\sqrt{n/\pi}e^2}{v_{\mathrm{F}}\hbar}$.

The four terminal resistivity of the device, Figure 2.23, can then be expressed as:

$$\rho = \rho_S + \frac{1}{e\mu^{\mathrm{in}}\sqrt{n_0^2 + n(V_{\mathrm{gs}})^2}} \tag{2.43a}$$

that is equivalent to:

$$\rho = \rho_S + \frac{1}{e\mu^{\mathrm{in}}\sqrt{n_0^2 + (C_{\mathrm{gate}}(V_{\mathrm{gs}} - V_{\mathrm{min}})/e)^2}} \tag{2.43b}$$

where ρ_S is a n-independent contribution to the resistivity due to short-range scatterers (see next paragraph). ρ is extracted from the measured device resistance R using $\rho = \frac{A}{L^2}R$, where L is the distance between the probing contacts and A is the area of graphene enclosed between the probing contacts. Note that the 2D resistivity is given in units of ohms rather than ohms×cm as in the 3D case [140].

2.3.6 Carriers mobility

The room temperature (RT) intrinsic mobility μ^{in} of the device in Figure 2.22c is remarkably high (Figure 2.22e). It spans $\mu^{\mathrm{in}} \sim 3000 - 12000$ cm² V^{-1}s^{-1} in the concentration range $n \sim 1 - 0.1 \times 10^{12}$ cm^{-2}. Employing Einstein's relation, the scattering time of about:

$$\tau = \frac{\hbar\sigma(\pi/n)^{1/2}}{e^2 v_{\mathrm{F}}} \sim 2\mathrm{ns} \tag{2.44}$$

a mean free path on the range:

$$l = v_{\mathrm{F}}\tau \sim 55\text{-}75\mathrm{nm} \tag{2.45}$$

at room temperature.

The mobility is limited by different factors such as scattering by charged impurities or defects and electron-phonon scattering. In very clean and suspended samples (where the underling SiO$_2$ substrate has been etched away) the mean free path l increases by almost two order of magnitude, becoming comparabe to the device size, an indication that the ballistic transport regime is reached [146, 147].

The slope of the v-*shaped* transfer curve gives the low-field *field effect mobility*[5] [143] $\mu^{\mathrm{FE}} = (1/C_{\mathrm{gate}})(\partial\sigma/\partial V_{\mathrm{gs}})$ that is constant over a quite wide range of n (yielding in this case $\mu_{\mathrm{h}}^{\mathrm{FE}} \sim 1900$ cm^2 V^{-1} s^{-1} and $\mu_{\mathrm{e}}^{\mathrm{FE}} \sim 1800$ cm^2 V^{-1} s^{-1} for the low n region).

2.3.7 Charged impurities and conductivity minimum

The curve σ vs. V_{gs} resembles the v-*shaped* density of states of Figure 2.21b with the remarkable difference that it does not vanish for $E_{\mathrm{F}} = E_{\mathrm{D}}$[6], but it rather reaches a finite minimum value $\sigma_{\mathrm{min}} \neq 0$.

The exact σ_{min} value, and the fact that it doesn't vanish for zero carrier density n, has been the focus of intense debate [123, 129, 148, 149]. Many experiments [123, 140, 149, 150] report a σ_{min} values very close to $\approx 4e^2/h = 0.15\times10^{-3}\Omega^{-1}$. This value, being equal to e^2/h per carrier type (spin+valley), suggests that chirality may play a role in the conductivity quantization [123, 140]. It important to emphasize that it is the conductivity rather than the conductance that seems to be quantized in graphene (that is, conductance G measured experimentally scaled in the usual manner as $G = \sigma w/L$ with L and σ indicating length and width of the devices), thus such an effect would be completely different from the conductance quantization observed previously in quantum transport experiments [123, 140].

Indeed, a number of theories [151–154], based on Kubo's and Landauer's formalisms, propose the finite conductivity minimum for vanishing charge density as a fundamental characteristic of two-dimensional Dirac fermions. Nevertheless the value suggested by those works, $\sigma_{\mathrm{min}} = 4e^2/h\pi$, is about π times smaller than that observed in experiments [123, 140, 149, 150]. Moreover for all other known materials, such a low conductivity unavoidably leads to a metal-insulator transition at low T, but no sign of such a transition has been observed in graphene down to liquid-helium T [123].

Other theories [148, 155, 156], taking into account the effect of *short-* and *long-*range scatterers, rule out the conductivity minimum as a fundamental characteristic and attribute its origin to scattering by charged impurities, that are always present in the SiO_2 substrate [157], Figure **??**. Indeed, while the presence of short-range scatterers is found to lead to a square-root dependence of conductivity on density together with a $\sigma_{\mathrm{min}} = 0$ for $n = 0$, in contradiction with the experimental observations, the presence of long-range scatterers [148] is predicted to gives rise to both the observed linear σ vs. n and $\sigma_{\mathrm{min}} = 4e^2/h$ value. Both predictions were confirmed experimentally, charged impurities (long-range scatterers) are found [149] to increase the linearity of the σ vs. V_{gs} and to saturate σ_{min} at the value $4e^2/h$, while the introduction of defects (short-range scatterer) lowers σ_{min} even below theoretical $4e^2/h\pi$ and is found to induce a metal-to-insulator transition at low temperatures [158].

---

[5]to not be confused with the *intrinsic* Drude mobility $\mu^{\mathrm{in}} = \sigma/ne$ or the Hall mobility $\mu_e^H = -\sigma_e R_H$.

[6]since E_D marks the threshold between electron and hole transport, the Dirac point is also called *charge neutrality point.*

2.3.8 Electron-hole puddles at low carrier densities

The effect of charge impurities described above corroborates the picture of disorder-induced *electron-hole puddles* at the charge neutrality point [131, 148, 159, 160].
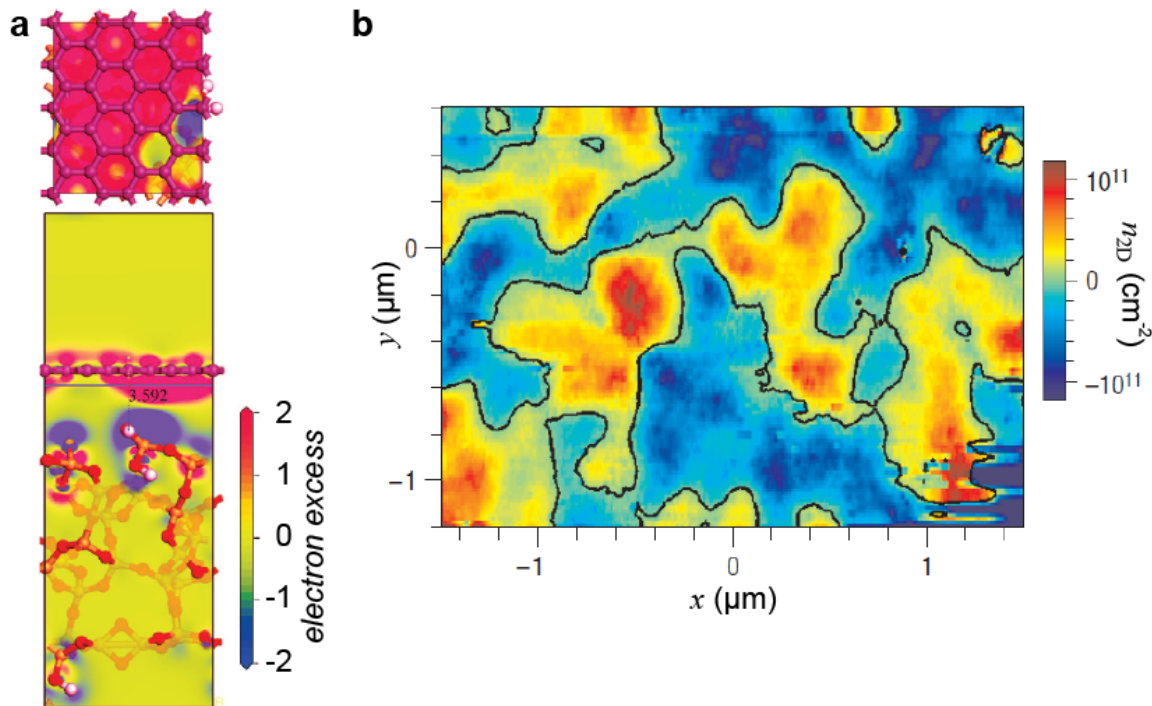
Figure 2.24: Electron-hole puddles induced by charged impurities. a) Charged impurities in SiO$_2$ substrate (From: [157]). b) Electron-hole puddles induced in graphene (From: [161]).

Charge impurities, that are invariably present in the substrate, create an inhomogeneous potential background for the graphene lying on it (Figure 2.24a) [157]. For large external gate voltages, the induced carrier concentration n is substantially much larger than n_{imp} so, the effect of these fluctuations can be neglected. But at low carrier densities, potential fluctuations locally dope the graphene segregating it into puddels (i.e. islands) of electrons and holes. This state of electron-hole puddles can be regarded as the final/ultimate limit of a vanishing band gap. The fact that this state is not insulating ($\sigma_{min} \neq 0$) is taken as evidence of Klein tunneling which imposes *percolation* of the puddles at the charge neutrality point [139]. The presence of percolating areas with different doping level have been experimentally observed using different scanning probe techniques (Figure 2.24b) [161].

2.3.9 Chemical doping

As shown in Figure 2.22d, in ambient conditions $\sigma_{\min} = 1/\rho_{\min}$ occurs at $V_{gs} = V_{\min} > 0$ due to the effect of both the adventitius charges present on the surface of the gate dielectric (SiO_2) and to the adsorbed water layer. The latter also gives rise to a hysteretic behavior noticeable for subsequent gate sweeps , Figure 2.22d. [162–165].

The position of $V_{\min}$ is thus sensitive to chemical doping and can be used to monitor the presence of molecular adsorbates [166].
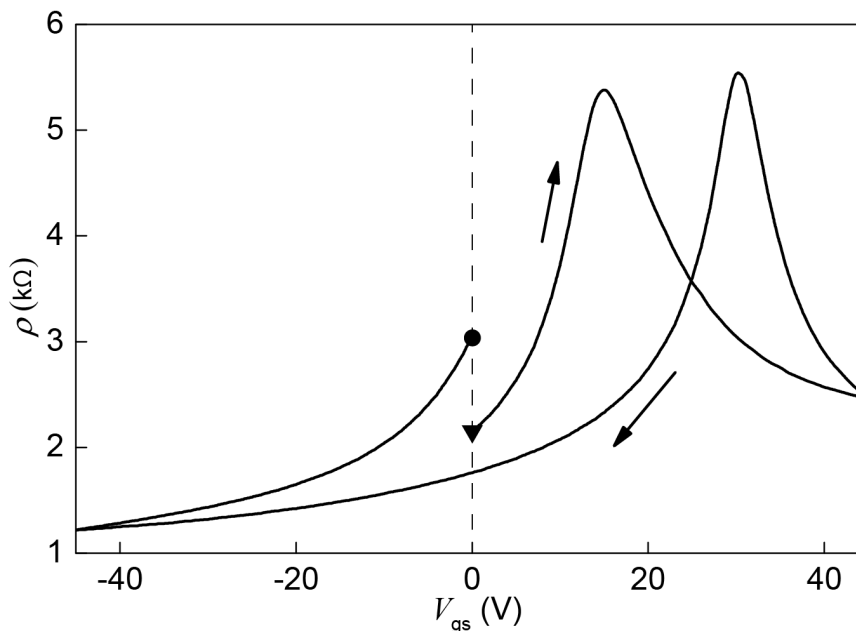
Figure 2.25: Detection of chemical adsorbates at room temperature. ρ vs. V_{gs}, showing the characteristic hysteretic behaviour due to adsorbed water. The solid circle and the inverted triangle indicate start and end points of the gate sweep respectively.

Being Graphene an open surface its 2DEG is readily accessible and sensitive to external functionalization. This opens up a the opens unique possibilities for designing and tailoring its electronic, optical and magnetic properties by either combining it with other 2D materials in heterostructure or by decoration with self-assembling molecular species with specific properties.

2.3.10 Synthesis of graphene: scaling it up

The easiest way to produce graphene is the so-called *micromechanical cleavage* of graphite [140], in which graphene layers are directly cleaved from a graphite nugget using common adesive tape and then pressed on the wanted substrate. While the obtained graphene flakes are of extremely high crystalline quality and purity, they are randomly distributed on the sample and their lateral size is limited to 10-20 micrometers, making this method not viable

for commercial applications (see Section 4.1 for more details). Since industrial exploitation requires wafer- sized graphene layers [167, 168] on various substrates [169, 170], increasing effort is being devoted to the synthesis and the characterization of large-area graphene via different methods.

Chemical vapor deposition (CVD) has become one of the most promising production methods for large-area graphene, providing sheets up to 30 inches long [171] that can be transferred onto different substrates [172].

The CVD process is based on the decomposition of hydrocarbons (CH_4 for istance) on a transition metal substrate [169, 173–175].
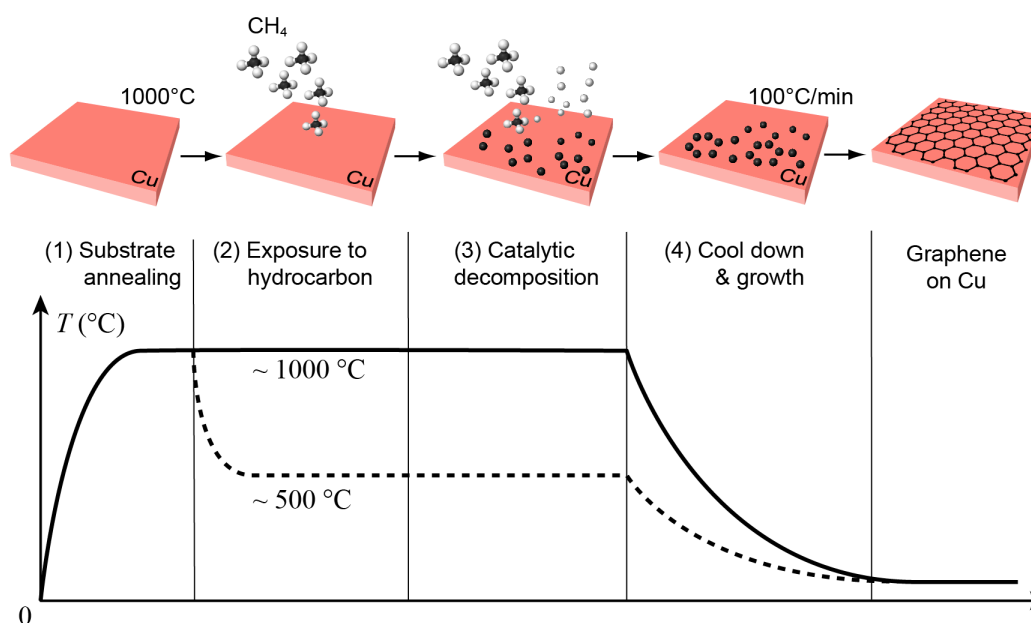
Figure 2.26: CVD graphene synthesis. (1) Annealing of the catalyst film induces recrystallization of large size grains and minimizes nucleation sites for amorphous carbon and multilayer graphene [173]. (2-3) The temperature at the hydrocarbon exposure determines the growth mechanism. For high temperatures $\sim 1000\,°C$ carbon diffuses into the film bulk and subsequent cooling (4) induces carbon segregation on the surface. A lower temperature $\sim 500\,°C$ inhibits bulk diffusion and graphene grows by direct carbon adsorption upon cooling.

The reaction describing the decomposion is:

$$CH_4 \quad \to \quad 2H_2(g) + C(s)$$
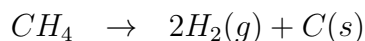
Transition metals, typically Cu, Ni or Ru, are extensively used in this process because of their ability to catalyze the dehydrogenation of hydrocarbons and produce high quality graphitic crystals over their surface [173].

CVD large-area graphene can then be trasferred on an arbitrary substrate by etching away the metallic substrate [169, 175].

Bibliography

[1] Chappert, C., Fert, A., Van Dau, F. N. & Dau, F. V. The emergence of spin electronics in data storage. *Nature materials* **3**, 1–36 (2007).

[2] Zutic, I., Fabian, J., Das Sarma, S. & Sarma, S. D. Spintronics: Fundamentals and applications. *Rev. Mod. Phys.* **76**, 323–410 (2004).

[3] Binasch, G., Grünberg, P., Saurenbach, F. & Zinn, W. Enhanced magnetoresistance in layered magnetic structures with antiferromagnetic interlayer exchange. *Phys. Rev. B* **39**, 4828–4830 (1989).

[4] Baibich, M. N., Broto, J. M., Fert, A., Van Dau, F. N. & Petroff, F. Giant Magnetoresistance of (001)Fe/(001)Cr magnetic superlattices. *Phys. Rev. Lett.* **61**, 2472–2475 (1988).

[5] Pratt, W. *et al.* Perpendicular giant magnetoresistances of Ag/Co multilayers. *Phys. Rev. Lett.* **66**, 3060–3063 (1991).

[6] Pratt, W. *et al.* Giant magnetoresistance with current perpendicular to the multilayer planes. *Journal of Magnetism and Magnetic Materials* **126**, 406–409 (1993).

[7] Bass, J. & Pratt, W. P. Current-perpendicular (CPP) magnetoresistance in magnetic metallic multilayers. *Journal of Magnetism and Magnetic Materials* **200**, 274–289 (1999).

[8] Valet, T. & Fert, A. Theory of the perpendicular magnetoresistance in magnetic multilayers. *Phys. Rev. B* **48**, 7099–7113 (1993).

[9] Fert, A., Duvail, J.-L. & Valet, T. Spin relaxation effects in the perpendicular magnetoresistance of magnetic multilayers. *Phys. Rev. B* **52**, 6513–6521 (1995).

[10] Mott, N. F. The electrical conductivity of transition metals. *Proceedings of the Royal Society of London. Series A, Mathematical and Physical Sciences* **153**, 699–717 (1936).

[11] Mott, N. F. The resistance and thermoelectric properties of the transition metals. *Proceedings of the Royal Society A: Mathematical, Physical and Engineering Sciences* **156**, 368–382 (1936).

[12] Mott, N. F. Electrons in transition metals. *Advances in Physics* **13**, 325–422 (1964).

[13] Fert, A. & Campbell, I. A. Two-current conduction in nickel. *Phys. Rev. Lett.* **21**, 1190–1192 (1968).

[14] Tsymbal, E. Y. & Pettifor, D. G. Perspectives of giant magnetoresistance. *Solid State Physics - Advances in Research and Applications* **56**, 113–237 (2001).

[15] Zhang, S., Levy, P. & Fert, A. Conductivity and magnetoresistance of magnetic multilayered structures. *Phys. Rev. B* **45** (1992).

[16] Grünberg, P., Schreiber, R., Pang, Y., Brodsky, M. B. & Sowers, H. Layered magnetic structures: evidence for antiferromegnetic coupling of Fe layers across Cr interlayers. *Phys. Rev. Lett.* **57**, 2442 (1986).

[17] Carbone, C. & Alvarado, S. F. Antiparallel coupling between Fe layers separated by a Cr interlayer: Dependence of the magnetization on the film thickness. *Phys. Rev. B* **36**, 2433–2435 (1987).

[18] Parkin, S. S. P., More, N. & Roche, K. P. Oscillations in exchange coupling and magnetoresistance in metallic superlattice structures: Co/Ru, Co/Cr, and Fe/Cr. *Phys. Rev. Lett.* **64**, 2304–2307 (1990).

[19] Parkin, S. Systematic variation of the strength and oscillation period of indirect magnetic exchange coupling through the 3d, 4d, and 5d transition metals. *Phys. Rev. Lett.* **67**, 3598–3601 (1991).

[20] Parkin, S. & Mauri, D. Spin engineering: Direct determination of the Ruderman-Kittel-Kasuya-Yosida far-field range function in ruthenium. *Phys. Rev. B* **44**, 7131–7134 (1991).

[21] Bruno, P. & Chappert, C. Oscillatory coupling between ferromagnetic layers separated by a nonmagnetic metal spacer. *Phys. Rev. Lett.* **67**, 1602–1605 (1991).

[22] Bruno, P. & Chappert, C. Erratum: Oscillatory coupling between ferromagnetic layers separated by a nonmagnetic metal spacer. *Phys. Rev. Lett.* **67**, 2592 (1991).

[23] Parkin, S. S. P., Bhadra, R. & Roche, K. P. Oscillatory magnetic exchange coupling through thin copper layers. *Phys. Rev. Lett.* **66**, 2152–2155 (1991).

[24] Stiles, M. D. Interlayer exchange coupling. In *Ultrathin Magnetic Structures III: Fundamentals of Nanomagnetism*, vol. 200, chap. 4, 99–142 (Springer, Berlin Heidelberg, 2005).

[25] Unguris, J., Celotta, R. & Pierce, D. Observation of two different oscillation periods in the exchange coupling of Fe/Cr/Fe (100). *Phys. Rev. Lett.* **67** (1991).

[26] Takagishi, M. *et al.* The applicability of CPP-GMR heads for magnetic recording. *IEEE Transactions on Magnetics* **38**, 2277–2282 (2002).

[27] Parkin, S. *et al.* Magnetically engineered spintronic sensors and memory. *Proceedings of the IEEE* **91**, 661–679 (2003).

[28] Childress, J. R. *et al.* Fabrication and recording study of all-metal dual-spin-valve CPP read heads. *INTERMAG 2006 - IEEE International Magnetics Conference* **42**, 277 (2006).

[29] Parkin, S. Origin of enhanced magnetoresistance of magnetic multilayers: Spin-dependent scattering from magnetic interface states. *Phys. Rev. Lett.* **71**, 1641–1644 (1993).

[30] Dieny, B. *et al.* Giant magnetoresistive in soft ferromagnetic multilayers. *Phys. Rev. B* **43**, 1297–1300 (1991).

[31] Parkin, S., Yang, H., Yang, S.-H. and Hayashi, M. Magnetic Tunnel Junctions. In *Handbook of Magnetism and Advanced Magnetic Materials Vol. 5*, 1–21 (2007).

[32] Tsymbal, E. Y., Mryasov, O. N. & LeClair, P. R. Spin-dependent tunnelling in magnetic tunnel junctions. *Journal of Physics: Condensed Matter* **15**, R109–R142 (2003).

[33] Julliere, M. Tunneling between ferromagnetic films. *Physics Letters A* **54**, 225–226 (1975).

[34] Miyazaki, T. & Tezuka, N. Giant magnetic tunneling effect in Fe/Al2O3/Fe junction. *Journal of Magnetism and Magnetic Materials* **139**, L231–L234 (1995).

[35] Moodera, J. S., Kinder, L. R., Wong, T. M. & Meservey, R. Large magnetoresistance at room temperature in ferromagnetic thin film tunnel junctions. *Phys. Rev. Lett.* **74**, 3273–3276 (1995).

[36] Parkin, S. S. P. *et al.* Giant tunnelling magnetoresistance at room temperature with MgO (100) tunnel barriers. *Nature materials* **3**, 862–7 (2004).

[37] Yuasa, S., Nagahama, T., Fukushima, A., Suzuki, Y. & Ando, K. Giant room-temperature magnetoresistance in single-crystal Fe/MgO/Fe magnetic tunnel junctions. *Nature materials* **3**, 868–71 (2004).

[38] Mathon, J. & Umerski, a. Theory of tunneling magnetoresistance of an epitaxial Fe/MgO/Fe(001) junction. *Phys. Rev. B* **63**, 220403 (2001).

[39] Mavropoulos, P., Papanikolaou, N. & Dederichs, P. Complex band structure and tunneling through ferromagnet /insulator /ferromagnet junctions. *Phys. Rev. Lett.* **85**, 1088–1091 (2000).

[40] Butler, W., Zhang, X.-G., Schulthess, T. & MacLaren, J. Reduction of electron tunneling current due to lateral variation of the wave function. *Phys. Rev. B* **63**, 092402 (2001).

[41] Butler, W., Zhang, X.-G., Schulthess, T. & MacLaren, J. Spin-dependent tunneling conductance of Fe—MgO—Fe sandwiches. *Phys. Rev. B* **63**, 054416 (2001).

[42] Belashchenko, K., Tsymbal, E., Oleynik, I. & van Schilfgaarde, M. Positive spin polarization in Co/Al2O3/Co tunnel junctions driven by oxygen adsorption. *Phys. Rev. B* **71**, 224422 (2005).

[43] Tsymbal, E. & Pettifor, D. Modelling of spin-polarized electron tunnelling from 3d ferromagnets. *Journal of Physics: Condensed Matter* **411** (1997).

[44] Wunnicke, O. *et al.* Effects of resonant interface states on tunneling magnetoresistance. *Phys. Rev. B* **65**, 064425 (2002).

[45] Tsymbal, E. Y., Oleinik, I. I. & Pettifor, D. G. Oxygen-induced positive spin polarization from Fe into the vacuum barrier. *Journal of Applied Physics* **87**, 5230 (2000).

[46] Belashchenko, K. *et al.* Effect of interface bonding on spin-dependent tunneling from the oxidized Co surface. *Phys. Rev. B* **69**, 174408 (2004).

[47] Kaiser, C., Van Dijken, S., Yang, S. H., Yang, H. & Parkin, S. S. P. Role of tunneling matrix elements in determining the magnitude of the tunneling spin polarization of 3d transition metal ferromagnetic alloys. *Phys. Rev. Lett.* **94**, 247203 (2005).

[48] Raman, K. V. Interface-assisted molecular spintronics. *Applied Physics Reviews* **1** (2014).

[49] Raman, K. V. *et al.* Interface-engineered templates for molecular spin memory devices. *Nature* **493**, 509–513 (2013).

[50] Santos, T. *et al.* Room-temperature tunnel magnetoresistance and spin-polarized tunneling through an organic semiconductor barrier. *Phys. Rev. Lett.* **98**, 016601 (2007).

[51] Barraud, C. C. *et al.* Unravelling the role of the interface for spin injection into organic semiconductors. *Nature Physics* **6**, 615–620 (2010).

[52] Atodiresei, N. *et al.* Design of the local spin polarization at the organic-ferromagnetic interface. *Phys. Rev. Lett.* **105**, 1–4 (2010).

[53] Datta, S. & Das, B. Electronic analog of the electrooptic modulator. *Applied Physics Letters* **665**, 10–13 (1990).

[54] Behin-Aein, B., Datta, D., Salahuddin, S. & Datta, S. Proposal for an all-spin logic device with built-in memory. *Nature nanotechnology* **5**, 266–270 (2010).

[55] Datta, S., Salahuddin, S. & Behin-Aein, B. Non-volatile spin switch for Boolean and non-Boolean logic. *Applied Physics Letters* **101**, 252411 (2012).

[56] Manipatruni, S., Nikonov, D. E. & Young, I. a. All-spin nanomagnetic state elements. *Applied Physics Letters* **103**, 063503 (2013).

[57] Fabian, J. & Sarma, S. D. Spin relaxation of conduction electrons. *Journal of Vacuum Science Technology B* **17**, 1708 (1999).

[58] Wolf, S. A. *et al.* Spintronics: a spin-based electronics vision for the future. *Science* **294**, 1488–1495 (2001).

[59] Koo, H. C. *et al.* Control of spin precession in a spin-injected field effect transistor. *Science* **325**, 1515–1518 (2009).

[60] Jackson, J. D. *Classical electrodynamics* (Wiley, New York, 1999), 3rd edn.

[61] Ihn, T. *Semiconductor Nanostructures* (Oxford University Press, New York, 2010).

[62] D'yakonov, M. I. & Perel, V. I. Possibility of orienting electron spins with current. *ZhETF Pis. Red.* **13**, 657–660 (1971).

[63] Dyakonov, M. & Perel, V. Current-induced spin orientation of electrons in semiconductors. *Physics Letters A* **35**, 459–460 (1971).

[64] Dresselhaus, G. Spin-orbit coupling effects in zinc blende structures. *Phys. Rev.* **100**, 580–586 (1955).

[65] Elliott, R. J. Theory of the effect of spin-orbit coupling on magnetic resonance in some semiconductors. *Phys. Rev.* **96**, 266–279 (1954).

[66] Yafet, Y. Calculation of the g factor of metallic sodium. *Phys. Rev.* **85**, 478 (1952).

[67] Yafet, Y. g Factors and Spin-Lattice Relaxation of Conduction Electrons. In Turnbull, D. & Ehrenreich, H. (eds.) *Solid state physics Vol. 14*, 1–96 (Academic Press, New York, 1963).

[68] Overhauser, A. W. Paramagnetic relaxation in metals. *Phys. Rev.* **89**, 689–700 (1953).

[69] Fabian, J. & Wu, M. Spin Relaxation and Spin Dynamics in Semiconductors. In *Handbook of Spin Transport and Magnetism*, 303–327 (2011).

[70] Boguslawski, P. Electron-electron spin-flip scattering and spin relaxation in IIIV and IIVI semiconductors. *Solid State Communications* **33**, 389–391 (1980).

[71] Bir, G. L., Aronov, a. G. & Pikus, G. E. Spin relaxation of electrons due to scattering by holes. *Zh. Eksp. Teor. Fiz* **42**, 705–712 (1975).

[72] Pershin, Y. V. & Privman, V. Spin relaxation of conduction electrons in semiconductors due to interaction with nuclear spins. *Nano Letters* **3**, 695–700 (2003).

[73] Bychkov, Y. a. & Rashba, E. I. Oscillatory effects and the magnetic susceptibility of carriers in inversion layers. *Journal of Physics C* **17**, 6039–6045 (1984).

[74] Bychkov, Y. a. & Rashba, E. I. Properties of a 2D electron gas with lifted spectral degeneracy. *JETP Letters* **39**, 78–81 (1984).

[75] Schliemann, J., Egues, J. C. & Loss, D. Nonballistic spin-field-effect transistor. *Phys. Rev. Lett.* **90**, 146801 (2003).

[76] Gatteschi, D., Sessoli, R. & Villain, J. *Molecular Nanomagnets.* Mesoscopic Physics and Nanotechnology (OUP, Oxford, 2006).

[77] Gatteschi, D. & Sessoli, R. Quantum Tunneling of Magnetization and Related Phenomena in Molecular Materials. *Angewandte Chemie International Edition* **42**, 268–297 (2003).

[78] Sessoli, R., Gatteschi, D., Caneschi, A. & Novak, M. A. Magnetic bistability in a metal-ion cluster. *Nature* **365**, 141–143 (1993).

[79] Wernsdorfer, W. & Sessoli, R. Quantum Phase Interference and Parity Effects in Magnetic Molecular Clusters. *Science* **284**, 133–135 (1999).

[80] Thomas, L. & Barbara, B. Quantum Tunneling of the Magnetization In Mn12-Ac. *Journal of Low Temperature Physics* **113**, 1055–1060 (1998).

[81] Ardavan, A. *et al.* Will Spin-Relaxation Times in Molecular Magnets Permit Quantum Information Processing? *Phys. Rev. Lett.* **98**, 57201 (2007).

[82] Bogani, L. *et al.* Single-molecule-magnet carbon-nanotube hybrids. *Angewandte Chemie - International Edition* **48**, 746–50 (2009).

[83] Politi, P., Rettori, A., Hartmann-Boutron, F. & Villain, J. Tunneling in mesoscopic magnetic molecules. *Phys. Rev. Lett.* **75**, 537–540 (1995).

[84] Cornia, A. *et al.* Energy-Barrier Enhancement by Ligand Substitution in Tetrairon(III) Single-Molecule Magnets. *Angewandte Chemie - International Edition* **116**, 1156–1159 (2004).

[85] Cervetti, C., Heintze, E. & Bogani, L. Interweaving spins with their environment: novel inorganic nanohybrids with controllable magnetic properties. *Dalton transactions* **43**, 4220–32 (2014).

[86] Chudnovsky, E. M. & Garanin, D. A. Spin Tunneling via Dislocations in Mn_{12} Acetate Crystals. *Phys. Rev. Lett.* **87**, 187203 (2001).

[87] Cornia, A. *et al.* Origin of second-order transverse magnetic anisotropy in Mn12-Acetate. *Phys. Rev. Lett.* **89**, 257201 (2002).

[88] Bogani, L. *et al.* Magneto-Optical Investigations of Nanostructured Materials Based on Single-Molecule Magnets Monitor Strong Environmental Effects. *Advanced Materials* **19**, 3906–3911 (2007).

[89] Mannini, M. *et al.* Quantum tunnelling of the magnetization in a monolayer of oriented single-molecule magnets. *Nature* **468**, 417–421 (2010).

[90] Timco, G. a., Faust, T. B., Tuna, F. & Winpenny, R. E. P. Linking heterometallic rings for quantum information processing and amusement. *Chemical Society reviews* **40**, 3067–3075 (2011).

[91] Faust, T. B. *et al.* Chemical Control of Spin Propagation between Heterometallic Rings. *Chemistry – A European Journal* **17**, 14020–14030 (2011).

[92] Barra, A.-l. *et al.* New Single-Molecule Magnets by Site-Specific Substitution: Incorporation of Alligator Clips into Fe$_4$ Complexes. *European Journal of Inorganic Chemistry* **2007**, 4145–4152 (2007).

[93] Kyatskaya, S. *et al.* Anchoring of Rare-Earth-Based Single-Molecule Magnets on Single-Walled Carbon Nanotubes. *J. Am. Chem. Soc* **131**, 15143–15151 (2009).

[94] Pineider, F. *et al.* Deposition of intact tetrairon(iii) single molecule magnet monolayers on gold: an STM, XPS, and ToF-SIMS investigation. *J. Mater. Chem.* **20**, 187–194 (2010).

[95] Corradini, V. *et al.* Grafting molecular CrNi rings on a gold surface. *Dalton transactions* **39**, 4928–4936 (2010).

[96] Heersche, H. B. *et al.* Electron Transport through Single Mn12 Molecular Magnets. *Phys. Rev. Lett.* **96**, 206801 (2006).

[97] Timco, G. A. G., McInnes, E. J. L. E., Pritchard, R. G., Tuna, F. & Winpenny, R. E. P. Heterometallic rings made from chromium stick together easily. *Angewandte Chemie International Edition* **47**, 9681–9684 (2008).

[98] Affronte, M. *et al.* Linking Rings through Diamines and Clusters: Exploring Synthetic Methods for Making Magnetic Quantum Gates. *Angewandte Chemie International Edition* **44**, 6496–6500 (2005).

[99] Timco, G. A. *et al.* Engineering the coupling between molecular spin qubits by coordination chemistry. *Nat Nano* **4**, 173–178 (2009).

[100] Candini, A. *et al.* Entanglement in Supramolecular Spin Systems of Two Weakly Coupled Antiferromagnetic Rings Cr7Ni. *Phys. Rev. Lett.* **104**, 37203 (2010).

[101] Bellini, V. *et al.* Propagation of Spin Information at the Supramolecular Scale through Heteroaromatic Linkers. *Phys. Rev. Lett.* **106**, 227205 (2011).

[102] Faust, T. B. *et al.* Controlling magnetic communication through aromatic bridges by variation in torsion angle. *Dalton Trans.* **41**, 13626–13631 (2012).

[103] Venkataraman, L., Klare, J. E., Nuckolls, C., Hybertsen, M. S. & Steigerwald, M. L. Dependence of single-molecule junction conductance on molecular conformation. *Nature* **442**, 904–907 (2006).

[104] Barra, A. L. *et al.* Single-Molecule Magnet Behavior of a Tetranuclear Iron(III) Complex. The Origin of Slow Magnetic Relaxation in Iron(III) Clusters. *Journal of the American Chemical Society* **121**, 5302–5310 (1999).

[105] Cornia, A. *et al.* Slow quantum relaxation in a tetrairon (III) single-molecule magnet. *Inorganica Chimica Acta* **361**, 3481–3488 (2008).

[106] Accorsi, S. *et al.* Tuning anisotropy barriers in a family of tetrairon (III) single-molecule magnets with an S= 5 ground state. *J. Am. Chem. Soc* **128**, 4742–4755 (2006).

[107] Blundell, S. *Magnetism in condensed matter* (Oxford University Press, 2001).

[108] Stevens, K. W. H. Matrix Elements and Operator Equivalents Connected with the Magnetic Properties of Rare Earth Ions. *Proceedings of the Physical Society. Section A* **65**, 209 (1952).

[109] Görller-Walrand, C. & Binnemans, K. Rationalization of crystal-field parametrization. In *Handbook on the Physics and Chemistry of Rare Earths* (1996).

[110] Misra, S. K., Poole, C. P. & Farach, H. a. A review of spin Hamiltonian forms for various point-group site symmetries. *Applied Magnetic Resonance* **11**, 29–46 (1996).

[111] Buckmaster, H. a. & Chatterjee, R. The analysis of EPR spectra using tesseral tensor angular momentum operators. *Physica Status Solidi B* **209**, 433–441 (1998).

[112] Carretta, S. *et al.* Intra- and inter-multiplet magnetic excitations in a tetrairon(III) molecular cluster. *Phys. Rev. B* **70**, 214403 (2004).

[113] Rastelli, E. & Tassi, A. Magnetization steps in nanomagnets induced by a time-dependent magnetic field: Application to Fe4. *Phys. Rev. B* **75**, 134414 (2007).

[114] Rastelli, E. & Tassi, A. Relaxation time of the nanomagnet Fe4. *Phys. Rev. B* **79**, 104415 (2009).

[115] Hartmann-Boutron, F., Politi, P. & Villain, J. Tunneling and magnetic relaxation in mesoscopic molecules. *International Journal of Modern Physics B* **10**, 2577–2638 (1996).

[116] Fort, A., Rettori, A., Villain, J., Gatteschi, D. & Sessoli, R. Mixed quantum-thermal relaxation in Mn12 acetate molecules. *Phys. Rev. Lett.* **80**, 612–615 (1998).

[117] Leuenberger, M. N. & Loss, D. Spin tunneling and phonon-assisted relaxation in Mn12-acetate. *Phys. Rev. B* **61**, 1286–1302 (2000).

[118] Gregoli, L. *et al.* Magnetostructural Correlations in Tetrairon (III) Single-Molecule Magnets. *Chemistry - A European Journal* **15**, 6456–6467 (2009).

[119] Thomas, L. *et al.* Macroscopic Quantum Tunneling of Magnetization in a Single-Crystal of Nanomagnets. *Nature* **383**, 145–147 (1996).

[120] Friedman, J. R., Sarachik, M. P., Tejada, J. & Ziolo, R. Macroscopic measurement of resonant magnetization tunneling in high-spin molecules. *Phys. Rev. Lett.* **76**, 3830–3833 (1996).

[121] Hernandez, J. M. *et al.* Evidence for resonant tunneling of magnetization in Mn12-acetate complex (1997).

[122] Hirsch, A. The era of carbon allotropes. *Nature materials* **9**, 868–871 (2010).

[123] Geim, A. K. & Novoselov, K. S. The rise of graphene. *Nat. Mater.* **6**, 183–191 (2007).

[124] Castro Neto, A. H., Guinea, F., Peres, N. M. R., Novoselov, K. S. & Geim, A. K. The electronic properties of graphene. *Rev. Mod. Phys.* **81**, 109–162 (2009).

[125] Wallace, P. R. The band theory of graphite. *Phys. Rev.* **329**, 622–634 (1947).

[126] Slonczewski, J. C., Weiss, P. R., State, T. & Brgnsmck, X. Band Structure of Graphite. *Phys. Rev.* **109**, 272–279 (1958).

[127] Painter, G. S. & Ellis, D. E. Electronic band structure and optical properties of graphite from a variational approach. *Phys. Rev. B* **1**, 4747–4752 (1970).

[128] Lee, C., Wei, X., Kysar, J. W. & Hone, J. Measurement of the Elastic Properties and Intrinsic Strength of Monolayer Graphene. *Science* **321**, 385–388 (2008).

[129] Novoselov, K. S. *et al.* Two-dimensional gas of massless Dirac fermions in graphene. *Nature* **438**, 197–200 (2005).

[130] Sprinkle, M. *et al.* First direct observation of a nearly ideal graphene band structure. *Phys. Rev. Lett.* **103**, 1–4 (2009). arXiv:0907.5222.

[131] Das Sarma, S., Adam, S., Hwang, E. H. & Rossi, E. Electronic transport in two-dimensional graphene. *Rev. Mod. Phys.* **83**, 407–470 (2011).

[132] Avouris, P. Graphene: Electronic and Photonic Properties and Devices. *Nano Letters* **10**, 150–496 (2010).

[133] McEuen, P. L., Bockrath, M., Cobden, D. H., Yoon, Y.-G. & Louie, S. G. Disorder, Pseudospins, and Backscattering in Carbon Nanotubes. *Phys. Rev. Lett.* **83**, 5098–5101 (1999).

[134] Ando, T. Theory of Electronic States and Transport in Carbon Nanotubes. *Journal of the Physical Society of Japan* **74**, 777–817 (2005).

[135] Kane, C. L. & Mele, E. J. Size, Shape, and Low Energy Electronic Structure of Carbon Nanotubes. *Phys. Rev. Lett.* **78**, 1932–1935 (1997).

[136] Shon, N. & Ando, T. Quantum Transport in Two-Dimensional Graphite System. *Journal of the Physical Society of Japan* **67**, 2421–2429 (1998).

[137] Ando, T. & Nakanishi, T. Impurity scattering in carbon nanotubes: absence of back scattering. *Journal of the Physical Society of Japan* (1998).

[138] Recher, P. & Trauzettel, B. A defect controls transport in graphene. *Physics* **4**, 3–5 (2011).

[139] Katsnelson, M. I., Novoselov, K. S. & Geim, A. K. Chiral tunnelling and the Klein paradox in graphene. *Nature Physics* **2**, 620–625 (2006).

[140] Novoselov, K. S. *et al.* Electric field effect in atomically thin carbon films. *Science* **306**, 666–669 (2004).

[141] Kim, S. *et al.* Realization of a high mobility dual-gated graphene field-effect transistor with Al2O3 dielectric. *Applied Physics Letters* **94**, 62107 (2009).

[142] Xu, H. H., Zhang, Z., Wang, Z., Wang, S. & Peng, L.-m. L. Top-Gated Graphene Field-Effect Transistors with High Normalized Transconductance and Designable Dirac Point Voltage. *ACS Nano* **5**, 5031–5037 (2011).

[143] Meric, I. *et al.* Current saturation in zero-bandgap, top-gated graphene field-effect transistors. *Nature Nanotechnology* **3**, 654–659 (2008).

[144] Luryi, S. Quantum capacitance devices. *Applied Physics Letters* **52**, 501 (1988).

[145] Xia, J., Chen, F., Li, J. & Tao, N. Measurement of the quantum capacitance of graphene. *Nature nanotechnology* **4**, 505–9 (2009).

[146] Bolotin, K. I., Sikes, K. J., Hone, J., Stormer, H. L. & Kim, P. Temperature-Dependent Transport in Suspended Graphene. *Phys. Rev. Lett.* **101**, 096802 (2008).

[147] Du, X., Skachko, I., Barker, A. & Andrei, E. Y. Approaching ballistic transport in suspended graphene. *Nature Nanotechnology* **3**, 491–495 (2008).

[148] Adam, S., Hwang, E. H., Galitski, V. M. & Das Sarma, S. A self-consistent theory for graphene transport. *Proceedings of the National Academy of Sciences* **104**, 18392 (2007).

[149] Chen, J. H. *et al.* Charged-impurity scattering in graphene. *Nature Physics* **4**, 8–11 (2008).

[150] Tan, Y.-W. *et al.* Measurement of Scattering Rate and Minimum Conductivity in Graphene. *Phys. Rev. Lett.* **99**, 246803 (2007).

[151] Fradkin, E. Critical behavior of disordered degenerate semiconductors. II. Spectrum and transport properties in mean-field theory. *Phys. Rev. B* **33**, 3263–3268 (1986).

[152] Ludwig, A. W. W., Fisher, M. P. A., Shankar, R. & Grinstein, G. Integer quantum Hall transition: An alternative approach and exact results. *Phys. Rev. B* **50**, 7526–7552 (1994).

[153] Tworzydo, J. *et al.* Sub-Poissonian Shot Noise in Graphene. *Phys. Rev. Lett.* **96**, 246802 (2006).

[154] Katsnelson, M. I. Zitterbewegung, chirality, and minimal conductivity in graphene. *The European Physical Journal B* **51**, 157–160 (2006).

[155] Ziegler, K. Robust transport properties in graphene. *Phys. Rev. Lett.* **97**, 2–5 (2006). arXiv:`0604537v2`.

[156] Nomura, K. & MacDonald, A. H. Quantum Transport of Massless Dirac Fermions. *Phys. Rev. Lett.* **98**, 76602 (2007).

[157] Romero, H. E. *et al.* n-Type behavior of graphene supported on Si/SiO(2) substrates. *ACS nano* **2**, 2037–44 (2008).

[158] Chen, J.-H., Cullen, W. G., Jang, C., Fuhrer, M. S. & Williams, E. D. Defect Scattering in Graphene. *Phys. Rev. Lett.* **102**, 236805 (2009).

[159] Adam, S., Hwang, E. & Das Sarma, S. Scattering mechanisms and Boltzmann transport in graphene. *Physica E* **40**, 1022–1025 (2008).

[160] Adam, S., Hwang, E. H., Rossi, E., Sarma, S. D. & Das Sarma, S. Theory of charged impurity scattering in two-dimensional graphene. *Solid State Communications* **149**, 1072–1079 (2009).

[161] Martin, J. *et al.* Observation of electron-hole puddles in graphene using a scanning single-electron transistor. *Nature Physics* **4**, 144–148 (2008).

[162] Kim, W. *et al.* Hysteresis Caused by Water Molecules in Carbon Nanotube Field-Effect Transistors. *Nano Letters* **3**, 193–198 (2003).

[163] Sabio, J. *et al.* Electrostatic interactions between graphene layers and their environment. *Phys. Rev. B* **77**, 195409 (2008).

[164] Veligura, A. *et al.* Relating hysteresis and electrochemistry in graphene field effect transistors. *Journal of Applied Physics* **110**, 113708 (2011).

[165] Wang, H., Wu, Y., Cong, C., Shang, J. & Yu, T. Hysteresis of Electronic Transport in Graphene Transistors. *ACS nano* **4**, 7221–7228 (2010).

[166] Schedin, F. *et al.* Detection of individual gas molecules adsorbed on graphene. *Nat. Mater.* **6**, 652–655 (2007).

[167] Kim, K. S. K. S. *et al.* Large-scale pattern growth of graphene films for stretchable transparent electrodes. *Nature* **457**, 706–710 (2009).

[168] Eda, G., Fanchini, G. & Chhowalla, M. Large-area ultrathin films of reduced graphene oxide as a transparent and flexible electronic material. (2008).

[169] Reina, A. *et al.* Large Area, Few-Layer Graphene Films on Arbitrary Substrates by Chemical Vapor Deposition. *Nano Letters* **9**, 30–35 (2009).

[170] Wang, X., Zhi, L. & Müllen, K. Transparent, conductive graphene electrodes for dye-sensitized solar cells. *Nano letters* **8**, 323–7 (2008).

[171] Bae, S. *et al.* Roll-to-roll production of 30-inch graphene films for transparent electrodes. *Nature Nanotechnology* **5**, 574–578 (2010).

[172] Liang, X. *et al.* Toward clean and crackless transfer of graphene. *ACS Nano* **5**, 9144–9153 (2011).

[173] Reina, A. & Kong, J. Graphene Growth by CVD Methods. In Murali, R. (ed.) *Graphene Nanoelectronics: From Materials to Circuits*, chap. Ch 7, 167–203 (Springer, Berlin Heidelberg, 2012).

[174] Yi, P., Dong-Xia, S. & Hong-Jun, G. Formation of graphene on Ru(0001) surface. *Chinese Physics* **16**, 3151–3153 (2007).

[175] Yu, Q. *et al.* Graphene segregated on Ni surfaces and transferred to insulators. *Applied Physics Letters* **93**, 23–25 (2008). arXiv:`0804.1778`.

Chapter 3

Determination of scatteres influence in large-area graphene by sub-THz spectroscopy

The major factor limiting the electronic quality of large-area graphene is the presence of *grain boundaries* [1], *defects* [2], *ripples* [3], and importantly *metallic residues* from the underlying metal substrate, mostly in the form of micro- and nanosized Cu or Ni particles (see supplementary information in [4, 5]). As a consequence, broadly varying electronic quality has been reported, as reflected for example in a carrier mobility range [6–9] from 100 to 45000 cm^2 s^{-1} V^{-1}.

As such residues can influence the performance of the final devices [10, 11], protocols have been developed to yield reasonably-clean CVD graphene. In this regards, low-energy optical techniques have recently emerged as powerful tool to study fundamental phenomena in graphene [12] such as, excited carrier dynamics by pump-probe experiments [13–15] and time-domain spectroscopy [16, 17] Dirac fermion behavior using Fourier transform infrared spectroscopy [18–21] and the effect of substrate [22] and doping [23, 24] on the graphene optical response.

Despite this progress, the correlation between residual metal contaminants and the electronic quality of graphene is still unclear. Here we address this issue by performing quasi-optical sub-terahertz (sub-THz) spectroscopy to detect the presence of sub-micron conducting contaminants in CVD. We show that the technique provides direct access to the optical conductivity of graphene, with the high accuracy necessary for probing the subtle influence of a low density of metal residues. Moreover, it can be easily expanded to gated structures to extract the intrinsic electronic properties of individual graphene domains such as carrier mobility, enabling us to identify the limiting scattering mechanisms in a contact-less fashion.

3.1 Transferred CVD graphene: structure

Commercially-available CVD graphene grown on polycrystalline Cu was transferred onto ultrapure Si and crystalline Al_2O_3 substrates, both with a lateral size of 1 cm^2 and a thickness of 500μm.
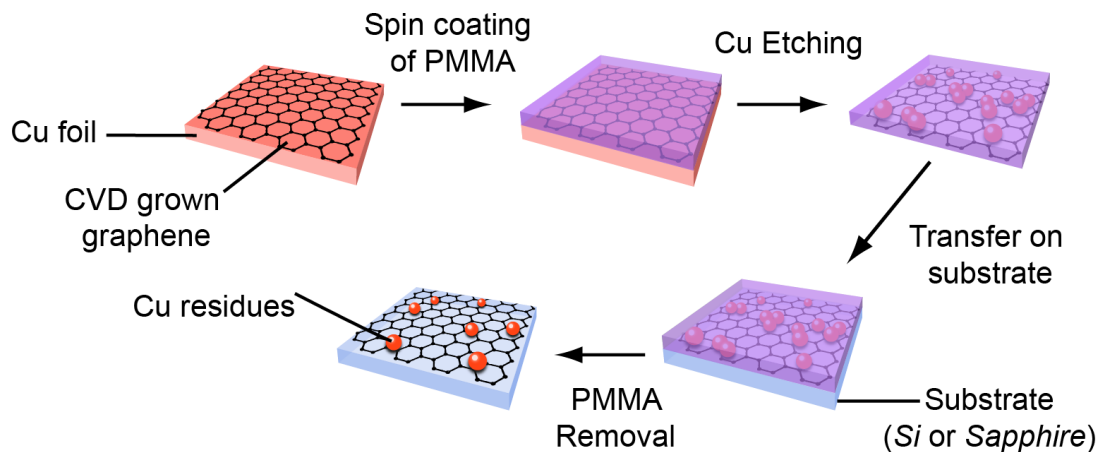

Figure 3.1: Transfer of CVD graphene on arbitrary substrates. Residues of the catalyst are a major source of degradation of graphene electronic quality.

These substrates are suitable for graphene-based solar cells and detectors, and highly transparent to THz and infrared radiation. The transfer process (Figure 3.2a) starts with the deposition of a polymethylmethacrylate (PMMA) layer onto the Cu/graphene by spin coating. This polymeric film will hold the graphene during the etching of the catalyst foil. The latter is performed by placing the Cu/Graphene/PMMA stack floating for a time t_{etch} on the surface of the etching solution prepared by dissolving 8.4 g of FeCl$_3$ in 50 ml of deionized water and adding 10 ml of 1:10 HCl water solution. The etching procedure is carried out at room temperature. Substitution reaction between the Cu foil and Fe[III]-ions present in solution dissolves the metallic substrate effectively:

$$2Fe^{3+} + Cu(s) \quad \leftrightarrow \quad 2Fe^{2+} + Cu^{2+}$$
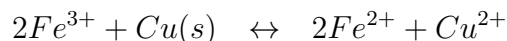
To remove residual etchant, the stack is then immersed for 1 hour in dilute hydrochloric acid, and then transferred into a deionized water bath. The graphene/PMMA bilayer is then picked up from the bottom using the desired substrate. Slow drying on a hotplate at 50°C minimized ruptures in the graphene membrane, while subsequent annealing at 160°C for 2 hours ensured a smoother film surface.

Finally, the PMMA layer is removed via several consecutive soak steps in organic solvents: 4 hours in hot (40 °C) acetone, 30 minutes in fresh 2-propanol, 15 minutes in 1,2-dichloroethane and 15 minutes in 2-propanol.

After PMMA removal, the graphene layer still covers the whole sample area, Figure 3.2a. It exhibits some fractures and folds, which is typical of CVD graphene. The presence of
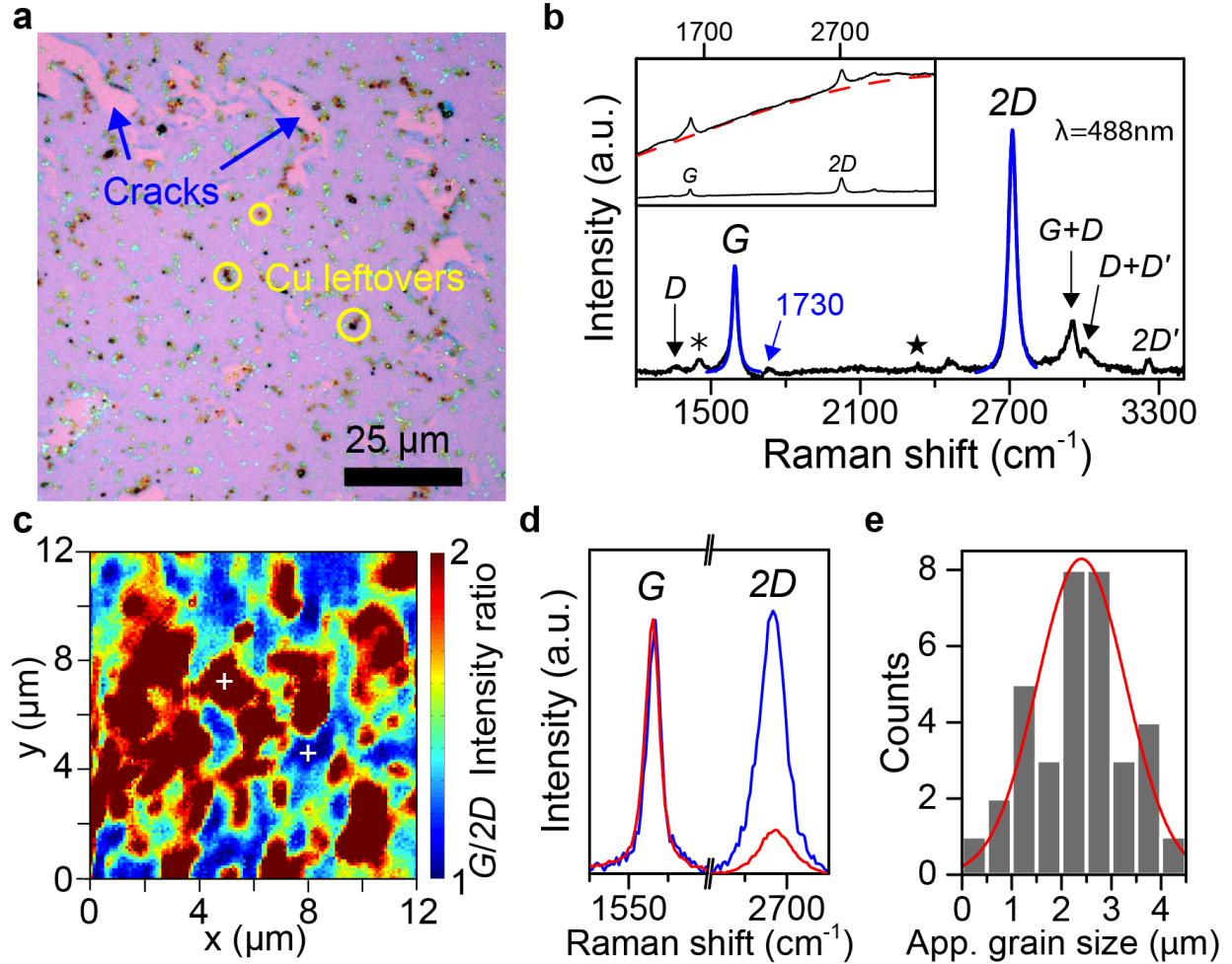
Figure 3.2: a) Optical image of CVD graphene transferred on SiO$_2$ after t_{etch} = 15min. b) Raman spectrum of graphene on SiO$_2$. Blue lines are fits with single Lorentz function. The $*$ and $\star$ symbols indicate SiO$_2$ transverse optical (TO) phonon mode and ambient N$_2$, respectively. Inset: spectra at different sample positions revealing a variable luminescence background due to Cu residues. c) Raman map of the G/2D intensity ratio of a two-layers graphene stack. e) Raman spectra, as acquired at the positions of the white crosses in c). d) Statistical analysis of the apparent grain lateral size extracted from c). Red solid line is a fit with Gaussian function.

copper contaminants, which size and amount depend on t_{etch}, is clearly visible.

The graphene films were investigated by micro-Raman spectroscopy (Figure 3.2b). The Raman 2D peak at 2700 cm^{-1}, associated with the second order zone-boundary phonons, is sensitive to the number of graphene layers [25]. For the present samples, the 2D peak can be fitted with a single Lorentzian function, confirming the presence of single-layer graphene. A G peak, due to the doubly-degenerate zone-centre E$_{2g}$ phonon, is detected at 1596 cm^{-1}, and its upshift of 16 cm^{-1} indicates moderate doping [26] corresponding to a

residual carrier density of $\sim 10^{12}$ cm^{-2}. The very weak D peak at 1350 cm^{-1}, connected to the A$_{1g}$ breathing mode at the Brillouin zone boundary and only activated by the presence of lattice defects, indicates very little disorder in the present sample and gives rise to additional combined modes in the upper part of the spectrum (see Section 4.1.3 for more details on Raman spectrum of graphene). A small peak at $\sim$ 1730 cm^{-1} is typical of C=O stretching mode in PMMA residues [27]. Raman spectra acquired at different positions exhibit a variable background photoluminescence testifying the presence of Cu residues [28], inset in Figure 3.2b, as also confirmed by scanning electron microscopy.

CVD graphene grown on polycrystalline Cu foil, is composed of high quality crystalline grains with random crystallographic orientations [4]. One way to reveal the CVD grain structure is to exploit the Raman intensity dependence on the twist angle in a stacked two layers graphene system [29]. The two-layers stack was fabricated by first etching both graphene layers for 14hours and trasferred one on top of the other following the procedure of Figure3.1. In order to maximize the interlayer interaction, the stack was annealed in forming gas overnight at 400C after each graphene transfer. The different crystallographic orientations between the top and bottom layers modulates the interlayer interaction between the domains. On this basis, monitoring the spatial distribution of the G/2D intensity ratio, enables probing the grain structure (Figure 3.2c, d). Statistical analysis (Figure 3.2e) yields an apparent grain size distribution peaked at $2.40 \pm 0.13 \mu$m corresponding to a mean grain size of $\sim 5 \mu$m for the single layer.

3.2   Sub-THz Mach-Zehnder spectrometry of graphene

For the optical investigations, we used a Mach-Zehnder interferometer-based spectrometer [30], Figure 3.3a, comprising backward-wave oscillators [30] as coherent sources of continuous sub-THz radiation.

Their frequency can be continuously tuned between 0.03 and 1.5 THz, corresponding to 1 - 50 cm^{-1}, and 6 - 0.1 meV. The radiation is detected by either Golay cells or ^{4}He-cooled Si bolometers. The frequency resolution $\Delta\nu/\nu$ is better than 10^{-5}, and the dynamic range is between 40 and 50 dB. The Mach-Zehnder interferometric configuration enabled detecting both amplitude and phase shift of the transmitted radiation, thus opening the possibility to determine the complex electromagnetic response of graphene without involving Kramers-Kronig relations [31]. A round slit sets the beam diameter to 5 mm, so that several graphene domains are homogeneously irradiated. The plane-parallel undoped Si or Al$_2$O$_3$ substrates implemented a Fabry-Perot resonator formed by the graphene-substrate and substrate-air interfaces (Figure 3.3b). The resulting multiple reflections allow maximizing the interaction of sub-THz radiation with graphene, and thus to significantly enhance the sensitivity. The electrodynamic response of the resulting multilayer was analysed using the Fresnel formulas [31], according to which the complex transmission $\hat{t}_{ij}$ and reflection $\hat{r}_{ij}$ coefficients at each interface are given by:
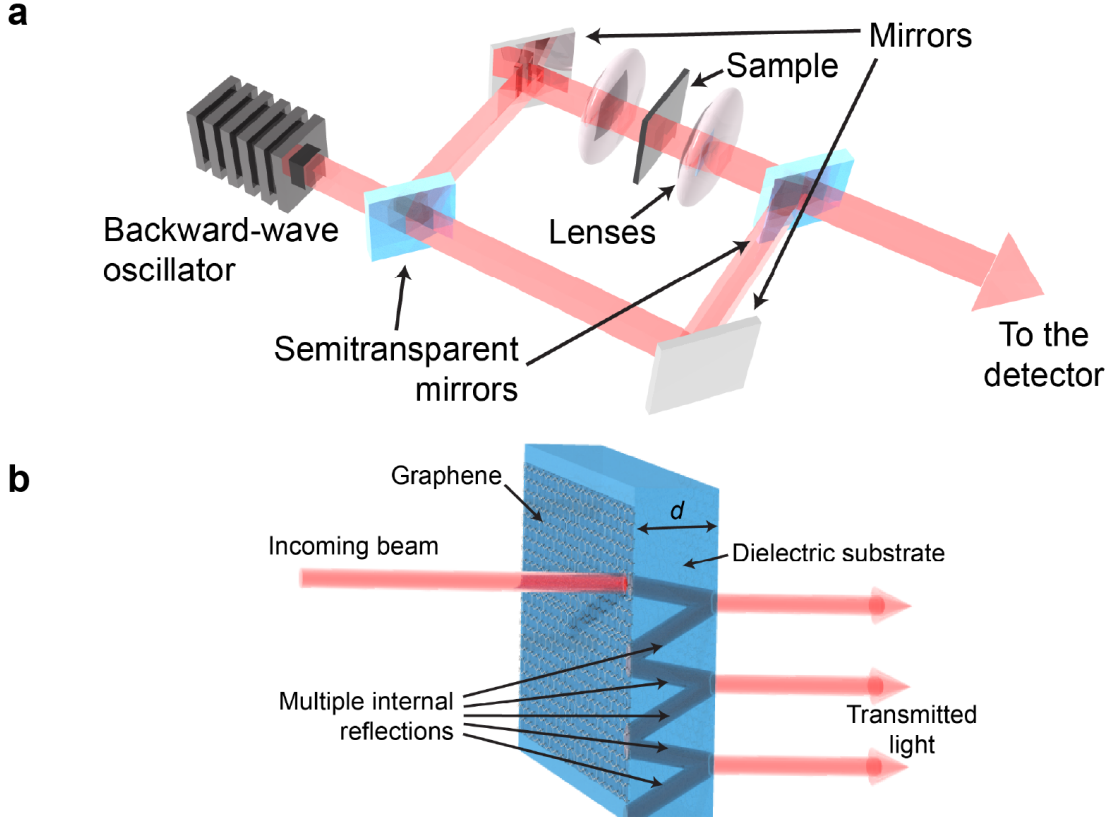
Figure 3.3: a) Scheme of sub-THz spectrometer. (b) Scheme of the multiple internal reflections within the dielectric that lead to Fabry-Perot interferences.

$$\hat{t}_{ij} = \frac{\hat{n}_i - \hat{n}_j}{\hat{n}_i + \hat{n}_j} \;, \quad \hat{r}_{ij} = \frac{2\hat{n}_i}{\hat{n}_i + \hat{n}_j} \tag{3.1}$$

where i and j are the material indices, and $\hat{n}_i = n_i + ik_i$ the complex refractive indexes (n_i and k_i are the *refraction* and *extinction* indexes respectively). Phase shift and attenuation are described by $e^{i\delta_i}$ terms where $\delta_i = \hat{n}_i d_i c/\omega$, $\omega = 2\pi c\nu$ is the radiation frequency, and d_i is the i-layer thickness. For air, $n_1 = n_4 = 1$ and $k_1 = k_4 = 0$, while for the dielectric substrate, n_3, k_3 and d_3 are determined beforehand. The total $\hat{t}$ can thus be written as [30, 31]:

$$\hat{t} = \frac{\hat{t}_{12}\hat{t}_{23}\hat{t}_{34}e^{i(\delta_2+\delta_3)}}{1 + \hat{r}_{23}\hat{r}_{34}e^{2i\delta_3}}\left(1 + \hat{r}_{12}\frac{\hat{r}_{23} + \hat{r}_{34}e^{2i\delta_3}}{1 + \hat{r}_{23}\hat{r}_{34}e^{2i\delta_3}}e^{2i\delta_2}\right)^{-1} \tag{3.2}$$

with the measured transmission coefficient $Tr = |t|^2$.

The sample is mounted in a ^{4}He cryostat equipped with mylar windows for optical access, enabling the investigation of the temperature dependence of the optical response.

3.3   Effect of adsorbates on large-area graphene

Figure 3.4a compares the frequency dependence of the transmission coefficient for the bare Si substrate and four graphene samples transferred under the same conditions. Thickness and refractive index of the dielectric substrate determine the period of the interferometric fringes [30], while the amplitude of the maxima gives the optical conductance of the sample. Phase shifts observable in the interference pattern of different graphene samples result from small differences in the substrate thickness of about 25 μm. The latter does not affect the amplitude of the patterns, that are all equal and 30% smaller than those for the empty substrate. By fitting the spectra with equation (3.2), the graphene *optical conductance G* was obtained. The G values were corrected for the small but finite substrate absorption.

To explore the effect of contaminants and Cu residues on the electronic quality of graphene, we measured the optical conductance G for different t_{etch}, Figure 3.4b, while keeping the PMMA layer on top (step 4 in Figure 3.2a). G is seen to increase monotonously with t_{etch} reaching a saturation value of $(2.3 \pm 0.1) \cdot 10^{-3}\Omega^{-1}$ after 14 hours. Moreover assuming a constant graphene Fermi velocity $v_{\mathrm{F}} = 10^6$ m/s, illumination in the wavenumber range 26 - 35 cm^{-1} is expected to induce a lateral carrier displacement $l = \frac{v_{\mathrm{F}}}{\nu}$ between 1.3 and 1μm. Correspondingly, in order for an object to be non-transparent, its size must exceed $\sim 1\mu$m, which is well above the average size of molecular contaminants and Cu impurities already at $t_{etch} > 15$ min. This is further confirmed by the flat frequency dependence at lower wavenumbers (9 - 20 cm^{-1}).

These observations show that Cu residues may contribute to the sample optical conductance only for very short t_{etch}, while for long t_{etch}, Cu residues behave as charged scatterers, possibly together with other contaminants, degrading the electronic quality of graphene [32]. Increasing t_{etch}, the amount of Cu impurities decreases and the electronic quality of pristine graphene is gradually approached.

Upon removal of the PMMA layer (step 5 in Figure 3.2a), the optical conductance decreases sharply to $(1.0 \pm 0.1) \cdot 10^{-3}\Omega^{-1}$ (Figure 3.4c). As PMMA is fully transparent at these frequencies, this difference reveals the doping effect of a higher-κ dielectric environment. Air has a κ-value almost half that of PMMA ($\kappa_{\mathrm{air}} = 1$, $\kappa_{\mathrm{PMMA}} \sim 2.6$); removal of the latter shifts the Fermi level closer to charge neutrality point, driving G toward the well-known conductance minimum.

3.4   Electronic quality of large area graphene

The optical conductance of graphene is predicted to assume the universal value $G_0 = e^2/4\hbar = 6.1 \cdot 10^{-5}\Omega^{-1}$ (with e the electron charge and $\hbar$ Plank's constant) independent of frequency as an intrinsic property of massless Dirac fermions [33–35]. For the present bare graphene (without PMMA) samples, a much higher conductance of approximately $G \approx 30G_0$ is detected at the lowest frequency, Figure 3.5a. Similarly large values have been observed at higher frequencies [18, 21, 36] and in time-resolved measurements [16, 19]
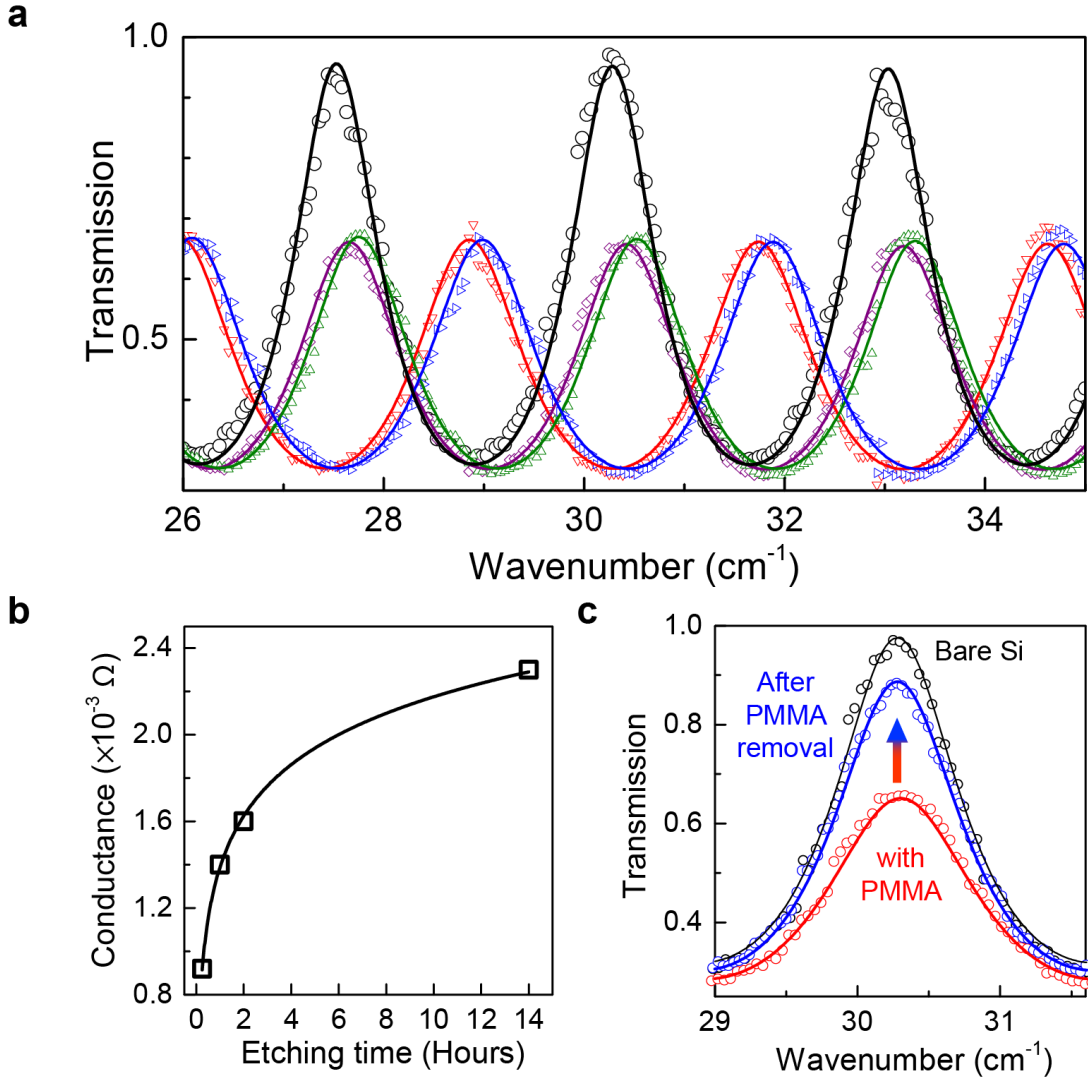
Figure 3.4: Effect of Cu and PMMA leftovers a) Transmission spectra of a Si substrate without (black) and with (colour) graphene/PMMA stack on top ($t_{etch} = 14$ hours). Different colours indicate different samples. b) Conductivity of graphene for different Cu etching time. The line is a guide to the eye. c) Comparison of transmission amplitudes for graphene on Si, before (red) and after (blue) PMMA removal.

on large-area graphene. It is noteworthy that in contrast to previous works that use higher frequencies [37], in our experiments the conductance is independent of the type of substrate. The high value of $G \approx 30G_0$ suggests that the optical response of graphene at such low frequencies is notably affected by inhomogeneities and the finite temperature. In this context, it is relevant that the dc conductance minimum of graphene at the Dirac point is governed by extrinsic factors, most prominently the presence of charged impurities on the substrate [38, 39] and residual Cu. In the present case, the carrier scattering that

arises from such impurities can be accounted for by the Drude model [30, 31] and complementing the sub-THz measurements with higher-frequency absorption data gained by Fourier-transform spectroscopy. The combined frequency-dependence, displayed in Figure 3.5a, is fitted with $\sigma(\nu) = \sigma_0 \gamma^2/(\nu^2 + \gamma^2)$, where σ_0 is the DC conductivity and γ is the carrier scattering rate [30, 31]. The value of γ was found to be 270 cm^{-1} at high temperature T, in agreement with previous reports [20, 21]. The T-dependence of γ, Figure 3.5b, shows a T-independent contribution below 100 K and a marked increase at higher frequencies, indicating two different scattering contributions. The first, associated with defects and charged impurities, is the dominant factor limiting the conductance of graphene at low temperatures [38–40]. Fitting by a power dependence T^β yielded $\beta > 2$, which cannot be attributed to scattering by longitudinal graphene phonons as this mechanism would afford $\beta = 1$ [40]. Instead, such strong temperature dependence indicates scattering by substrate phonons to be the dominant mechanism limiting G at high temperatures [41–43]. The residual $\gamma = 86 \pm 1$ cm^{-1} corresponds [21] to a concentration of scatterers of $3.4 \pm 0.5 \cdot 10^{11}$ cm^{-2}, in agreement with previous reports for CVD graphene [9, 20] and comparable to typical exfoliated graphene flakes at room temperature [44, 45].

The latter observation is a hint that grain boundaries do not represent the dominant source of scattering in these samples, as also suggested by transport measurements [4].

With the aim of determining the carrier mobility and compensate for the residual doping, we introduced a gate that allows tuning the graphene charge density n. To maintain the transparency necessary for investigation at sub-THz energies, we fabricated the multilayer structure depicted in Figure 3.5c. It is composed of a Al$_2$O$_3$ substrate, a 20 nm-thick Ni:Cr alloy layer, with a $d = 300$ nm-thick e-gun evaporated SiO$_2$ layer serving as gate dielectric on top of which the CVD graphene is transferred. The Ni:Cr alloy was chosen because it forms closed, electrically conducting thin films of sufficient high transparency in the sub-THz range. The resulting device has an overall transmission coefficient of 0.15 in the $9 - 20$cm^{-1} range. The gate voltage V_{gate} is applied between graphene, contacted with Au/Cr contacts, and the Ni:Cr layer.

The optical conductance at 9 cm^{-1} recorded as a function of gate voltage is shown in Figure 3.5d. The characteristic minimum at $V_{\text{gate}} \neq 0$ indicates the Dirac point. Similar to dc electrical transport measurements, the V_{gate}- dependence exhibited hysteretic behaviour under ambient conditions, owing to polar impurities and adsorbed water [46]. The ρ vs. V_{gate} curve reveals a pronounced electron-hole asymmetry at high carrier densities. As the present contact-less technique is not affected by work-function mismatch at the electrical contacts like in dc transport studies [47], it follows that in graphene charge impurities have different scattering cross-sections for electrons and holes [48]. As discussed in Section 2.3, fitting with [49]:

$$R(V_{\text{gate}}) = R_S + \left(e\mu_c \sqrt{n_0^2 + n(V_{\text{gate}})^2} \right)^{-1} \tag{3.3}$$

yields a mobility of $\mu_e = (4.5 \pm 0.5) \cdot 10^4$ cm^{2}V^{-1}s^{-1} for electrons and $\mu_h = (4.7 \pm 0.7) \cdot 10^4$ cm^{2}V^{-1}s^{-1} for holes, (R_S is the short-range scattering contribution to resistance, n_0 the
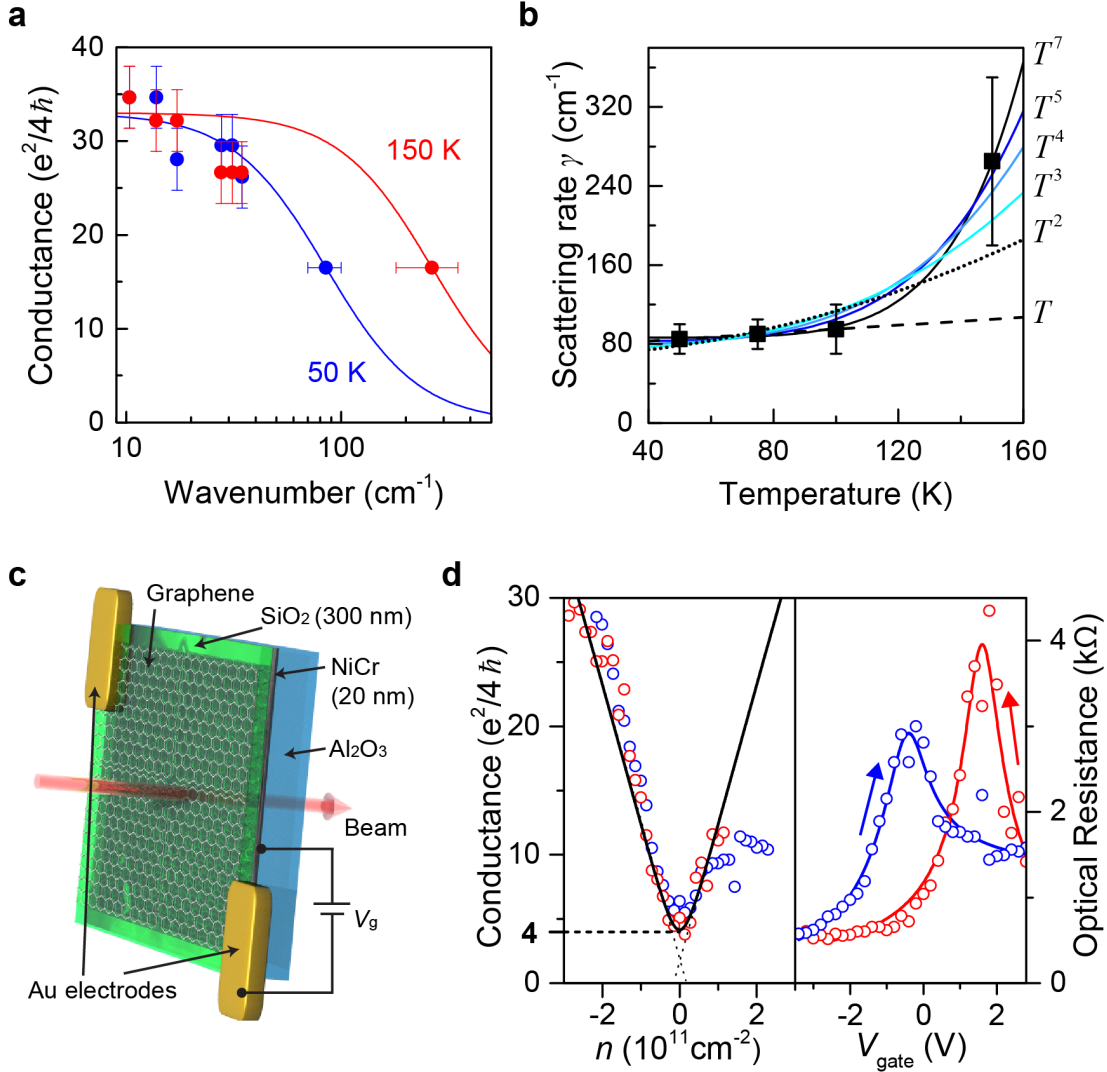
Figure 3.5: a) Frequency-dependence of the graphene conductance at two different temperatures on Al_2O_3 substrate. Lines are fits using the Drude model. b) Temperature dependence of the carriers scattering rate, as extracted from the Drude fits. The solid line is a simulation of the T^β dependence for different β. Dashed line, $\beta = 1$, indicates electron-extrinsic phonons scattering. c) Structure of the THz-transparent multilayer structure for the optical characterization of the n-dependence of the conductance. d) Gate dependence of the optical behaviour at 300 K recorded at 9 cm^{-1} (red and blue are different sweeps), showing: (left) G vs. n, (right) resistance vs. V_{gate}. Lines are fits to the data. The dashed black line indicates $4e^2/\hbar$.

residual carrier density at the charge-neutrality point due to electron-hole puddles [50] and $n = \dfrac{\epsilon_0 \kappa_{\mathrm{SiO_2}}}{ed} V_{\mathrm{gate}}$ where ϵ_0 is the vacuum permittivity and $\kappa_{SiO_2} = 3.9$).

The extracted mobilities are one to two orders of magnitude higher than those typically derived from dc measurements of CVD graphene on SiO_2 [7, 51] while they closely match those of clean exfoliated flakes [9] or single-grain CVD crystals [8]. This finding supports the conclusion that sub-THz optical detection probes the intrinsic conductance of the domains that constitute the CVD layer, as expected from the fact that at $9\mathrm{cm}^{-1}$ it induces electronic oscillations over lengths $l \sim 5\mu m$, below the average domain size in CVD graphene. It follows that the observed mobilities are limited by surface-scatterers, analogous to other, solid-supported graphene sheets.

Contact effects, which play a significant role in dc transport measurements [47], certainly do not affect the conductance determined by optical means. Hence, the density of charged long-range scatterers can be estimated [38] close to the Dirac point. From the two branches of the curve, values of $(7 \pm 2) \cdot 10^{10}$ cm^{-2} and $(9.5 \pm 1) \cdot 10^{10}$ cm^{-2} are extracted, which are only slightly lower than estimated above from the T-dependence of γ. Comparison with electrical transport experiments on large CVD surfaces indicates that crystal defects contribute a density of $\sim 10^2$ cm^{-2} to short range scattering.

Importantly, the applied gate voltage allows compensating for the extrinsic doping by charged impurities, yielding a condactance of $G \approx 4G_0$, much lower than previously reported [16, 18, 19]. This provides further support that larger conductance values arise from extrinsic doping (i.e. Cu and molecular contaminants or surface charges).

3.5   Conclusions

In conclusion, we demonstrated that the electronic response of individual domains in wafer-sized CVD graphene can be directly addressed by using contact-less sub-THz interferometry. Moreovere, this thechnique allows to quantify the graphene intrinsic optical conductance, validating important theoretical predictions. The mobility values measured in contact-less fashion, are orders of magnitude larger than those obtained on equivalent CVD graphene, by traditional dc transport measurements [7, 51], matching values obtained for high-quality samples [8, 9, 45, 51]. The mobility is found to be mainly limited by charged scatterers on the substrate, and our observations validate previous theoretical predictions [38]. The high sensitivity of the sub-THz response to contaminants can be used to address the electronic quality of large graphene structures, essential for applications in touchscreens, wearable and optoelectronic devices. The Cu contamination of both surfaces of the graphene layer, as observed here, is an important result for device fabrication, showing that adequate treatment is required for complete removal of the catalyst.

Bibliography

[1] Tsen, A. W. *et al.* Tailoring electrical transport across grain boundaries in polycrystalline graphene. *Science* **336**, 1143–6 (2012).

[2] Lahiri, J., Lin, Y., Bozkurt, P., Oleynik, I. I. & Batzill, M. An extended defect in graphene as a metallic wire. *Nature Nanotechnology* **5**, 326–329 (2010).

[3] Ni, G.-X. *et al.* Quasi-Periodic Nanoripples in Graphene Grown by Chemical Vapor Deposition and Its Impact on Charge Transport. *ACS Nano* **6**, 1158–1164 (2012).

[4] Huang, P. Y. *et al.* Grains and grain boundaries in single-layer graphene atomic patchwork quilts. *Nature* **469**, 389–392 (2011).

[5] Liang, X. *et al.* Toward clean and crackless transfer of graphene. *ACS Nano* **5**, 9144–9153 (2011).

[6] Reina, A. *et al.* Large Area, Few-Layer Graphene Films on Arbitrary Substrates by Chemical Vapor Deposition. *Nano Letters* **9**, 30–35 (2009).

[7] Li, X. *et al.* Graphene Films with Large Domain Size by a Two-Step Chemical Vapor Deposition Process. *Nano Letters* **10**, 4328–4334 (2010).

[8] Petrone, N. *et al.* Chemical vapor deposition-derived graphene with electrical performance of exfoliated graphene. *Nano letters* **12**, 2751–6 (2012).

[9] Li, X. *et al.* Large-area synthesis of high-quality and uniform graphene films on copper foils. *Science* **324**, 1312–4 (2009).

[10] Pi, K. *et al.* Electronic doping and scattering by transition metals on graphene. *Phys. Rev. B* **80**, 75406 (2009).

[11] McCreary, K. M. *et al.* Effect of cluster formation on graphene mobility. *Phys. Rev. B* **81**, 115453 (2010).

[12] Docherty, C. J. & Johnston, M. B. Terahertz properties of graphene. *Journal of Infrared, Millimeter, and Terahertz Waves* **33**, 797–815 (2012).

[13] Jnawali, G., Rao, Y., Yan, H. & Heinz, T. F. Observation of a transient decrease in terahertz conductivity of single-layer graphene induced by ultrafast optical excitation. *Nano Letters* **13**, 524–530 (2013).

[14] Shi, S. F. *et al.* Controlling graphene ultrafast hot carrier response from metal-like to semiconductor-like by electrostatic gating. *Nano Letters* **14**, 1578–1582 (2014).

[15] Frenzel, a. J. *et al.* Observation of suppressed terahertz absorption in photoexcited graphene. *Applied Physics Letters* **102**, 1–5 (2013).

[16] Tomaino, J. L. *et al.* Terahertz imaging and spectroscopy of large-area single-layer graphene. *Optics express* **19**, 141–146 (2011).

[17] Maeng, I. *et al.* Gate-controlled nonlinear conductivity of Dirac fermion in graphene field-effect transistors measured by terahertz time-domain spectroscopy. *Nano Letters* **12**, 551–555 (2012).

[18] Horng, J. *et al.* Drude conductivity of Dirac fermions in graphene. *Phys. Rev. B* **83**, 165113 (2011).

[19] Ren, L. *et al.* Terahertz and infrared spectroscopy of gated large-area graphene. *Nano letters* **12**, 3711–5 (2012).

[20] Li, Z. Q. *et al.* Dirac charge dynamics in graphene by infrared spectroscopy. *Nat. Phys.* **4**, 532–535 (2008).

[21] Yan, H. *et al.* Infrared Spectroscopy of Wafer-Scale Graphene. *ACS Nano* **5**, 9854–9860 (2011).

[22] Kim, J. Y. *et al.* Far-infrared study of substrate-effect on large scale graphene. *Applied Physics Letters* **98**, 10–13 (2011).

[23] Docherty, C. J. *et al.* Extreme sensitivity of graphene photoconductivity to environmental gases. *Nat. Commun.* **3**, 1228 (2012).

[24] Liu, F., Chong, Y. D., Adam, S. & Polini, M. Gate-tunable coherent perfect absorption of terahertz radiation in graphene. *2D Materials* **1**, 031001 (2014).

[25] Ferrari, A. C. *et al.* Raman spectrum of graphene and graphene layers. *Physical Review Letters* **97**, 187401 (2006).

[26] Casiraghi, C., Pisana, S., Novoselov, K. S., Geim, A. K. & Ferrari, A. C. Raman fingerprint of charged impurities in graphene. *Applied Physics Letters* **91**, 233108 (2007).

[27] Wang, Q. H. *et al.* Understanding and controlling the substrate effect on graphene electron-transfer chemistry via reactivity imprint lithography. *Nat. Chem.* **4**, 724–32 (2012).

[28] Costa, S. D. *et al.* Resonant Raman spectroscopy of graphene grown on copper substrates. *Solid State Communications* **152**, 1317–1320 (2012).

[29] Havener, R. W., Zhuang, H., Brown, L., Hennig, R. G. & Park, J. Angle-resolved raman imaging of interlayer rotations and interactions in twisted bilayer graphene. *Nano Letters* **12**, 3162–3167 (2012).

[30] Gorshunov, B. *et al.* Terahertz BWO-Spectrosopy. *International Journal of Infrared and Millimeter Waves* **26**, 1217–1240 (2005).

[31] Pracht, U. S. *et al.* Electrodynamics of the superconducting state in ultra-thin films at THz frequencies. *IEEE Transactions on Terahertz Science and Technology* **3**, 269–280 (2013).

[32] Kretinin, a. V. *et al.* Electronic properties of graphene encapsulated with different two-dimensional atomic crystals. *Nano Letters* **14**, 3270–3276 (2014).

[33] Mishchenko, E. G. Effect of Electron-Electron Interactions on the Conductivity of Clean Graphene. *Phys. Rev. Lett.* **98**, 216801 (2007).

[34] Stauber, T., Peres, N. M. R. & Castro Neto, A. H. Conductivity of suspended and non-suspended graphene at finite gate voltage. *Phys. Rev. B* **78**, 85418 (2008).

[35] Nair, R. R. *et al.* Fine structure constant defines visual transparency of graphene. *Science* **320**, 1308 (2008).

[36] Mak, K. F. *et al.* Measurement of the Optical Conductivity of Graphene. *Phys. Rev. Lett.* **101**, 196405 (2008).

[37] Scharf, B., Perebeinos, V., Fabian, J. & Avouris, P. Effects of optical and surface polar phonons on the optical conductivity of doped graphene. *Phys. Rev. B* **87**, 1–9 (2013).

[38] Adam, S., Hwang, E. H., Galitski, V. M. & Das Sarma, S. A self-consistent theory for graphene transport. *Proceedings of the National Academy of Sciences* **104**, 18392 (2007).

[39] Morozov, S. V. *et al.* Giant intrinsic carrier mobilities in graphene and its bilayer. *Phys. Rev. Lett.* **100**, 16602 (2008).

[40] Hwang, E. & Das Sarma, S. Screening-induced temperature-dependent transport in two-dimensional graphene. *Phys. Rev. B* **79**, 165404 (2009).

[41] Castro, E. V. *et al.* Limits on Charge Carrier Mobility in Suspended Graphene due to Flexural Phonons. *Phys. Rev. Lett.* **105**, 266601 (2010).

[42] Hwang, E. H. & Das Sarma, S. Acoustic phonon scattering limited carrier mobility in two-dimensional extrinsic graphene. *Phys. Rev. B* **77**, 115449 (2008).

[43] Mariani, E. & von Oppen, F. Temperature-dependent resistivity of suspended graphene. *Phys. Rev. B* **82**, 195403 (2010).

[44] Kim, K. S. K. S. *et al.* Large-scale pattern growth of graphene films for stretchable transparent electrodes. *Nature* **457**, 706–710 (2009).

[45] Novoselov, K. S. *et al.* Two-dimensional gas of massless Dirac fermions in graphene. *Nature* **438**, 197–200 (2005).

[46] Kim, W. *et al.* Hysteresis Caused by Water Molecules in Carbon Nanotube Field-Effect Transistors. *Nano Letters* **3**, 193–198 (2003).

[47] Huard, B., Stander, N., Sulpizio, J. A. & Goldhaber-Gordon, D. Evidence of the role of contacts on the observed electron-hole asymmetry in graphene. *Phys. Rev. B* **78**, 121402 (2008).

[48] Novikov, D. S. Numbers of donors and acceptors from transport measurements in graphene. *Applied Physics Letters* **91**, 102102 (2007).

[49] Kim, S. *et al.* Realization of a high mobility dual-gated graphene field-effect transistor with Al2O3 dielectric. *Applied Physics Letters* **94**, 62107 (2009).

[50] Martin, J. *et al.* Observation of electron-hole puddles in graphene using a scanning single-electron transistor. *Nature Physics* **4**, 144–148 (2008).

[51] Geim, A. K. & Novoselov, K. S. The rise of graphene. *Nat. Mater.* **6**, 183–191 (2007).

Part I

Single Molecule Magnets-Graphene hybrids

Chapter 4

Creation of Graphene functional structures

Being graphene an all-surface open material, the self-assembly of supramolecular architectures on its surface [1–8] can be used to tailor graphene electronic and magnetic properties. [9–16]. Here we explore the possibility to modify the graphene magnetic properties by combining it with single-molecule magnets (SMMs) [17–22]. Owing to the SMMs magnetic and quantum features [23, 24], such hybrid material is interesting for the study of environmental spin-interactions in carbon-based materials [25–30]. The theoretical and experimental investigations presented in the following chapters demonstrate that controlling the aggregation and surface organization of SMMs on graphene is essential to rationally design the magnetic behavior of the SMM-graphene hybrids. In this framework, it is thus very important to understand the assembly regimes and associated parameters, and explore the possibility of induce changes in the sopramolecular arrangement on the surface. Up to now, little is known on how SMM-graphene hybrids are formed and the major factors that govern molecular assembly on graphene remain yet to be unraveled.

4.1 Identification of single layer graphene

4.1.1 Exfoliated graphene

The most common and easy procedure to produce graphene is the so-called micromechanical cleavage of graphite (Figure 4.1) [31]. In this procedure, graphene layers are cleaved directly from a piece of graphite using a common adesive tape. The tape is subsequently pressed onto a Silicon substrate with a 300 nm-thick oxide layer thermally grown on top. This SiO_2 thickness is found to give the highest optical contrast, making single layer graphene visible using an optical microscope (Figure 4.1c) [32].
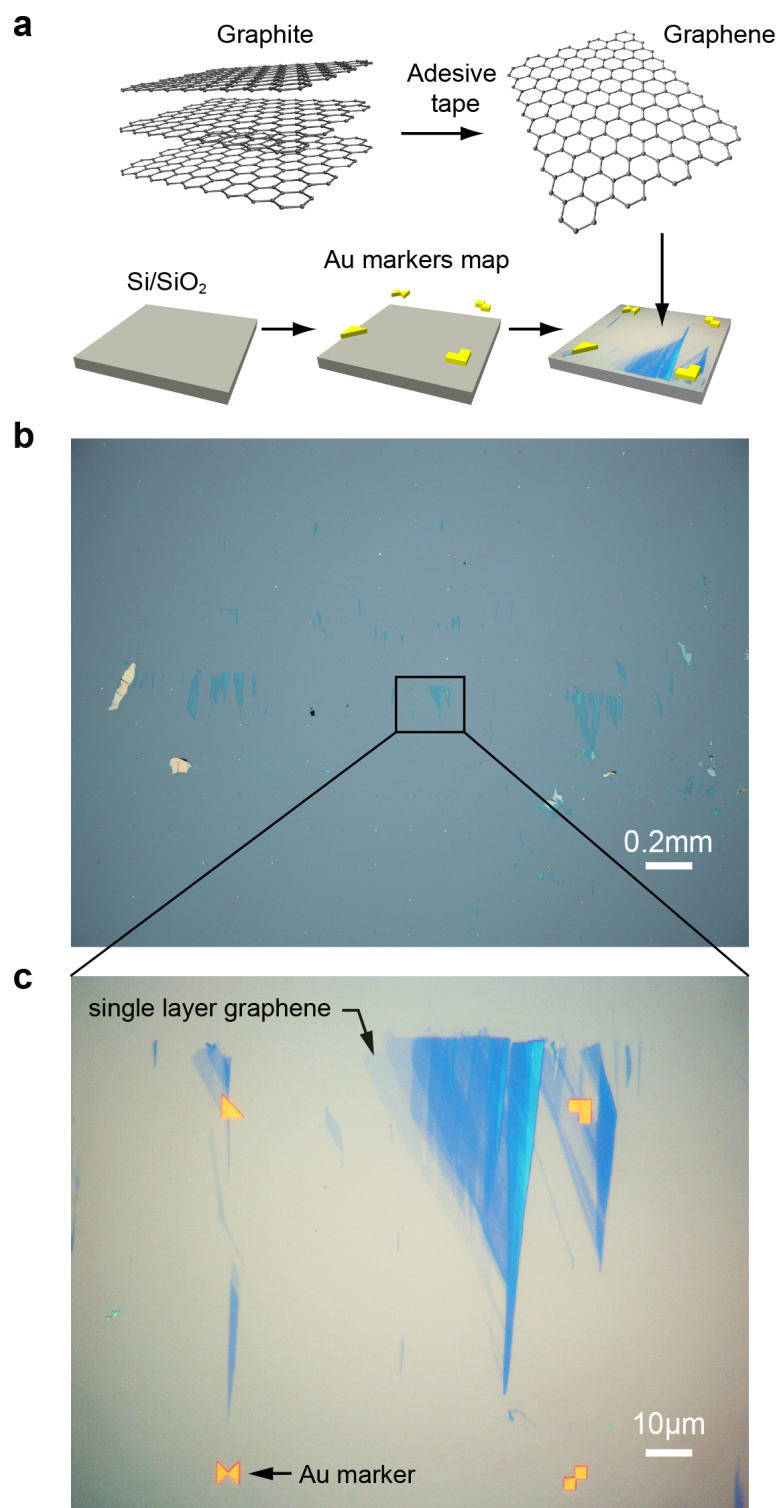
Figure 4.1: a) Transfer of exfoliated graphene to a SiO_2/Si substrate mapped with Au/Ti markers. b) Optical image of the substrate showing several graphitic residues. c) Zoom-in of a multilayer graphene stack.

4.1.2 Microscopy

The sample is then carefully scanned at 50x magnification to identify and locate monolayer graphene, Figure 4.1a. This method produces graphene flakes with an average lateral size of 10 - 20 micrometers and of extremely high crystalline quality. The flakes are randomly distributed on the substrate and often surrounded by thicker graphitic residues, Figure 4.1b. For this reason, the substrates are pre-patterned with a map of Ti/Au markes to help to locate the suitable flakes and to enable accurate alignment during the lithographic process, Figure 4.1c. The properties of graphene change drastically with the number of layers [33–37], it is thus important to correctly determine the layers number prior to any experiment.
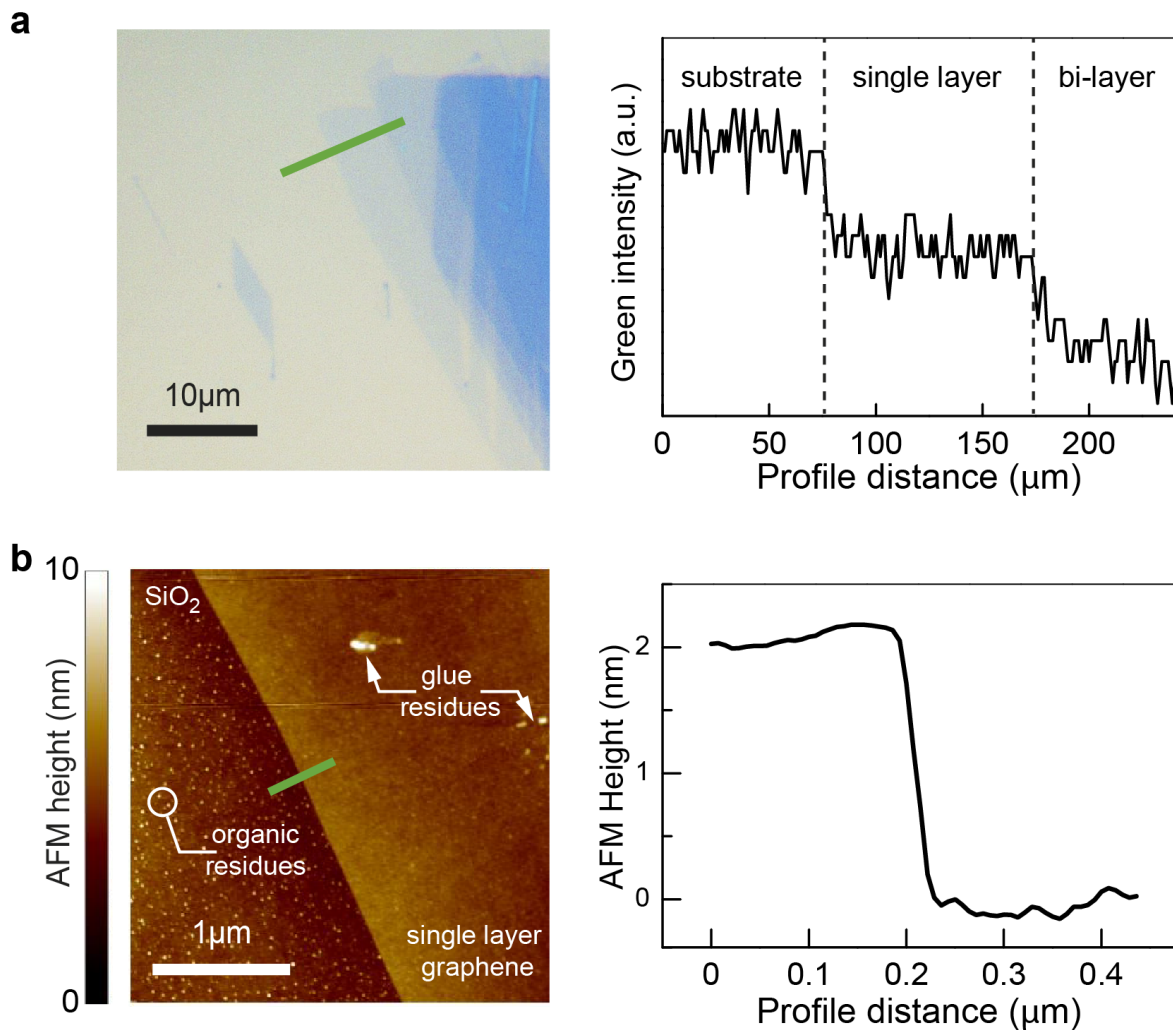

Figure 4.2: Single layer graphene a) Intensity profile with a green filter helps determining the number of layers. b) The apparent AFM height profile of graphene is altered by the substrate roughness and by the presence of organic residues on it (small white spots).

In these regards, the intensity profile in the green channel, [32, 36] of the optical picture provides good hints about the number of layers constituting the flake, Figure 4.2a .
The finite substrate roughness and the presence of contaminants at the substrate/graphene interface affect the flake edge profile as acquired with an atomic force microscope (AFM), Figure 4.2b. As a consequence, the apparent single-layer thickness is often found to be in the range $\sim 1-2$ nm instead of the nominal graphene thickness (0.3 Å as determined from diffraction measurements on graphite).

4.1.3 Raman Spectroscopy

Raman spectroscopy [38] is an important tool for the characterization of graphene and carbon-based materials in general [39]. It provides important information about structural modifications and extrinsic doping and constitutes a fast and reliable method to quantify the number of graphene layers.
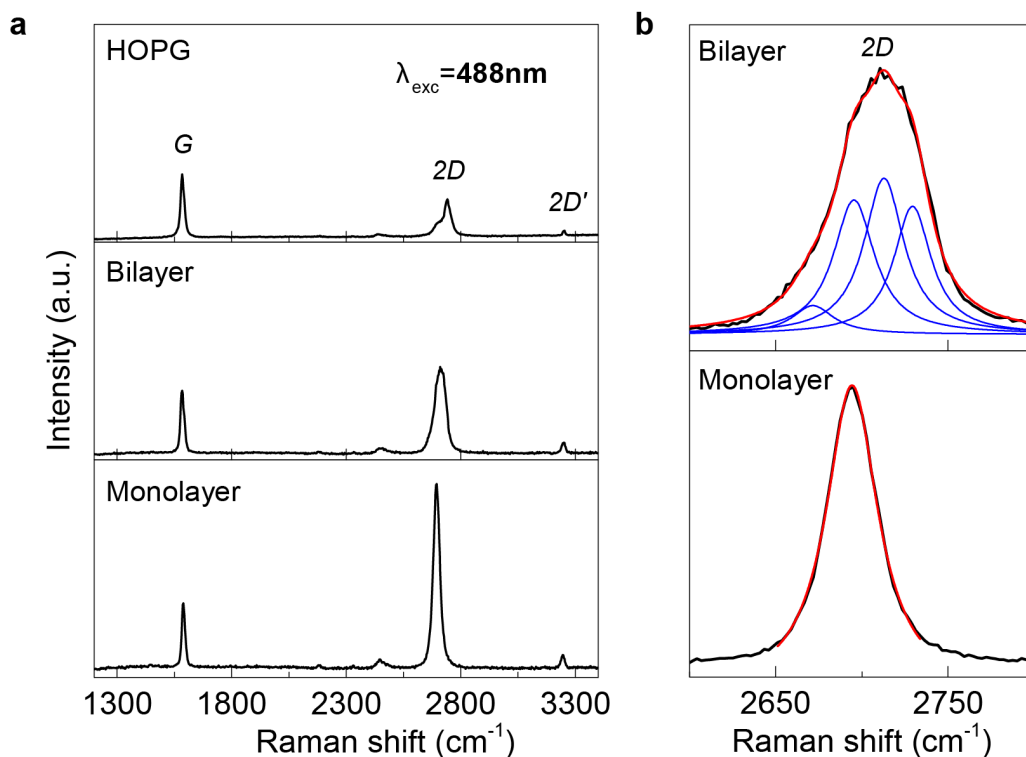

Figure 4.3: Evolution of the Raman spectrum with the number of graphene layers. a) Comparison between monolayer, bilayer and graphite. b) Shape of the 2D peak for single and bilayer graphene. Red lines are fitting with Lorentzian line shapes. Monolayer graphene gives rise to a single Lorentzian contribution whereas bilayer shows four contributions due to interlayer interaction (Blue lines).

The Raman spectrum of graphene is relatively simple [40, 41], Figure 4.4. It exhibits

a G peak at $\sim$1580 cm^{-1} and a $2D$ band at $\sim$2700 cm^{-1}. The G peak arises from the doubly-degenerate zone center E_{2g} mode while the 2D band is due to a second order process involving zone-boundary phonons. The shape of the latter is sensitive to the number of graphene layers, Figure 4.3. For single-layer graphene the 2D peak is a single Lorentzian contribution, while for bilayer it is composed of four contributions reflecting the splitting of the π, π^* bands in four bands due to the interlayer interaction.

Both G and $2D$ peaks are sensitive to extrinsic doping. The G band up-shifts (stiffens) and becomes narrower for both n- and p-doping [42, 43] while the 2D band discriminates between holes and electron dopings, upshifting for the former and softening for the latter.
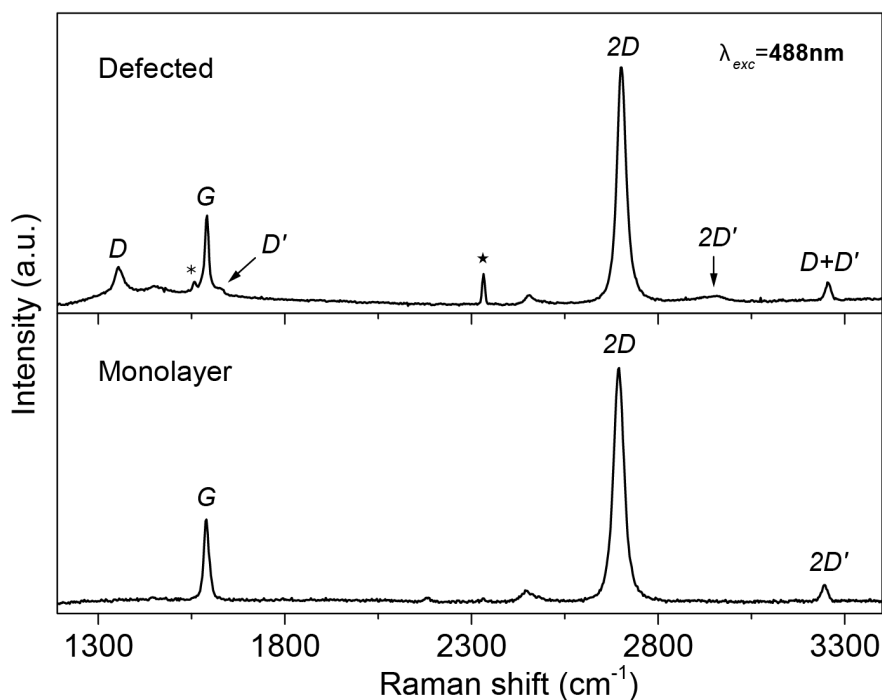

Figure 4.4: Raman spectrum of high quality single layer graphene (bottom) and defected graphene (top).

Raman spectrum of graphene is modulated by structural modifications such as the presence of defects or dimensional confinement. In the first case, the presence of inter-valley scattering sites makes the A_{1g} breathing mode at the Brillouin zone boundary Raman active to the first order, leading to the appearance of an additional peak at $\sim$1350 cm^{-1} called D [44].

The $I(D)/I(G)$ intensity ratio can be used as a measure of the defects concentration in the flakes using the empirical Tunstra-könig relation [45, 46]:

$$\frac{I(D)}{I(G)} = C(\lambda)/L_D^2 \tag{4.1}$$

where $C(\lambda)$ is a coefficient proportional to the fourth power of the excitation wavelength λ, and L_D^2 is the average distance between the defects [47].

It is common, for graphene derived from highly ordered pyrolitic graphite (HOPG) not to have enough structural defects for the D peak to be Raman active ($D/G < 10^{-3}$), so that it can only be observable for spectra acquired at the edges [48].

4.2 Fe$_4$Py: a graphene-binding SMM

To study the detailed arrangement and aggregation state of molecules on graphene, we use the cluster [Fe$_4$(L)$_2$(dpm)$_6$], **1** [22, 49], where L indicates the triply deprotonated H$_3$L=2-hydroxymethyl-2-(4-(pyren-1-yl)butoxy)met hylpropane-1,3-diol and dpm^- the deprotonated dipivaloylmethane (Figure 4.5a).
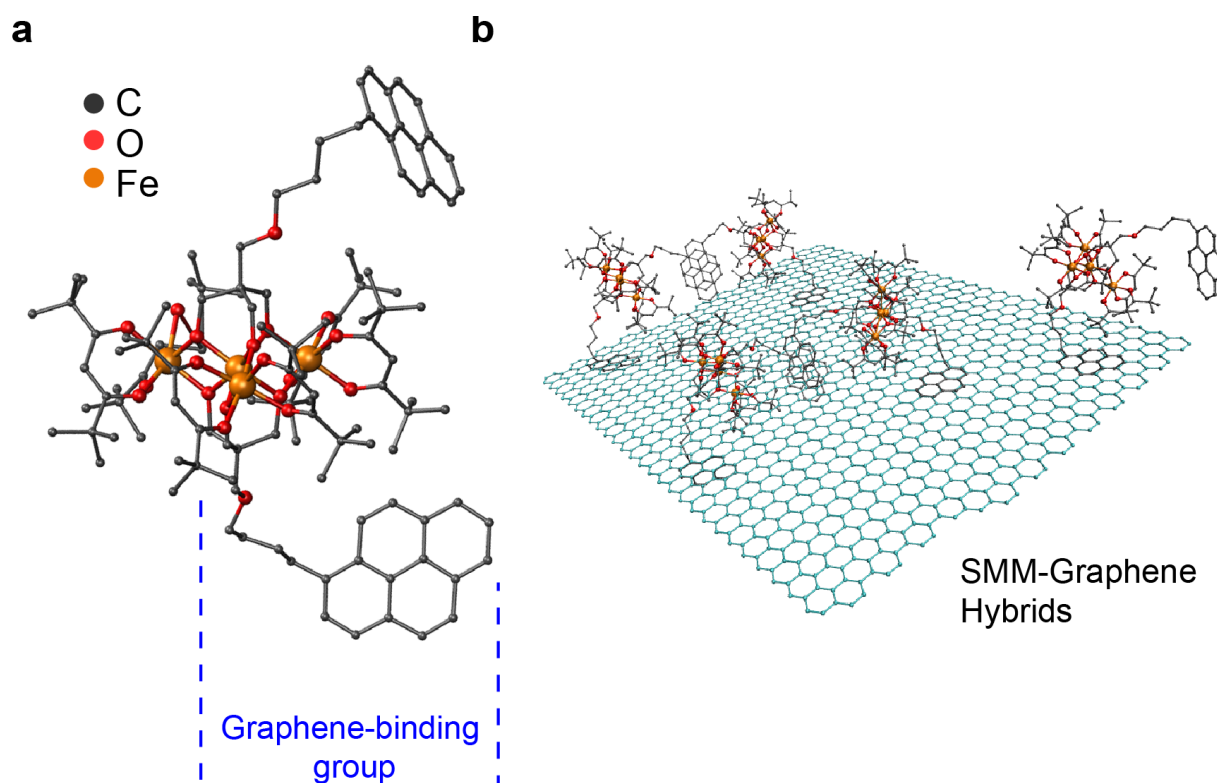

Figure 4.5: Synthesis scheme of the non-covalent graphene hybrids. a) Molecular structure of **1**, hydrogen atoms are omitted for clarity; b) Molecular self-assembly on graphene in solution.

This cluster compound comprises a core of four Fe(III) ions surrounded by a shell of dpm$^-$ ligands. The core is stabilized by two tripodal L^{3-} ligands, whose oxygens bridge the peripheral Fe(III) atoms to the central one. Each ligand also supports a pyrene group attached via a short alkyl chain, Figure 4.5a, so that the molecule has two axial pyrene

systems that promote non-covalent grafting to the graphene sheet, Figure 4.5b. The molecular size, as extracted from crystallographic data, is 2.3 nm along the molecule axis and 1.6 nm along in the transverse direction, a size comparable to that of small proteins and inorganic nanoparticles. The sizable molecular mass, $Mr = 2101.87$ amu, is also similar to that of small proteins and ensures a relatively low surface diffusion [50–53], such that the assembly process can be monitored at room temperature.

Functionalization of the graphene surface is accomplished via self-assembly in solutions of **1** in the solvents mixture ClCH$_2$CH$_2$Cl:CH$_2$Cl$_2$ (9:1, v/v). The structural stability of **1** in solution has been tested by means of matrix-assisted laser desorption/ionization time of flight mass spectrometry (MALDI-TOF MS). Figure 4.6a shows the high mass range of **1** powder spectrum. The few visible peaks at 1919, 1763, and 1736 amu can only be associated with intact clusters of **1** undergoing the sequential removal of one or more external dpm- ligands during the desorption/ionization process. Solutions of **1**, Figure 4.6b, shows the same fragmentation behavior as the starting powder, thus proving the stability in solution. Moreover, all peaks show isotopic patterns consistent with simulations (Right panels in Figure 4.6). The fragmentation behavior and the associated isotopic patterns, demonstrate that the tripodal ligand L^{3-} is stably bound to the **1** core, improving the overall cluster stability [54].

The spectra were acquired using a Bruker Reflex IV MALDI-TOF spectrometer equipped with a nitrogen laser pulsed at 3-5 Hz and adjustable power. The samples were prepared by simply depositing the material onto the spectrometer target and are loaded right away in the high vacuum chamber. Dithranol (1,8-Dihydroxy-9(10H)-anthracenone) can be used as matrix compound to improve the ionization process and the measurement sensitivity. The matrix is first dispersed in 9:1 ClCH$_2$CH$_2$Cl:CH$_2$Cl$_2$ and then drop casted on the target sample. As shown in Figure 4.6c and d, the matrix does not influence the characteristic fragmentation of the pristine compound. The feature at 1919 amu remains unaltered while the feature at 1736 amu reduces in combination with the appearance of an intense peak at 1778 amu associated with the capture of a dithranol molecule by the [M-2dpm]$^-$ fragment. In addition, owing to the enhanced sensitivity, the molecular peak becomes visible at 2123 amu, further confirming the cluster stability in solution. These results fully agree with the mass spectra of **1** parent compounds reported in literature [55, 56]. The stability of **1** after deposition has been checked by multiple technique and is is reported in the following sections.
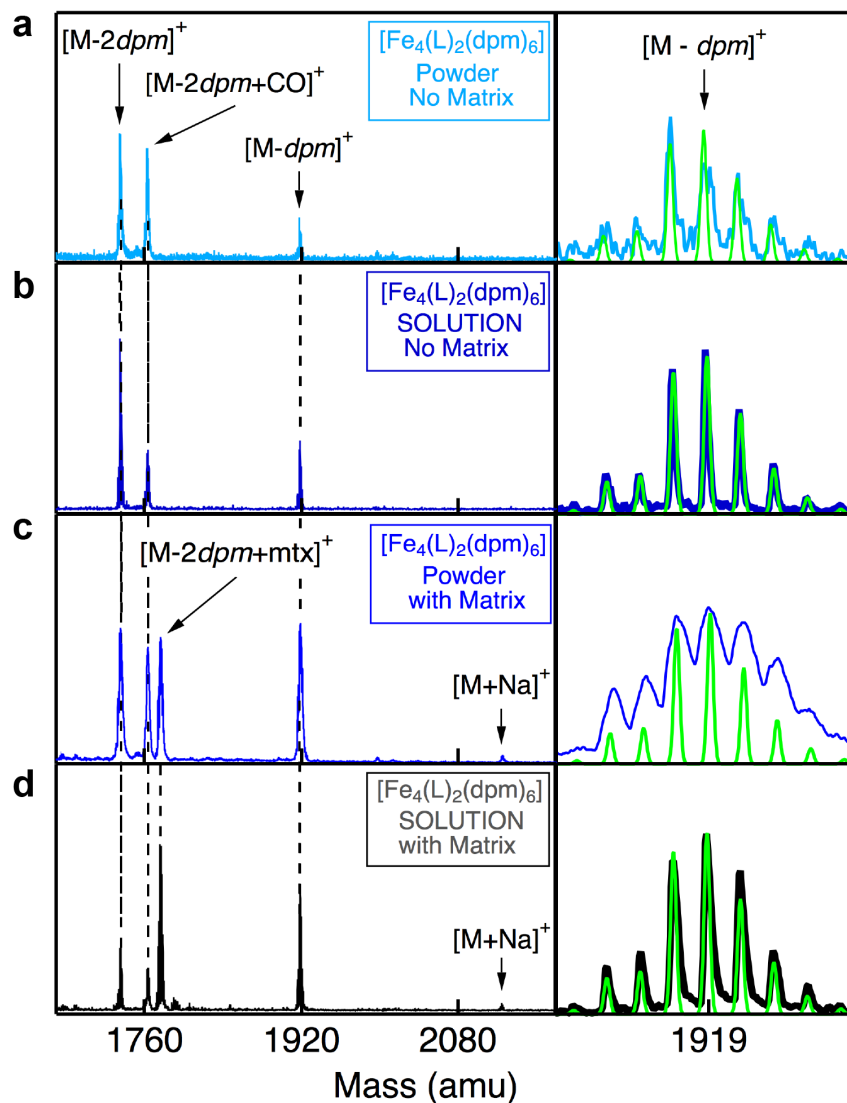
Figure 4.6: Structural stability of $[\text{Fe}_4(\text{L})_2(\text{dpm})_6]$ in solution. a) MALDI-TOF spectrum of **1** powder as synthetized. b) Spectrum of **1** in 9:1 ClCH$_2$CH$_2$Cl:CH$_2$Cl$_2$. Spectrum of **1** powder c) and in solution d) with Dithranol matrix. The right panels show the isotopic pattern of the 1919 amu fragment compared with simulations (green lines)

4.3   Molecular self-assembly on graphene

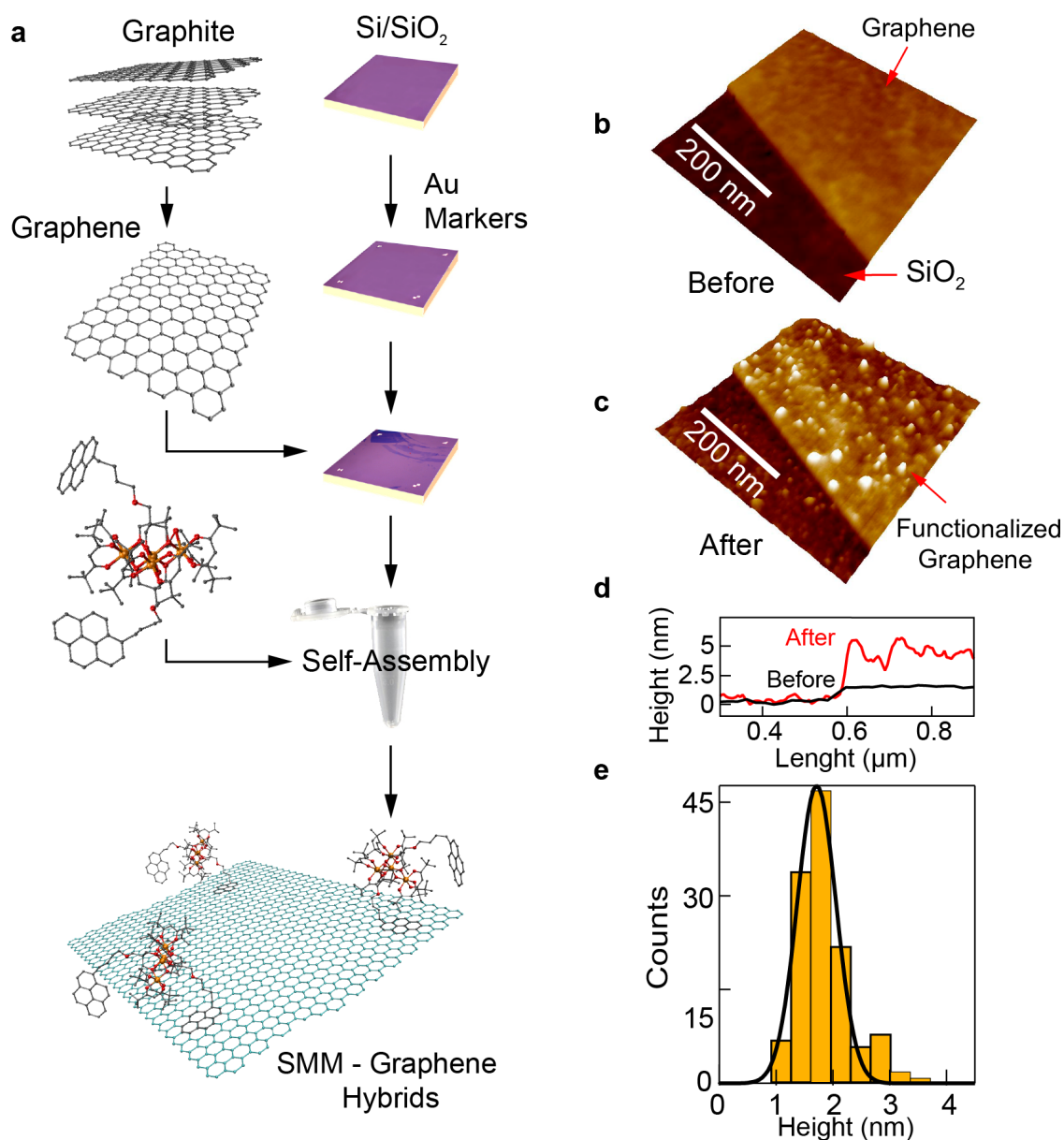## 4.3.1   Topography of SMMs on graphene

Figure 4.7: Graphene-SMM hybrids. a) Synthesis of graphene-SMMs hybrids by liquid-phase grafting. b) Graphene surface before functionalization. c) Randomly-distributed SMMs islands on graphene after grafting of **1**. d) Graphene profile height before (black) and after (red) functionalization ($C = 2.5 \cdot 10^{-10}$ M). e) The narrow distribution of island heights is centered at the molecular size.

Single-layer graphene flakes are obtained by mechanical exfoliation of natural graphite [31]. The flakes are transferred onto Si substrates with a 300 nm thick SiO_2 upperlayer. Molecular assembly is achieved by immersing the substrates in a solution of **1** (concentration C) in $ClCH_2CH_2Cl:CH_2Cl_2$ (9:1, v/v) at room temperature. After a deposition time t, the samples are rinsed with pure solvent mixture, followed by isopropanol, and dried under Ar jet.
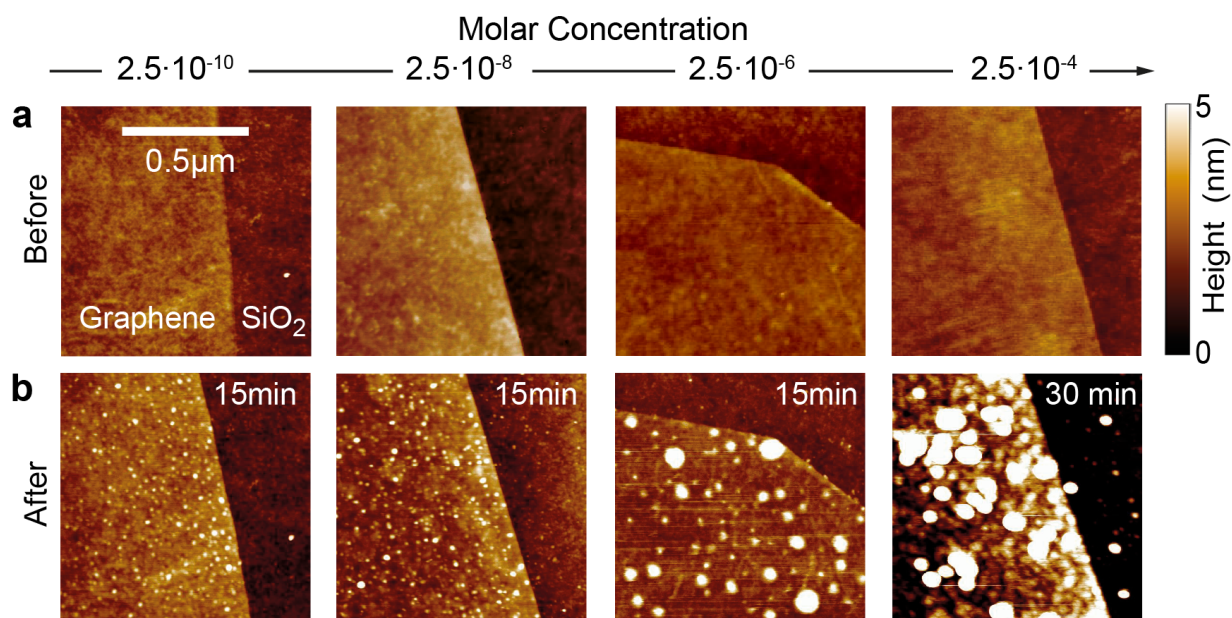

Figure 4.8: Selective molecular decoration of the graphene surface a) AFM topographic images of exfoliated graphene as transferred on SiO_2 b) after (right column) non-covalent functionalization with **1**, performed at different concentrations C.

Marker structures on the substrate enable the inspection of the same graphene flake before and after decoration by **1**, Figure 4.5b. Tapping-mode atomic force microscopy (AFM) before and after deposition of **1** reveals highly selective functionalization of the graphene surface with respect to the SiO_2 one, Figure 4.8, with only minimal grafting appearing on the SiO_2 surface even for the highest concentrations.

The images are acquired employing a Veeco Dimension Icon atomic force microscope and high resolution Olympus OMCL-AC200TS-R3 Silicon tips. The nominal tips radius is 7 nm and the cantilever free resonance frequency is 150 kHz. The tips have a tetrahedral shape with 0° tilt angle for the retrace that greatly reduces the convolution error on the lateral size of the imaged objects [57, 58]. Scan rate is 1 Hz and each image contains 1024 points and 1024 lines. The selectivity of the pyrene groups for the conjugated structure of graphene can be quantified by considering the surface roughness R_a, i.e. the mean deviation of the AFM profile $Z(x)$ within a sampling length L:

$$R_a = \frac{1}{L} \int |Z(x)| dx \qquad (4.2)$$

in $600 \times 600 \text{nm}^2$ square areas of the AFM images. Before functionalization, $R_a = 0.17 \pm 0.03$ nm for both graphene and SiO_2. After functionalization, the graphene surface shows increased roughness $R_a = 0.25 \pm 0.03$ nm already at the lowest C, Figure 4.9a, while almost no variation is observed for SiO_2 for all C.
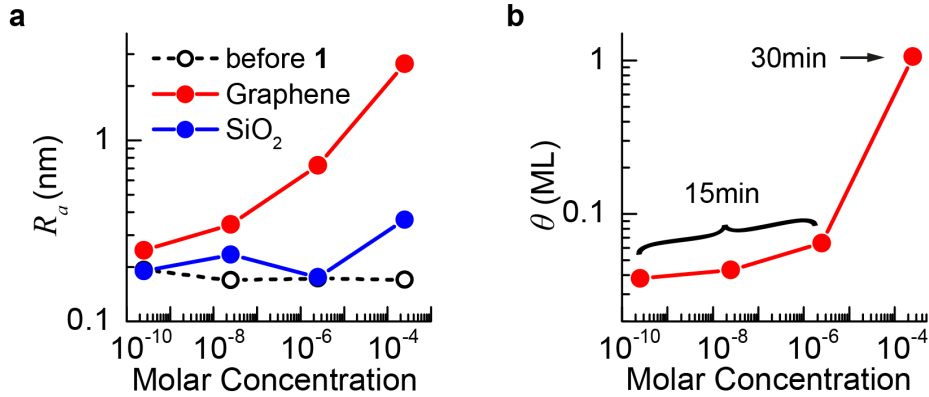

Figure 4.9: a) Comparison of the surface roughness parameter R_a for graphene (red) and SiO_2 (blue) after functionalization using different concentrations of **1**. b) Molecular coverage θ of the graphene surface, as determined from AFM images, plotted vs. C.

Increasing the concentration C or the adsorption time t, causes the fraction of molecule-covered graphene surface θ to raise, allowing tuning the coverage from sub-monolayer to above one monolayer Figure 4.9b.
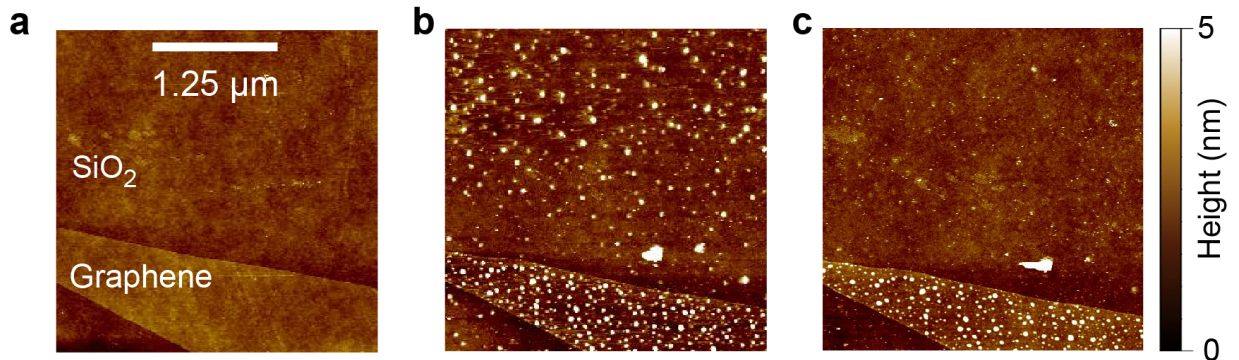

Figure 4.10: Removal of **1** from the SiO_2 surface by the AFM tip in tapping mode. a) SiO_2/graphene system before functionalization, b) Same spot as a after functionalization with $[Fe_4(L)_2(dpm)_6]$ with $C = 2.5 \cdot 10^{-6}$, 15 minutes adsorption time. c) same spot after the first AFM scan. b) and c) images were acquired in sequence.

The few objects visible on the SiO$_2$ surface can be easily removed by the AFM tip (Figure 4.10), further demonstrating the essential role of the pyrene groups. No difference in the selectivity is found for different number of graphene layers (Figure4.11).
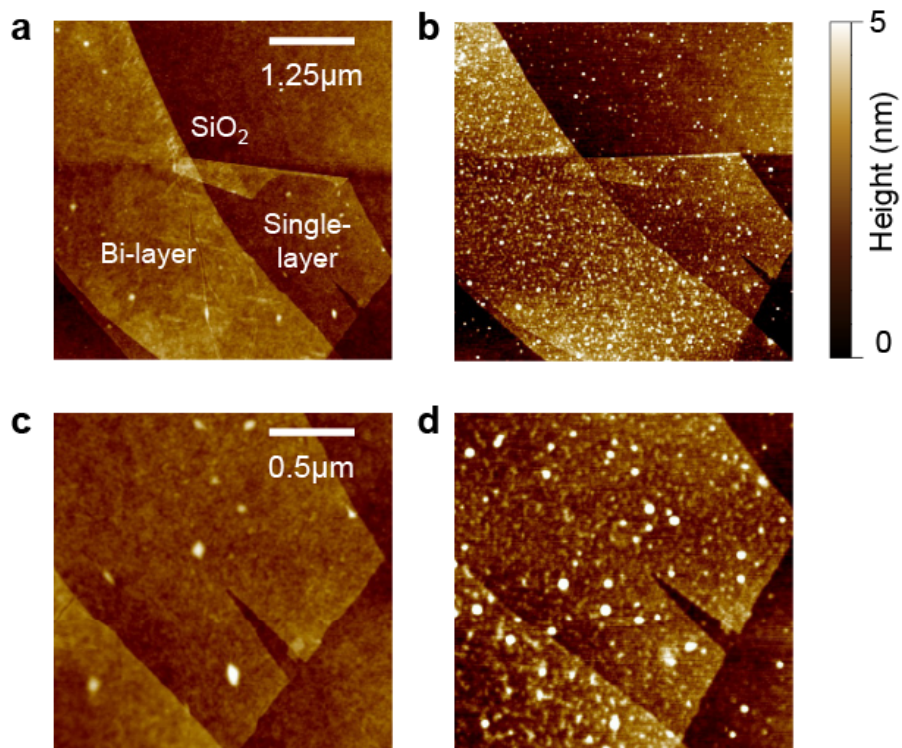

Figure 4.11: Molecular self-assembly on single and bi-layer graphene. Single and bi-layer graphene before functionalization a) and after functionalization b) with [Fe$_4$(L)$_2$(dpm)$_6$] ($C = 3.1 \cdot 10^{-6}$ M, $t = 10$ min adsorption time. c) and d) are zoom-ins of a) and b) respectively.

4.3.2 Dynamic scaling behavior

To evaluate the molecular assembly process, we increase C while keeping the deposition time constant $t = 15$min, Figure 4.12a.
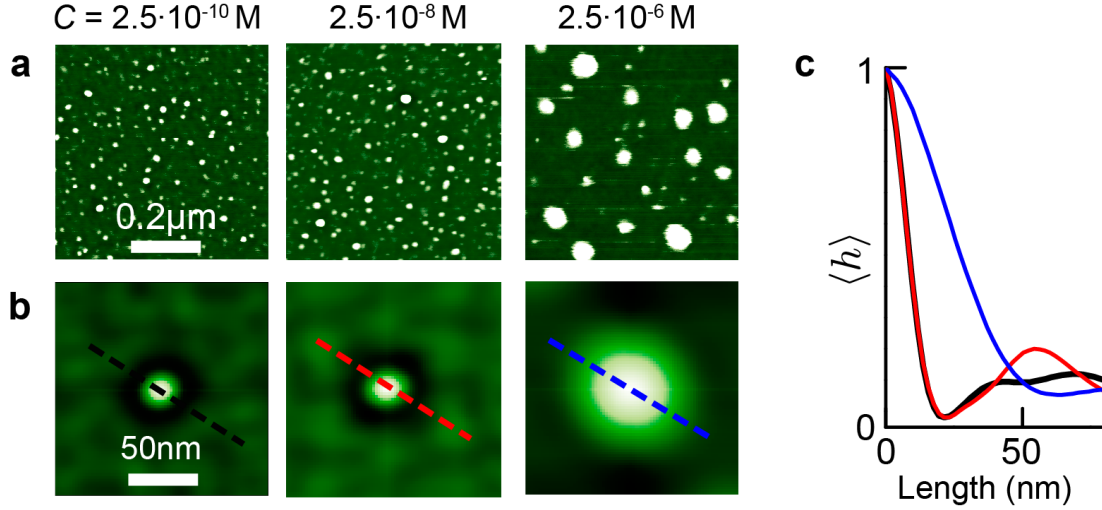

Figure 4.12: Evolution of the 2D autocorrelation function $h(x,y)$ with increasing C. a) 600×600 nm images from which $\langle h \rangle$ is extracted. b) 2D autocorrelation function $\langle h \rangle$. c) Autocorrelation function profile.

The two-dimensional autocorrelation $\langle h \rangle$ of the AFM height profile $h(x,y)$:

$$\langle h \rangle = \int \int_{-\infty}^{+\infty} h(x,y)h(x+X,y+Y)dxdy \qquad (4.3)$$

and N the density of molecular islands per adsorption site, Figure 4.12b,c and 4.13a indicate two distinct assembly regimes: one below and one above $C \approx 2.5 \cdot 10^{-8}$ M, Figure 4.13a. The single peak in $h(x,y)$ indicates randomly-placed objects, Figure 4.12b,c. Although *long-range* ordering is absent, as expected for weak $\pi - \pi$ grafting, there is a hint of hexagonal structuring around $C = 2.5 \cdot 10^{-8}$ M, Figure 4.12b,c, suggesting a weak template effect of the graphene lattice.

The islands height distribution peaks around the molecular size, Figure 4.13b suggesting that molecules deposited on top of an existing island migrate towards the island edges favoring lateral island growth rather than three-dimensional structures.

For $C < 2.5 \cdot 10^{-8}$ M, N increases only slightly over a range of C of several orders of magnitude, this indicates that newly adsorbed molecules *aggregate* to existing islands and *nucleation* of new stable islands is rare.

The assembly behavior can be modeled in the framework of dynamic scaling theory [59–62], already employed for epitaxial [52, 53] and molecular assemblies on surfaces [57, 63–65]. It involves two processes with characteristic rates: the first is the deposition rate F, associated with the *adsorption* of new molecular islands from solution; the second is the *diffusion*
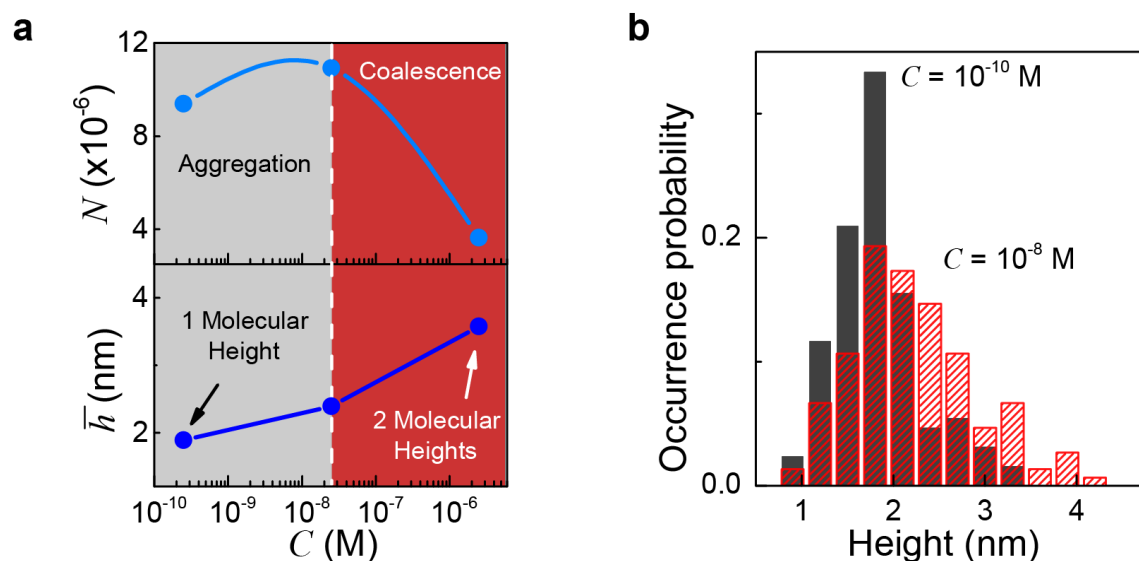
Figure 4.13: Self-assembly on graphene a) Concentration dependence of the density of islands N per adsorption site (top) and the island average height $\bar{h}$ (bottom). Lines are guides to the eye. c) Island height distribution for different C (red).

coefficient D, related to *aggregation* into stable molecular islands, followed by *coalescence* into larger islands, Figure 4.14.
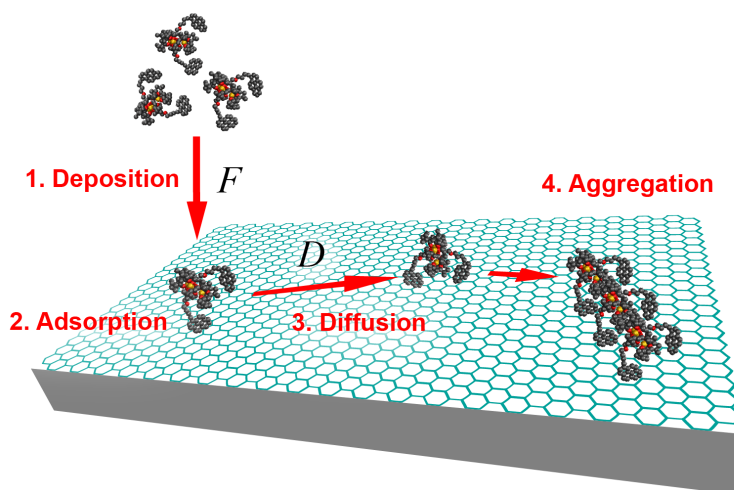
Figure 4.14: Self-assembly process. Molecules are deposited (1) with rate F (dependent on C). Once adsorbed (2), molecules diffuseon the graphene surface (3) with "diffusivity" D. Diffusion leads to aggregation of molecular islands (4).

The kinetics of the self-assembly process depends on several factors such as the details of the undelying lattice (i.e. symmetry, lattice constant, insulator/metallic character), the binding groups that impart intermolecular and molecule-substrate interactions, as well as

the deposition conditions (i.e. temperature, deposition rate). In dynamic scaling theory, the role of these factors is modeled by defining a *critical island size i* [53, 61] that correspond to *one less* the number of molecule that must aggregate to form the smallest stable (non-diffusing) island [53, 66, 67]. i can be determined experimentally from n_a, the distribution of island-size, that is the density *per site* of islands containing a molecules at coverage θ:

$$n_a = \theta A^{-2} f_i(u) \tag{4.4}$$

A is the average island size and $u = a/A$.

In the present case, an absorption/nucleations site correspond to a single graphene hexagonal unit cell 5.2 Å^2, a diffusion hop length equals the lattice unit vector 2.46 Å, such that **1** occupies $\sim$54 adsorption sites.

$f_i(u)$ is called *scaled island-size distribution* and for $i > 0$ is has the analitic expression:

$$f_i(u) = n_a A^2/\theta = c_i u^i e^{-\frac{i u^{b_i}}{b_i}} \tag{4.5}$$

where $\int_0^\infty f_i(u) du = \int_0^\infty u f_i(u) du = 1$ is imposed via the c_i and b_i normalization parameters.
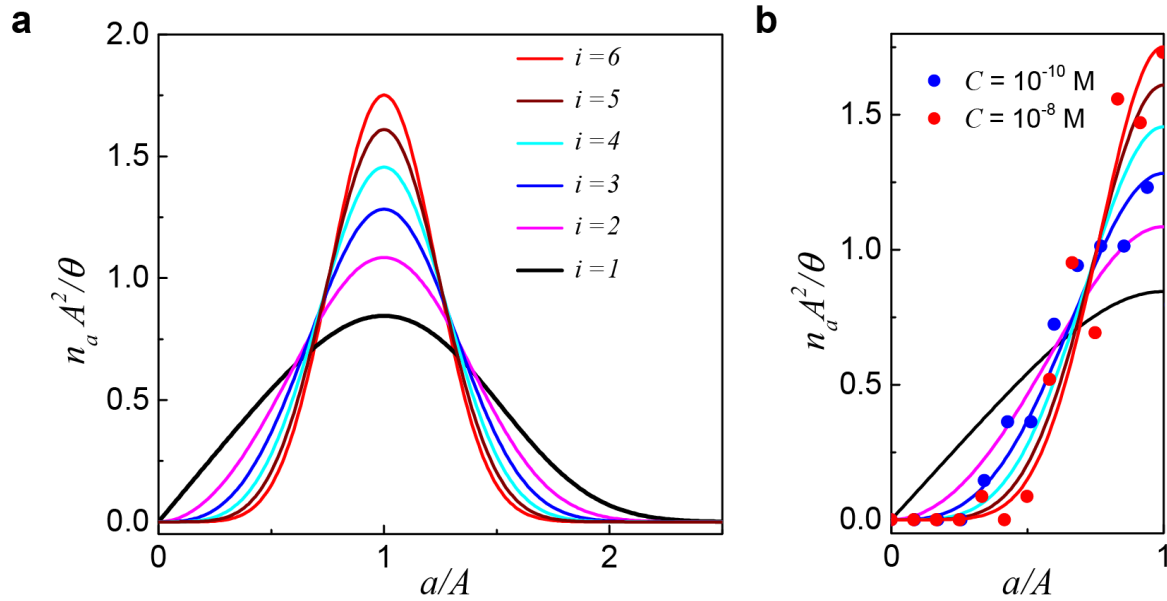
Figure 4.15: Simulation of the dynamic scaling function $f_i(u)$ for different critical island sizes i. For $i = 1$ (black curve) single molecules are free to diffuse and dimers are stable (non-diffusing) on the surface. $i > 0$ indicates that molecular islands larger than dimers diffuse on the surface.

As shown in Figure 4.15, the function $f_i(u)$, which quantifies the occurrence of cluster diffusion, depends sensitively on i, becoming significantly sharper with increasing i. The larger i the faster the island size distribution n_a below the critical size reaches zero, implying

that larger islands are mobile on the surface. For $i = 1$ single molecules diffuse freely on the surface and the merging of two molecules creates a stable non-diffusing *dimer* that behaves as nucleation site. In this case, $f_i(u)$ extrapolates to zero following approximately a linear behavior for small u (Figure4.15 *black curve*). Getting in contact with the stable dimer, additional diffusing molecules are also irreversibly embedded in it leading to *island growth* and eventually to the formation of a complete monolayer. For $i > 1$ larger clusters are also free to diffuse, hence smaller islands have lower density and $f_i(u)$ goes to zero faster than linear.

Figure 4.16a depicts the experimental $f_i(u)$ for different C values in the aggregation regime. As expected, the distribution is centered around $u = 1$ and extrapolates to zero faster than linear, indicating that aggregates *larger than dimers* ($i > 1$) are mobile and diffuse on the surface.
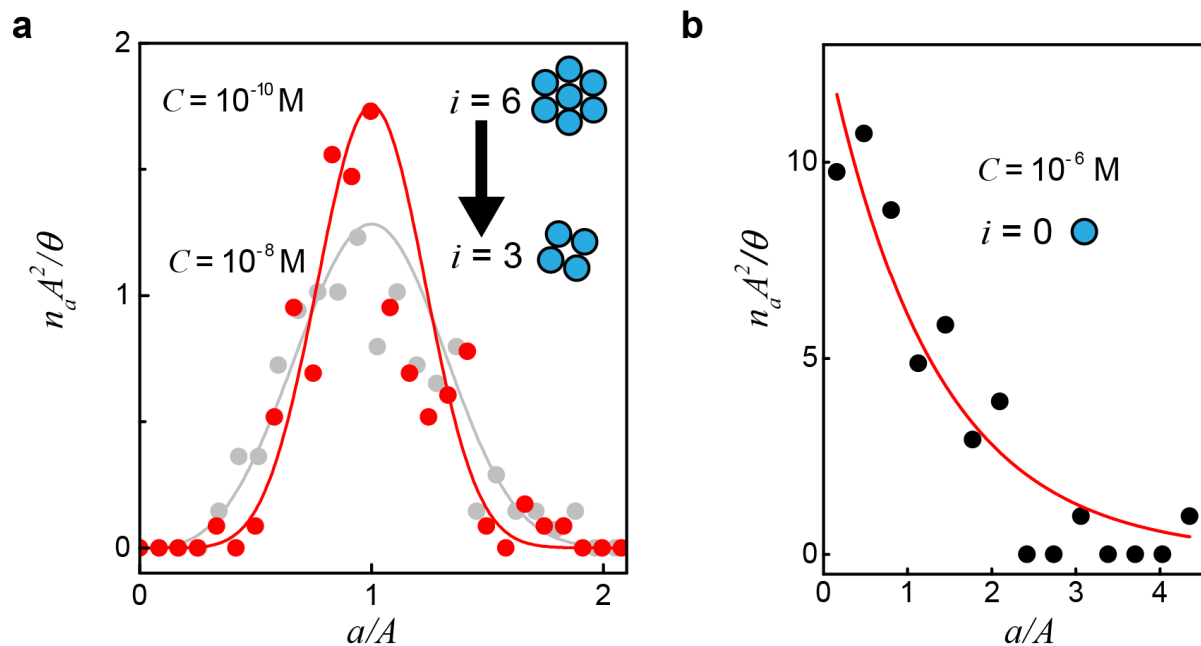
Figure 4.16: Different self-assembly regimes a) Scaled island-size distribution $n_a A^2/\theta$ vs. the normalized island size a/A, for different C in the aggregation regime. Circles are data, and lines simulations based upon the dynamic scaling function (red points correspond to $C = 2.5 \cdot 10^{-10}$ M, blue to $C = 2.5 \cdot 10^{-8}$ M). b) Plot of $n_a A^2/\theta$ vs. a/A in the coalescence regime, for $C = 2.5 \cdot 10^{-6}$ M.

By increasing C from $2.5 \cdot 10^{-10}$ Mto $2.5 \cdot 10^{-8}$ M, i decreases from 6 to 3, showing that size of stable islands decreases with C. The fact that the diffusion/deposition ratio D/F depends on C opens the possibility to tune the assembly mode.

The analytical expression (4.5) is based [61] in part on the experimental observation that, for small u the island size distribution n_a goes to zero as $\sim u^i$ [60]. Figure4.17 shows a power law fitting of the experimental data in the small u region. Fittings of $C = 2.5 \cdot 10^{-10}$ M and

$C = 2.5 \cdot 10^{-8}$ M data give $i = 6.1 \pm 0.5$ and $i = 2.9 \pm 0.8$ respectively, in perfect agreement with the outcome of the comparison between simulated and experimental scaled island-size distribution in Figure4.16a.
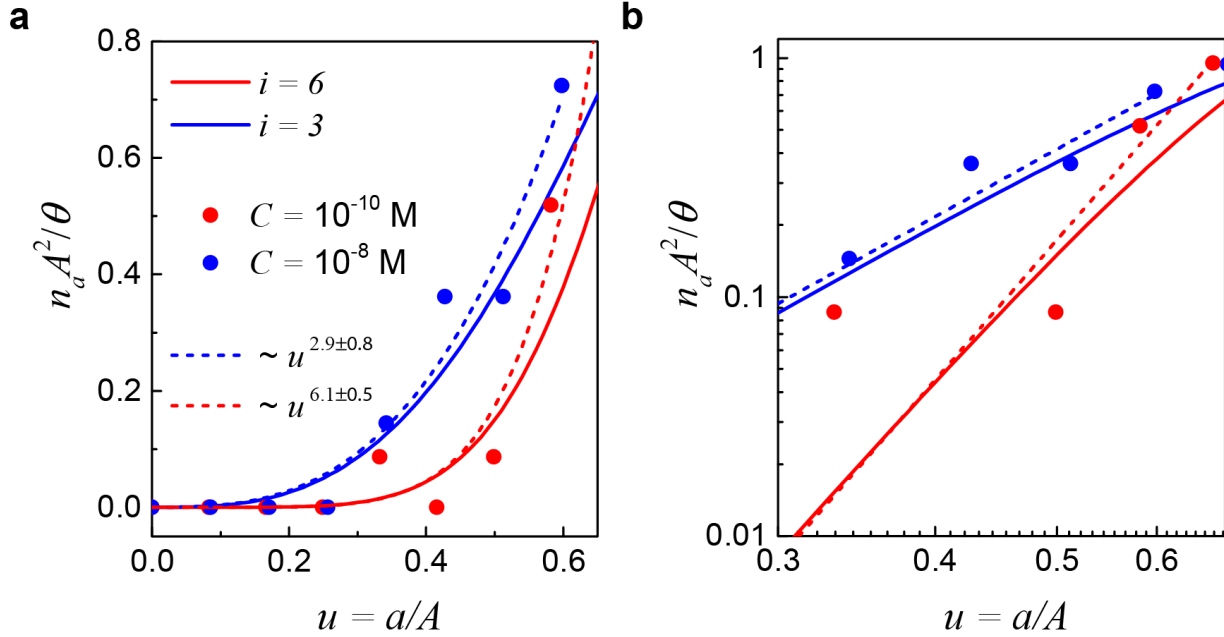

Figure 4.17: Fitting of the small u region. a) Dotted lines are fittings to the experimental data (dots). Solid line are scaling function simulations. b) *log-log* plot of a)

These observations demonstrate that the same theoretical framework used for vapor-phase epitaxial growth can describe molecular self-assembly on graphene.

Theoretically, for big enough C it should be possible to approach $i = 0$, where single molecules stably graft onto the surface and irreversibly add to existing islands. Indeed N drops rapidly above $C = 2.5 \cdot 10^{-8}$ M, indicating a different regime of *island coalescence*. Concomitantly, $\langle h \rangle$ reflects merging of originally-separate islands, with the average island size becoming larger than the average inter-islands distance at lower C, Figure 4.12b. Under these assembly conditions the scaling behavior breaks down, i.e. f_i does not extrapolate to the origin and exhibits an exponential decrease, Figure 4.16b. This can be described by a coalescence function:

$$f_{coal.}(u) = ae^{-bu} \tag{4.6}$$

where $a = 13.3 \pm 1.4$ and $b = 0.8 \pm 0.1$ are empirical parameters [60]. Concurrently, an increase of the average island height $\bar{h}$ also occurs, indicating the onset of *bilayer growth*, Figure 4.13a *bottom*. This may indicate the crossover form $i = 3$ to $i = 0$. The latter correspond to the case where single molecules are non-diffusing and act as nucleation sites and the island density becomes independent of D/F thus C.

For $C > 2.5 \cdot 10^{-4}$ M (or longer adsorption times, Figure 4.8*b*) *monolayer-plus-islands* structure form. This is characteristic of *Stranski-Krastanov* growth mode [68], in which the interaction with the substrate is altered by the already-formed molecular layer.

4.3.3   Stimuli-driven molecular reorganization on graphene

The above observations demonstrate sizable molecular diffusion on graphene. Moreover, sequential AFM imaging also shows that isolated molecules are found to be displaced at different times, confirming that the relatively weak $\pi - \pi$ interactions allow the SMMs to remain mobile on graphene at room temperature. Such residual diffusivity can be exploited to create extended supramolecular structures on graphene, Figure4.19a. Indeed, upon providing energy via external stimuli, such as light irradiation, the molecules on graphene re-organize into completely different topologies. Figure4.19b,c shows the graphene surfaces before and after a 30 s irradiation with laser light (wavelength 632.8 nm, power <7 mW). The molecular islands transform into a two-dimensional random network [69, 70] and, as a result, the original autocorrelation $\langle h \rangle$ peak sharpens considerably, passing from 28 to 6 nm, and additional ring structures develop at 33 and 76 nm, *insets* in Figure4.19b,c. Such circular features indicate *medium-range* order [71, 72] and are typical of random networks with homogeneous intra-filament distances, Figure 4.19d.

Statistical analysis of the network, Figure4.19e, shows that nodes with three- and four-fold connectivity are the most stable, and it is their combination that sets the final network structure [71].

Analogous changes can be induced by heating in a controlled atmosphere, Figure4.18. We probed the molecular reorganization at different temperatures in a controlled He atmosphere, so as not to chemically alter the clusters. No molecular reorganization was observed in a period of weeks at 0 and 10°C. On the contrary as shown in Figure4.18, reorganization was observed in a period of 7 days at 30°C and in ca. 24 hours at 60°C.
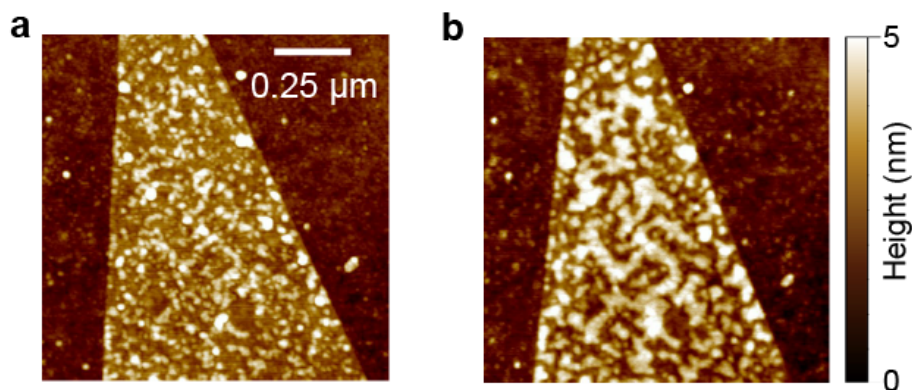
Figure 4.18: SMMs-functionalized graphene a) as synthetized b) after 24 hours at 60°C.
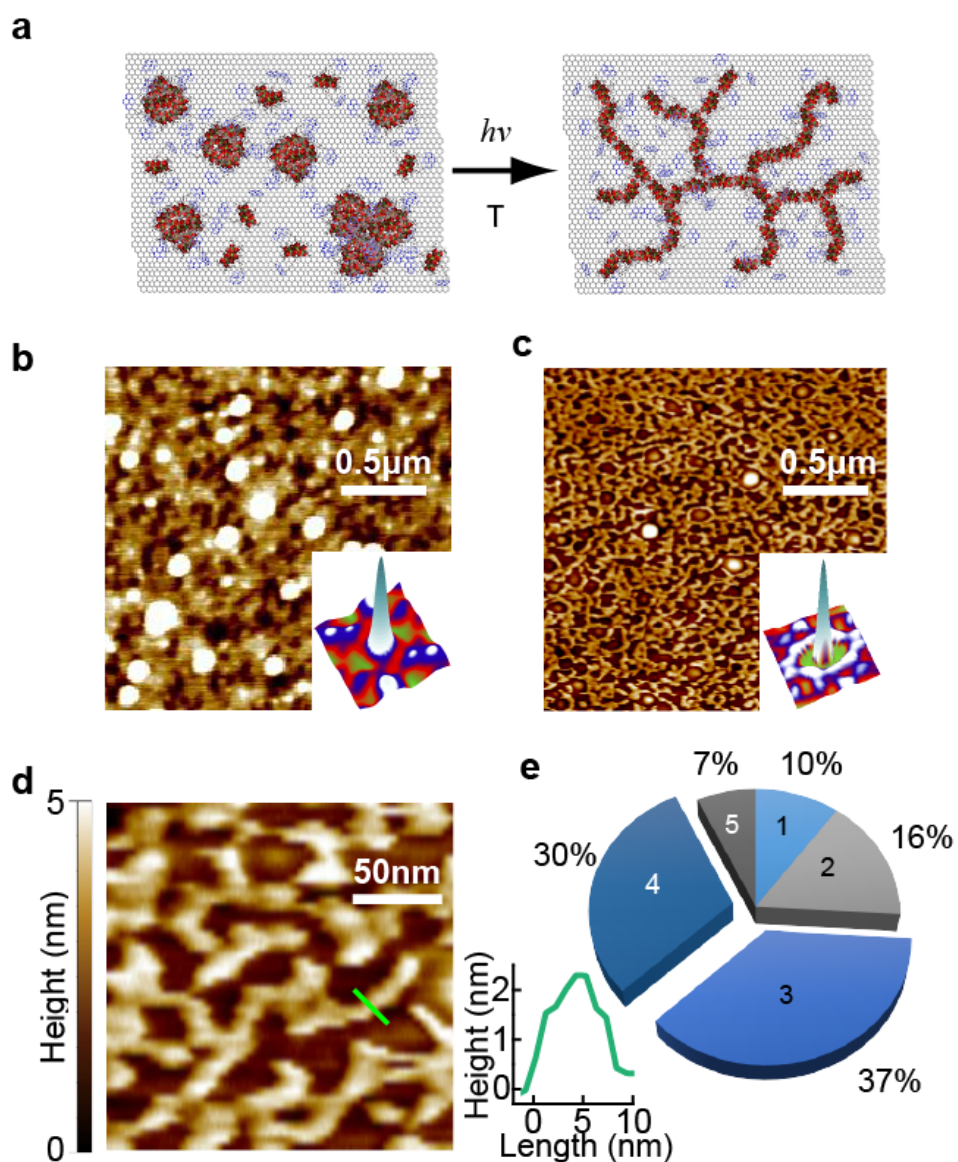
Figure 4.19: Molecular reorganization induced by light exposure. a) Scheme of the island-to-network transition. b) AFM of functionalized graphene before light exposure. c) Supramolecular network obtained after light exposure. d) Zoom-in of the network showing the molecular filaments. e) Statistical analysis of the network nodes. Inset: AFM height profile of one filament constituting the network.

4.4 Electronic properties of graphene functionalized with SMMs

To test how the molecular functionalization influences the graphene electronic properties, both Raman spectroscopy and electronic transport measurements were performed before and after SMMs decoration (Figure4.20).

4.4.1 Raman spectrum of SMMs-graphene hybrids

Raman spectra were acquired at the center of the same graphene flake before and after grafting of $[Fe_4(L)_2(dpm)_6]$ ($C = 2.5 \cdot 10^{-6}$ M). The bare flake shows a G peak at 1582 cm^{-1} with an full-width-half-maximum of 14 cm^{-1} (Figure4.20a). Decoration with **1** leads to a slight G band up-shift of about 4 cm^{-1} correlated with a narrowing of the FWHM to 9.8 cm^{-1}, indicating a very small doping effect [42], compatible with π-stacked pyrene. No enhancement of the molecular Raman signal was detected and a quenching is likely present, contrarily to previous reports [73].

4.4.2 Electronic transport in SMMs-graphene hybrids

To estimate the charge transferred per molecule, transport measurements were performed on graphene-based 5-terminal field-effect transistors with a 300nm-thick SiO_2 gate dielectric (Figure 4.20b,c). The devices were fabricated, using electron beam lithography on a two-layer poly-methyl-methacrylate PMMA mask. To improve contact adhesion a 2nm Ti buffer-layer was employed (see Chapter 8). The contact material, Au (50nm), was deposited by thermal evaporation at residual pressure $< 10^{-7}$mbar. To ensure a minimum amount of resist residues on the graphene surface, the final lift-off step was extended over 14 hours. Measurement were performed at room temperature, by suppling a dc current ($\pm 1\mu$A) in the linear I-V regime and measuring the voltage drop between the inner electrodes as depicted in Figure 4.20b.

The graphene differential resistance $R = \partial V/\partial I_{sd}$ (where I_{sd} is the source-drain current and V is the measured potential difference) reaches a maximum when the back-gate voltage V_{gate} is scanned through the Dirac point. In the pristine devices, black curve in Figure 4.20d, instead of being at $V_{gate} = 0$ V, the maximum is found at $V_{gate} \approx 10$ V due to hole-doping by air exposure. The maximum upshifts of about 8 V after treatment with the solvent mixture alone, Figure 4.20d blue curve, and it gradually shifts back to the original V_{gate} value as the solvent evaporates. Grafting of $[Fe_4(L)_2(dpm)_6]$ permanently shifts the maximum to V_D, red curve in Figure 4.20d.

By evaluating the minimum number density of molecules δ from the AFM images, the maximum charge transferred per molecule can be determined using equation (2.40) of section 2.3 [74]:
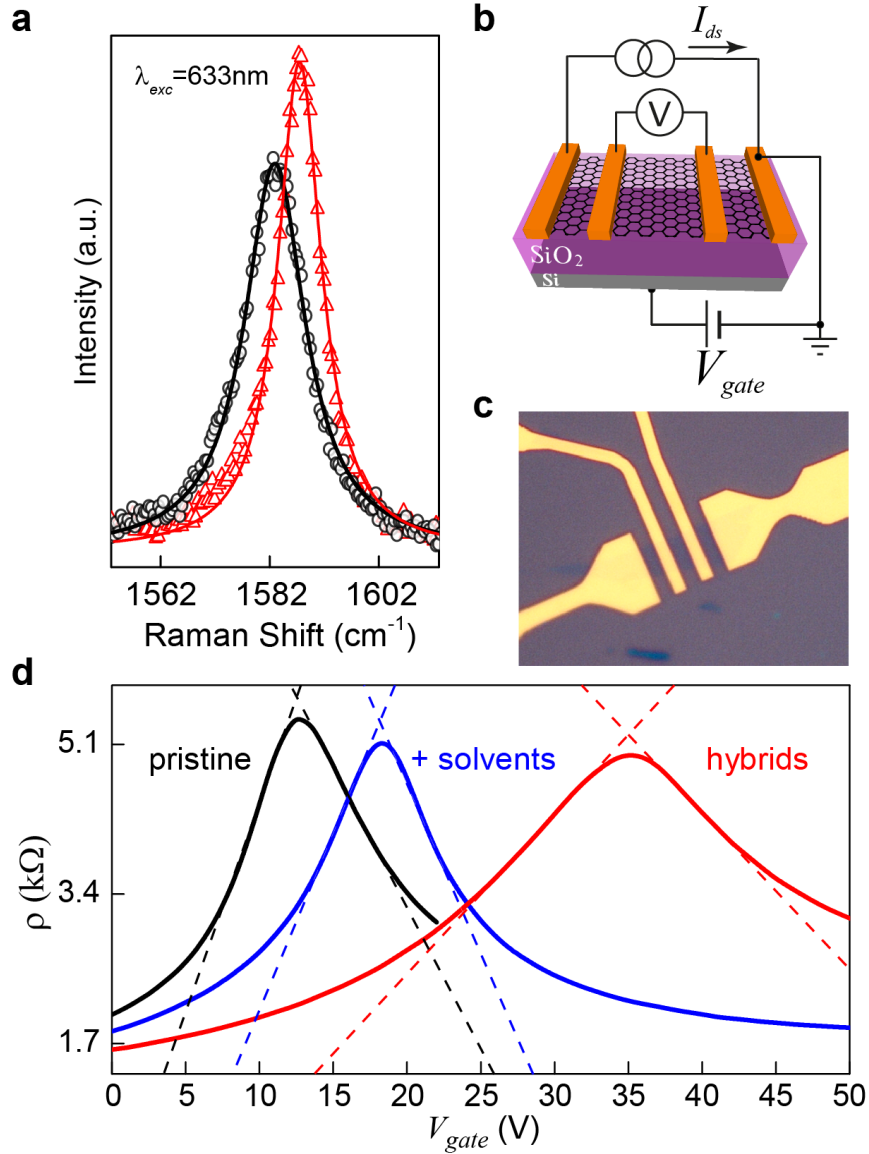
Figure 4.20: Effect of molecular functionalization on graphene electronic properties. a) Raman G band, before (black) and after (red) functionalization. Solid lines are fits with single Lorentzian function. b) Scheme of the graphene-based field-effect transistor with four-terminal measurement geometry and global back-gate. c) Optical photograph of the device. d) Gate-dependence of the graphene resistance for the pristine device (black), after treatment with solvent alone (blue) and after functionalization with **1** ($C = 2.5 \cdot 10^{-6}$ Molar solution).

$$\Theta_M = \frac{\epsilon_0 \kappa V_D}{ed} \frac{1}{\delta} = 0.08 e^- \tag{4.7}$$

where ϵ_0 is the vacuum dielectric constant, κ the SiO_2 relative dielectric permittivity, e the electron charge and d the gate-dielectric thickness. This value is very close to what found for neutral gas adsorbates [9], and confirms that charge transfer per molecule is negligible, the shift being likely due not to charge trasfer processes but to the formation of a surface dipole at the graphene-molecule interface [75]. In addition, the ρ vs. V_{gate} characteristics is seen to broaden and ρ_{max} decreases by 8%, a clear indication that molecular adsorbates affect appreciably holes and electron mobilities. The latter can be determined using equation (2.43) of section 2.3. The induced change is aysmmetric, hole mobility drops pronouncedly from 1600 to 500 $cm^2V^{-1}s^{-1}$ while the electron one is only slightly affected, from 1180 to 1140 $cm^2V^{-1}s^{-1}$. Such effect is not observed for the solvent alone, in agreement with what already reported for atomic magnetic adsorbates [76]. The decrease in the maximum resistivity ($\sim 10\%$) agrees with previous reports on very clean graphene devices functionalized with neutral scatterers, and might hint at the possible creation of midgap states [77]. In conclusion, both Raman and dc-transport measurements confirm the absence of appreciable charge transfer process in the hybrid.

4.5 Bulk hybrid samples

4.5.1 Graphene by liquid phase exfoliation

To achieve a detectable magnetic signal, graphene-$[Fe_4(L)_2(dpm)_6]$ hybrid samples with weight in the ~ 10 mg order are needed. Bulk graphene samples were produced by sonicating of 8.4 mg graphite powder (NGS Naturalgraphit GmbH, grain size $> 0.2\mu$m) in 20 ml of the organic solvents mixture 1,2-dichloroethane:dichloromethane (9/1, v/v) for 48 hrs using a low-power ultrasonic bath, Figure 4.21a. The sonication process separates the graphite layers and forms a graphene dispersion containing single (30%) and multilayer graphene, Figure 4.21b,c, in agreement with previous studies [78–81].

Bulk graphene-SMM hybrid samples were produced by non-covalent grafting of the SMM via solution-based self-assembly. 11.5 mg of $[Fe_4(L)_2(dpm)_6]$ powder were dissolved in 20 ml of solvent mixture and shaken for at least 30 minutes, until the solution acquired a dark-yellow color. No solid sediment was seen after 30 minutes of rest, indicating that all crystallites were completely dissolved and the solution is not saturated. The obtained solution was then mixed with the previously prepared graphene dispersion. The graphene-$[Fe_4(L)_2(dpm)_6]$ solution was stirred for 45 minutes and finally filtered through PTFE membranes of 0.2 m average pore size (Whatman).

Atomic force microscopy (AFM) reveals the appearance of randomly distributed objects on the graphene surface after the functionalization, confirming successful decoration of graphene by SMM, Figure 4.7c,d. The objects height distribution is peaked at 1.8 ± 0.3 nm, Figure 4.7c, in close agreement with the size of individual $[Fe_4(L)_2(dpm)_6]$ molecules.
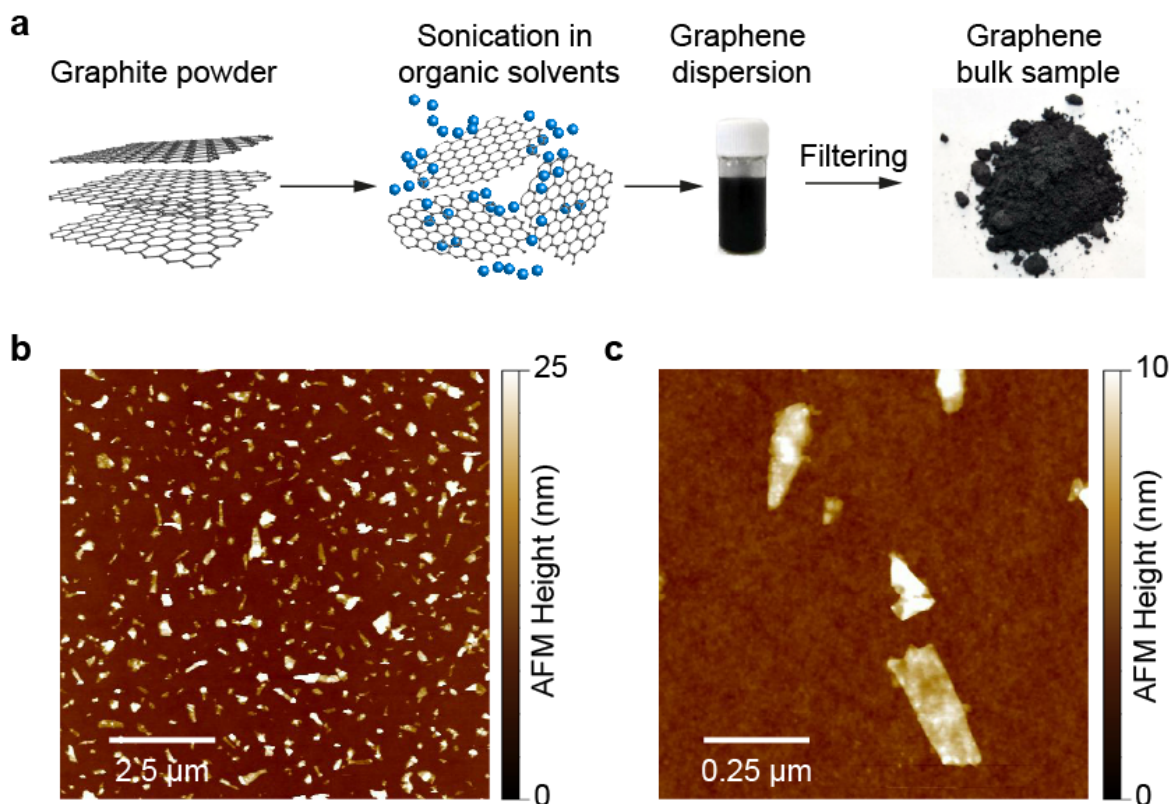
Figure 4.21: Sonication-assisted liquid-phase exfoliation. a) Scheme of the process. b) AFM image of the resulting graphene dispersion deposited on SiO_2 substrate. c) AFM detail showing some few-layer graphene flakes.

Similar coverage was observed for single-, double- or multi-layer graphene. As shown in Chapter 4, sufficiently low concentrations of $[Fe_4(L)_2(dpm)_6]$ ($C < 10^{-6}$ M) ensure graphene decoration by individual molecules without notable aggregation, while a full molecular layer is formed for $C > 10^{-5}$ M.

4.5.2 Structural stability

As seen in Chapter 2, the characteristic SMM magnetic response arises from the specific combination of compositional and structural details. Testing the structural stability of the $[Fe_4(L)_2(dpm)_6]$ once anchored on the graphene is thus essential to ensure the applicability of the spin-Hamiltonian model, and to interpret hybrid properties unambiguously.

Matrix-assisted laser desorption/ionization mass spectrometry coupled with time-of-flight detection (MALDI-TOF) is an excellent method for the characterization of high molecular weight compounds. Its gentle ablation and ionization process prevents high levels of fragmentation and its high sensitivity allows inspecting very diluted samples (sub-monolayer levels of deposition).

The different samples are prepared by simply pressing the material onto a metallic target and are immediately loaded into the spectrometer without any intermediate processing. The characterization has been carried out using a Bruker Reflex IV MALDI-TOF mass spectrometer, equipped with a nitrogen laser pulsed at 3-5 Hz and adjustable power.
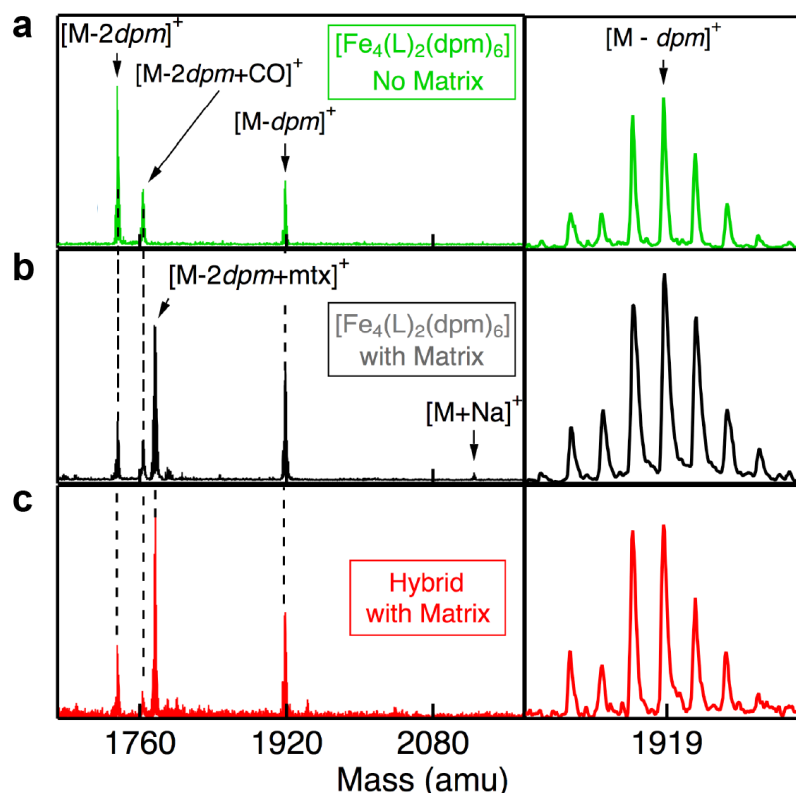
Figure 4.22: MALDI-TOF mass spectroscopy of a) pure $[Fe_4(L)_2(dpm)_6]$ powder. b) pure $[Fe_4(L)_2(dpm)_6]$ powder plus matrix (dithranol). c) bulk $[Fe_4(L)_2(dpm)_6]$-graphene hybrids. The hybrids exhibit the same fragmentation behavior as the starting SMM powder.

The spectrum of the pristine $[Fe_4(L)_2(dpm)_6]$ powder reveals several intense peaks in the range 0 - 1919 amu, Figure 4.22a, in full agreement with what reported on $[Fe_4(L)_2(dpm)_6]$ parent compounds [55, 56]. Peaks at 1919 and 1736 amu correspond to intact clusters undergoing the removal of respectively one and two dpm^- (Hdpm=dipivaloylmethane) ligands during the desorption/ionization process. Other peaks are summarized in Table 4.1.

Since the hybrid material contains a very diluted amount of SMMs, a matrix compound (Dithranol: $C_{14}H_{10}O_3$) was used to improve the ionization process and the overall measurement sensitivity. The matrix was dispersed in the 1,2-dichloroethane:dichloromethane mixture (9/1, v/v) and drop-casted on the powder sample, previously pressed on the target. As shown in Figure 4.22b, the matrix does not alter the fragmentation behavior of the

Mass (amu)	Fragment	Molecular formula
1919	[M−dpm]$^+$	Fe$_4$(O$_4$C$_5$H$_8$)$_2$(C$_4$H$_8$)$_2$(C$_{16}$H$_9$)$_2$(C$_{11}$H$_{19}$O$_2$)$_5$
1763	[M−2dpm+CO]$^+$	Fe$_4$(O$_4$C$_5$H$_8$)$_2$(C$_4$H$_8$)$_2$(C$_{16}$H$_9$)$_2$(C$_{11}$H$_{19}$O$_2$)$_4$CO
1736	[M−2dpm]$^+$	Fe$_4$(O$_4$C$_5$H$_8$)$_2$(C$_4$H$_8$)$_2$(C$_{16}$H$_9$)$_2$(C$_{11}$H$_{19}$O$_2$)$_4$
1552	[M−3dpm]$^+$	Fe$_4$(O$_4$C$_5$H$_8$)$_2$(C$_4$H$_8$)$_2$(C$_{16}$H$_9$)$_2$(C$_{11}$H$_{19}$O$_2$)$_3$

Table 4.1: Masses of the assigned MALDI-TOF peaks for *crystalline* [Fe$_4$(L)$_2$(dpm)$_6$] (left column) and the assignment of their respective fragments, described with respect to the intact molecule M (middle column) and with the fragment formula (right column).

pure compound. In particular, the feature at 1919 amu remains unaltered, while the 1736 amu peak is greatly reduced in combination with the appearance of an intense feature at 1777 amu, characteristic of [M - 3dpm]$^-$ fragments that 'captured' a dithranol molecule.

Mass (amu)	Fragment	Molecular formula
1919	[M−dpm]$^+$	Fe$_4$(O$_4$C$_5$H$_8$)$_2$(C$_4$H$_8$)$_2$(C$_{16}$H$_9$)$_2$(C$_{11}$H$_{19}$O$_2$)$_5$
1777	[M−3dpm+dtr−H]$^+$	Fe$_4$(O$_4$C$_5$H$_8$)$_2$(C$_4$H$_8$)$_2$(C$_{16}$H$_9$)$_2$(C$_{11}$H$_{19}$O$_2$)$_3$(C$_{14}$H$_9$O$_3$)
1763	[M−2dpm+CO]$^+$	Fe$_4$(O$_4$C$_5$H$_8$)$_2$(C$_4$H$_8$)$_2$(C$_{16}$H$_9$)$_2$(C$_{11}$H$_{19}$O$_2$)$_4$CO
1736	[M−2dpm]$^+$	Fe$_4$(O$_4$C$_5$H$_8$)$_2$(C$_4$H$_8$)$_2$(C$_{16}$H$_9$)$_2$(C$_{11}$H$_{19}$O$_2$)$_4$
1552	[M−3dpm]$^+$	Fe$_4$(O$_4$C$_5$H$_8$)$_2$(C$_4$H$_8$)$_2$(C$_{16}$H$_9$)$_2$(C$_{11}$H$_{19}$O$_2$)$_3$

Table 4.2: Masses of the assigned MALDI-TOF peaks for the *hybrids* (left column) and the assignment of their respective fragments, described with respect to the intact molecule M (middle column) and with the fragment formula (right column).

The hybrids show clear fingerprints of intact [Fe$_4$(L)$_2$(dpm)$_6$] on graphene at 1919, 1777, 1763 and 1736 amu, Figure 4.22c and table 4.2. All peaks with mass above 1100 exhibit isotopic patterns in very good agreement with simulations, Figure 4.23a, and necessarily associated with intact molecular core comprising four Fe as evidenced by the characteristic asymmetric shape of the pattern. Moreover, it is evident that the tripodal ligands L^{3-} are stably bound to the Fe$_4$ core, likely helping the stability of the whole cluster [54] and confirming the structural robustness.

The isotopic abundance of Fe (^{54}Fe 5.8%, ^{56}Fe 91.72% ^{57}Fe 2.2%, ^{58}Fe 0.28%), combined with that of the other elements present in the cluster, imparts a characteristic asymmetry to the [Fe$_4$(L)$_2$(dpm)$_6$] isotopic pattern, reflecting the number of Fe atoms. The lower the Fe content the more pronounced is the asymmetry, Figure 4.23b.

4.5.3 Electronic stability

X-ray photoemission spectroscopy is widely employed for the investigation of surface deposited coordination molecular clusters due to its submonolayer sensitivity. XPS spectra
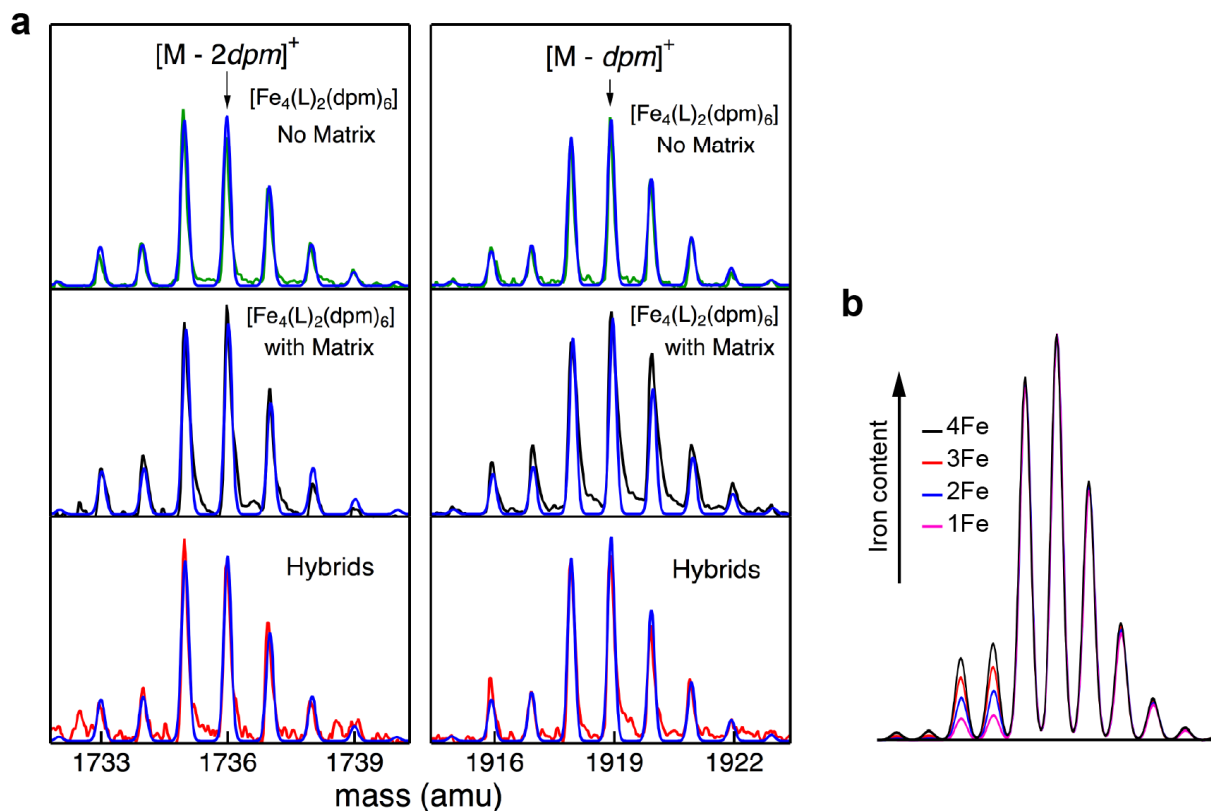
Figure 4.23: Isotopic patterns of high-mass peaks a) Comparison between the experimental and simulated (blue) isotopic patterns for the different samples. b) The asymmetric shape of the isotopic patterns confirms the composition of an intact molecular core.

can provide important information about the oxidation state of the metallic ions constituting the molecular core, thus enabling a clear identification of important structural modifications. We use XPS as complement to the MALDI-TOF analysis to demonstrate the intactness of the $[Fe_4(L)_2(dpm)_6]$ molecules after dispersion and deposition.

Figure 4.24 shows a comparison between the XPS spectra of bulk graphene-$[Fe_4(L)_2(dpm)_6]$ hybrids and the pure $[Fe_4(L)_2(dpm)_6]$. Since XPS spectroscopy is sensitive to the charging behavior of the substrate, the pure compound was deposited on highly-oriented pyrolitic graphite (HOPG) from a saturated solution. Big crystallites were clearly visible to the naked eye.

The XPS spectrum of the hybrids reveals a well resolved Fe2p double peak, in the binding energy (BE) spectral region 740 - 700 eV. Several studies (see [82–84] and references therein) have shown that the positions of Fe2$p_{3/2}$ and Fe2$p_{1/2}$ components depend strongly on the ionic state of the Fe ions present in the sample. For compounds containing only Fe^{3+} coordinated with six oxygen atoms, such as Fe_2O_3 and $[Fe_4(L)_2(dpm)_6]$, the Fe2$p_{3/2}$ component ranges between 710.6 to 711.5 eV, appreciably shifted towards higher binding energies if compared with the neutral elemental Fe, which Fe2$p_{3/2}$ component lies at 707.0eV. For
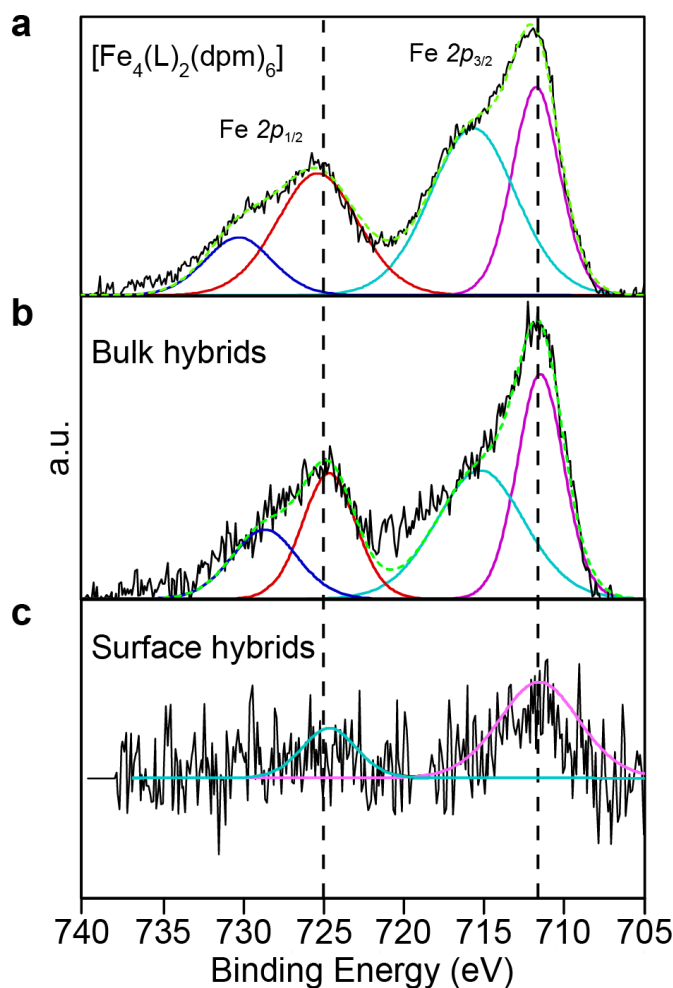
Figure 4.24: Comparison between the XPS spectra of the Fe$2p$ transition for a) pure [Fe$_4$(L)$_2$(dpm)$_6$] deposited on HOPG from saturated solution and b) bulk graphene-[Fe$_4$(L)$_2$(dpm)$_6$] hybrids c) surface graphene-[Fe$_4$(L)$_2$(dpm)$_6$] hybrids, measured on a large exfoliated flake (lateral size $> 50\mu$m) functionalized using a $2.5 \cdot 10^{-6}$ Molar solution.

the bulk hybrids the Fe$2p_{3/2}$ and Fe$2p_{1/2}$ are found at 711.4 eV and 724.6 eV respectively, Figure 4.24b, in very good agreement with the spectrum of pure [Fe$_4$(L)$_2$(dpm)$_6$], Figure 4.24a. This confirms intact coordination bonds with oxygen, and no change in the oxidation state of the Fe ions after dispersion and deposition. It is important to note that XPS studies [82, 84] for compounds where iron is present only in the Fe^{2+} state, such as 2FeOSiO$_2$, report a Fe$2p_{3/2}$ peak at substantially lower binding energy ($\sim$ 709 eV). In the present case there is no evidence of such lower energy contribution. The above observations bring strong evidence that the [Fe$_4$(L)$_2$(dpm)$_6$] molecules remain intact after dispersion and deposition, in fully agreement with other studies on structurally-related compounds [55, 85] carried out in both powder and surface deposited conditions.

The XPS spectrum was also acquired for surface hybrids on a Si/SiO$_2$ substrate function-alized using a $2.5 \cdot 10^{-6}$ M solution for 15min, Figure 4.24c. The spectrum was acquired in the sample region containing an isolated graphene flake with a lateral size of several tens of micrometers. After averaging over four days of acquisition, a weak asymmetric Fe2p double peak appears in the spectral region BE=740 - 700eV. However, accurate fitting was not possible due to the poor signal-to-noise ratio given by the extremely small lateral size of the sample, and the consequently small amount of [Fe$_4$(L)$_2$(dpm)$_6$] grafted on it.

The survey spectra do not reveal the presence of any contaminant for all samples. All spectra were acquired using an Axis ULTRA system by Kratos Analytical Ltd. (Manchester) equipped with a monocromatized Al Kα (1486.6eV) X-ray source and a 8 channels hemispherical detector. Inelastic background was subtracted by means of Shirley method and the data analysis was carried out assuming G/L=30 Gaussian/Lorentzian basic line shapes. The strong and narrow C1s peak due to the presence of graphite/graphene enabled a precise correction of charging effect. The C1s peak was set at 285.2 eV.

4.6   Conclusions

π-stacking interaction between pyrene and the graphene conjugated structure promotes effective grafting of Fe$_4$ SMM to graphene. SMMs deposited from solution self-assemble in molecular islands, owing to their appreciable surface diffusion. The latter is well described by dynamic scaling behavior. Scaling analysis identifies the transition between distinct assembly regimes at different solute concentrations. The residual surface diffusion can be used to induce re-organization of the supramolecular arrangement, and the formation of an extended two-dimensional molecular network on graphene by external means e.g. light exposure. This opens up new strategies for the synthesis of molecular arrangements on graphene. The present findings constitute a basic step forward for the understanding and development of self-assembled SMMs-graphene hybrids, as the organization behavior of molecules on graphene is important for magnetically- and optically-active graphene hybrids. Measurement of Raman spectrum and electronic transport in graphene field effect transistor demonstrate negligible charge transfer between SMMs and graphene, as expected for non-covalently bound adsorbates. The hybrid MALDI-TOF and X-ray photoelectron spectra demonstrate that the SMMs are both structurally and electronically stable.

Bibliography

[1] Barth, J. V., Costantini, G. & Kern, K. Engineering atomic and molecular nanostructures at surfaces. *Nature* **437**, 671–679 (2005).

[2] Macleod, J. M. & Rosei, F. Molecular self-assembly on graphene. *Small* **10**, 1038–1049 (2014).

[3] Garnica, M. *et al.* Long-range magnetic order in a purely organic 2D layer adsorbed on epitaxial graphene. *Nat. Phys.* **9**, 368–374 (2013).

[4] Deshpande, A. *et al.* Self-assembly and photopolymerization of sub-2 nm one-dimensional organic nanostructures on graphene. *J. Am. Chem. Soc* **134**, 16759–16764 (2012).

[5] Rao, C. N. R., Sood, a. K., Subrahmanyam, K. S. & Govindaraj, a. Graphene: The new two-dimensional nanomaterial. *Angewandte Chemie - International Edition* **48**, 7752–7777 (2009).

[6] Huang, X. *et al.* Graphene-based materials: Synthesis, characterization, properties, and applications. *Small* **7**, 1876–1902 (2011).

[7] Rodríguez-López, J. *et al.* Quantification of the surface diffusion of tripodal binding motifs on graphene using scanning electrochemical microscopy. *J. Am. Chem. Soc* **134**, 6224–6236 (2012).

[8] Saywell, A. *et al.* Self-assembled aggregates formed by single-molecule magnets on a gold surface. *Nat. Commun.* **1**, 1 (2010).

[9] Schedin, F. *et al.* Detection of individual gas molecules adsorbed on graphene. *Nat. Mater.* **6**, 652–655 (2007).

[10] Elias, D. C. *et al.* Control of graphene's properties by reversible hydrogenation: evidence for graphane. *Science* **323**, 610–3 (2009).

[11] Zhang, Z., Huang, H., Yang, X. & Zang, L. Tailoring Electronic Properties of Graphene by π–π Stacking with Aromatic Molecules. *Journal of Physical Chemistry Letters* **2**, 2897–2905 (2011).

[12] Qi, X. *et al.* Amphiphilic graphene composites. *Angewandte Chemie - International Edition* **49**, 9426–9429 (2010).

[13] Nair, R. R. *et al.* Dual origin of defect magnetism in graphene and its reversible switching by molecular doping. *Nat. Commun.* **4**, 2010 (2013).

[14] Englert, J. M. *et al.* Covalent bulk functionalization of graphene. *Nat. Chem.* **3**, 279–286 (2011).

[15] Wang, Q. H. & Hersam, M. C. Room-temperature molecular-resolution characterization of self-assembled organic monolayers on epitaxial graphene. *Nat. Chem.* **1**, 206–211 (2009).

[16] Quintana, M. *et al.* Selective organic functionalization of graphene bulk or graphene edges. *Chemical Communications* **47**, 9330–9332 (2011).

[17] Candini, A., Klyatskaya, S., Ruben, M., Wernsdorfer, W. & Affronte, M. Graphene spintronic devices with molecular nanomagnets. *Nano letters* **11**, 2634–2639 (2011).

[18] Bogani, L. *et al.* Effect of sequential grafting of magnetic nanoparticles onto metallic and semiconducting carbon-nanotube devices: towards self-assembled multi-dots. *J. Mater. Chem.* **20**, 2099–2107 (2010).

[19] Kyatskaya, S. *et al.* Anchoring of Rare-Earth-Based Single-Molecule Magnets on Single-Walled Carbon Nanotubes. *J. Am. Chem. Soc* **131**, 15143–15151 (2009).

[20] Khlobystov, A. N. *et al.* Molecular Motion of Endohedral Fullerenes in Single-Walled Carbon Nanotubes. *Angewandte Chemie - International Edition* **43**, 1386–1389 (2004).

[21] Giménez-López, M. D. C. *et al.* Encapsulation of single-molecule magnets in carbon nanotubes. *Nat. Commun.* **2**, 407 (2011).

[22] Bogani, L. *et al.* Single-molecule-magnet carbon-nanotube hybrids. *Angewandte Chemie - International Edition* **48**, 746–50 (2009).

[23] Gatteschi, D., Sessoli, R. & Villain, J. *Molecular Nanomagnets.* Mesoscopic Physics and Nanotechnology (OUP, Oxford, 2006).

[24] Wernsdorfer, W. & Sessoli, R. Quantum Phase Interference and Parity Effects in Magnetic Molecular Clusters. *Science* **284**, 133–135 (1999).

[25] Bogani, L. & Wernsdorfer, W. L. Molecular spintronics using single-molecule magnets. *Nat. Mater.* **7**, 179–186 (2008).

[26] Tombros, N. *et al.* Electronic spin transport and spin precession in single graphene layers at room temperature. *Nature* **448**, 571–574 (2007).

[27] Pesin, D. & MacDonald, A. H. Spintronics and pseudospintronics in graphene and topological insulators. *Nat. Mater.* **11**, 409–416 (2012). arXiv:1308.3428.

[28] Wäckerlin, C. *et al.* Controlling spins in adsorbed molecules by a chemical switch. *Nat. Commun.* **1**, 61 (2010).

[29] Sanvito, S. Molecular spintronics. *Chem. Soc. Rev.* **40**, 3336 (2011).

[30] Jiang, S. *et al.* An introduction to molecular spintronics. *Science China Chemistry* **55**, 867–882 (2012).

[31] Novoselov, K. S. K. S. *et al.* Electric field effect in atomically thin carbon films. *Science* **306**, 666–669 (2004).

[32] Blake, P. *et al.* Making graphene visible. *Applied Physics Letters* **91**, 63124 (2007).

[33] Zhu, W., Perebeinos, V., Freitag, M. & Avouris, P. Carrier scattering, mobilities, and electrostatic potential in monolayer, bilayer, and trilayer graphene. *Phys. Rev. B* **80**, 235402 (2009).

[34] Novoselov, K. S. *et al.* Two-dimensional gas of massless Dirac fermions in graphene. *Nature* **438**, 197–200 (2005).

[35] Novoselov, K. S. *et al.* Unconventional quantum Hall effect and Berry's phase of 2pi in bilayer graphene. *Nat. Phys.* 177–180 (2006).

[36] Craciun, M. F. *et al.* Trilayer graphene is a semimetal with a gate-tunable band overlap. *Nat. Nanotech.* **4**, 383–388 (2009).

[37] Han, W. & Kawakami, R. K. Spin Relaxation in Single-Layer and Bilayer Graphene. *Phys. Rev. Lett.* **107**, 47207 (2011).

[38] Cardona, M. Raman Spectroscopy Applied To The Characterization Of Semiconductors And Semiconductor Microstructures. In *Proc. SPIE 0822, Raman and Luminescence Spectroscopy in Technology, 2*, vol. 822, 2–15 (1988).

[39] Dresselhaus, M. S., Jorio, A., Hofmann, M., Dresselhaus, G. & Saito, R. Perspectives on carbon nanotubes and graphene Raman spectroscopy. *Nano Letters* **10**, 751–758 (2010).

[40] Ferrari, A. C. *et al.* Raman spectrum of graphene and graphene layers. *Physical Review Letters* **97**, 187401 (2006).

[41] Malard, L. M., Pimenta, M. A., Dresselhaus, G. & Dresselhaus, M. S. Raman spectroscopy in graphene. *Physics Reports* **473**, 51–87 (2009).

[42] Casiraghi, C., Pisana, S., Novoselov, K. S., Geim, A. K. & Ferrari, A. C. Raman fingerprint of charged impurities in graphene. *Applied Physics Letters* **91**, 233108 (2007).

[43] Casiraghi, C. Probing disorder and charged impurities in graphene by Raman spectroscopy. *Physica Status Solidi - Rapid Research Letters* **3**, 175–177 (2009).

[44] Thomsen, C. & Reich, S. Double Resonant Raman Scattering in Graphite. *Phys. Rev. Lett.* **85**, 5214–5217 (2000).

[45] Tuinstra, F. & Koenig, J. L. Raman Spectrum of Graphite. *The Journal of Chemical Physics* **53**, 1126–1130 (1970).

[46] Matthews, M., Pimenta, M., Dresselhaus, G., Dresselhaus, M. & Endo, M. Origin of dispersive effects of the Raman D band in carbon materials. *Physical Review B* **59**, R6585–R6588 (1999).

[47] Cançado, L. G. *et al.* Quantifying Defects in Graphene via Raman Spectroscopy at Different Excitation Energies. *Nano Letters* **11**, 3190–3196 (2011).

[48] Casiraghi, C. *et al.* Raman Spectroscopy of Graphene Edges. *Nano Letters* **9**, 1433–1441 (2009).

[49] Danieli, C. *et al.* A novel class of tetrairon(III) single-molecule magnets with graphene-binding groups. *Polyhedron* **28**, 2029–2035 (2009).

[50] Antczak, G. & Ehrlich, G. Mechanism of cluster diffusion. In *Surface Diffusion*, 517–555 (Cambridge University Press, Cambridge, 2010). URL `http://ebooks.cambridge.org/ref/id/CBO9780511730320A082`.

[51] Röder, H., Hahn, E., Brune, H., Bucher, J.-P. & Kern, K. Building one- and two-dimensional nanostructures by diffusion-controlled aggregation at surfaces. *Nature* **366**, 141–143 (1993).

[52] Brune, H., Bales, G. S., Jacobsen, J., Boragno, C. & Kern, K. Measuring surface diffusion from nucleation island densities. *Phys. Rev. B* **60**, 5991–6006 (1999).

[53] Stroscio, J. a. & Pierce, D. T. Scaling of diffusion-mediated island growth in iron-on-iron homoepitaxy. *Phys. Rev. B* **49**, 8522–8525 (1994).

[54] Cornia, A. *et al.* Energy-Barrier Enhancement by Ligand Substitution in Tetrairon(III) Single-Molecule Magnets. *Angewandte Chemie - International Edition* **116**, 1156–1159 (2004).

[55] Rigamonti, L. *et al.* Enhanced Vapor-Phase Processing in Fluorinated Fe4 Single-Molecule Magnets. *Inorganic Chemistry* **52**, 5897–5905 (2013).

[56] Margheriti, L. *et al.* Thermal Deposition of Intact Tetrairon(III) Single-Molecule Magnets in High-Vacuum Conditions. *Small* **5**, 1460–1466 (2009).

[57] Loske, F., Lübbe, J., Schütte, J., Reichling, M. & Kühnle, A. Quantitative description of \textbf{C}_{60} diffusion on an insulating surface. *Phys. Rev. B* **82**, 155428 (2010).

[58] Rahe, P., Bechstein, R., Schütte, J., Ostendorf, F. & Kühnle, A. Repulsive interaction and contrast inversion in noncontact atomic force microscopy imaging of adsorbates. *Phys. Rev. B* **77**, 195410 (2008).

[59] Vicsek, T. & Family, F. Dynamic scaling for aggregation of clusters. *Physical review letters* **52**, 1669 (1984).

[60] Amar, J. G. J., Family, F. & Lam, P. P.-M. Dynamic scaling of the island-size distribution and percolation in a model of submonolayer molecular-beam epitaxy. *Phys. Rev. B* **50**, 8781–8797 (1994).

[61] Amar, J. G. & Family, F. Critical Cluster Size: Island Morphology and Size Distribution in Submonolayer Epitaxial Growth. *Phys. Rev. Lett.* **74**, 2066–2069 (1995).

[62] Amar, J. G. & Family, F. Kinetics of submonolayer and multilayer epitaxial growth. *Thin Solid Films* **272**, 208–222 (1996).

[63] Doudevski, I., Hayes, W. A. & Schwartz, D. K. Submonolayer Island Nucleation and Growth Kinetics during Self-Assembled Monolayer Formation. *Phys. Rev. Lett.* **81**, 4927–4930 (1998).

[64] Doudevski, I. & Schwartz, D. K. Dynamic scaling of the submonolayer island size distribution during self-assembled monolayer growth. *Phys. Rev. B* **60**, 14–17 (1999).

[65] So, C. R. *et al.* Controlling Self-Assembly of Engineered Peptides on Graphite by Rational Mutation. *ACS Nano* **6**, 1648–1656 (2012).

[66] Chambliss, D. D. & Johnson, K. E. Nucleation with a critical cluster size of zero: Submonolayer Fe inclusions in Cu(100). *Phys. Rev. B* **50**, 5012–5015 (1994).

[67] Müller, B., Nedelmann, L., Fischer, B. r., Brune, H. & Kern, K. Initial stages of Cu epitaxy on Ni(100): Postnucleation and a well-defined transition in critical island size. *Phys. Rev. B* **54**, 17858–17865 (1996).

[68] Venables, J. A., Spiller, G. D. T. & Hanbucken, M. Nucleation and growth of thin films. *Reports on Progress in Physics* **47**, 399 (1984).

[69] Barabasi, A.-L. & Albert, R. Emergence of scaling in random networks. *Science* **286**, 11 (1999).

[70] Bray, D. Molecular networks: the top-down view. *Science* **301**, 1864–1865 (2003).

[71] Marschall, M. *et al.* Random two-dimensional string networks based on divergent coordination assembly. *Nat. Chem.* **2**, 131–137 (2010).

[72] Otero, R. *et al.* Elementary structural motifs in a random network of cytosine adsorbed on a gold(111) surface. *Science* **319**, 312–315 (2008).

[73] Lopes, M. *et al.* Surface-Enhanced Raman Signal for Terbium Single-Molecule Magnets Grafted on Graphene. *ACS Nano* **4**, 7531–7537 (2010).

[74] Chen, S. *et al.* Adsorption/desorption and electrically controlled flipping of ammonia molecules on graphene. *New Journal of Physics* **12** (2010). arXiv:1006.2591.

[75] Murali, R. Graphene Transistors. In Murali, R. (ed.) *Graphene Nanoelectronics*, 51–91 (Springer, Berlin Heidelberg, 2012).

[76] Pi, K. *et al.* Electronic doping and scattering by transition metals on graphene. *Phys. Rev. B* **80**, 75406 (2009).

[77] Wehling, T. O., Katsnelson, M. I. & Lichtenstein, A. I. Impurities on graphene: Midgap states and migration barriers. *Phys. Rev. B* **80**, 85428 (2009).

[78] Hernandez, Y. *et al.* Measurement of Multicomponent Solubility Parameters for Graphene Facilitates Solvent Discovery. *Langmuir* **26**, 3208–3213 (2010).

[79] Hernandez, Y. *et al.* High-yield production of graphene by liquid-phase exfoliation of graphite. *Nature Nanotechnology* **3**, 563–568 (2008).

[80] O'Neill, A. *et al.* Graphene Dispersion and Exfoliation in Low Boiling Point Solvents. *The Journal of Physical Chemistry C* **0**, 5422–5428 (2011).

[81] Qian, W. *et al.* Solvothermal-assisted exfoliation process to produce graphene with high yield and high quality. *Nano Research* **2**, 706–712 (2009).

[82] Yamashita, T. & Hayes, P. Analysis of XPS spectra of Fe2+ and Fe3+ ions in oxide materials. *Applied Surface Science* **254**, 2441–2449 (2008).

[83] Graat, P. C. J. & Somers, M. a. J. Simultaneous determination of composition and thickness of thin iron-oxide films from XPS Fe 2p spectra. *Applied Surface Science* **100-101**, 36–40 (1996).

[84] Roosendaal, S., van Asselen, B., Elsenaar, J., a.M. Vredenberg & Habraken, F. The oxidation state of Fe(100) after initial oxidation in O2. *Surface Science* **442**, 329–337 (1999).

[85] Pineider, F. *et al.* Deposition of intact tetrairon(iii) single molecule magnet monolayers on gold: an STM{,} XPS{,} and ToF-SIMS investigation. *J. Mater. Chem.* **20**, 187–194 (2010).

Chapter 5

Classical and quantum dynamics of molecular spins on graphene

Carbon-based spintronics [1–7] offers a mean to electrically manipulate localized spins in close proximity of a carbon nanotube or graphene sheet. This task requires understanding and tuning of the interaction between the components, in order to improve the spin performance [8–10], e.g. by minimizing quantum-decoherence [6], and to enable spin manipulation, e.g. by altering the magnetic anisotropy or the electronic coupling. However, there is little current understanding of how the spin states in such devices are affected by the environment.

Here, we exploit the exceptionally clean magnetic features of single-molecule-magnets (SMMs) [11, 12] to explore how spins interact with the graphene substrates. A comprehensive magnetic characterization is carried out by means of *dc-* and *ac-* magnetometries. The classical and quantum relaxation mechanisms are probed independently by applying an external magnetic field. While isolated molecules on graphene exhibit unaltered static magnetic properties, the spin dynamics is strongly influenced by interaction with the graphene substrate.

5.1 Hybrids static magnetic response

The temperature (T) dependence of the dc magnetic susceptibility χ_m and isothermal magnetization curves provide important information about the molecular spin-ground state and the leading magnetic anisotropy terms.

The measurements were performed on bulk samples, obtained by removing the hybrid powder from PTFE membranes and pressing it to form a pallet. The $\chi_m T$ curve (where χ_m is the static molar magnetic susceptibility, defined as the ratio between magnetization and the applied magnetic field, M/H) was extracted by measuring the magnetization M in the temperature range 1.8 - 230 K, using a commercial SQUID-based magnetometer at a fixed external field $H = 1$ kOe.

All data were corrected for the diamagnetism of the sample and the sample holder. For the
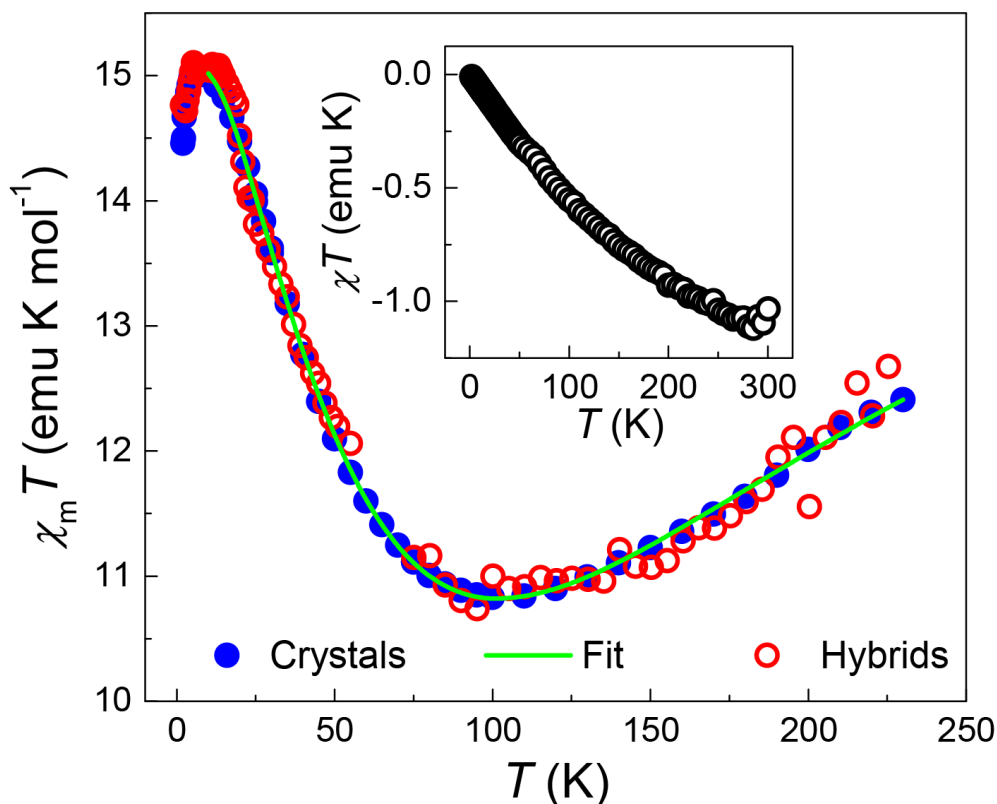
Figure 5.1: Temperature dependence of the product of the static magnetic susceptibility χ_m for $[\mathrm{Fe_4(L)_2(dpm)_6}]$ (solid circles) and the hybrids (empty circles), with $H = 1$ kOe. The solid line is a fit based on Equation (2.5). Inset: dc susceptibility of an unfunctionalized graphene bulk sample.

former a diamagnetic correction of $-1283 \cdot 10^{-6}$ emu/mol, estimated from Pascal constants, was used, while the latter was independently determined. The diamagnetic contribution of the graphene matrix was determined from un-functionalized samples, Figure 5.1 inset. Figure 5.1 shows the comparison between the hybrids $\chi_m T$ vs. T and that of the crystalline $[\mathrm{Fe_4(L)_2(dpm)_6}]$. Hybrids data were rescaled to account for the different amount of SMMs present in the sample.

The hybrids $\chi_m T$ vs. T curve matches that of the pure crystalline compound, and both can be fitted by using Equation (2.5) and the same set of magnetic parameters, $J_1 = -14.85 \pm 0.05$ cm^{-1} and $J_2 = 0.09 \pm 0.05$ cm^{-1}, as known for the intact SMM core. This confirms that, owing to the cluster excellent structural and electronic stability, the leading uniaxial anisotropy term remains unaltered after grafting to graphene, and SMMs embedded in the graphene matrix behave as model spins with ground state $S = 5$. This is further confirmed by adiabatic magnetization data acquired at different temperatures (Figure 5.2).
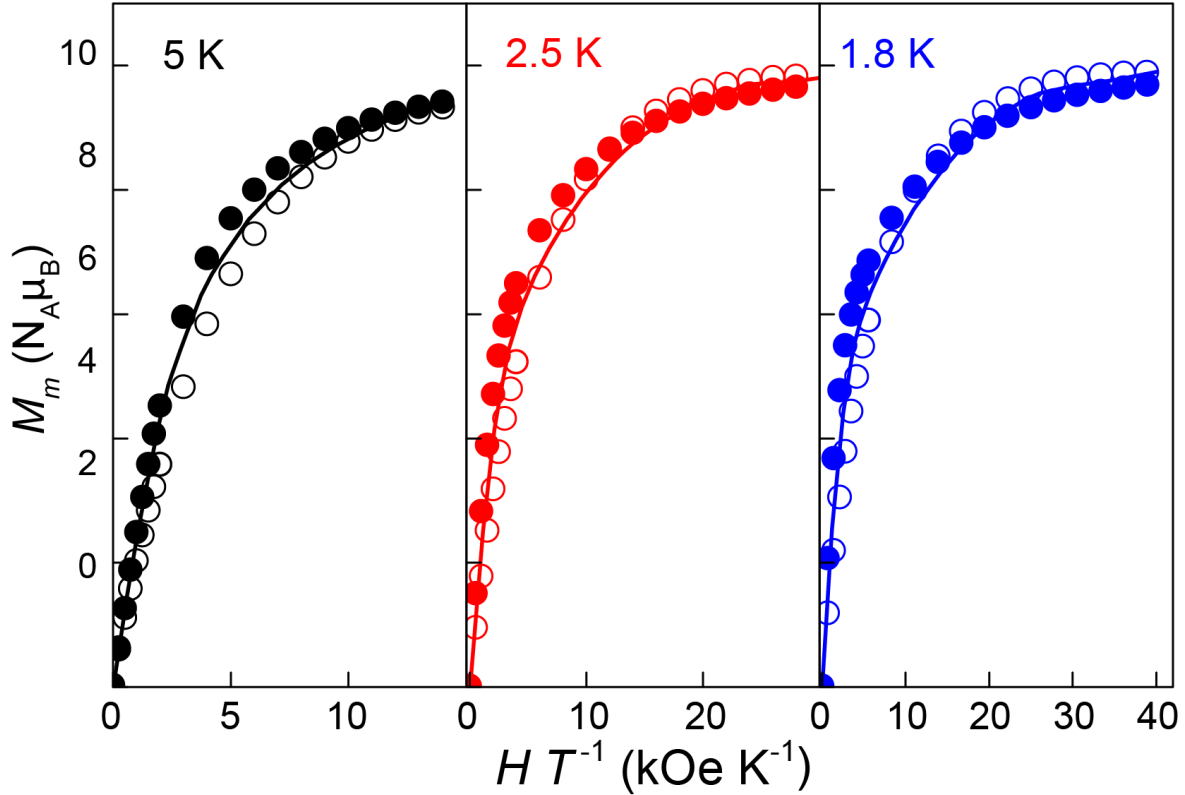
Figure 5.2: Comparison of the low-temperature magnetization curves of crystalline $[Fe_4(L)_2(dpm)_6]$ (solid points) and the hybrids (open dots), showing the M_m vs H/T curves acquired at 5 K (left), 2.5 K (middle) and 1.8 K (right) after subtracting the graphene matrix contribution and rescaling for the different number of molecules. Solid lines are fits to the data based on Equation (2.6).

5.2 Dynamics of molecular spins on graphene

As seen in Section 2.2, the low-temperature magnetic behavior of SMMs is characterized by the presence of a large magnetic anisotropy, that creates an energy barrier ΔE separating the $|m\rangle$ sublevels of the $S = 5$ multiplet (Figure 2.10). Two spin-relaxation mechanisms are then possible: a classical one, where phonon absorption allows overcoming ΔE, and a quantum tunneling (QT) one, active between those $|m\rangle$ and $|-m\rangle$ levels at the opposite sides of the barrier, that are mixed by transverse anisotropy terms.

5.2.1 Effect of graphene on the thermal relaxation

To examine the effect of graphene on the thermal relaxation mechanism only, a small static magnetic field ($H = 1$ kOe) is applied, so as to place the $|m\rangle$ and $|-m\rangle$ levels off

resonance, thus suppressing quantum tunneling. The spin dynamics is probed by measuring the real χ' and imaginary χ'' susceptibility components in response to a small magnetic field oscillating at frequency ω, using a commercial gradiometer combined with SQUID-based amplification.

Figure 5.3 shows the comparison between the *ac*-susceptibility of the crystalline Fe_4Py (Figure 5.3a) and two graphene-SMMs hybrid samples, one containing molecular aggregates (Figure 5.3b) and the other with isolated molecules on graphene (Figure 5.3c). Owing to the smaller amount of SMMs present in the hybrid samples, the magnetic signal is three to four orders of magnitude lower than the crystal one, and the signal to noise ratio is much reduced as the sensitivity limit of the instrument is almost reached. In order to maximize the signal, the field dependence of the ac-susceptibility was recorded, Figure 5.4, and the constant value $H = 1\text{kOe}$ was chosen accordingly. Moreover, the hybrid samples show a clear diamagnetic contribution arising from graphene.

Molecular aggregates on graphene show an almost unvaried spin dynamics as compared to the crystalline compound. Arrhenius analysis yields the same barrier $\Delta E = 13.6 \pm 1.1$ K, and a slightly changed pre-factor $\tau_0 = (7.4 \pm 1.7) \cdot 10^{-7}$s, suggesting a modulation of the spin-phonon interaction due to the altered phononic environment (Figure 5.3d).

On the crontrary, isolated SMMs on graphene show a much faster spin dynamics, as the peak in χ'' shifts appreciably towards lower temperatures. No Arrhenius analysis could be carried out in this case, nevertheless, the increase in χ'' is clearly visible as the temperature is lowered, hinting to a much strongly altered phononic environment for single isolated SMMs in contact with graphene.

The above observations suggest that, as Fe_4Py assemble on graphene in smaller and smaller aggregates, towards isolated molecules, the interaction with the graphene two-dimensional phononic bath starts to dominate the spin thermal relaxation. On the contrary, for big aggregates the phononic environment resembles that of the crystal, yielding an almost unvaried dynamics. To verify these assumptions, a more detailed modeling of the thermal relaxation for the case of a two-dimensional phonon bath is necessary. This will be the focus of the next Chapter.
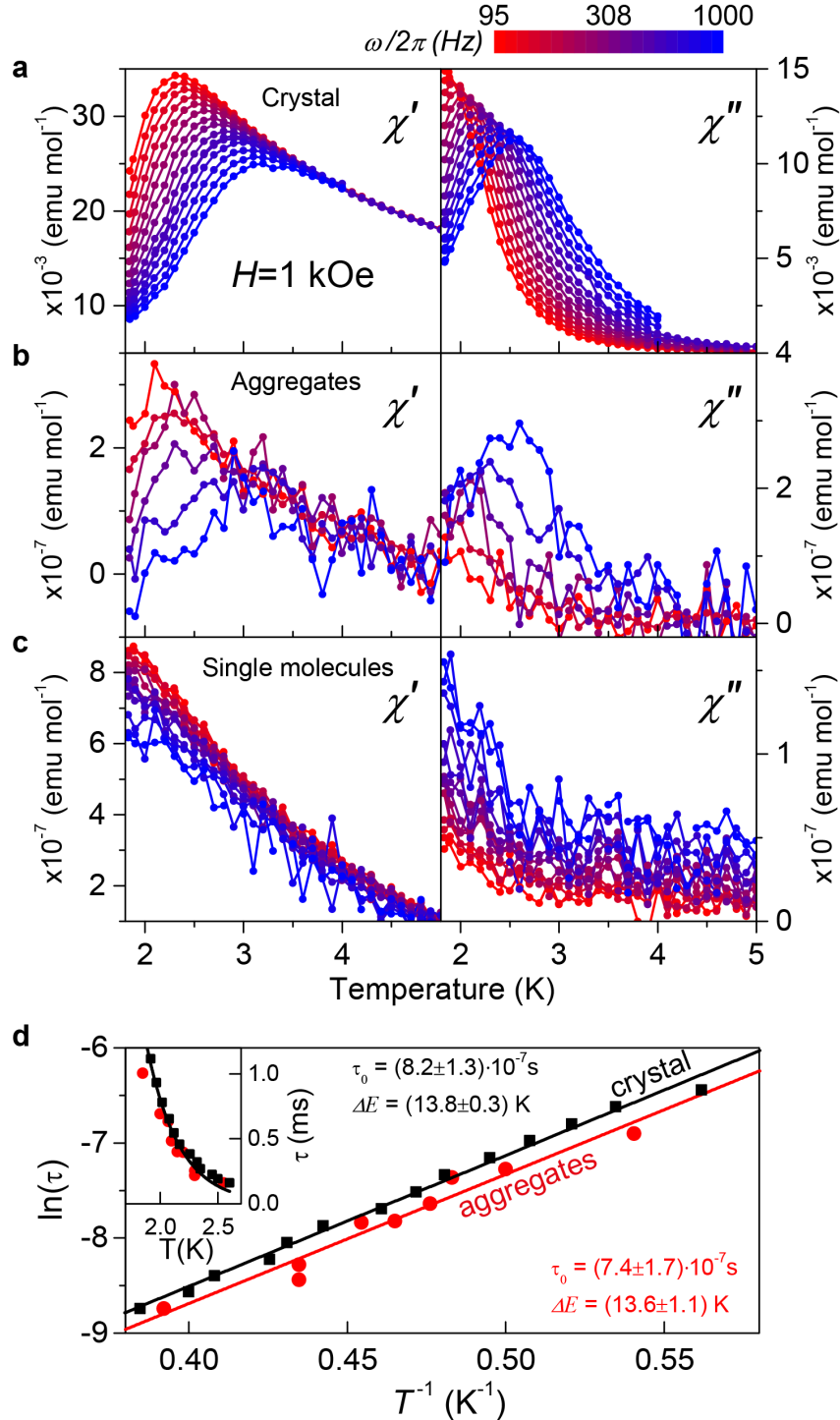
Figure 5.3: Effect of graphene on the thermal spin relaxation mechanism. Temperature and frequency dependence of ac-susceptibility a) for crystalline Fe_4Py; b) hybrids containing aggregated SMMs on the graphene surface; c) hybrids with isolateds SMMs on the graphene surface. d) Arrhenius analysis for a) and b)
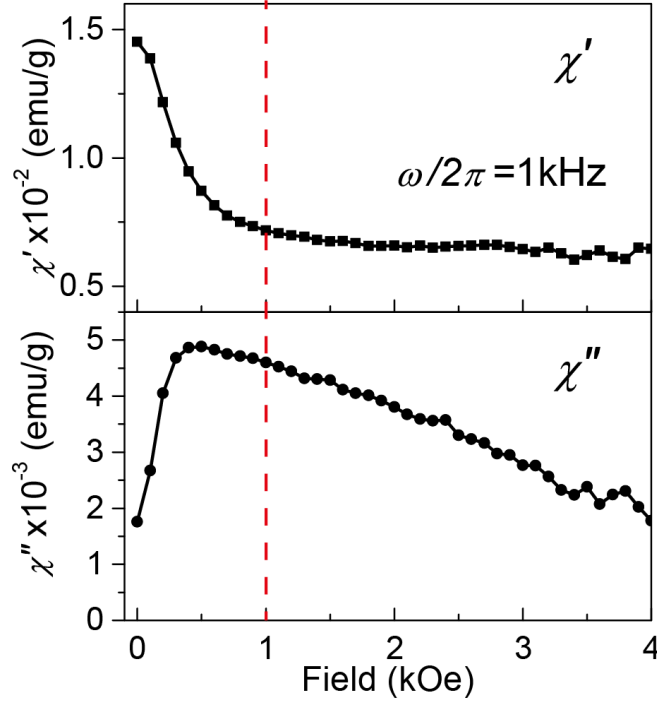
Figure 5.4: Field dependence of the ac-susceptibility for the crystalline Fe_4Py at 1kHz (χ'' is maximum in the range 0.5-1kOe).

5.2.2 Effect of graphene on the spin quantum relaxation

The quantum relaxation of isolated spins on graphene is investigated by switching off the external magnetic field, so that $|m\rangle$ and $|-m\rangle$ levels fall back into resonance. In this case χ' and χ'' are measured using an home-made system based on an on-chip micro-SQUID sensor mounted in the mixing chamber of a ^{3}He -^{4}He dilution cryostat. This system affords a larger frequency range, spanning 5 decades from 1.7 Hz to 0.17 MHz, and can be operated at ultra-low temperatures down to 13 mK. The sensitivity is also improved being the sample directly glued onto one of the squid pickup coils.

Figure 5.5a,b compares the frequency dependence of the ac-susceptibility of isolated molecules on graphene in $H = 0$ at two different temperatures $T = 4.2$ K and 20 mK. The same measurements on the crystal are shown for comparison.

At 4.2 K the thermal relaxation still dominates over the QT relaxation. χ' and χ'' can be fitted using the simple ($\alpha = 0$) Cole-Cole model, introduced in Section 2.2, confirming the absence of barrier height ΔE broadening, thanks to the structural and electronic stability of the Fe_4Py cluster. The hybrid χ' was corrected for the appreciable graphene diamagnetic contribution, that as seen in Figure 5.5c, almost compensate the spin signal for $\omega/2\pi \to 0$. The $\chi'' \neq 0$ in Figure 5.5c confirms graphene metallic character. At this temperature, isolated SMMs on graphene exhibit a slightly faster spin relaxation, $\tau \sim 9 \cdot 10^{-7}$ s, compared to the crystal, $\tau \sim 1.7 \cdot 10^{-6}$ s.

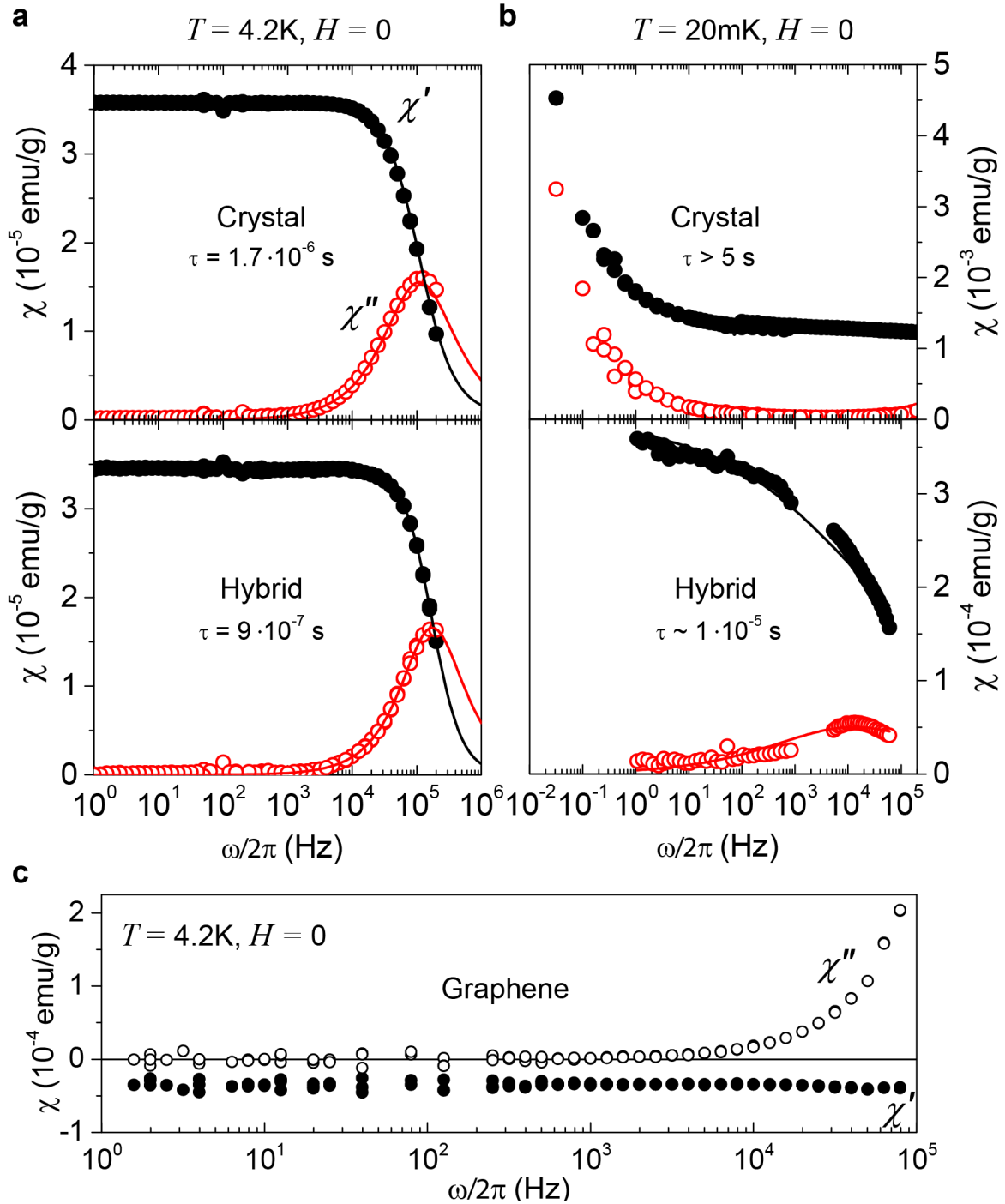Figure 5.5: Mixed thermal and quantum spin relaxation in $H = 0$. Frequency dependence of the real (empty circles) and imaginary (solid circles) parts of the ac-susceptibility for crystalline Fe_4Py compound and graphene-SMMs hybrids with isolated molecules at a) $T = 4.2$ K and b) 20 mK. Solid lines are fits with the Cole-Cole model. The hybrid data are corrected for the diamagnetic bare graphene contribution c).
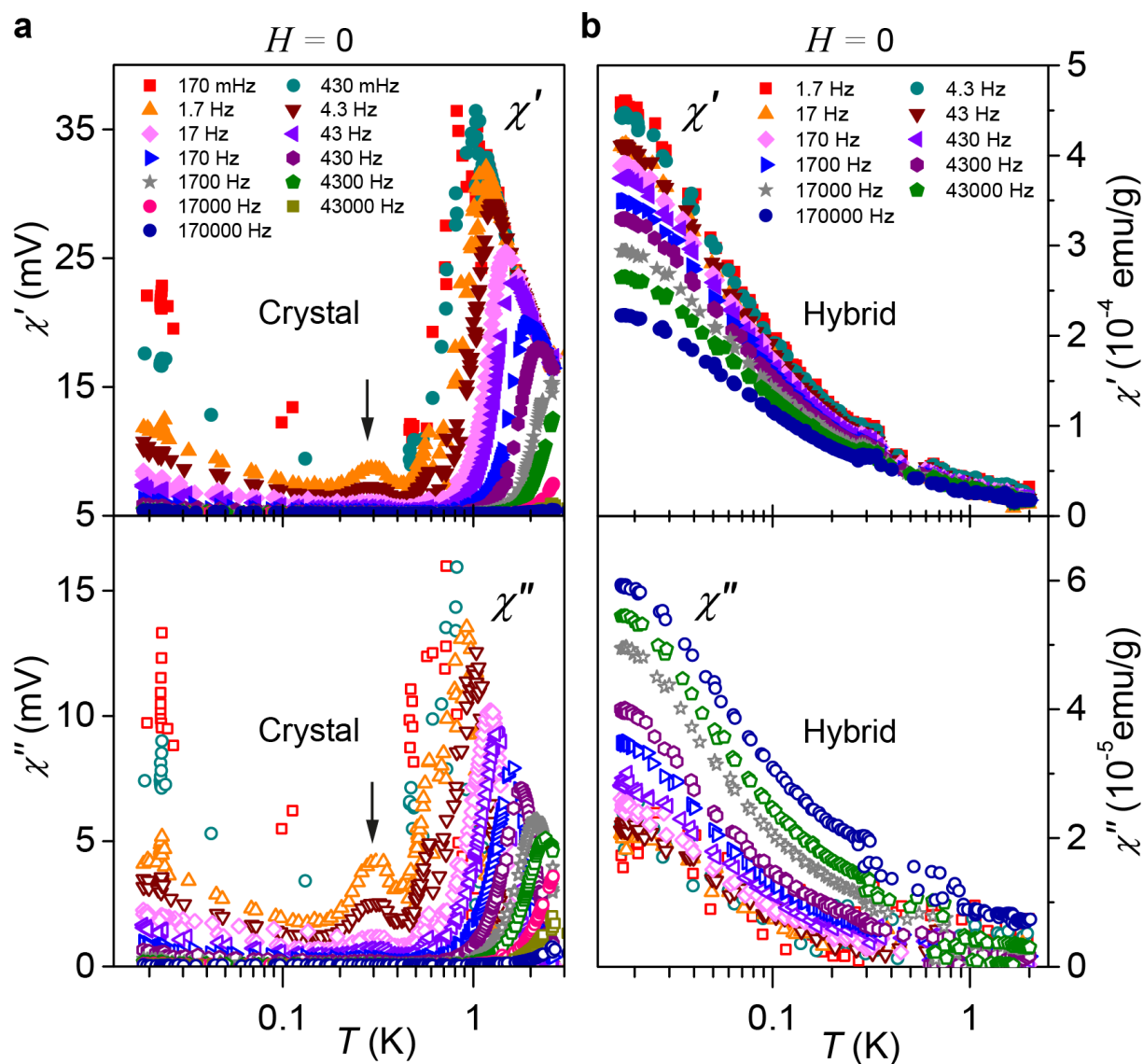
Figure 5.6: Temperature dependence of χ for a) crystalline Fe_4Py and b) isolated molecules on graphene at different frequencies in the QT dominated temperature range. Arrows in a) indicate a contribution from molecular spins coupled via dipole-dipole interaction.

A strikingly faster dynamics of isolated SMMs on graphene becomes evident as the temperature is lowered down to $T = 20$mK, where phononic excitations are frozen and QT is the dominant relaxation mechanism. While the crystalline sample shows slow relaxation, with τ in the order of seconds ($\tau \approx 5$ s), due to the characteristic susceptibility blocking, the relaxation of isolated molecules on graphene diverges from that by several orders of magnitude, $\tau \sim 1 \cdot 10^{-5}$s. Since for the crystalline sample the maximum in χ'' fall outside the experimentally accessible regions of temperature and frequency, τ has been estimated using the approximate expression $\tau \approx \chi''/(\chi'\omega)$ using data points at $\omega/2\pi = 1.6$Hz.

To investigate the transition from the classical (thermal) to the pure quantum spin relaxation, the complete temperature dependence of the ac-susceptibility at $H = 0$ is measured (Figure 5.6). The crystalline sample shows the characteristic (frequency-dependent) susceptibility blocking ($T \sim 0.8$ K for $\omega/2\pi = 0.17 - 170$ Hz), marking the suppression of the thermal relaxation channel and the transition to QT-dominated relaxation at lower temperatures. By contrast, no clear blocking is observed for isolated SMMs on graphene, which nevertheless show clear maxima in both χ' and χ'' at much lower temperatures. The weak temperature dependence for $0.1 < T < 4$K suggests that the quantum relaxation mechanism is enhanced by the interaction with graphene.

For the crystalline sample, a second peak at $T \sim 0.25$ K is also seen, which is likely attributed to a phase transition to a magnetically-ordered state induced by dipolar interactions among the SMM spins in the crystal. This low temperature contribution is absent in the hybrids, as expected for highly-diluted systems where dipolar interactions are drastically reduced. In the next Chapter we will see that the latter is a fundamental condition to explain the observed quantum behavior.

The relaxation time at different temperatures can be accurately determined from the frequency dependence of the ac-susceptibility, Figure 5.7. A roll-over of χ' combined with a maximum in χ'' between $10^4 - 10^5$ Hz reveal the fast relaxation process of isolated SMMs grafted on graphene, Figure 5.7b. Moreover the low-frequency limit of χ' (i.e. χ_T) increases, while the onset of the χ'' peak shifts towards lower frequencies as the temperature decreases, in full agreement with SMM behavior. At lower frequencies, χ' shows a close to logarithmic dependence on frequency, accompanied by a nearly constant χ'', in agreement with Kramers-Kronig relation $\chi'' = -\frac{\pi}{2}\frac{d\chi'}{d\ln\omega}$.

Isoterm curves of Figure 5.7 were fitted employing the extended Cole-Cole model (Equation 2.24) to take into account the logaritmic graphene contribution and a potential distribution of relaxation times:

$$\chi'(\omega) = \chi_S + (\chi_T - \chi_S)\frac{1 + (\omega\tau)^\beta \cos(\beta\pi/2)}{1 + 2(\omega\tau)^\beta \cos(\beta\pi/2) + (\omega\tau)^{2\beta}} - \Delta\chi_G\ln\omega$$

$$(5.1)$$

$$\chi''(\omega) = (\chi_T - \chi_S)\frac{1 + (\omega\tau)^\beta \sin(\beta\pi/2)}{1 + 2(\omega\tau)^\beta \cos(\beta\pi/2) + (\omega\tau)^{2\beta}} + \frac{\pi}{2}\Delta\chi_G$$

At $T > 0.8$ K, each isotherm of the crystalline Fe_4Py, Figure 5.7a, is well characterized by a single relaxation time τ, affording relaxation time broadening factor β very close to 1 as expected for an ensemble of monodisperse energy barriers. Obviously, no correction for the graphene contribution was used in this case. The relaxation time τ increases exponentially with decreasing T in agreement with thermally-dominated relaxation regime. The T-dependence of the spin relaxation time τ is shown in Figure 5.8.

For temperatures around $T \approx 0.8$ K, β is found to decrease with decreasing T, thus revealing a gradual broadening of the relaxation time distribution. The other fitting parameter χ_T follows the Curie-Weiss law $\chi_T \propto 1/T$, in agreement with spin-lattice relax-

ation, whereas χ_S is approximately independent of T. These conditions mark the crossover temperature region between the thermally-activated relaxation and the quantum spin-tunneling regime, in which *thermally-assisted tunneling* plays an important role, inducing a distribution of *effective* energy barriers (see next Chapter for more details). At lower temperatures $T < 0.8$ K, the relaxation time shows a gradual saturation with decreasing T, with a sudden drop at $T = 0.3$ K, below which it becomes approximately temperature
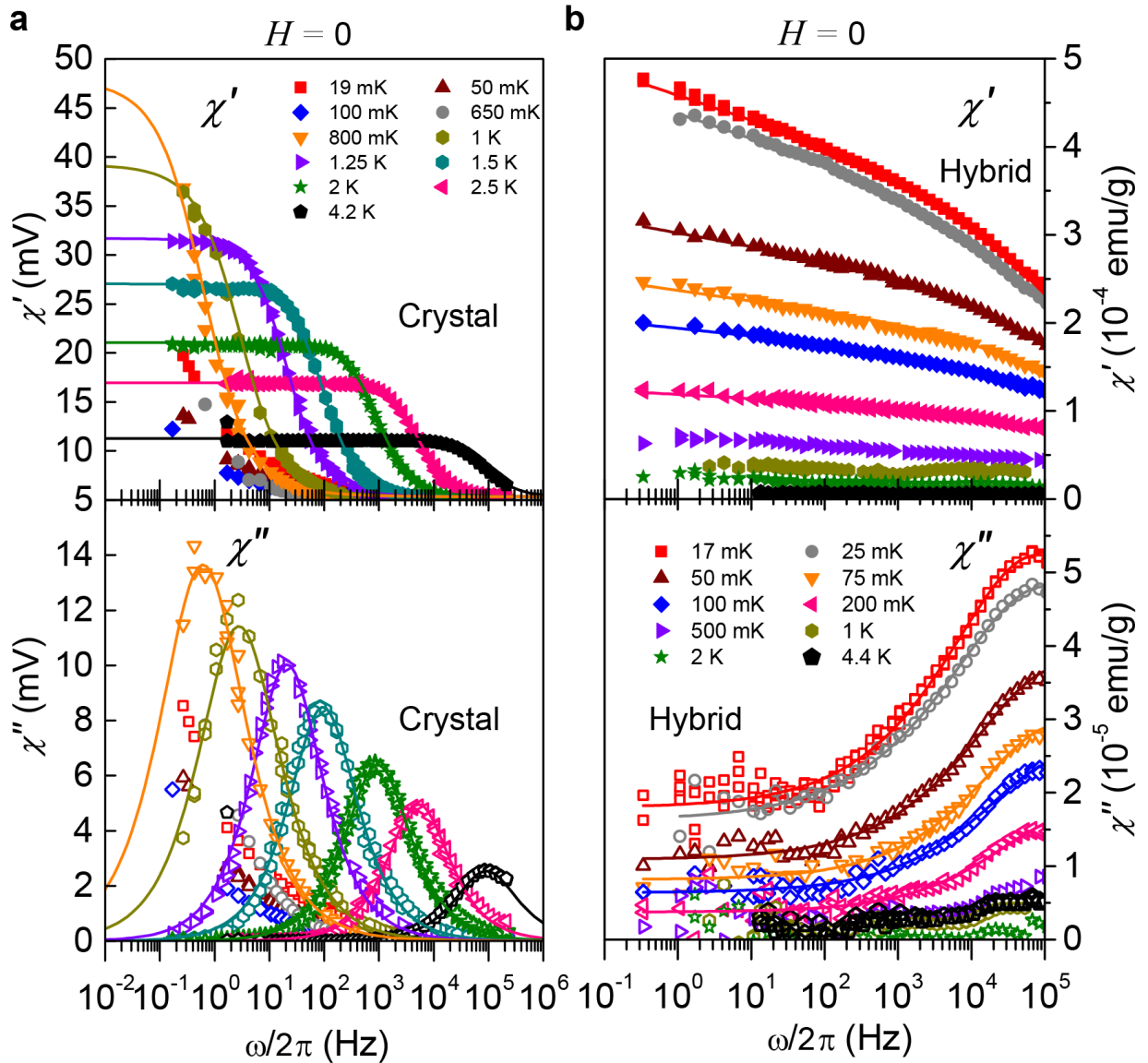

Figure 5.7: Frequency dependence of χ for a) crystalline Fe_4Py and b) isolated molecules on graphene at different temperatures in the QT dominated temperature range. Solid lines are fits a) with the extended Cole-Cole model (Eq. (2.24)) and b) with the extended Cole-Cole model modified to include the graphene contribution (Eq. (5.1)).

independent. The drop in τ vs T takes place near the magnetic ordering temperature, indicated by the additional peak at $T \approx 0.25$ K in Figure 5.6a. It can be attributed to a narrowing of the distribution of local magnetic bias associated with the onset of dipolar long-range magnetic correlations, which enhances the rates of spin tunneling processes. For $T < 0.8$ K, the χ'' maximum lies below the lowest accessible frequency, so τ was derived considering the ratio $r = \frac{\chi''}{\chi'-\chi_S}$ at a fixed frequency, which gives the approximate Cole-Cole relation:

$$\tau \approx \left[\frac{r}{\sin\left(\frac{\beta\pi}{2}\right) - r\cos\left(\frac{\beta\pi}{2}\right)} \right]^{\frac{1}{\beta}} \omega^{-1} \tag{5.2}$$

χ_S was kept equal to its high temperature value above 0.8 K and β was extrapolated using a Boltzmann function (inset Figure 5.8). Equation (5.2), results to be a very good approximation also for higher temperature data, as shown by the light blue crosses in Figure 5.8 for $\omega/2\pi = 1.7$ Hz.
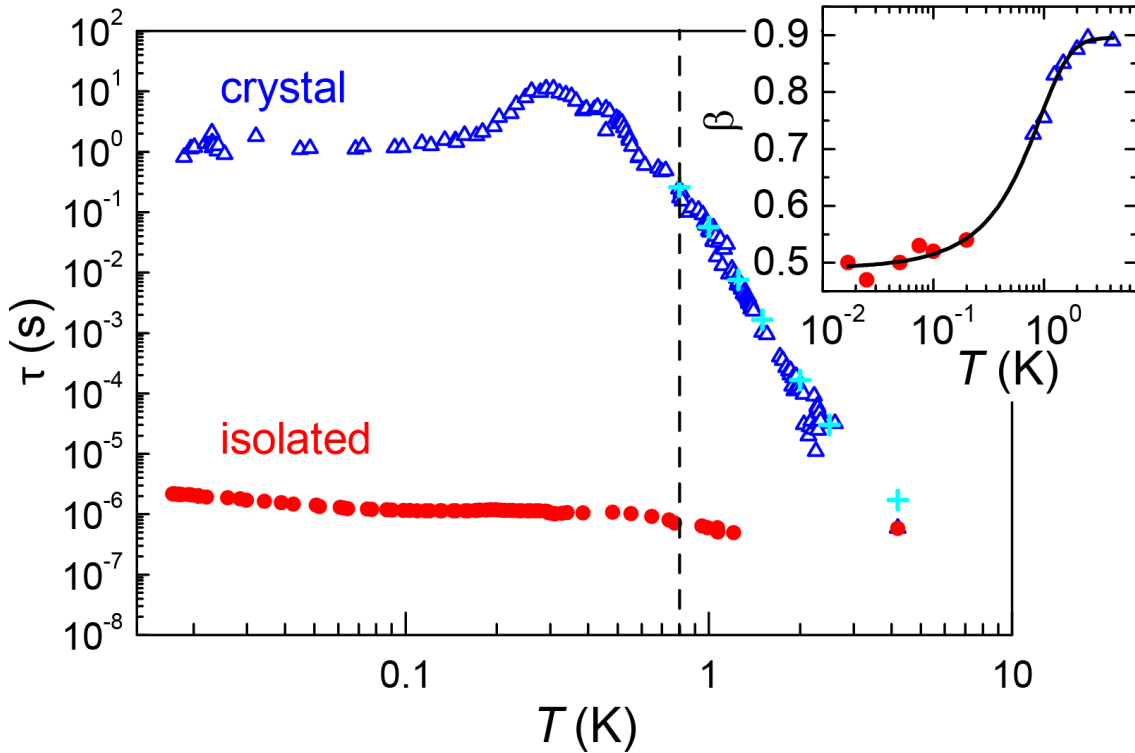
Figure 5.8: Temperature dependence of τ for Fe_4Py crystal (empty symbols) and isolated SMMs on graphene (full symbols). Light blue crosses are points extracted using Equation (5.2) at $\omega/2\pi = 1.7$ Hz, showing the excellent level of approximation. *Inset*: relaxation time broadening factor β afforded by the fit. Black solid line is the Boltzmann function.

Fot the hybrid sample, the quality of the fit employing the correction (5.1) is excellent, Figure 5.7b. The non-zero contribution at low frequencies suggests the presence of another

magnetic contribution characterized by an almost-flat distribution of relaxation times attributed to either a distribution of Fe_4Py small aggregates or more likely from spins embedded in the graphene layer e.g. electrons localized close to defects, or close to single SMMs. Susceptibility data measured below $T \approx 0.2$ K have been fitted by using Equation (5.1) with $\chi_S = 0$, as shown in Figure 5.7b. For $T > 0.2$ K, the χ'' maximum lies above the maximum attainable frequency, so the relaxation time was extracted using Equation (5.2) with $r = \frac{\chi'' - \frac{\pi}{2\Delta\chi_G}}{\chi' + \Delta\chi_G \ln\omega}$ now including the graphene correction $\Delta\chi_G$.

While for crystalline Fe_4Py the thermally-activated region persists down to 800 mK, below which QT sets in, the spin relaxation in the hybrids is fully dominated by QT already below 2K, and at the lowest temperatures the quantum tunneling rate is about one million times higher $\tau \sim 10^6$ s compared to the crystal. Furthermore the relaxation time of the hybrid exhibits a weak dependence on temperature, as τ increases with decreasing T.

5.3 Conclusions

The above observations univocally demonstrate that the spin-dynamics of isolated SMMs is greatly modulated by interaction with graphene. On the one hand, measurements in field, suggest that the classical (thermal) spin relaxation machenism is modulated by the different graphene phononic bath. On the other hand, a strong enhancement of the quantum relaxation at low temperatures suggests a more complex interaction with the graphene environment. To shed light on the nature of such an interaction, a more sophisticated modeling is necessary. This will presented in the next chapter.

Bibliography

[1] Nair, R. R. *et al.* Spin-half paramagnetism in graphene induced by point defects. *Nat Phys* **8**, 199–202 (2012).

[2] Nair, R. R. *et al.* Dual origin of defect magnetism in graphene and its reversible switching by molecular doping. *Nat. Commun.* **4**, 2010 (2013).

[3] Han, W., Kawakami, R. K., Gmitra, M. & Fabian, J. Graphene spintronics. *Nature nanotechnology* **9**, 794–807 (2014).

[4] Pesin, D. & MacDonald, A. H. Spintronics and pseudospintronics in graphene and topological insulators. *Nat. Mater.* **11**, 409–416 (2012). arXiv:1308.3428.

[5] Hueso, L. E. *et al.* Transformation of spin information into large electrical signals using carbon nanotubes. *Nature* **445**, 410–413 (2007).

[6] Laird, E. a., Pei, F. & Kouwenhoven, L. P. A valley-spin qubit in a carbon nanotube. *Nature nanotechnology* **8**, 565–8 (2013). arXiv:1210.3085.

[7] Kuemmeth, F., Ilani, S., Ralph, D. C. & McEuen, P. L. Coupling of spin and orbital motion of electrons in carbon nanotubes. *Nature* **452**, 448–52 (2008).

[8] Miyamachi, T. *et al.* Stabilizing the magnetic moment of single holmium atoms by symmetry. *Nature* **503**, 1–5 (2013).

[9] Warner, M. *et al.* Potential for spin-based information processing in a thin-film molecular semiconductor. *Nature* **503**, 504–508 (2013).

[10] Oberg, J. C. *et al.* Control of single-spin magnetic anisotropy by exchange coupling. *Nature nanotechnology* **9**, 64–8 (2014).

[11] Gatteschi, D. & Sessoli, R. Quantum Tunneling of Magnetization and Related Phenomena in Molecular Materials. *Angewandte Chemie International Edition* **42**, 268–297 (2003).

[12] Gatteschi, D., Sessoli, R. & Villain, J. *Molecular Nanomagnets.* Mesoscopic Physics and Nanotechnology (OUP, Oxford, 2006).

Chapter 6

Development of a theory of magnetic relaxation on graphene

Fundamental questions are still open on how the dynamics of mesoscopic spins is modulated by the interaction with the surroundings (e.g. phonons, neighboring spin, and substrate charge carriers) [1–3]. In particular the question whether spatial confinement plays a role in the spin-phonon coupling [4–8] and in the interaction between spins and charge carriers (e.g. of an underlying substrate) remained so far unanswered [9, 10]. The latter is intimately linked to the appealing opportunity of using graphene massless Dirac particles to manipulate and probe the states of mesoscopic spins and to integrate graphene in future nano-spintronic schemes. An appropriate theoretical modeling of this problem, corroborated by experimental evidence, represents a fundamental step towards the understanding of the dynamics of spins on surfaces, and a rational design of spin-based logic [1, 11] and quantum computing [12–16] architectures.

This Chapter aims at modeling the relaxation time of SMMs under the influence of graphene environment. A new model for the spin-phonon interaction for a two-dimensional phononic dispersion is developed to simulate transition between spin-states induced by graphene phonons. The effect of dipolar and hyperfine interactions, as well as the effect of the graphene charge distribution on the tunneling transition rates is modeled using a perturbative approach. Interaction with graphene charge distribution is found to play a major role in the quantum spin-relaxation at low temperature and by changing the magnitude of the interaction term drives the system through different perturbative tunneling regimes with different level of coherence. Eventually the temperature dependence of the relaxation time τ is simulated and it is found to match very well the experimental data in the broad temperature range here investigated.

6.1 Modelling spin interactions

To model the effect of the environment we consider the effective Hamiltonian:

$$\mathcal{H} = g\mu_{\text{B}}SH + \sum_{i,j} B_i^j \hat{O}_i^j + \mathcal{H}_{sp-ph} + \mathcal{H}_{\text{dip}} + \mathcal{H}_{\text{hyp}} \tag{6.1}$$

where the first term describes the Zeeman interaction between the molecular spin S and the external magnetic field H, the second models the magnetic anisotropy, the third accounts for the interaction between the spin and lattice vibrations, while $\mathcal{H}_{\text{dip}}$ and $\mathcal{H}_{\text{hyp}}$ are the dipolar and hyperfine interactions, respectively. Here, μ_{B} is the Bohr magneton, g is the Landé factor and the $\hat{O}_i^j$ terms are the Stevens' operator equivalents, introduced in Section 2.2.3, each weighted by a coefficient B_i^j.
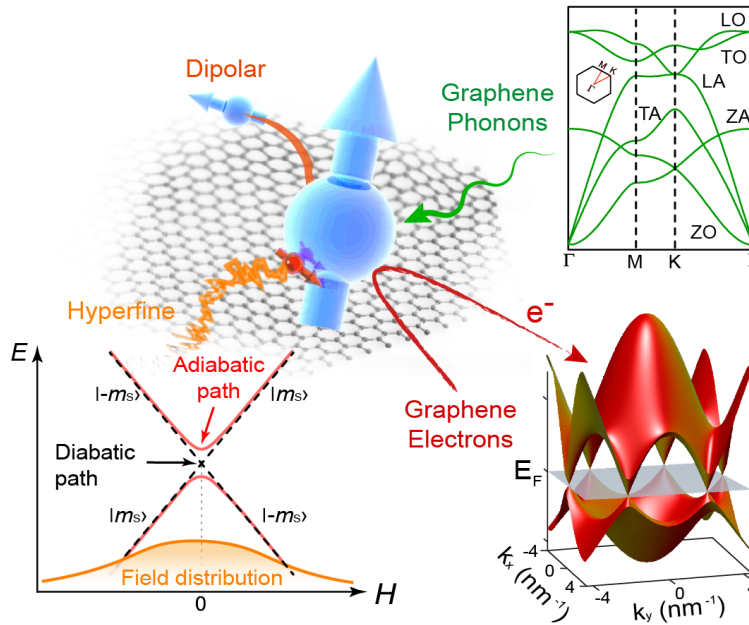

Figure 6.1: Graphical representation of the different environmental interactions acting on the spin in graphene-SMMs hybrids.

The effect of each contribution in Equation (6.1) on the spin dynamics can be studied by treating the relative term perturbatively.

6.2 Dynamics of molecular spins on graphene

As seen in the previous chapter, grafting to graphene alters substantially the dynamics of molecular spins, while leaving the static magnetic response unaltered.
The modulation of the spin dynamics due to different environments can be described using the *master equation approach* introduced in Section 2.2:

$$\frac{d}{dt}N_m(t) = \sum_{m'} \left[W_{m',m}N_{m'}(t) - W_{m,m'}N_m(t) \right] \tag{6.2}$$

that describes how the occupation probability $N_m(t)$ of a spin state $|m\rangle$ evolves in time due to the *combined thermal and tunneling relaxation paths*. As one can see from Equation (6.2), the occupation probability N_m increases in time owing to transitions from all other states $|m'\rangle$ to $|m\rangle$ and decreases owing to transitions from $|m\rangle$ to all the other states $|m'\rangle$. For the Fe$_4$Py system, Equation (6.2) translates into a system of eleven differential equations, one for each spin level $|m\rangle$ with the form:

$$\frac{dN_m}{dt} = -N_m \sum_{m'} W_{m,m'} + \sum_{m'} N_{m'} W_{m',m} + \Gamma_m (N_m - N_{-m}) \tag{6.3}$$

where the first and second sums describe the *phonon-assisted spin transitions from* and *to* a given state $|m\rangle$, that are characterized by the *transition rates* $W_{m,m'}$ and $W_{m',m}$ respectively. The number of terms in each sum is imparted by the specific excitation processes taking place in the system. The third term models the *tunneling transitions* between $|m\rangle$ and $|-m\rangle$ states, that are described by the *tunneling rates* Γ_m.

We base our modeling on a new procedure, substantially different from what reported in previous works [17, 18] and that is found to be more accurate also when applied to the standard 3D case:

1) the theory of spin-phonon interaction is extended to include confinement effects for the case of a *two-dimentional* phonon bath;

2) intrinsic hyperfine interactions and dipolar coupling to neighboring spins are included in the model (6.1) as essential for energy conservation in the tunneling processes at low temperature;

3) the probabilities $W_{m',m}$ of spin transitions assisted by graphene phonons are calculated via the Fermi golden rule;

4) the interaction with the underlying graphene carriers is modeled by altered high order anisotropy terms $B_i^j O_i^j$ in the spin-Hamiltonian (2.9);

5) tunneling frequencies $\omega_T^{m,m'}$ are calculated using perturbation theory;

6) interaction-modulated tunneling rates $\Gamma_{m',m}$ are calculated taking into account the population of spin states due to phonon-assisted transitions. These include tunneling transitions from excited spin levels populated at high temperatures via thermal excitation, and the emission of phonons in the tunneling processes between the lowest lying spin states at low temperature;

7) the occupation probabilities N_m for all the $|m\rangle$ states are calculated via a system of master equations. The relaxation time at different temperatures is finally simulated being it the reciprocal of the smallest non-zero eigenvalue of the system;

6.3   Spin relaxation due to a 2D phonon bath

The goal of this paragraph is the theoretical description of the phonon-assisted transition rates $W_{m,m'}$ due to the graphene lattice vibrations.

The interaction between phonons and molecular spins, has been explored extensively in the literature for the case of 3D phonon baths [19, 20], so as to model the spin relaxation of SMMs in bulk crystals. Here we outline the extension of the existing theoretical background to the case of phonons *confined in two dimensions*, such as the ones in graphene.

Under the effect of lattice vibrations, each molecular group undergoes a superposition of local *rotations* and local *strains*, which produce a time-dependent modulation of the anisotropy and enables transitions between eigenstates $|m\rangle$ of the static Hamiltonian (2.9). The *transition rate $W_{m,m'}$* between any pair of magnetic states $|m\rangle \to |m'\rangle$ is given by the Fermi golden rule summed over all the initial Φ and final Φ' phonon states:

$$W_{m,m'} = \frac{2\pi}{\hbar} \sum_{\Phi} \sum_{\Phi'} |\langle m\Phi|\mathcal{H}_{sp-ph}|m'\Phi'\rangle|^2 \delta(E_{m'} - E_m + \epsilon_{\Phi'} - \epsilon_{\Phi}) \qquad (6.4)$$

$|m\Phi\rangle$ are eigenvectors of the spin *plus* phonons system total Hamiltonian:

$$\mathcal{H} = \mathcal{H}_{\mathrm{sp}} + \mathcal{H}_{\mathrm{ph}} + \mathcal{H}_{sp-ph} \qquad (6.5)$$

where $\mathcal{H}_{\mathrm{sp}}$ is the spin hamiltonian (2.9), $\mathcal{H}_{\mathrm{ph}}$ is the *harmonic phonon hamiltonian*:

$$\mathcal{H}_{\mathrm{ph}} = \sum_{\mathbf{q},\lambda} \hbar\omega_{\mathbf{q},\lambda}(c^{\dagger}_{\mathbf{q},\lambda}c_{\mathbf{q},\lambda} + \frac{1}{2}) \qquad (6.6)$$

and $\mathcal{H}_{sp-ph}$ is the *spin-phonon interaction* term[1].

Compared to the initial state $|m\Phi\rangle$, the final state $|m'\Phi'\rangle$ in (6.4) has one phonon with wavevector $\mathbf{q}$ and wavelength λ more:

$$|\Phi'\rangle = |\Phi + (\mathbf{q},\lambda)\rangle \equiv (1/\sqrt{n_{\mathbf{q},\lambda}+1})c^{+}_{\mathbf{q},\lambda}|\Phi\rangle \quad \text{if} \quad E_m > E_{m'} \qquad (6.9)$$

or one phonon less:

$$|\Phi'\rangle = |\Phi - (\mathbf{q},\lambda)\rangle \equiv (1/\sqrt{n_{\mathbf{q},\lambda}})c_{\mathbf{q},\lambda}|\Phi\rangle \quad \text{if} \quad E_m < E_{m'} \qquad (6.10)$$

depending on the energy difference $E_{m'} - E_m$ between the final and inital magnetic states.

---

[1]In absence of spin-phonon interaction (6.11), the eigenvectors $|m, \Phi\rangle$ would just be the direct product:

$$|m\Phi\rangle = |m\rangle|\Phi\rangle \qquad (6.7)$$

of the eigenvectors $|m\rangle$ of the spin hamiltonian (2.9) and the eigenvectors $|\Phi\rangle$ of the harmonic phonon hamiltonian (6.6), where:

$$\mathcal{H}_{\mathrm{ph}}|\Phi\rangle = \epsilon_{\Phi}|\Phi\rangle \qquad (6.8)$$

The *spin-phonon interaction* [21, 22]:

$$\mathcal{H}_{sp-ph} = i \sum_{\mathbf{q},\lambda} \sqrt{\frac{\hbar}{2m_c\omega_{\mathbf{q},\lambda}}} V_{\mathbf{q},\lambda}(\mathbf{S})(c_{\mathbf{q},\lambda} - c_{\mathbf{q},\lambda}^{\dagger}) \qquad (6.11)$$

enables transitions between two states $|m\Phi\rangle$, $|m'\Phi'\rangle$ differing in m by $\delta m = \pm 1$ or $\delta m = \pm 2$ [20–22] as result of either the absorption or emission of one phonon, Figure 6.2.
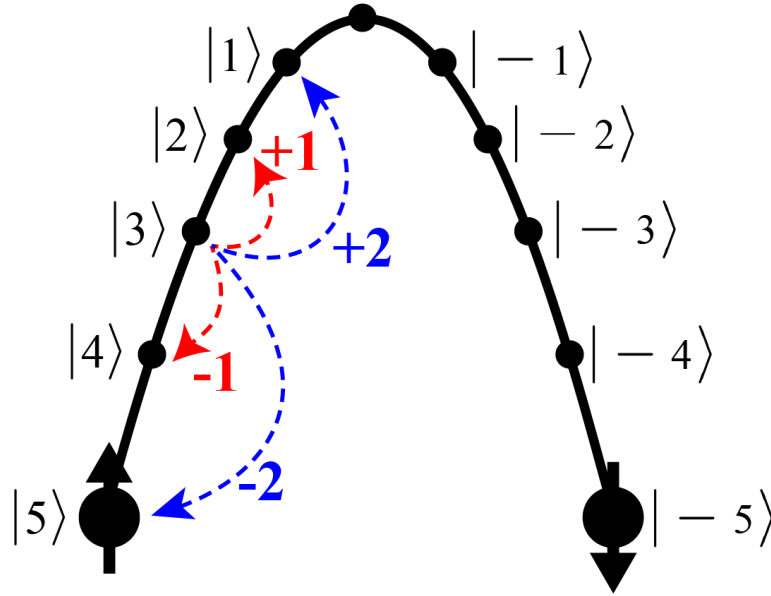

Figure 6.2: Phonon-induced excitation of magnetic states. The spin can climb the anisotropy barrier in $\delta m = \pm 1$ or $\delta m = \pm 2$ steps by absorbing or emitting phonons. Reported in colors are examples of the two possible excitation/relaxation from/to the state $m = +3$.

In (6.11) the sum runs over all the wavevectors $\mathbf{q}$ of the first Brillouin zone; $\omega_{\mathbf{q},\lambda}$ is the phonon dispersion relation of the branch λ; $c_{\mathbf{q},\lambda}$ and $c_{\mathbf{q},\lambda}^{\dagger}$ are the anihilation and creation operators of a phonon with wavevector $\mathbf{q}$ belonging to the branch λ; $\hbar$ is the reduced Planck constant and m_c is the mass of one Fe_4 unit cell.

The *spin-phonon potential* $V_{\mathbf{q},\lambda}(\mathbf{S})$ depends on both the phonon parameters $\mathbf{q}, \lambda$ and the value of the molecular spin $\mathbf{S}$. Its most general form for a trigonal lattice is [21]:

$$\begin{aligned} V_{\mathbf{q},\lambda}(\mathbf{S}) &= [A_1(\mathbf{q},\lambda) + iA_2(\mathbf{q},\lambda)]S_-^2 + [A_1(\mathbf{q},\lambda) - iA_2(\mathbf{q},\lambda)]S_+^2 \\ &= [B_1(\mathbf{q},\lambda) + iB_2(\mathbf{q},\lambda)]\{S_-, S_z\} + [B_1(\mathbf{q},\lambda) - iB_2(\mathbf{q},\lambda)]\{S_-, S_z\} \end{aligned}$$

where $\{,\}$ indicates the anticommutator and:

$$
\begin{aligned}
A_1(\mathbf{q}, \lambda) &= \frac{1}{8}\gamma_2(q_x e_{\mathbf{q},\lambda}^x - q_y e_{\mathbf{q},\lambda}^y) \\
A_2(\mathbf{q}, \lambda) &= \frac{1}{8}\gamma_2(q_x e_{\mathbf{q},\lambda}^y + q_y e_{\mathbf{q},\lambda}^x) \\
B_1(\mathbf{q}, \lambda) &= \frac{1}{8}[(\gamma_3 + \gamma_4)q_x e_{\mathbf{q},\lambda}^z + (\gamma_3 - \gamma_4)q_z e_{\mathbf{q},\lambda}^x] \\
B_2(\mathbf{q}, \lambda) &= \frac{1}{8}[(\gamma_3 + \gamma_4)q_y e_{\mathbf{q},\lambda}^z + (\gamma_3 - \gamma_4)q_z e_{\mathbf{q},\lambda}^y]
\end{aligned}
\tag{6.12}
$$

$e_{\mathbf{q},\lambda}^i$ is the ith cartesian component of the polarization vector associated with the $(\mathbf{q}, \lambda)$ phonon. The γ_m terms are the *magneto-elastic coupling costants* which describes how much a given phonon mode can perturb the molecular spin. γ_2 and γ_3 are associated to lattice strain while γ_4 to lattice rotations.

By substituting (6.11) in (6.4) we have:

$$
W_{m,m'} = \frac{\pi}{m_c}\sum_{\mathbf{q},\lambda}\frac{q^2}{\omega_{\mathbf{q},\lambda}}|\langle m|V_{\mathbf{q},\lambda}|m'\rangle|^2 \cdot
$$

$$
\cdot \left\{ \frac{\delta(E_{m'} - E_m - \hbar\omega_{\mathbf{q},\lambda})}{e^{\frac{\hbar\omega_{\mathbf{q},\lambda}}{k_B T}} - 1} + \frac{\delta(E_{m'} - E_m + \hbar\omega_{\mathbf{q},\lambda})}{1 - e^{-\frac{\hbar\omega_{\mathbf{q},\lambda}}{k_B T}}} \right\}
\tag{6.13}
$$

where T is the absolute temperature and k_B the Boltzmann constant.

6.3.1 Spin-phonon relaxation in 3D crystals

The above expression (6.13) for the transition rates in crystalline three-dimensional materials has already been deduced in literature [19]:

$$
W_{m,m'}^{3D} = \frac{\gamma^2(E_{m'} - E_m)^3}{96\pi\hbar^4\rho c_c^5} \cdot \frac{n(E_{m'} - E_m)}{k_B T} \cdot
$$

$$
\cdot \left\{ |\langle m'|S_-^2|m\rangle|^2 + |\langle m'|S_+^2|m\rangle|^2 + \right.
$$

$$
\left. + 2|\langle m'|\{S_-, S_z\}|m\rangle|^2 + 2|\langle m'|\{S_+, S_z\}|m\rangle|^2 \right\}
\tag{6.14}
$$

where $n = (e^x - 1)^{-1}$ is the Bose factor and c_c is the *sound velocity* in the crystal and ρ is the crystal density.

The contribution:

$$|\langle m'|S_-^2|m\rangle|^2 + |\langle m'|S_+^2|m\rangle|^2 \tag{6.15}$$

accounts for the $\delta m = \pm 2$ transitions, while:

$$2|\langle m'|\{S_-, S_z\}|m\rangle|^2 + 2|\langle m'|\{S_+, S_z\}|m\rangle|^2 \tag{6.16}$$

accounts for $\delta m \pm 1$ transitions.

To simplify the calculation, the phonon dynamics has been approximated to only three acoustic branches with:

$$\omega_{\mathbf{q},\lambda} = cq \tag{6.17}$$

for both longitudinal and transverse modes, so that the sound velocity in the material c is assumed to be independent of the phonon polarization $c = c_{\mathrm{L}} = c_{\mathrm{T}}$. Moreover, since there is no experimental data about the magneto-elastic coupling constants, they are assumed to have the same value $\gamma_2 = \gamma_3 = \gamma_4 = \gamma$. The latter will then be extracted by considering the relaxation time at $T = 4.2$ K and $H = 0$ T.

6.3.2 Spin-phonon relaxation in 2D environments

We now extend the above result to a collection of non-interacting $[\mathrm{Fe}_4(L)_2(dpm)_6]$ SMMs, placed on a two-dimensional graphene surface where the main contribution to the spin-phonon interaction is due to the two-dimensional phononic modes.

By transforming the sum in (6.13):

$$\frac{1}{\mathcal{N}} \sum_{\mathbf{q},\lambda} \quad \rightarrow \quad 2\frac{a^2}{(2\pi)^2} \int d^2q \tag{6.18}$$

and solving the integral we obtain:

$$W_{m,m'}^{\mathrm{2D}} = \frac{\gamma^2(E_{m'} - E_m)^2}{64\hbar^3 \sigma c_{\mathrm{h}}^4} \cdot \frac{n(E_{m'} - E_m)}{k_{\mathrm{B}}T} \cdot$$

$$\cdot \left\{ |\langle m'|S_-^2|m\rangle|^2 + |\langle m'|S_+^2|m\rangle|^2 + \right.$$

$$\left. + 2|\langle m'|\{S_-, S_z\}|m\rangle|^2 + 2|\langle m'|\{S_+, S_z\}|m\rangle|^2 \right\} \tag{6.19}$$

where σ and c_{h} are the speed of sound and the surface density of the two-dimensional hybrid material respectively.

Using Equation (6.19) we can calculate the spin-phonon transition rates $W_{m,m'}^{\mathrm{2D}}$ for each couple of $|m\rangle$, $|m+1\rangle$ and $|m\rangle$, $|m+2\rangle$ states.

It is now important to compare the two $W_{m,m'}$. As a direct result of the different dimensionality of the phononic bath, the formulas for transition rate for the 2D and the 3D case

exhibit different power dependences on c, $\hbar$ and $(E_{m'} - E_m)$. By considering the numerical prefactors only:

$$R^{3D} = \frac{\gamma^2}{96\pi\hbar^4 \rho c_c^5} \tag{6.20}$$

$$R^{2D} = \frac{\gamma^2}{64\hbar^3 \sigma c_h^4} \tag{6.21}$$

we find the relation:

$$\frac{R^{3D}}{R^{2D}} = \frac{2}{3} \frac{\sigma k_B c_h}{\rho\pi\hbar^4 c_c^5} \tag{6.22}$$

which describes the relation between the spin dynamics in the hybrids and in the crystalline form in the thermally-activated regime, where phonons are fundamental for the relaxation of the magnetization.

The quantities ρ, c_c are known as extracted from measurements on crystalline sample by different techniques [23]. The magnitude of the magneto-elastic coupling γ constant is unknown and microscopic derivation of this parameter has never been attempted in the literature. Nevertheless, it is safe to assume that γ remains unaltered since it mainly depends on:

a) the spin-obit coupling of the ions (which remains the same whether the molecules are in crystals or in hybrids);

b) the very local environment of the Fe ions, which transmits the vibrational distortion to the d orbitals (and this latter contribution also remains unvaried, for intact $[Fe_4(L)_2(dpm)_6]$ molecules).

The only unknown parameters in relation (6.22) are then the sound velocity c_h and the density σ of the hybrid material. Since σ is a parameter characteristic of the phononic bath, it is reasonable to assume it equal to the mass-surface ratio of graphene $\sigma = \sigma_{Graphene} = 7.7 \cdot 10^{-9} g/cm^2$ [24, 25].

c_h is the only unknown parameter. If fitting of the experimental data proves the equality:

$$c_h = c_{Graphene} = 2.1 \cdot 10^6 \, cm/s \tag{6.23}$$

then, equation (6.22) would demostrate the applicability of the above model and it would confirm that the dimensionality of the phonon bath has a clear effect on the thermal relaxation of a magnetic system.

6.4 The effect of the graphene phonon bath

Using the above model we can now move to reproduce the behavior of the hybrids for $H \neq 0$, where where the relaxation is expected to be dominated by spin-phonon interaction and QT is suppressed.

For crystalline $[Fe_4(L)_2(dpm)_6]$, EPR [23] and neutron scattering experiments on structurally related systems [18] yielded the following parameters:

$$
\begin{aligned}
B_2^0 &= (-0.136 \pm 0.003) \text{ cm}^{-1} \qquad B_2^2 = (8.1 \pm 0.7) \cdot 10^{-3} \text{ cm}^{-1} \\
B_4^0 &= (2.4 \pm 0.5) \cdot 10^{-5} \text{ cm}^{-1} \qquad B_4^3 < (5 \pm 1) \cdot 10^{-4} \text{ cm}^{-1} \\
g &= 2.000 \pm 0.005
\end{aligned}
$$

Since QT is suppressed, we can consider the dominant B_2^0 uniaxial component only and neglect the high order terms. Moreover we can neglect the presence of a distribution of fields induced by the random orientation of the molecules in a powder sample and the small contributions due to the dipolar and hyperfine couplings (see below).
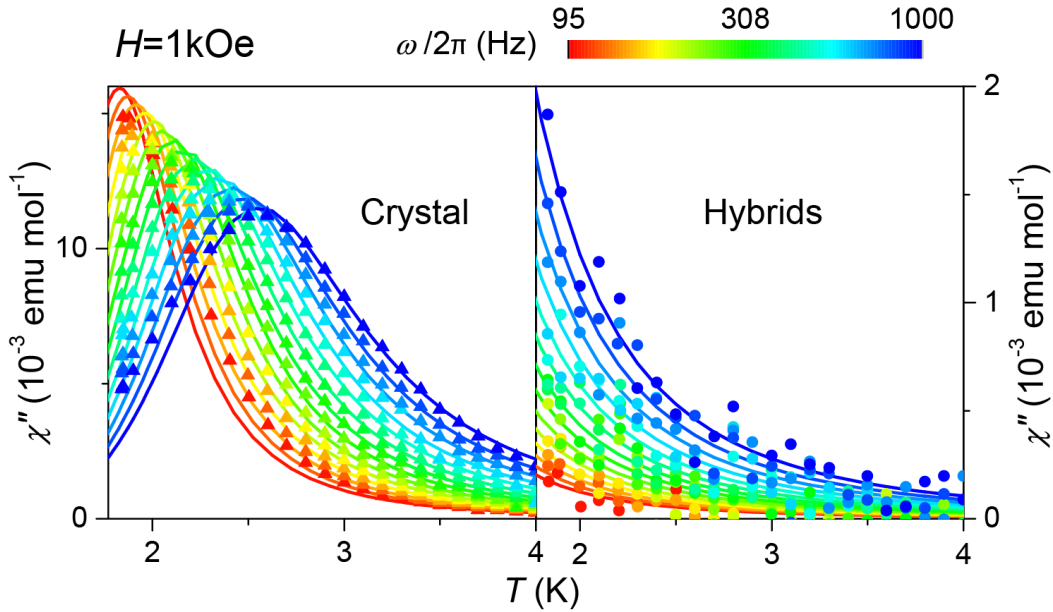

Figure 6.3: Simulated temperature dependence of χ'' for the crystalline Fe_4Py (left) and isolated molecules on graphene (right). Symbols are experimental data while solid lines are simulated curves.

The relaxation time τ is calculated by solving the system of eleven master equations (6.3) where the Γ_m terms are set to zero. The overall τ is given by the smallest eigenvalue of the system. Once τ is known, the temperature-dependence of the ac susceptibility can be calculated using the Cole-Cole equation (2.22), with $\chi_S = 0$.

As shown in Figure 6.3 we can perfectly reproduce the susceptibility curves of the crystals by setting $B_2^0 = -0.12 \pm 0.02$ cm^{-1} and $g = 2.004 \pm 0.003$, and by considering the 3D version of the transition rates $W_{m,m'}^{\text{3D}}$ with the speed of sound $c_c = 2.8 \cdot 10^5$ cm s^{-1} found in literature [26, 27].

It is important to notice that the c_c value extracted from the ac-susceptibility at 4.2 K, is in very good agreement with the literature, stressing the consistency and robustness of the results. (For the details on this procedure see references [17, 18, 28]).

The barrier values extracted from the simulated dynamics provides $B_2^0 = -0.13 \pm 0.01$ cm^{-1}, in agreement with the Arrhenius analysis.

The behavior of the hybrid, is very well reproduced by considering the 2D version of $W_{m,m'}^{\text{2D}}$ (see Equation (6.14)), while mantaining the same B_2^0 value and without introducing any distribution of relaxation times due to other effects. Axial distortions of the Fe$_4$Py on graphene can thus be excluded.

Importantly, an excellent match between simulated and experimental behaviors is achieved by assuming the density σ and the speed of sound c_h of the hybrid sample equal to those of graphene:

$$\sigma = \sigma_{\text{Graphene}} = 7.7 \cdot 10^{-9} g/cm^2$$
$$c_h = c_{\text{Graphene}} = 2.1 \cdot 10^6 \, cm/s$$

We wish to stress here that the above simulations (Figure 6.3) contain no fitting parameters, and only use the EPR coefficients and parameters known from the literature such as, density and speed of sound of graphene and the crystal speed of sound. These observations underscore the relevance of graphene vibrational modes for classical spin relaxation and confirm the effect of the dimensionality of the phonon bath on the thermal relaxation channel of SMMs.

6.5 Magnetic quantum tunneling for Fe$_4$ cluster on graphene

Now that the phononic effects are established, we can move to the behavior of the spins for $H = 0$, where QT is active. Our goal here is to calculate the tunneling transition rates Γ_m taking into account the modulation of the anisotropy induced by the interaction with graphene. To model the quantum relaxation path we consider the following Hamiltonian in the framework of high order perturbation theory:

$$\mathcal{H} = \mathcal{H}_0 + \mathcal{H}_1 \tag{6.24}$$

where the unperturbed Hamiltonian:

$$\mathcal{H}_0 = -AS_z^2 \tag{6.25}$$

contains only the uniaxial anisotropy term $B_2^0/3 = A$ responsible for the energy barrier. The perturbation:

$$\mathcal{H}_1 = \mathcal{H}_1^{(2)} + \mathcal{H}_1^{(3)} \tag{6.26}$$

contains the first two *next-order* terms allowed by the D_3 point group symmetry of the molecule:

$$\mathcal{H}_1^{(2)} = B(\hat{S}_+^2 + \hat{S}_-^2) \tag{6.27}$$

$$\mathcal{H}_1^{(3)} = C[\hat{S}_z(\hat{S}_+^3 + \hat{S}_-^3) + (\hat{S}_+^3 + \hat{S}_-^3)\hat{S}_z] \tag{6.28}$$

where, to simplify the notation, we wrote $B = B_2^2/2$, $C = B_4^3/4$ in the above formulas. At $H = 0$, only resonant tunneling between $|m\rangle$ and $|-m\rangle$ states at the opposite sides of the barrier takes place. $\hbar\omega_{T,m}$, the difference in energy between symmetric and antisymmetric solutions at the level anticrossing, is given by perturbation theory [19, 22]:

$$\omega_{T,m} = \frac{2}{\hbar} \left| \frac{\langle m|\mathcal{H}_1|m+q\rangle}{E_m - E_{m+q}} \frac{\langle m+q|\mathcal{H}_1|m+2q\rangle}{E_{m+q} - E_{m+2q}} \cdots \frac{\langle -m+q|\mathcal{H}_1|-m\rangle}{E_{-m+q} - E_{-m}} \right| \tag{6.29}$$

where the number of terms in the product are imparted by the form of $\mathcal{H}_1$.

6.5.1 Tunneling "selection rules"

As mentioned before, the high order terms in the spin Hamiltonian enable selectively the tunneling processes between certain $|m\rangle$ and $|-m\rangle$ states. The magnitude of the tunneling frequencies is a function of the B_i^j coefficients. The second order anisotropy $\mathcal{H}^{(2)}$ term introduces in Equation (6.29) terms with $q = 2$, thus playing a role in *all* the transitions between levels at the opposite sides of the barrier. On the other hand, the third order anisotropy term $\mathcal{H}^{(3)}$ plays a role in tunneling transitions between spin states for which $q = 3$, thus directly modulating the tunnel frequency $\omega_{T,3}$ only. Nevertheless given the presence of both second and third order terms, combined processes ($q = 2$ plus $q = 3$) have also to be included in the perturbative treatment (Figure 6.4).

As a consequence the third order term $\mathcal{H}^{(3)}$ plays a role in the modulation of the tunnel frequencies $\omega_{T,4}$ and $\omega_{T,5}$ too. Considering the effect of the ladder operators on the $|m\rangle$ levels (Equation (2.12)) the tunneling frequencies are:

$$\omega_{T,1} = \frac{k_B}{\hbar} 60B \tag{6.30}$$

$$\omega_{T,2} = \frac{k_B}{\hbar} 420B^2 \frac{1}{|A|} \tag{6.31}$$

$$\omega_{T,3} = \frac{k_B}{\hbar} 630 \frac{1}{|A|} \left(64C^2 + \frac{B^3}{|A|} \right) \tag{6.32}$$
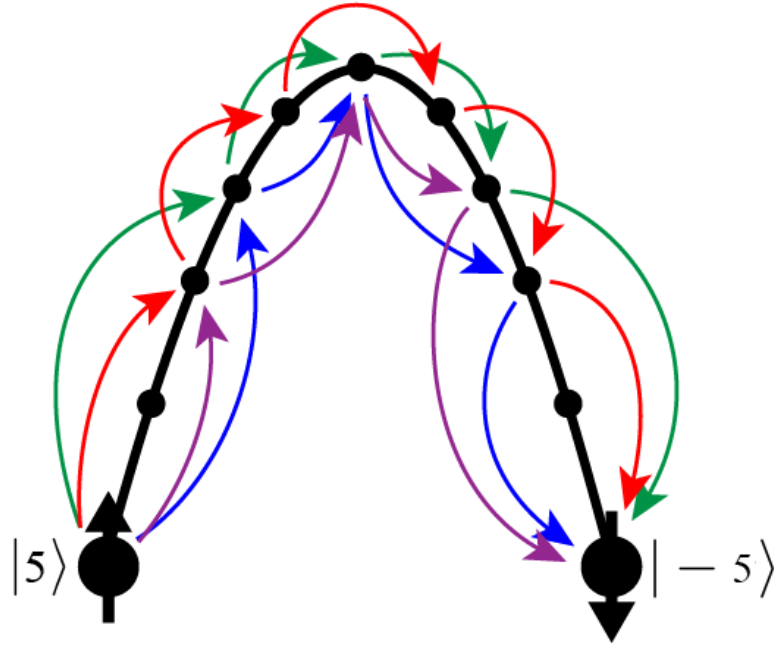
Figure 6.4: Graphical representation of virtual processes due to the $\mathcal{H}^{(2)}$ and $\mathcal{H}^{(3)}$ perturbative terms connecting the $|5\rangle$ and $|-5\rangle$ states and included in Equation (6.29). The tunnel rate $\omega_{\text{T},5}$ is determined by the combination of virtual processes connecting $|m\rangle$ states by steps of 2 (red arrows) and combined "3+2" processes (blue, green and purple arrows). Other combined "3+2" paths are omitted for clarity.

$$\omega_{\text{T},4} = \frac{k_{\text{B}}}{\hbar} 315 \frac{B}{A^2} \left(384 C^2 + \frac{B^3}{|A|} \right) \tag{6.33}$$

$$\omega_{\text{T},5} = \frac{k_{\text{B}}}{\hbar} \left(\frac{1575}{32} \frac{B^5}{A^4} + 66150 \frac{B^2 C^2}{|A|^3} \right) \tag{6.34}$$

We can now proceed with the calculation of the tunneling rates Γ_m. The Γ_m's are functions of the tunnel frequencies $\omega_{\text{T},m}$ and the mean life time τ_m of the of the initial $|m\rangle$ state imparted by the phonon-induced transitions above:

$$\Gamma_m = 4\omega_{\text{T},m}^2 \frac{\tau_m}{1 + \tau_m^2 (E_m - E_{-m})^2/2} \tag{6.35}$$

where:

$$\tau_m = \frac{1}{W_{m,m-1} + W_{m,m-2} + W_{m,m+1} + W_{m,m+2}} \tag{6.36}$$

This treatment implicitly includes combined relaxation paths called *phonon-assisted tunneling* [20, 22, 29], in which the spin, initially in the state $|m\rangle$, makes a transition to the

state $|m\pm1\rangle$ $(|m\pm2\rangle)$ by absorbing a phonon and then tunnels to $|-m\mp1\rangle$ $(|-m\mp2\rangle)$ on the other side of the barrier, Figure 6.5a. Emission of a phonon after the tunneling process is also included, and is of particular importance at low temperature for tunneling between the lowest lying states in presence of hyperfine and dipolar interactions [19], Figure 6.5a.
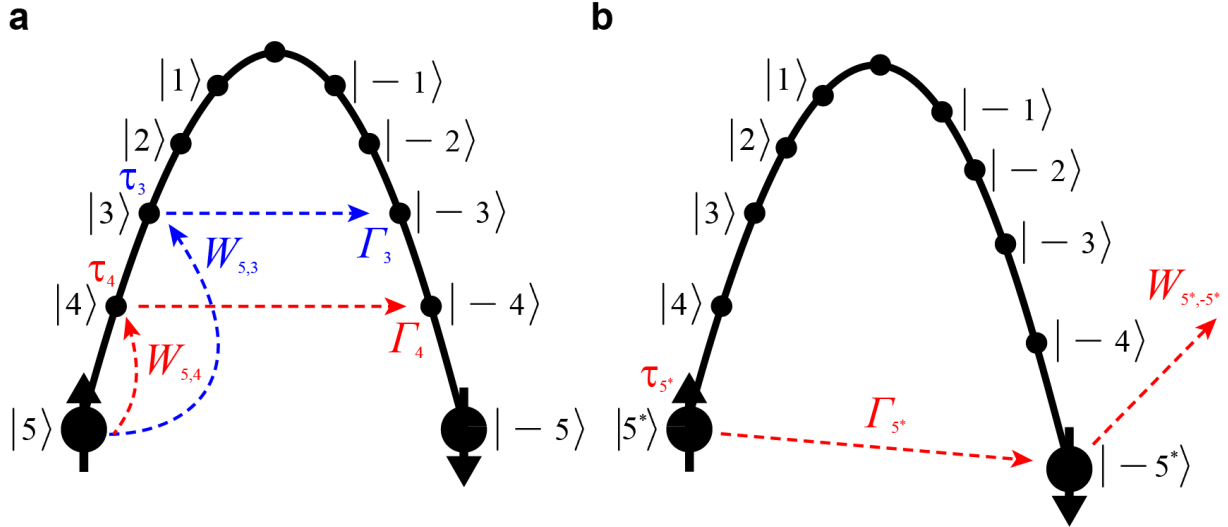

Figure 6.5: a) Phonon-assisted tunneling between excited magnetic states. At sufficiently high temperatures the spin climbs the anisotropy barrier in $\delta m = \pm1$ or $\delta m = \pm2$ steps by absorbing or emitting phonons and then tunnels through it. b) At low temperatures the tunneling process between the lowest-lying ground states is enabled by hyperfine and dipolar interaction. Energy conservation in the spin-flip process requires emission of phonons.

6.6 Effect of dipolar and hyperfine interactions

While the hyperfine interaction couples the (electronic) spin of each core magnetic ion to the spin of its nucleus [19, 22], the long range dipolar interaction is responsible for the coupling between the total spins S of neighboring molecules [22].

6.6.1 Hyperfine coupling

Hyperfine interaction creates an effective fluctuating magnetic field H_{hyp} that broadens the energy span of each $|m\rangle$ level. This relaxes the resonance condition enabling tunneling when the levels are off-resonance by less than the hyperfine energy span. The effect of hyperfine interactions in Fe_4 clusters have been investigated experimentally for crystalline samples [22, 30], and resulted to be relatively weak $H_{hyp} \approx 1$ Oe due to the small isotopic abundance (2.12%) of the spin carrying ^{57}Fe nuclei.

6.6.2 Dipolar interaction: *coherent* and *incoherent* tunneling

The effect of dipolar interaction is to introduce an effective magnetic field H_{dip} that shifts the $|m\rangle$ and $|-m\rangle$ relative to the resonance condition [19, 22]. Because of level mixing, at $H = 0$ the lowest lying states $|5^*\rangle$ and $|-5^*\rangle$ are not pure eigenstates of the uniaxial anisotropy term but are the superpositions:

$$|5^*\rangle = \sum_{i=0}^{10} l_{5,5-i}|5-i\rangle \tag{6.37a}$$

$$|-5^*\rangle = \sum_{i=0}^{10} r_{-5,-5+i}|-5+i\rangle \tag{6.37b}$$

where $r_{m,m'}$ and $l_{m,m'}$ indicate the weights of the different $|m\rangle$ components on the left and right sides of the barrier, while $i = 2$ and 3 is given by the high order anisotropy terms B_2^2 and B_4^3 in the Hamiltonian (6.24) (responsible for the mixing of states such that $|m - m'| = ik$, with k is an integer).

For $H_{dip} = 0$ the weights at the opposite sides are the same $r_{m,m'} = l_{m,m'}$, thus the $|5^*\rangle$, $|-5^*\rangle$ are fully *delocalized* between the two sides of the barrier, favoring tunneling. This represent the ideal case of an isolated spin, whose tunnel motion is characterized by a periodic oscillation between the left- and right-hand sides of the barrier. In this case, the wavefunction describing the spin has a well defined phase (and frequency $\omega_{\mathrm{T},m}$), so the tunneling process is *coherent*.

In real spin systems, such as SMMs in crystals, a dipolar field $H_{dip} \neq 0$ unbalances the weights of the components in the superpositions $|5^*\rangle$ and $|-5^*\rangle$. For intermediate values of H_{dip}, such that $g\mu_\mathrm{B}S_zH_{dip} < \hbar\omega_{\mathrm{T},5}$ the wavefunction is *partially localized* on one side of the barrier, so the spin oscillates between the two wells but is partially trapped in one of the two sides. As consequence the tunneling rate $1/\tau_m$ is reduced and the phase information is lost, leading to *incoherent* tunneling. When the energy shift induced by H_{dip} is larger than the energy associated with the tunnel frequency $g\mu_\mathrm{B}S_zH_{dip} >> \hbar\omega_{\mathrm{T},5}$, the eigenstates $|5^*\rangle$ and $|-5^*\rangle$ are *fully localized* on the two sides of the barrier and tunneling is fully suppressed.

Experimental investigations on pure and diluted Fe_4 clusters proved that the tunneling rate increases on lowering the dipolar interactions [30]. An upper limit of $H_{dip} \approx 200$ Oe was found for the crystal. Moreover in graphene hybrids the graphene layer is predicted to shield effectively the molecular dipolar interactions [31].

6.7 Effect of the B_4^3 term: Villain's coherent tunneling

The standard treatment of the tunneling probabilities is due to Landau, Zener and Stuckelberg [9, 29, 32, 33], and mainly concentrates on the regime where the perturbation introducing the level mixing (modelled by high orders terms in the spin Hamiltonian) is small.

Another regime, predicted by Jacques Villain (see chapter 10 in [22]), considers a situation more challenging to obtain where the perturbation introducing the level mixing is very strong, causing a very significant mixing of the levels albeit still weak enough to be treated perturbatively.
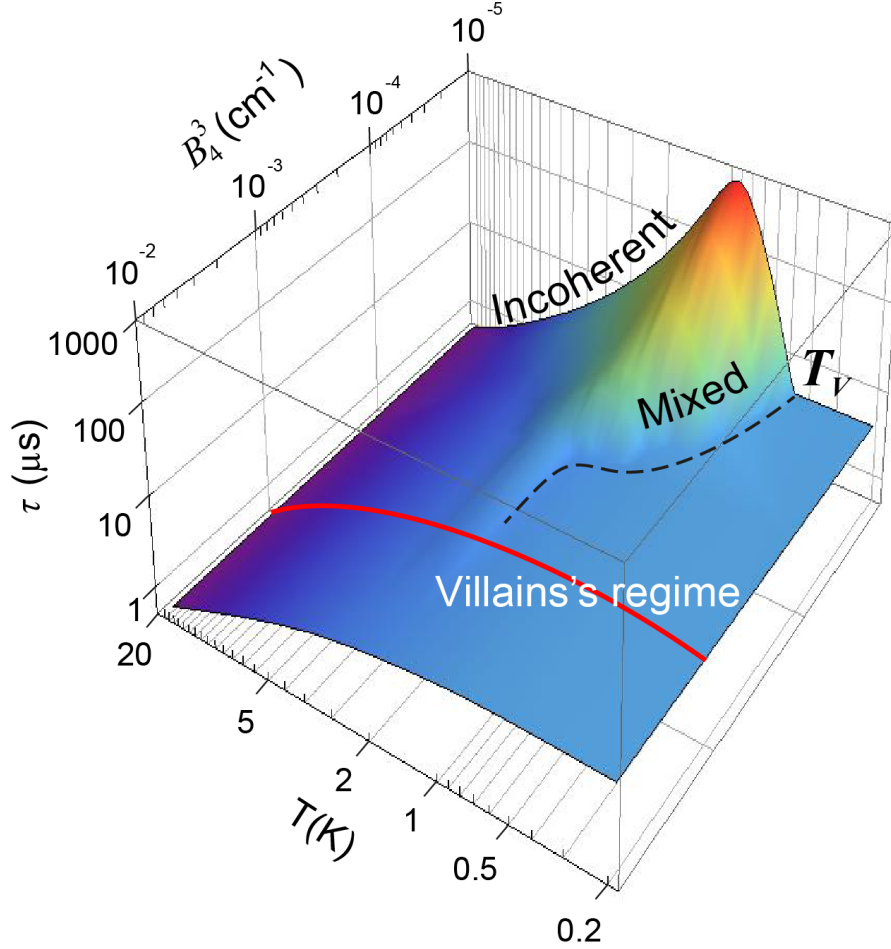

Figure 6.6: Temperature dependence of the relaxation time τ as function of the B_4^3 term. For large values of $B_4^3 > 10^{-3}$ cm^{-1} τ exhibits a smoothly increasing trend as the temperature is decreased. The black dashed line indicates the Villain's threshold.

Figure 6.6 shows the simulated temperature dependence of the relaxation time τ as function of the magnitude of the perturbation term B_4^3. For low perturbations ($B_4^3 < 10^{-4}$ cm^{-1}), τ vs. T shows a pronounced maximum $\tau_{\max}$ (e.g. at $T \approx 0.8$ K for $B_4^3 \approx 10^{-5}$ cm^{-1}) as the temperature is lowered. By further decreasing the temperature, the relaxation time decreases rapidly and becomes temperature independent above a certain threshold temperature T_V called *Villain's threshold* (black dashed line in Figure 6.6). By increasing the magnitude of the perturbation B_4^3, the Villain's threshold shifts towards higher temperatures, together with a gradual reduction of $\tau_{\max}$. For strong perturbations, $B_4^3 > 10^{-3}$ cm^{-1} (red line in Figure 6.6), the peak in τ vs. T disappears and the relaxation time

increases monotonously toward a saturation value of $\tau \approx 4.5$ μs as the temperature decreases. In this perturbation regime the spin relaxes very fast ($\tau \sim 10^{-6}$ s). Above the Villain's threshold τ is independent of B_4^3.

The Villain's threshold is predicted [22] to mark the transition between the incoherent and coherent tunneling regimes. Above the threshold (i.e. at temperatures $> T_V$ or low perturbation values), the tunneling process is largely incoherent, and is strongly affected by phonon absorption and other interactions with the environment. On the contrary, overcoming of the Villain's threshold leads to a *saturated* quantum tunneling regime (the τ stays constant when the perturbation is further increased in magnitude), where the spin tunnels adiabatically through the barrier, oscillating coherently between the two wells.

6.7.1 Effect of graphene on quantum tunneling

For isolated Fe_4Py grafted on graphene we expect the following conditions to be fulfilled:

i) Dipolar interactions are strongly suppressed, and hyperfine interaction is intrinsically low, leading to true degeneracy of the $|m\rangle$ and $|-m\rangle$ levels;

ii) The interaction with the graphene electron density introduces a very significant perturbation that we model via an enhanced B_4^3 term.

The effect of these conditions on the tunneling frequencies $\omega_{T,m}$ can be modeled by making use of Equation (6.29) with the extended spin-Hamiltonian:

$$\mathcal{H}_{sp} = B_2^0 \hat{O}_2^0 + B_4^0 \hat{O}_4^0 + B_2^2 \hat{O}_2^2 + B_4^3 \hat{O}_4^3 + \mathcal{H}_{dip} + \mathcal{H}_{hyp}. \tag{6.38}$$

The relaxation time is then extracted by solving the system of master equations (6.3) with the tunneling rates Γ_m given by (6.35). It is important to remember that in the latter, spin-phonon interaction not only plays an important role for high temperatures, but also for $T \to 0$ as it accounts for emission of phonons imparted by energy conservation in the tunneling process at low temperatures [19].

Figure 6.7 shows the impact of the different interactions on the relaxation time τ and its temperature dependence. As described above, the combined effect of hyperfine coupling and lowered dipolar interaction leads to an appreciable decrease in the relaxation time at low temperatures while it does not have appreciable effects for $T > 0.8$ K. In addition, the different $W_{m,m'}$ due to the 2D graphene phonons lead to a further reduction of τ at low temperatures. Nevertheless, these conditions cannot explain the striking enhancement of QT at $H = 0$, which requires introducing the coupling to graphene electrons. The latter is expressed by the perturbation integral $\langle m|V_I|\Psi_G\rangle$, where molecular and graphene electronic states ($|m\rangle$ and $|\Psi_G\rangle$ respectively) interact via the potential V_I, altering the spin state $|m\rangle$. The wavefunction $|\Psi_G\rangle$ has threefold symmetry, and the corresponding point-group rules permit non-vanishing integral terms only for B_i^j coefficients with j a multiple of 3, independently of the form of V_I. In the perturbation treatment of the spin-graphene interaction, all such terms have an identical effect on the level mixing and the QT rate
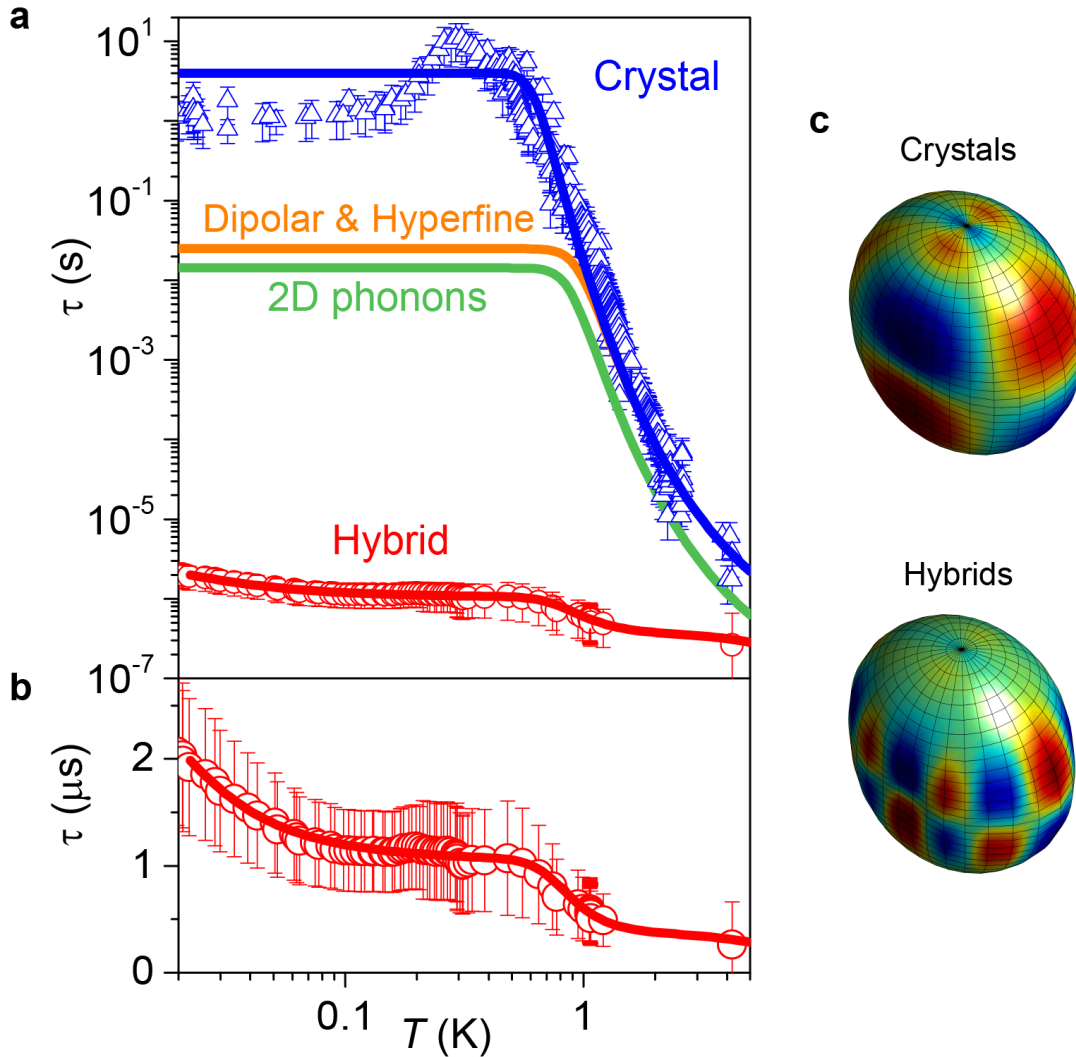
Figure 6.7: Effect of the interaction with graphene on the spin relaxation time. a) Simulated modulation of the spin relaxation time caused by the different interactions with graphene. Solid lines are simulations, while the empty symbols are the experimental data of Figure 5.8. b) Zoom-in of the τ vs. T curve of the hybrids. c) Representation of the total magnetic anisotropy for $[\text{Fe}_4(\text{L})_2(\text{dpm})_6]$ (left) and the graphene-SMMs hybrids (right). To highlight the effect of the B_4^3 term arising from interactions with Dirac electrons the dominant uniaxial anysotropy term B_2^0 is decreased tenfold.

of the lowest $|m\rangle$ levels, differing only in the perturbation order. Accordingly, to address QT, the overall graphene effect can be merged into the leading-order $B_4^3 \hat{O}_4^3$ term, which directly admixes only the $m = \pm 3$ states (direct mixing of lower levels would require lower symmetry terms, such as $B_2^2 \hat{O}_2^2$).
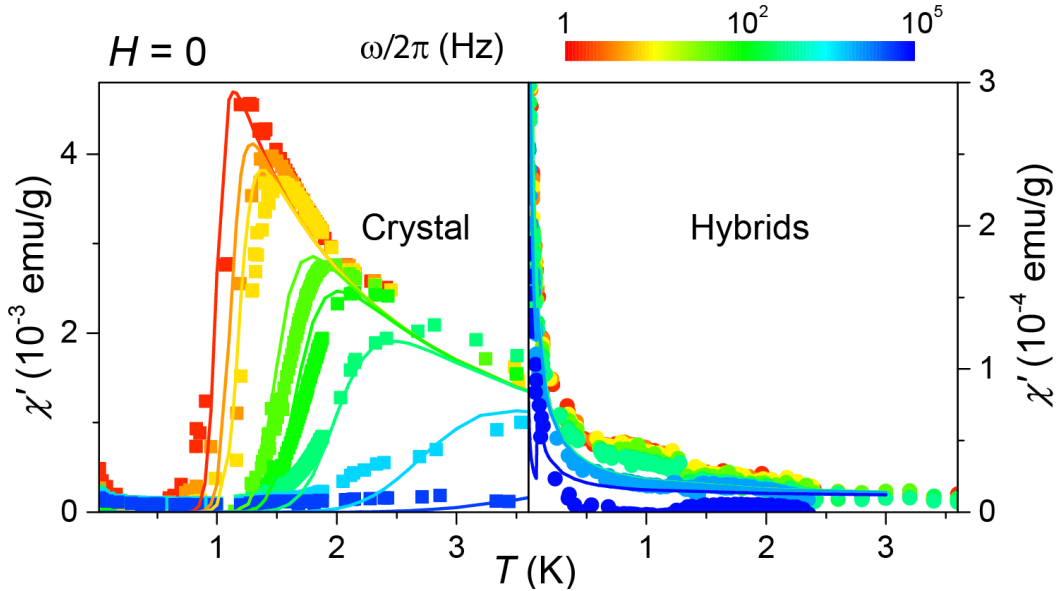

Figure 6.8: Temperature and frequency dependence of the real component of the dynamic susceptibility χ' in $H = 0$ for crystals (top) and isolated Fe_4Py on graphene (bottom). Lines are simulations with the theory.

By introducing a $B_4^3 > 2 \cdot 10^{-3}$ cm^{-1} term into the simulations, while mantaining all other parameters as in the $H \neq 0$ case, both the the ac susceptibility (Figure 6.8) and the T-dependence of τ and are indeed very well reproduced. The pictorial representation of the spin anisotropy in the crystals and hybrids in Figure 6.7c shows the significant weight of the additional $\hat{O}_4^3$ term and highlights the signature of the threefold rotational symmetry of graphene on the spin anisotropy.

The correct operator form of the microscopic interaction potential for V_I is debated. One possibility [34–36] is the Heisenberg form $\hat{\Theta} = (\hat{S}_+\hat{\sigma}_- + \hat{S}_-\hat{\sigma}_+ + 2\hat{S}_z\sigma_z)/2$ where σ_+, σ_-, σ_z, are the spin operators of the Dirac fermion, nevertheless the nature of the underlying scattering processes remains debated. For $[\text{Fe}_4(\text{L})_2(\text{dpm})_6]$ a direct quantitative comparison among the different proposals is intricate, because of the cumbersome *ab initio* evaluation of the amplitude cross-sections. Anyway, spin-flip processes as efficient as those observed are only predicted when scattering due to the presence of two K points is included in the theory [37], and the values here obtained can be used to validate the theoretical models proposed for spin-Dirac fermion interactions.

Strongly-perturbative QT of spins, predicted by Villain decades ago [22], strictly requires pronounced electronic perturbations combined with minimal dipolar interactions. These conditions are hard to fulfil in crystals, and Villains regime has so far eluded observation;

the graphene hybrids offer ideal conditions by simultaneously suppressing dipolar interactions and electronically enhancing the transverse terms. For suppressed dipolar fields, weak perturbations (as in crystals) would lead to a non-monotonic behaviour in the τ vs T plot, where standard tunnelling is followed by a slow descent into Villain's QT regime. In contrast, the B_4^3 perturbation term introduced by graphene is large enough to directly drive the spins into Villain's regime, leading to a monotonous temperature dependence of τ. The associated threshold yields a lower bound of 0.3 eV for the interaction between SMM spins and the Dirac electrons.

6.8 Conclusions

The above observations set the theoretical and experimental basis for the exploration of novel magnetic effects associated with localized spins on graphene. The unraveled vibrational and electronic interactions provide fundamental guidelines for the design of spin-nanomechanical and nanospintronic devices. Strong graphene-induced transverse terms open up possibilities to electrically tune the mixing of spin states, allowing control over quantum tunneling in ways hitherto demonstrated for other qubits [38] The realization of Villain's regime, being it coherent by definition, opens up novel perspectives for quantum operations. Our findings can be extended to the analysis of other spin-substrate system (e.g. SMMs on Au surfaces [39] and NV-centers on graphene [40]), to reveal unique details on symmetry-breaking quantum effects.

Bibliography

[1] Cervetti, C., Heintze, E. & Bogani, L. Interweaving spins with their environment: novel inorganic nanohybrids with controllable magnetic properties. *Dalton transactions* **43**, 4220–32 (2014).

[2] van der Sar, T. *et al.* Decoherence-protected quantum gates for a hybrid solid-state spin register. *Nature* **484**, 82–86 (2012).

[3] de Lange, G., Wang, Z. H., Ristè, D., Dobrovitski, V. V. & Hanson, R. Universal dynamical decoupling of a single solid-state spin from a spin bath. *Science* **330**, 60–63 (2010).

[4] Ganzhorn, M. & Wernsdorfer, W. Molecular Quantum Spintronics Using Single-Molecule Magnets. In Bartolomé, J., Luis, F. & Fernández, J. F. (eds.) *Molecular Magnets Physics and Applications*, chap. 13, 319–364 (Springer, Berlin Heidelberg, 2014).

[5] Garanin, D. A. & Chudnovsky, E. M. Quantum Entanglement of a Tunneling Spin with Mechanical Modes of a Torsional Resonator. *Phys. Rev. X* **1**, 11005 (2011).

[6] Kovalev, A. a., Hayden, L. X., Bauer, G. E. W. & Tserkovnyak, Y. Macrospin tunneling and magnetopolaritons with nanomechanical interference. *Phys. Rev. Lett.* **106**, 1–4 (2011).

[7] Kontos, T. Spintronics meets nanoelectromechanics. *Physics* **4** (2011).

[8] Ganzhorn, M., Klyatskaya, S., Ruben, M. & Wernsdorfer, W. Strong spin-phonon coupling between a single-molecule magnet and a carbon nanotube nanoelectromechanical system. *Nat. Nanotech.* **8**, 165–169 (2013).

[9] Oberg, J. C. *et al.* Control of single-spin magnetic anisotropy by exchange coupling. *Nature nanotechnology* **9**, 64–8 (2014).

[10] Taminiau, T. H. *et al.* Detection and control of individual nuclear spins using a weakly coupled electron spin. *Physical Review Letters* **109**, 1–5 (2012).

[11] Bogani, L. & Wernsdorfer, W. L. Molecular spintronics using single-molecule magnets. *Nat. Mater.* **7**, 179–186 (2008).

[12] Ardavan, A. *et al.* Will Spin-Relaxation Times in Molecular Magnets Permit Quantum Information Processing? *Phys. Rev. Lett.* **98**, 57201 (2007).

[13] Leuenberger, M. N. & Loss, D. Quantum computing in molecular magnets. *Nature* **410**, 789–793 (2001).

[14] Tejada, J., Chudnovsky, E. M., del Barco, E., Hernandez, J. M. & Spiller, T. P. Magnetic qubits as hardware for quantum computers. *Nanotechnology* **12**, 17 (2000).

[15] Hill, S., Edwards, R. S., Aliaga-Alcalde, N. & Christou, G. Quantum coherence in an exchange-coupled dimer of single-molecule magnets. *Science* **302**, 1015–1018 (2003).

[16] DiVincenzo, D. P. Quantum Computation. *Science* **270**, 255–261 (1995).

[17] Rastelli, E. & Tassi, A. Relaxation time of the nanomagnet Fe4. *Phys. Rev. B* **79**, 104415 (2009).

[18] Carretta, S. *et al.* Intra- and inter-multiplet magnetic excitations in a tetrairon(III) molecular cluster. *Phys. Rev. B* **70**, 214403 (2004).

[19] Hartmann-Boutron, F., Politi, P. & Villain, J. Tunneling and magnetic relaxation in mesoscopic molecules. *International Journal of Modern Physics B* **10**, 2577–2638 (1996).

[20] Fort, A., Rettori, A., Villain, J., Gatteschi, D. & Sessoli, R. Mixed quantum-thermal relaxation in Mn12 acetate molecules. *Phys. Rev. Lett.* **80**, 612–615 (1998).

[21] Politi, P., Rettori, A., Hartmann-Boutron, F. & Villain, J. Tunneling in mesoscopic magnetic molecules. *Phys. Rev. Lett.* **75**, 537–540 (1995).

[22] Gatteschi, D., Sessoli, R. & Villain, J. *Molecular Nanomagnets.* Mesoscopic Physics and Nanotechnology (OUP, Oxford, 2006).

[23] Bogani, L. *et al.* Single-molecule-magnet carbon-nanotube hybrids. *Angewandte Chemie - International Edition* **48**, 746–50 (2009).

[24] Bruinsma, R. F., Gennes, P. G. D., Freund, J. B. & Levine, D. Aroute to high surface area, porosity and inclusion of large molecules in crystals. *Nature* **427**, 523–527 (2004).

[25] Stankovich, S. *et al.* Graphene-based composite materials. *Nature* **442**, 282–286 (2006).

[26] Pinto, H. P. & Leszczynski, J. Fundamental Properties of Graphene. In D'Souza, F. & Kadish, K. M. (eds.) *Handbook of Carbon Nano Materials Vol. 5*, chap. 1, 1–37 (World Scientific, New York).

[27] Morozov, S. V. *et al.* Giant intrinsic carrier mobilities in graphene and its bilayer. *Phys. Rev. Lett.* **100**, 16602 (2008).

[28] Rastelli, E. & Tassi, A. Magnetization steps in nanomagnets induced by a time-dependent magnetic field: Application to Fe4. *Phys. Rev. B* **75**, 134414 (2007).

[29] Leuenberger, M. N. & Loss, D. Incoherent Zener tunneling and its application to molecular magnets. *Phys. Rev. B* **61**, 12200–12203 (2000).

[30] Vergnani, L. *et al.* Magnetic bistability of isolated giant-spin centers in a diamagnetic crystalline matrix. *Chemistry - A European Journal* **18**, 3390–3398 (2012).

[31] Koshino, M., Arimura, Y. & Ando, T. Magnetic Field Screening and Mirroring in Graphene. *Phys. Rev. Lett.* **102**, 177203 (2009).

[32] Zener, C. Non-Adiabatic Crossing of Energy Levels. *Proceedings of the Royal Society of London. Series A* **137**, 696–702 (1932).

[33] Landau, L. On the theory of transfer of energy at collisions II. *Phys. Z. Sowjetunion* **2**, 46 (1932).

[34] Miyamachi, T. *et al.* Stabilizing the magnetic moment of single holmium atoms by symmetry. *Nature* **503**, 1–5 (2013).

[35] Fransson, J. Spin inelastic electron tunneling spectroscopy on local spin adsorbed on surface. *Nano Letters* **9**, 2414–2417 (2009).

[36] Hirjibehedin, C. F. *et al.* Large magnetic anisotropy of a single atomic spin embedded in a surface molecular network. *Science* **317**, 1199–1203 (2007).

[37] Trauzettel, B., Bulaev, D., Loss, D. & Burkard, G. Spin qubits in graphene quantum dots. *Nature Physics* **3**, 0–5 (2007).

[38] Yamamoto, M. *et al.* Electrical control of a solid-state flying qubit. *Nature Nanotechnology* **7**, 247–251 (2012).

[39] Mannini, M. *et al.* Quantum tunnelling of the magnetization in a monolayer of oriented single-molecule magnets. *Nature* **468**, 417–421 (2010).

[40] Brenneis, A. *et al.* Ultrafast electronic read-out of diamond NV centers coupled to graphene. *Nat Nano* **10**, 135–139 (2014).

Part II

Spin-relaxation in functionalized graphene devices

Chapter 7

Theory of spin transport in graphene nanodevices

Among the different methods (Figure 7.1) used to induce spin-polarized transport in non-magnetic materials, *electrical spin-injection* is the most viable for spin-electronics [1, 2] (Figure 7.1c).
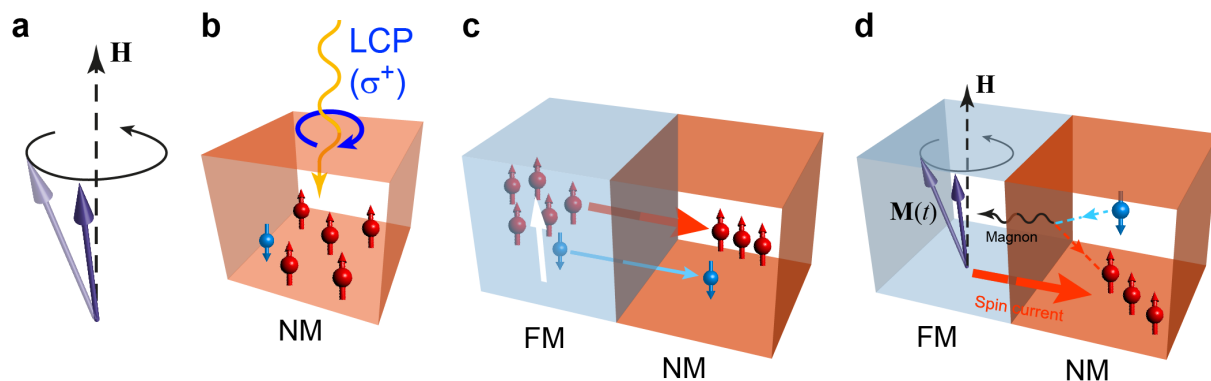

Figure 7.1: Spin-polarization methods. a) Direct polarization by an external magnetic field **H** [3]. b) Optical orientation: circularly-polarized light can orient spins in materials with spin-orbit interaction [4]. c) Electrical spin injection from a ferromagnetic material [1, 2]. d) Spin-pumping by ferromagnetic resonance [5–7].

A typical spin-injection device is composed of a non-magnetic channel (NM) in contact with a ferromagnetic material (FM), i.e. either metallic ferromagnets such as Fe, Ni Co, and their alloy, or magnetic half metals like LSMO or magnetite. Itinerant electrons in these materials naturally exhibit a certain level of spin-polarization. A voltage difference applied to the FM/NM junction thus creates a non-equilibrium imbalance (*spin-accumulation*) of spin-polarized carriers in the non-magnetic material, i.e. a spin polarized current is injected in the channel.

The following sections provide the theoretical framework necessary to model spin-injection

and transport of in a diffusive channel.

7.1 Electrical spin-injection

7.1.1 Spin-split bands

The natural spin-polarization of conduction electrons in a ferromagnet[1] originates from a subtle interplay between exchange interaction and spin-conserving scattering processes [9]. The exchange interaction, that favors parallel alignment of the electronic spins, splits the $3d$ band in two *spin-polarized subbands* shifted in energy by U_{exc} (Stoner criterion) [10]. As a result, the $3d$ up- and down-spins have different density of states (DOS) at the Fermi energy (Figure 7.2):

$$N_\uparrow(E_\mathrm{F}) \neq N_\downarrow(E_\mathrm{F}) \tag{7.1}$$

Although conduction electrons come mostly from the unpolarized $4s$ band [11, 12], $N_\uparrow(E_\mathrm{F})$ of one subband is larger than that of the $4s$ unsplit band, making more probable for a conduction electron to scatter into a final spin-polarized $3d$ state. This results in different number densities, $n_\uparrow \neq n_\downarrow$, for spin-up and spin-down conduction electrons. Another consequence of this is a different scattering rate for spin-up and spin-down electrons, $\tau_{e\uparrow}^{-1} \neq \tau_{e\downarrow}^{-1}$ (i.e. *spin-dependent scattering probability*). Since in typical ferromagnet, the electron scattering rate $\tau_e^{-1} = v_\mathrm{F}/l_e$ is much larger than the *spin-flip scattering rates* $\tau_{\uparrow,\downarrow}^{-1}$, charge carriers conserve their spin orientation over several scattering events, i.e electrons conserve their spin much longer than their momentum [13–15].

7.1.2 Two-spin channels

As a consequence of the spin-split bands, in a ferromagnet an electrical current $J = j_\uparrow + j_\downarrow$ is carried in parallel by two spin-polarized channels, which difference results in a *net spin current*:

$$J_S = j_\uparrow - j_\downarrow \tag{7.2}$$

The FM *polarization efficiency* is given by:

$$\gamma_F = \frac{j_\uparrow - j_\downarrow}{j_\uparrow + j_\downarrow} \tag{7.3}$$

Non-equilibrium carriers diffusion (i.e. electrical current) results from a carrier *density gradient* $\partial n/\partial x$ across the material, and is described by the diffusion equations:

$$j_\uparrow = -eD_\uparrow \frac{\partial n_\uparrow}{\partial x} \tag{7.4a}$$

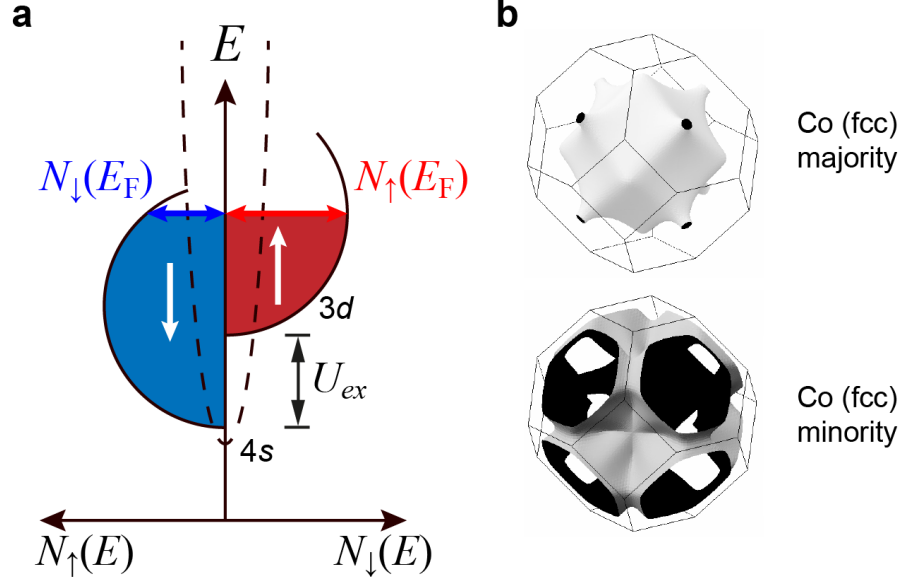[1]The degree of spin polarization γ_F is 45% for Co, 42% for Ni and 37% for Permalloy ($Ni_{80}Fe_{20}$) [8]

Figure 7.2: Cobalt exchange spin-split DOS. a) Schematic rappresentation of the Co spin-split DOS. Solid arrow rappresent densities of states at E_{F}: minority spins (red) have larger DOS at E_{F} than majority (blue) spins [16]. b) Example of spin-projected Fermi surface for fcc Cobalt (*Taken from* [17]).

$$j_{\downarrow} = -eD_{\downarrow}\frac{\partial n_{\downarrow}}{\partial x} \tag{7.4b}$$

where $D_{\downarrow}$ and $D_{\uparrow}$ are the *spin diffusion constants*.

For small deviations from equilibrium (i.e. linear response regime) [18] $\partial n/\partial\mu = N(E_{\mathrm{F}})$ and Equations (7.4) can be written in terms of electrochemical potentials $\mu_{\uparrow,\downarrow}$:

$$j_{\uparrow} = -\frac{\sigma_{\uparrow}}{e}\frac{\partial\mu_{\uparrow}}{\partial x} \tag{7.5a}$$

$$j_{\downarrow} = -\frac{\sigma_{\downarrow}}{e}\frac{\partial\mu_{\downarrow}}{\partial x} \tag{7.5b}$$

where we used the Einstein relations for the spin-dependent conductivities:

$$\sigma_{\uparrow} = e^2 D_{\uparrow} N_{\uparrow} \tag{7.6a}$$

$$\sigma_{\downarrow} = e^2 D_{\downarrow} N_{\downarrow} \tag{7.6b}$$

where $N_{\downarrow}$, $N_{\uparrow}$ are the spin-dependent densisties of states at E_{F} and $D_{\uparrow\downarrow}$ embody the spin-dependent Fermi velocities $v_{\mathrm{F}\uparrow,\downarrow}$ and mean free paths $l_{e\uparrow,\downarrow}$:

$$D_{\uparrow} = \frac{1}{3}v_{\mathrm{F}\uparrow}l_{e\uparrow} \tag{7.7a}$$

$$D_\downarrow = \frac{1}{3} v_{\mathrm{F}\downarrow} l_{e\downarrow} \tag{7.7b}$$

This is the essence of the *two current model* introduced by Mott in 1936 [13] that describes spin-transport in bulk ferromagnets in terms of *two parallel spin-polarized conduction channels*, each characterized by independent bulk conductivities and diffusion characteristics.

7.1.3 Spin-transport and spin-relaxation

By diffusing in the material, carriers will undergo spin-flip scattering events at rates $\tau_{\uparrow,\downarrow}^{-1}$ characteristic of the material. The spin-flip process, called *spin relaxation*, is modelled using the second law of diffusion[2], that in the steady state reads [19, 20]:

$$\frac{1}{e}\frac{\partial j_\uparrow}{\partial x} = -\frac{n_\uparrow}{\tau_\uparrow} + \frac{n_\downarrow}{\tau_\downarrow} \tag{7.8a}$$

$$\frac{1}{e}\frac{\partial j_\downarrow}{\partial x} = -\frac{n_\downarrow}{\tau_\downarrow} + \frac{n_\uparrow}{\tau_\uparrow} \tag{7.8b}$$

and in terms of electrochemical potentials reads:

$$D\frac{\partial^2(\mu_\uparrow - \mu_\downarrow)}{\partial x^2} = \frac{(\mu_\uparrow - \mu_\downarrow)}{\tau_s} \tag{7.9}$$

where D is the averaged spin-diffusion constant:

$$D = \frac{\sigma_\downarrow D_\uparrow + \sigma_\uparrow D_\downarrow}{\sigma_\uparrow + \sigma_\downarrow} \tag{7.10}$$

and τ_s is called *spin relaxation time*:

$$\tau_s^{-1} = \tau_\uparrow^{-1} + \tau_\downarrow^{-1} \tag{7.11}$$

Equation (7.9) show that the difference between the spin-up and spin-down electrochemical potentials $\mu_\uparrow - \mu_\downarrow$ (*spin accumulation* signal), decays exponentially over a *spin diffusion length* λ_s:

$$\lambda_s = \sqrt{D\tau_s} \tag{7.12}$$

meaning that the net spin-density is completely lost after a time τ_s characteristic of the material.

General solutions of Equation (7.9) are:

$$\mu_\uparrow = a + bx + \frac{c}{\sigma_\uparrow}\exp(-x/\lambda_s) + \frac{d}{\sigma_\uparrow}\exp(x/\lambda_s) \tag{7.13a}$$

$$\mu_\downarrow = a + bx - \frac{c}{\sigma_\downarrow}\exp(-x/\lambda_s) - \frac{d}{\sigma_\downarrow}\exp(x/\lambda_s) \tag{7.13b}$$

---

[2]Equations (7.4) and (7.8) are the equivalents of the 1th and 2nd Fick's law of diffusion in fluid dynamics.

7.1.4 Spin-accumulation

Any FM below its Curie temperature can be used in a FM/NM junction to introduce spin-polarized carriers into a NM material, Figure 7.3a-c.

Indeed, continuity of $\mu_{\uparrow,\downarrow}$ and current conservation at the interface induces a finite non-equilibrium spin-accumulation in the NM at the interface region (Figure 7.3d,e). This means that an electrical current flowing across the junction causes the spin-polarized electrochemical potentials to split at the boundary between the two materials (Figure 7.3d,e) [12, 22]

The spin-accumulation at the interface establishes a spin density gradient across NM that causes spins to diffuse in it (*spin-injection*) (Figure 7.3e). The spin accumulation follows Equation (7.9), with $\tau_s = \tau_s^N$ describing an exponential loss of spin polarization over a lengthscale $\lambda_s^N = \sqrt{D_N \tau_s^N}$.

In the ferromagnet the current polarization (7.3) is related to the spin accumulation by [23, 24]:

$$\gamma_F(x) = \frac{2}{J} \frac{\sigma_\uparrow \sigma_\downarrow}{\sigma_F} \frac{\partial(\mu_\uparrow^F - \mu_\downarrow^F)}{\partial x} + \frac{\Delta \sigma_F}{\sigma_F} \tag{7.14}$$

where $\Delta \sigma_F = \sigma_\uparrow - \sigma_\downarrow$, and $\sigma_F = \sigma_\uparrow + \sigma_\downarrow$ is the total conductivity of the FM.

In NM, being $\sigma_\uparrow = \sigma_\downarrow = \sigma_N/2$ and $D_\uparrow = D_\downarrow = D_N$, the current polarization is:

$$\gamma_N(x) = \frac{\sigma_N}{2J} \frac{\partial(\mu_\uparrow^N - \mu_\downarrow^N)}{\partial x} \tag{7.15}$$

Equations for the spin current J_S^F, J_S^N in the two materials can be obtain by just multiply the above equations by J. As discussed in the next paragraph, the *spin-injection* efficiency, i.e. the level of spin-polarization retained by crossing the FM/NM boundary, strongly depends on the properties of the interface.

7.1.5 Conductivity mismatch at the FM/NM interface

We include the properties of the interface into the picture by considering that, similar to equations (7.5), at the interface ($x = 0$) the spin-polarized current components obey the equation [23, 24]:

$$j_\downarrow(0) = \sigma_\downarrow^C \left[\mu_\downarrow^N(0) - \mu_\downarrow^F(0) \right] \tag{7.16a}$$

$$j_\uparrow(0) = \sigma_\uparrow^C \left[\mu_\uparrow^N(0) - \mu_\uparrow^F(0) \right] \tag{7.16b}$$

where to mantain the generality we assumed the interface to have different conductivities $\sigma_\uparrow^C$, $\sigma_\downarrow^C$ for up- and down- spins. The difference in spin accumulation at the interface reads:

$$\left(\mu_\uparrow^N(0) - \mu_\downarrow^N(0)\right) - \left(\mu_\uparrow^F(0) - \mu_\downarrow^F(0)\right) = 2R_C J \left(\gamma - \frac{\Delta \sigma_C}{\sigma_C}\right) \tag{7.17}$$
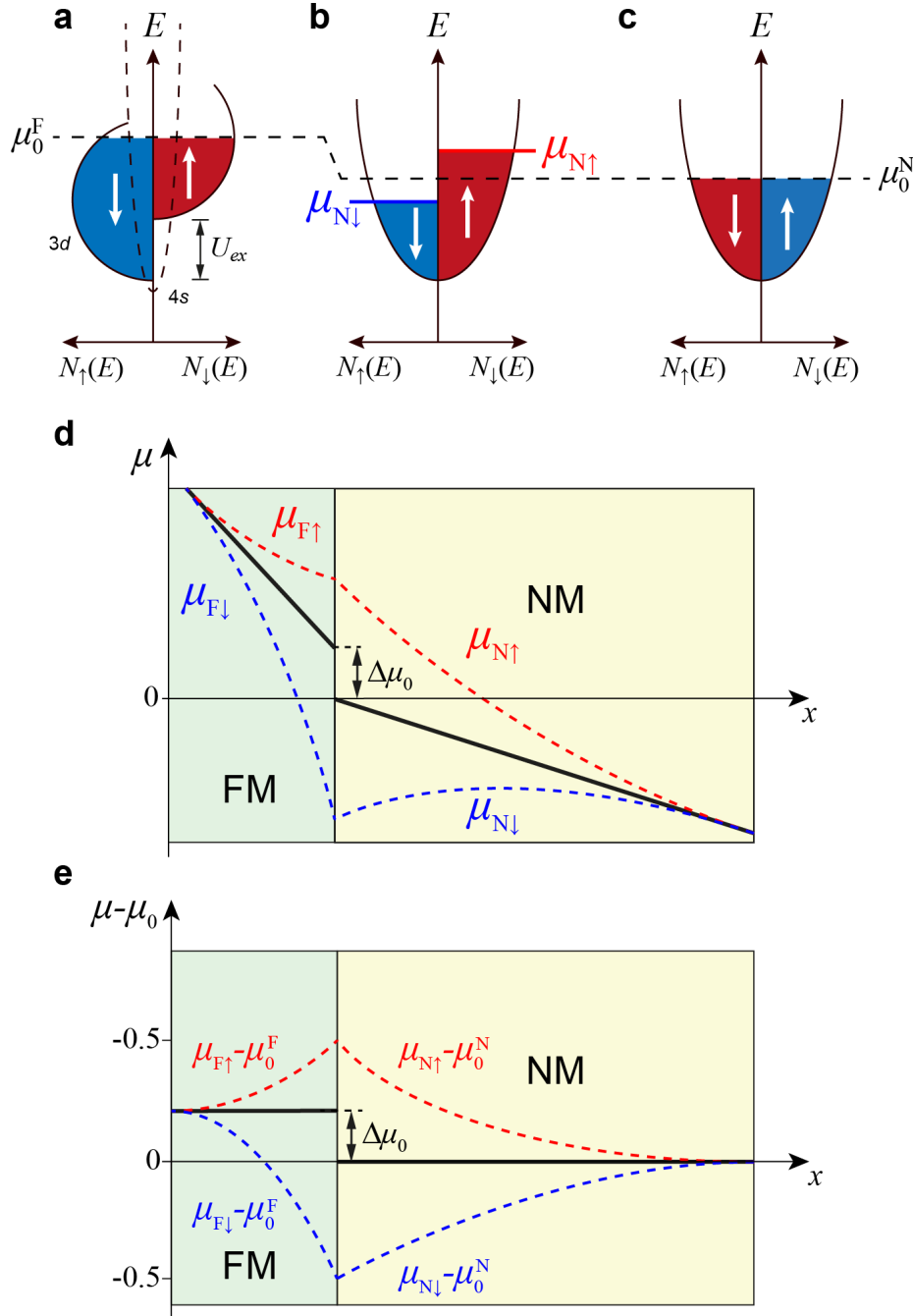
Figure 7.3: Spin-accumulation and injection at the FM/NM interface. A potential difference applied across the FM/NM junction induces a nonequilibrium increase of up-spins at the interface. Being $\sigma_\uparrow = \sigma_\downarrow$, in the NM this nonequilibrium increase must be compensated by an equal decrease in the population of down spins inducing a spin accumulation $(\mu_\uparrow - \mu_\uparrow)$ at the interface (b and d) [21]. To re-establish the equilibrium state of no net spin-polarization (c) the spin diffuses far from the interface (e). Due to spin-flip events spin polarization is completely lost after a distance λ_s and a time τ_s (e) [12].

where the properties of the interface $\Delta\sigma_C = \sigma_\uparrow^C - \sigma_\downarrow^C$, $\sigma_C = \sigma_\uparrow^C + \sigma_\downarrow^C$, $R_C = \sigma_C/4\sigma_\uparrow^C\sigma_\downarrow^C$ may depend on several details such as the FM/NM materials combination and the type of contact used (i.e tunneling, transparent etc..).

The spin polarization at the interface γ_{int} is found by applying the conservation of the spin current at the interface $J_S^F(0) = J_S^N(0)$ (i.e. assuming no spin flip at the interface) [21, 23–25]:

$$\gamma = \left(R_C\frac{\Delta\sigma_C}{\sigma_C} + R_F\frac{\Delta\sigma_F}{\sigma_F}\right)/(R_C + R_F + R_N) \tag{7.18}$$

where $R_F = \dfrac{\lambda_s^F\sigma_F}{4\sigma_\uparrow^F\sigma_\downarrow^F}$, $R_N = \lambda_s^N\sigma_N^{-1}$ are the effective resistances of FM and NM respectively [23].

Equation (7.18) shows that for a transparent ohmic contact (ideally $R_C = 0$), the polarization depends on the ratio R_F/R_N and, being $R_F << R_N$ for the ferromagnet/graphene interface, the current polarization is strongly reduced. This phenomenon is referred to as the *conductivity mismatch* and can be solved by either increasing R_C or by employing tunneling contacts [24].

7.2 Spin-transport in graphene spinvalves

7.2.1 Non-local lateral spin-valve geometry

To study the spin-transport in graphene, we fabricated graphene-based *lateral spinvalves* (SV) combined with a *non-local* measurement configuration (Figure 7.4) [1, 2, 26]. The graphene channel (G) is contacted with four ferromagnetic leads (Figure 7.4a). Spin-polarized carriers are *injected* into G by driving a current from the *injector* contact FM2, which has been previously magnetized to its saturation magnetization $\mathbf{M}_2$ (white arrow in Figure 7.4a), to FM1. Carriers injected into the channel have their spin preferentially aligned along $\mathbf{M}_2$. This produces a non-equilibrium *spin accumulation* in the area underneath FM2 (Figure 7.4b). Because the difference in spin densities at the different sides of the device, spins *diffuse* towards the *detector* contact FM3.

The advantage of a non-local configuration is to separate spin-transport from the charge flow, the latter being confined to the injector circuit area, (dashed line in Figure 7.4a). There is no charge transport happening in the region between FM2 and FM4, where the spin-accumulation signal (i.e. pure spin-current J_S) propagates. This singles out spin-diffusion effects from other phenomena, such as Hall effect, quantum interference [27], magneto-coulomb effect [28–30], or anisotropic magnetoresistance [31], found to obscure or even mimic the spin accumulation signal. Moreover in contrast to the CPP-GMR spinvalves of Chapter 2, the lateral geometry allows the manipulation of the spin information by external means such as electrostatic gates or chemical functionalizations.

The voltage drop V_{NL} between FM3 and FM4 (detection circuit) measures the spin-accumulation at a distance L from the injector. V_{NL} depends on the relative orientation of FM2 and FM3 magnetizations, $\mathbf{M}_2$ and $\mathbf{M}_3$ respectively. When $\mathbf{M}_3$ points in the same direction as $\mathbf{M}_2$, FM3 probes the electrochemical potential $\mu_\uparrow$ of the spin-up electrons (minority subband) (Figure 7.5a,d), giving rise to a positive voltage $V_{\text{NL}} = V_{\text{P}} > 0$. On the other hand, when $\mathbf{M}_3$ is antiparallel to $\mathbf{M}_2$, FM3 probes $\mu_\downarrow$ (majority subband) resulting in a negative $V_{\text{NL}} = V_{\text{AP}} < 0$ (Figure 7.5b,e). This gives rise to a magnetoresistive response characterized two resistance levels R_{P} and R_{AP}, corresponding to different configurations of injector and detector magnetizations (Figure 7.5c).

The resistance difference between parallel and anti-parallel contact configurations ΔR_{NL}, called *spin-signal*, is a characteristic quantity of every spinvalve device. ΔR_{NL} can be estimated by imposing the continuity of the spin-up and spin-down electrochemical potentials $\mu_\uparrow$, $\mu_\downarrow$ and conservation of spin currents $j_\uparrow$, $j_\downarrow$ at the FM/G interface, and by making use of Eqs.(7.13). For parallel magnetizations, the spin accumulation is:

$$\mu_\uparrow - \mu_\downarrow = \frac{2B}{\gamma_F} \tag{7.19}$$

while for anti-parallel configuration:

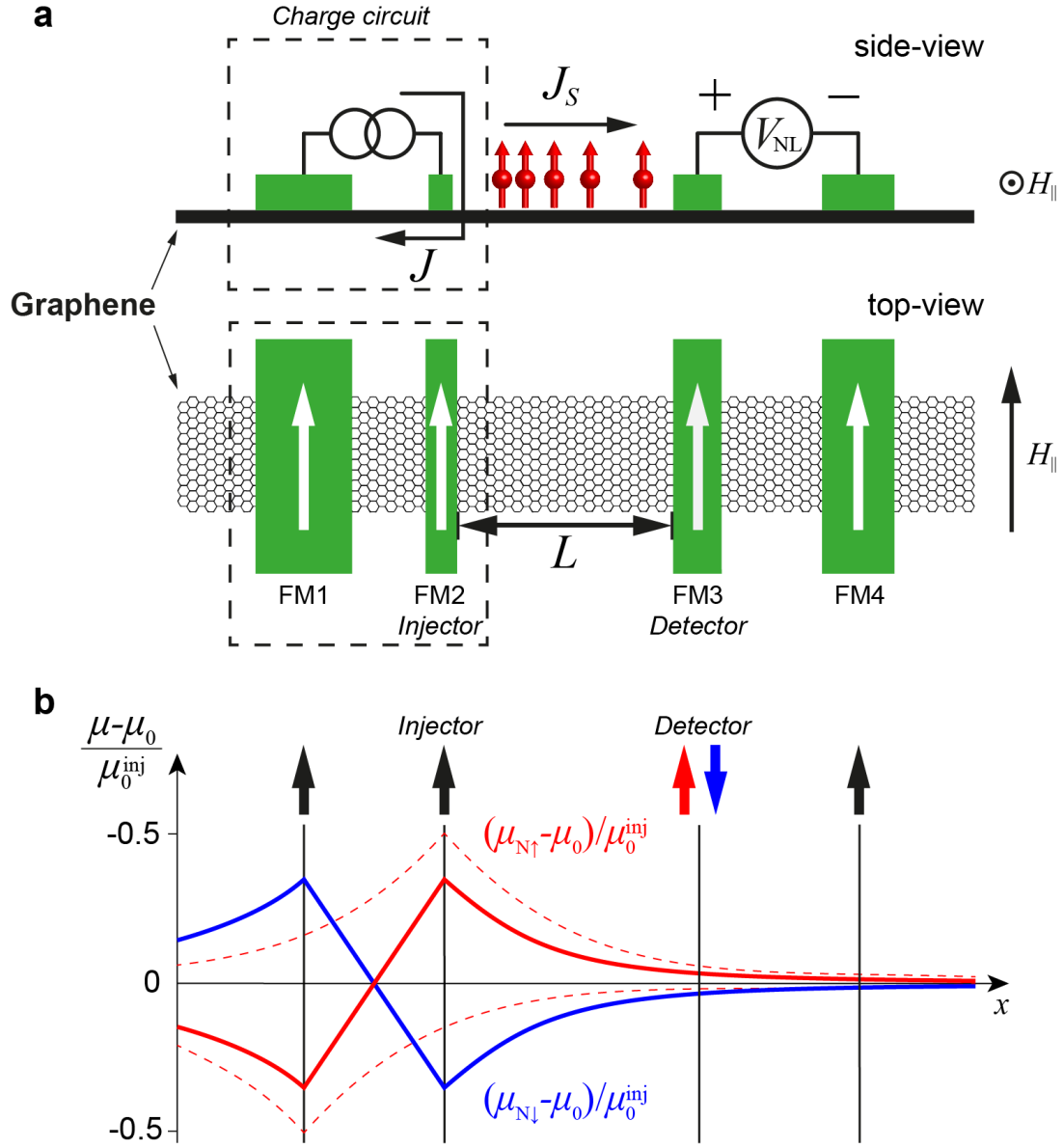$$\mu_\uparrow - \mu_\downarrow = -\frac{2B}{\gamma_F} \tag{7.20}$$

Figure 7.4: Scheme of a graphene-based non local spinvalve in lateral geometry. a) side and top view of the device geometry. The dashed square indicate the circuit section where charge transport takes place. L indicates the distance between injector and detector contacts. b) Evolution of spin-dependent electrochemical potentials [26]. The chemical potentials are normalized by the spin chemical potential at the injection point μ_0^{inj}.
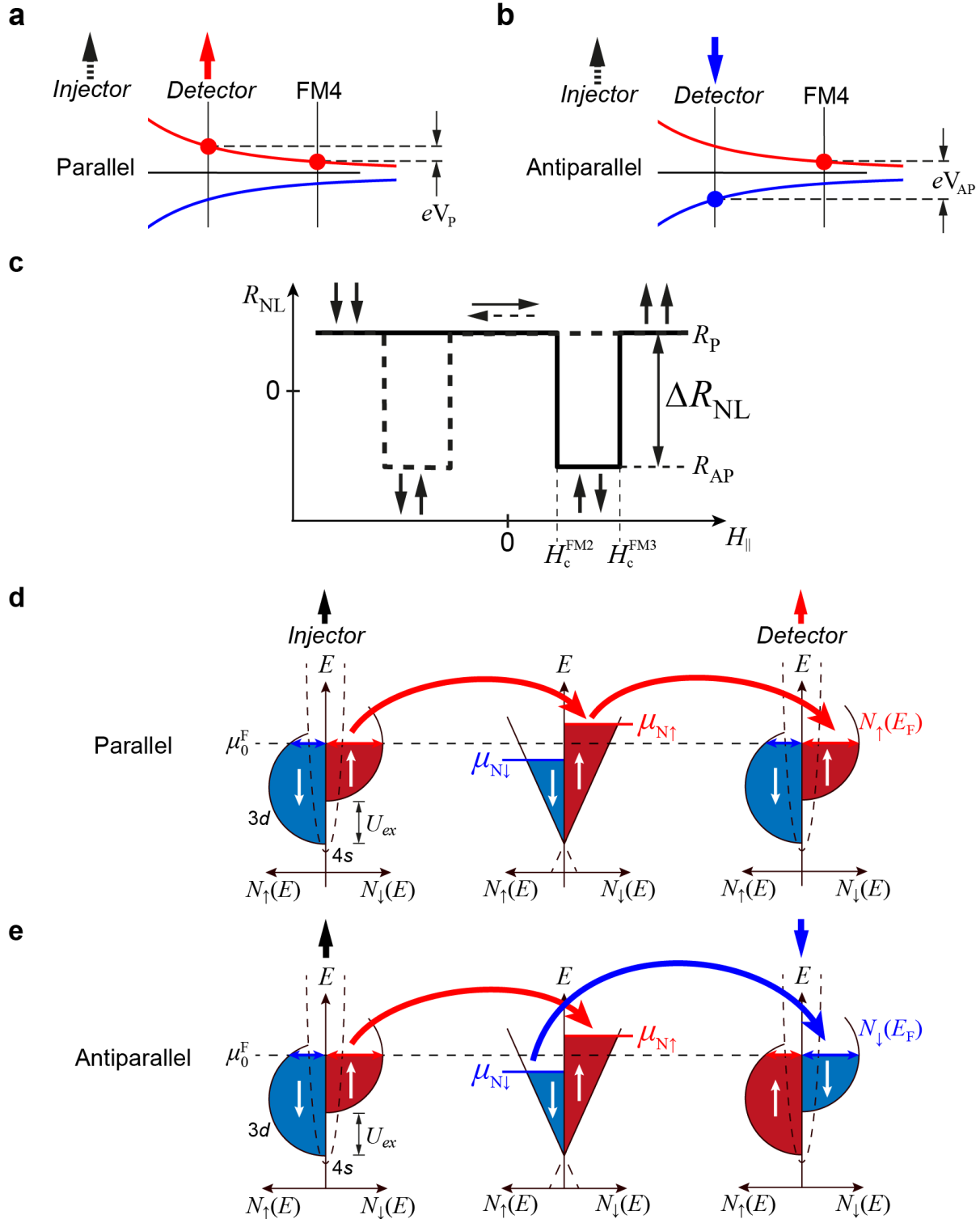
Figure 7.5: Spin-detection for a) parallel and b) anti-parallel configurations. c) Spin-valve behavior, with R_P and R_{AP} resistance levels. a) Spin-dependent DOS for a) parallel and b) antiparallel configurations.

where the prefactor B is:

$$B = Je \frac{\gamma_F^2 \dfrac{\lambda_N}{\sigma_N} \exp^{-L/2\lambda_N}}{2(M+1)\left[M\sinh\left(L/2\lambda_N\right) + \cosh\left(L/2\lambda_N\right)\right]} \qquad (7.21)$$

with:

$$M = \left(\frac{\sigma_F \lambda_N}{\sigma_N \lambda_F}\right)\left(1 - \gamma_F^2\right) \qquad (7.22)$$

The non-local spin-signal ΔR is:

$$\Delta R_{\mathrm{NL}} = \frac{2B}{eJ_S W} = \frac{\gamma_F}{eJ_S W}\Delta\mu \qquad (7.23)$$

Equations (7.23) - (7.22) suggest that, given a certain channel width W and spin-current in the FM J_S, the magnitude of the spin signal R_{NL} depends on the ratio L/λ_N of injector-detector distance and the spin-relaxation length of the channel, on the ratio σ_F/σ_N between the conductivities, and on the ratio λ_N/λ_F between the relaxation lengths of the two materials.

7.2.2 Spin-precession: Hanle measurement

The quantity λ_s characterizing spin-transport in a material, can be determined by means of a *Hanle spin-precession* measurement [26, 32–34]. It consists in preparing the spin valve in the parallel (P) or antiparallel (AP) configuration and then sweeping a magnetic field $H_\perp$ applied perpendicular to the device plane (Figure 7.6).

$H_\perp$ causes the injected spins to precess with frequency $\omega_L = -g\mu_{\mathrm{B}}H_\perp/\hbar$ while diffusing in the channel. The detector electrode detects their projection onto its own magnetization direction, as a consequence, the spin-signal ΔR_{NL} oscillates as function of $H_\perp$. For parallel alignment of injector/detector magnetizations, ΔR_{NL} is maximum at $H_\perp = 0$, it vanishes at fields for which the average spin precession angle is $\phi = \omega_L t = 90°$ and it reaches a minimum when the spins have precessed an average angle of $\phi = \omega_L t = 180°$, resulting in a sign reversal of the spin signal.

In an ideal ballistic 1D conductor, all spin diffuse along the same path and reach the detector electrode at the same time t and with the same precession angle $\phi = \omega_L t$. Accordingly, R_{NL} exhibits a cosine behavior as function of $H_\perp$.

In a diffusive conductor electrons cover different diffusion paths resulting in a spread of the diffusion time t and of the precession angles ϕ at the detector. As a consequence, a damping of the spin signal R_{NL}, which is the average of all contributions of the electron spins over all diffusion times t, occurs. Thus the effect of a perpendicular magnetic field $H_\perp$ is to randomize the spins because spin injected at different time accumulate different ϕ. In addition to the effect of $H_\perp$ spin-flip (spin-relaxation) mechanisms play a role and
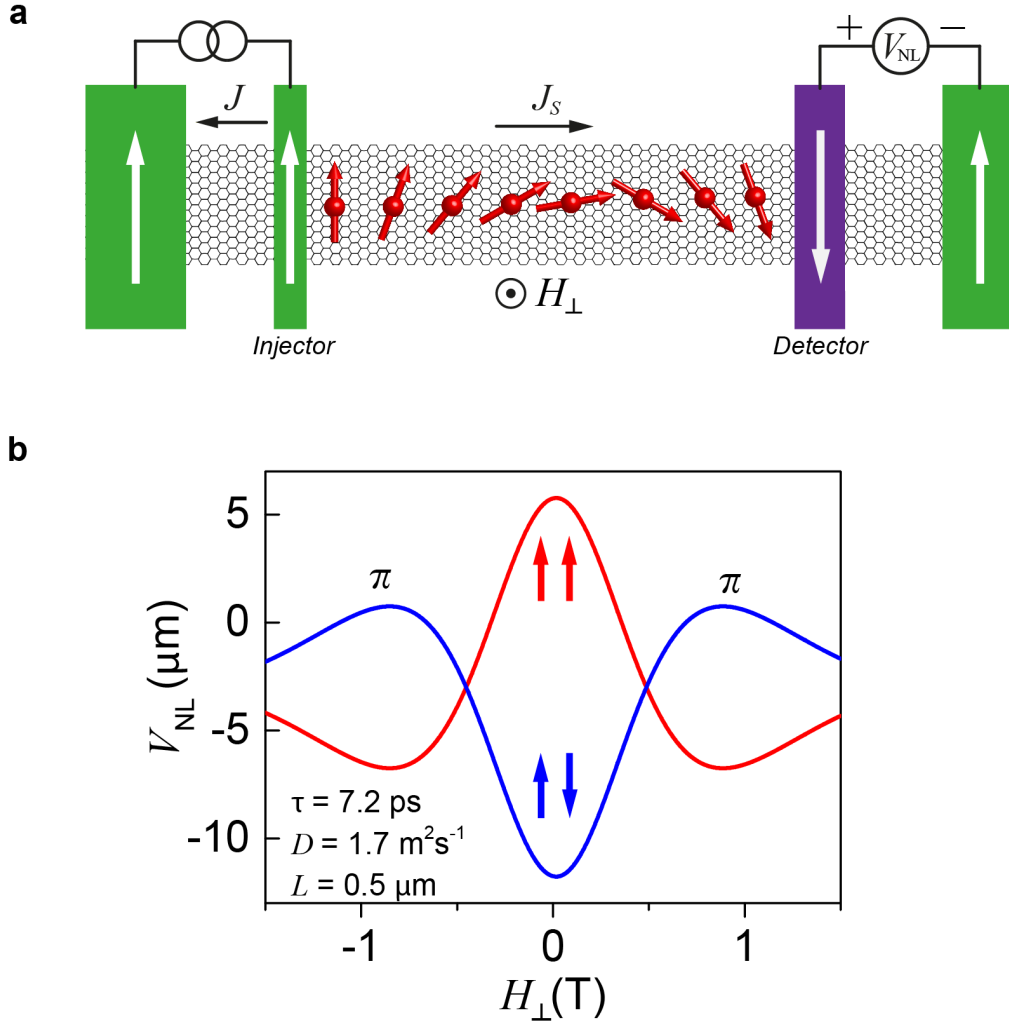
a

b

Figure 7.6: Scheme of a typical spin-precession measurement. a) The external magnetic field $H_\perp$ cause the spins to precess while they diffuse in the graphene channel. b) As a consequence the voltage V_{NL} measured at the detector shows central maximum (minimum) for $H_\perp = 0$ for parallel (antiparallel) configuration of the injector/detector magnetizations. A series of alternating minima and maxima (maxima and minima) occur at $H_\perp$ values at which the precession angle is a multiple of π.

modify the R_{NL} vs. $H_\perp$ curve. The density of spins with their direction parallel to the detector (FM3) magnetization is [20]:

$$n_\uparrow - n_\downarrow = \frac{JP}{eW} \int_0^\infty \varrho(t)\cos(\omega_L t)e^{-t/\tau_s}dt \tag{7.24}$$

where JP/e is the spin-injection rate, $\varrho(t)$ is the distribution of diffusion times, the cosine term models the precession induced by $H_\perp$ while e^{-t/τ_s} is the probability that the electron spin has not flipped after a diffusion time t.

Considering that $\mu_\uparrow - \mu_\downarrow = \frac{2}{N(E_F)} n_\uparrow - n_\downarrow$ and that for a diffusive conductor the distribution of diffusion times at a distance L reads:

$$\varrho(t) = \sqrt{1/4\pi Dt}\, e^{-L^2/4Dt} \tag{7.25}$$

the measured non-local signal V_{NL} for parallel injector/detector configuration is:

$$V_{\mathrm{NL}} = \frac{JP^2}{e^2 W N(E_F)} \int_0^\infty \frac{e^{-L^2/4Dt}}{\sqrt{4\pi Dt}} \cos(\omega_L t) e^{-t/\tau_s} dt \tag{7.26}$$

which analytical solution [20]:

$$V_{\mathrm{NL}} = \frac{JP^2}{e^2 W N(E_F)} Re\left(\frac{1}{2\sqrt{D}} \frac{\exp\left(-L\sqrt{\frac{1}{D\tau_s} - i\frac{\omega_L}{D}}\right)}{\sqrt{\frac{1}{\tau_s} - i\omega_L}} \right) \tag{7.27}$$

can be used to fit the Hanle curve.

Bibliography

[1] Johnson, M. & Silsbee, R. H. Coupling of electronic charge and spin at a ferromagnetic-paramagnetic metal interface. *Physical Review B* **37**, 5312–5325 (1988).

[2] Jedema, F. J., Filip, A. T. & van Wees, B. J. Electrical spin injection and accumulation at room temperature in an all-metal mesoscopic spin valve. *Nature* **410**, 345–348 (2001).

[3] A. Abragam, B. B. *Electron paramagnetic resonance of transition ions* (Dover Publications Inc., New York, 1986).

[4] Fiederling, R. *et al.* Injection and detection of a spin-polarized current in a light-emitting diode. *Nature* **402**, 787–790 (1999).

[5] Žutić, I. & Dery, H. Spintronics: Taming spin currents. *Nature materials* **10**, 647–8 (2011).

[6] Ando, K. *et al.* Electrically tunable spin injector free from the impedance mismatch problem. *Nature Materials* **10**, 655–659 (2011).

[7] Kurebayashi, H. *et al.* Controlled enhancement of spin-current emission by three-magnon splitting. *Nat Mater* **10**, 660–664 (2011).

[8] Coey, J. Materials for Spin Electronics. In *Spin electronics*, chap. 12, 277–297 (2001).

[9] Chappert, C., Fert, A., Van Dau, F. N. & Dau, F. V. The emergence of spin electronics in data storage. *Nature materials* **3**, 1–36 (2007).

[10] Kashyap, A., Sabirianov, R. & Jaswal, S. S. Spin-Polarized Electronic Structure. In *Advanced Magnetic Nanostructures*, chap. 2, 13–39 (2006).

[11] Stearns, M. B. Simple explanation of tunneling spin-polarization of Fe, Co, Ni and its alloys. *Journal of Magnetism and Magnetic Materials* **5**, 167–171 (1977).

[12] Johnson, M. Spin Injection, Accumulation, and Relaxation in Metals. In *Handbook of Spin Transport and Magnetism*, vol. 30, 115–136 (2011).

[13] Mott, N. F. The electrical conductivity of transition metals. *Proceedings of the Royal Society of London. Series A, Mathematical and Physical Sciences* **153**, 699–717 (1936).

[14] Fert, A. & Campbell, I. A. Two-current conduction in nickel. *Phys. Rev. Lett.* **21**, 1190–1192 (1968).

[15] Fert, A. & Campbell, I. A. Electrical resistivity of ferromagnetic nickel and iron based alloys. *Journal of Physics F: Metal Physics* **6**, 849 (1976).

[16] Johnson, M. *Magnetoelectronics* (Elsevier Academic Press, 2004).

[17] Lehmann, C., Sinning, S., P. Zahn, H. & Wonn, I. M. http://www.physik.tu-dresden.de/˜fermisur.

[18] Datta, S. *Electronic Transport in Mesoscopic Systems* (Cambridge University Press, 1997).

[19] Jedema, F., Nijboer, M., Filip, a. & van Wees, B. Spin injection and spin accumulation in all-metal mesoscopic spin valves. *Physical Review B* **67**, 085319 (2003).

[20] Jedema, F. *Electrical spin injection in metallic mesoscopic spin valves*. Ph.D. thesis, University of Groningen (2002). URL `http://irs.ub.rug.nl/ppn/244584443`.

[21] van Son, P. C., van Kempen, H., Wyder, P., Son, P. V. & Kempen, H. V. Boundary Resistance of the Ferromagnetic-Nonferromagnetic Metal Interface. *Physical review letters* **58**, 2271–2273 (1987).

[22] Johnson, M. *Spin Injection*, vol. 157, 279–307 (Springer Berlin Heidelberg, 2008).

[23] Rashba, E. I. Diffusion theory of spin injection through resistive contacts. *European Physical Journal B* **29**, 513–527 (2002).

[24] Rashba, E. I. Theory of electrical spin injection: Tunnel contacts as a solution of the conductivity mismatch problem. *Phys. Rev. B* **62**, 16267–16270 (2000).

[25] Son, P. V., van Kempen, H. & Wyder, P. van Son, van Kempen, and Wyder reply. *Physical review letters* **65**, 1988 (1988).

[26] Tombros, N. *et al.* Electronic spin transport and spin precession in single graphene layers at room temperature. *Nature* **448**, 571–574 (2007).

[27] Man, H. T. & Morpurgo, a. F. Sample-specific and ensemble-averaged magnetoconductance of individual single-wall carbon nanotubes. *Physical Review Letters* **95**, 6–9 (2005). arXiv:0411141.

[28] Ono, K., Shimada, H. & Ootuka, Y. Enhanced Magnetic Valve Effect and Magneto-Coulomb Oscillations in Ferromagnetic Single Electron Transistor (1997).

[29] Shimada, H., Ono, K. & Ootuka, Y. Driving the single-electron device with a magnetic field (invited). *Journal of Applied Physics* **93**, 8259–8264 (2003).

[30] van der Molen, S. J., Tombros, N. & van Wees, B. J. Magneto-Coulomb effect in spin-valve devices. *Phys. Rev. B* **73**, 220406 (2006).

[31] Jedema, F. J., Nijboer, M. S., Filip, a. T. & van Wees, B. J. Spin injection and spin accumulation in permalloy-copper mesoscopic spin valves. *Journal of Superconductivity* **15**, 8 (2001).

[32] Jedema, F. J. *et al.* Electrical detection of spin precession in a metallic mesoscopic spin valve. *Nature* **416**, 713–716 (2002).

[33] Johnson, M. & Silsbee, R. H. Interfacial charge-spin coupling: Injection and detection of spin magnetization in metals. *Physical review letters* **55**, 1790–1793 (1985).

[34] Johnson, M. & Silsbee, R. H. Spin-injection experiment. *Physical Review B* **37**, 5326–5335 (1988).

Chapter 8

Fabrication of graphene-based devices

This chapter is devoted to the techniques used for the fabrication of graphene nanodevices.

8.1 Electron beam lithography

Electron beam (ebeam) lithography is an important microfabrication technique, that allows creating structures with lateral size down to 30 nm routinely. The creation of structures with size below this limit is still possible but requires special efforts.
It is based on the chemical modification of PMMA-based resists[1], induced by irradiation with electrons. Upon electron irradiation, the resist polymer chains break and the exposed resist becomes more soluble and thus easily removable. The *sensitivity* to electron irradiation (i.e the minimum electron dose required to chemically modify the resist through the whole film thickness) depends on the polymer chain length and the film thickness. PMMA is available [1] in different lengths: short (50K), long (950K) and intermediate (200K, 600K), and different dilutions in organic solvents (e.g. chlorobenzene). The 50K PMMA possesses approximately 20% higher sensitivity as compared to the 950K polymer [1]. Figure 8.1 shows the different steps constituting the usual fabrication procedure.

8.1.1 Spin-coating

Homogeneous resist films of predefined thickness in the sub-μm range are created on top of the desired substrate by spin-coating, Figure 8.1(1). The thickness of the film is determined by the PMMA concentration and the spinning speed, which are chosen according to previous calibration (e.g. 950K PMMA spun at 3000 rpm for 5s followed by 30s at 8000 rpm produces a film of thickness of about $\sim$60 nm). After spin-coating, the sample is backed at 160 °C for 1 hour in an oven evacuated with Argon gas.

---

[1]PMMA=Polymethylmethacrylate
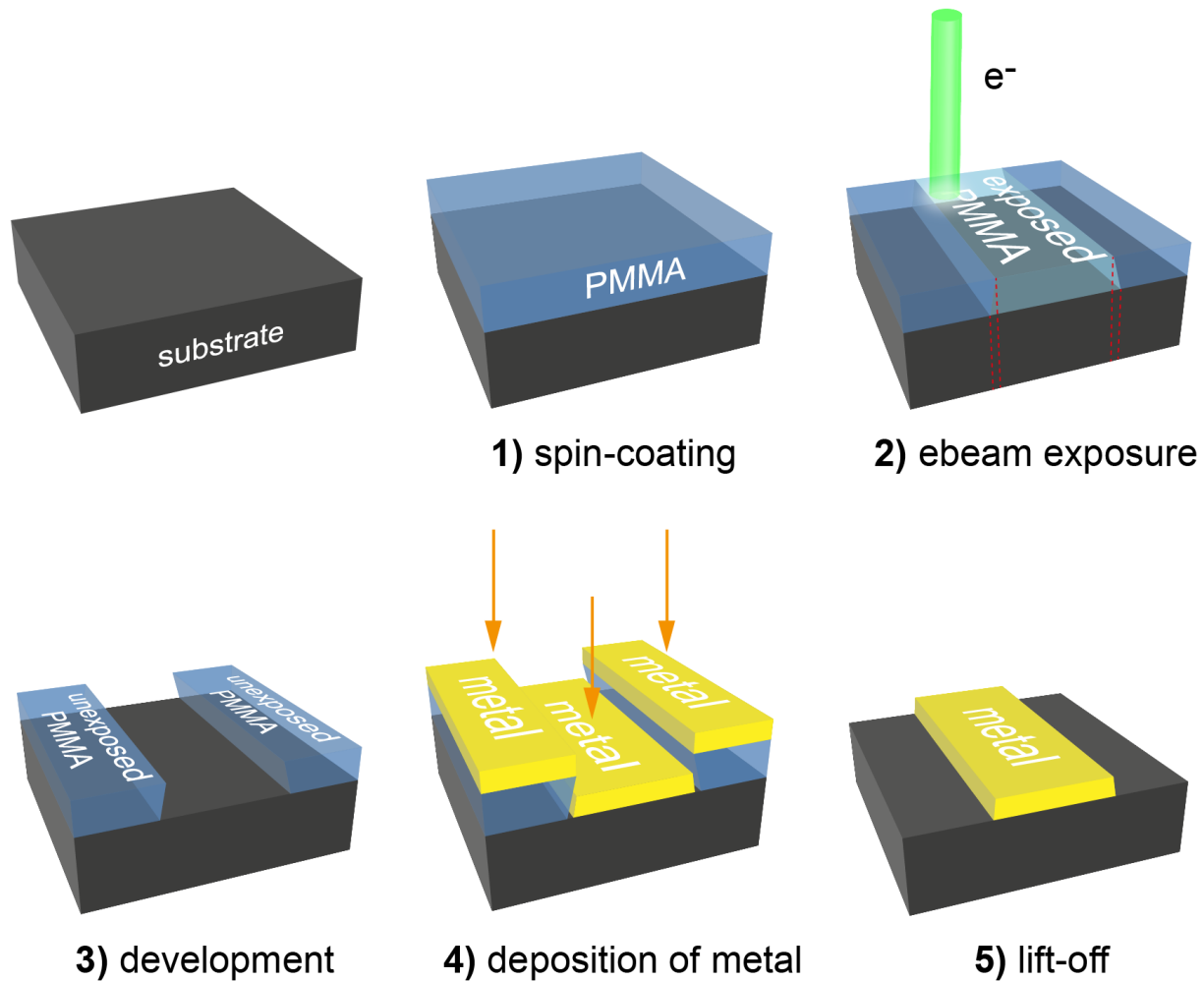
Figure 8.1: PMMA-based electron-beam lithography. A PMMA lithographic mask is created by controlled ebeam exposure (2) of a resist thin film previously deposited by spin-coating (1). In the development step (3), the resist areas exposed to the ebeam are removed, allowing direct metal deposition (4) onto the accessible substrate regions. In the final lift-off step (5) the unexposed PMMA is washed away together with the metal that is not in contact with the substrate. Red dashed lines indicate the small undercut due to forward scattering.

8.1.2 Exposure

After baking, the sample is loaded in the high-vacuum (HV) chamber of the ebeam system. The exposure is performed with a dedicated equipment (eLine system by Raith GmbH) which includes a stable high brightness field emission electron source, a sample movement stage, a beam blanker and a set of electromagnetic lenses that ensures a highly focused electron beam and allows precise beam deflection. Before the exposure, the user creates the design of the wanted pattern using the AutoCAD Mechanical software (Autodesk Inc.).
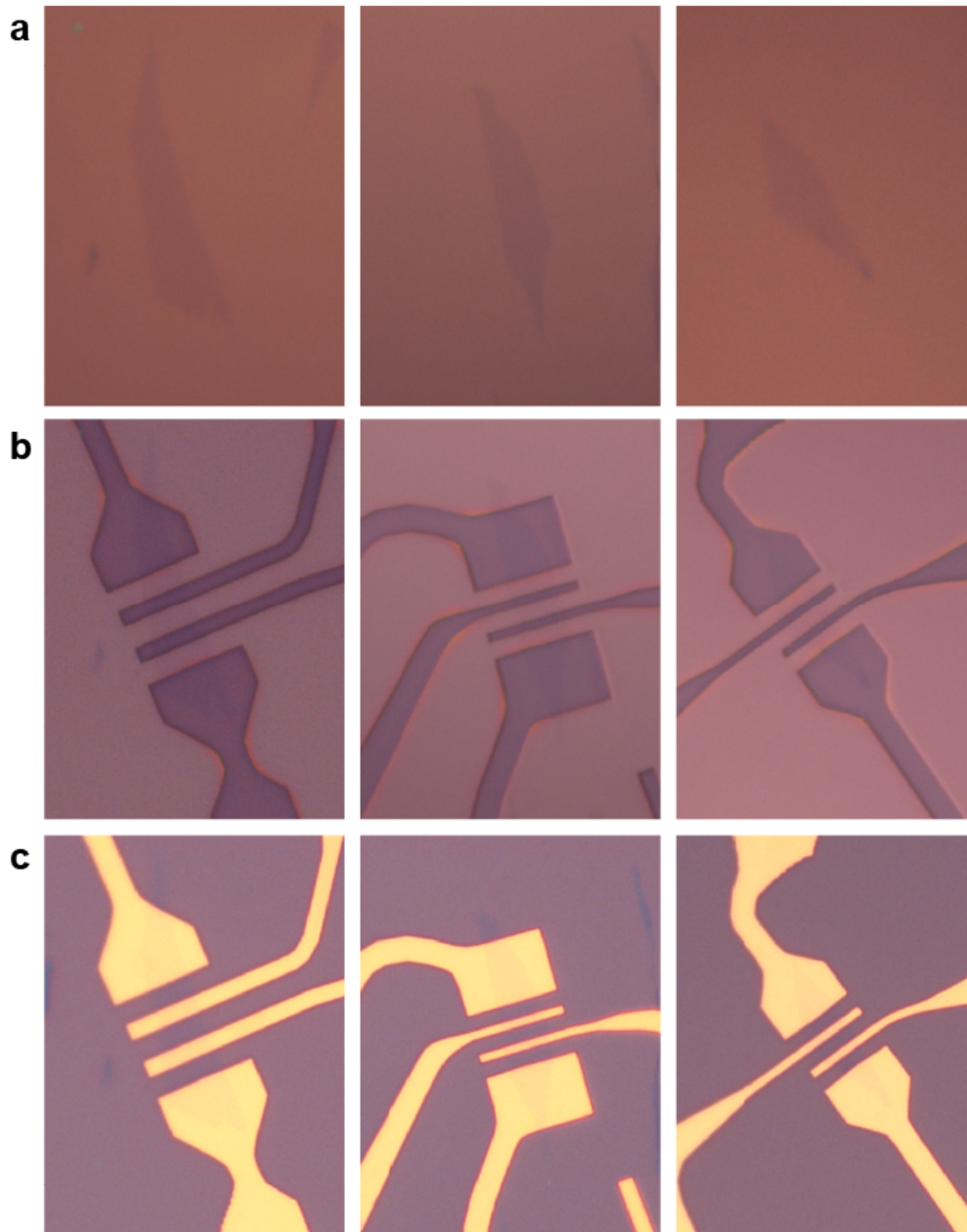
Figure 8.2: Electron beam lithography process for three example devices. a) Starting graphene flake. b) The same graphene flake after exposure and development. The exposed resist areas are removed and appear darker. c) The final device after Au/Ti deposition and lift-off step.

The output .dxf file is then used as reference to drive the ebeam system. The exposure starts with two alignment procedures. A first one to correct for the misalignments between sample and the reference frame of the moving stage (called XY reference system), and a second one to align the sample with the pattern design (UV reference system). It follows a procedure to compensate for the astigmatism of the lenses (that causes the beam spot to not have the expected round shape) and to ensure an optimal focus (i.e. the smallest achievable beam spot). The exposure is performed as direct writing or raster scan modes, Figure 8.1(2).

Upon ebeam irradiation the main chain of the PMMA molecule is broken into many radical fragments. For positive[2] resist at optimal electron doses, the fragments recombine forming polymers of reduced mass, for instance the initial molar mass of $950\,000$ g/mol of 950K PMMA drops to $5\,000-10\,000$ g/mol upon exposure. As a consequence the solubility of the exposed regions increases dramatically and the exposed resist can be easily removed in the *development* step. Larger dose values induce molecular *cross-linking* [1], resulting in a much lower solubility compared to the pristine resist, meaning that high doses convert the PMMA in a negative[3] resist that is hardly removable.

8.1.3   Proximity effect and dose test

To ensure a correct patterning, most of the electrons have to pass through the entire resist layer. This ensures also absence of resist residues at the contact interface that may cause high contact resistances. As an electron enters the resist, it undergoes multiple low energy elastic collisions, which deflect its trajectory. This *forward scattering* cause the image of the beam on the resist to be larger than the actual beam spot, reducing considerably the achievable writing resolution, Figure 8.3a. The use of thinner resist layers with longer chain lengths and higher beam energies reduces considerably the forward scattering of electrons, thus enhancing the resolution. On the one hand this broadening deteriorates the structural accuracy. On the other hand, it is useful in producing an *undercut* in two-layers resist stacks that help the final *lift-off*, Figure 8.3c,d. The two layers constituting the stack have different chain lengths, with the "softer"(shorter chain) PMMA at the bottom and the "harder" (longer chain) PMMA on top. Undergoing weaker broadening, the hard top layer ensures an high writing accuracy while the broadening of the bottom layer creates an hollow structure that facilitates the flow of solvent during the lift-off, easing the removal of the unexposed areas. In addition to forward scattering, a fraction of the electrons undergo enough large angle collisions (especially reflection at the substrate interface) to re-emerge into the resist at some distance from the set exposure point, Figure 8.3b. Depending on the beam energy, these *backscattered* electrons may cause exposure of the resist microns away from the wanted point [2–4], causing distortions in the pattern, loss of contrast [3, 5, 6] and, in the worse case, merging of two or more distinct features, Figure 8.4a. This is usually referred to as *proximity-effect* and to reduce its impact on the final structure, an optimal

---

[2]For positive resist the pattern areas that need to be revealed are exposed.
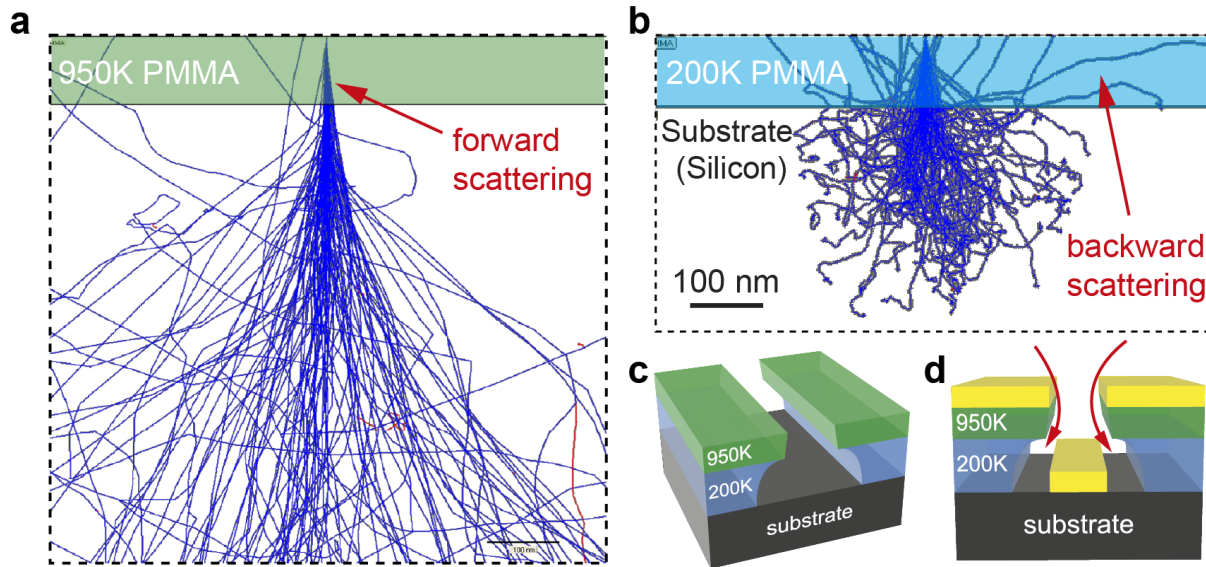[3]For negative resist the pattern areas that need to be remain covered are exposed.

Figure 8.3: Proximity effects. Given the same beam energy, a) "harder" PMMA (950K) exhibit limited proximity effects while b) "softer" PMMA (200K) exhibit enhanced forward and backward scattering. Stacks of PMMA layers with different chain lengths c) can be used to create an appreciable undercut in order to ease the lift-off of thick metal films d). Typical PMMA stacks for devices with lateral size in the μm range include a "soft" 200K PMMA bottom layer (thickness $\sim$ 140 nm) with a thinner (60nm) layer of "harder" 950K PMMA on top. Montecarlo simulations of electron diffusion are performed using a dedicated software by Raith GmbH.

electron dose (for the given pattern) has to be estimated beforehand by irradiating a test pattern at different electron doses, Figure 8.4a. Moreover an automated routine based on Montecarlo simulations of electron diffusion can be used to vary the dose along each single feature so as to ensure the most accurate patterning, Figure 8.4b.

8.1.4 Development

The exposed areas are removed by immersing the sample into a 3:1 mixture of isopropanol and MIBK (Methylisobutylketone) at room temperature (RT) for 30 seconds each 100 nm of resist thickness, plus 30 additional seconds. The sample is then washed for 60 s in fresh isopropanol. After development, only the unexposed areas are left, Figure 8.1(3).

8.1.5 Metal deposition by thermal evaporation

After development, the sample is loaded into the vacuum chamber of a thermal evaporator (Univex by Oerlikon-Leybold) where metallic films with thickness > 1 nm are deposited by passing a high current ($\sim$1-10A) through a tungsten boat loaded with the wanted metal,
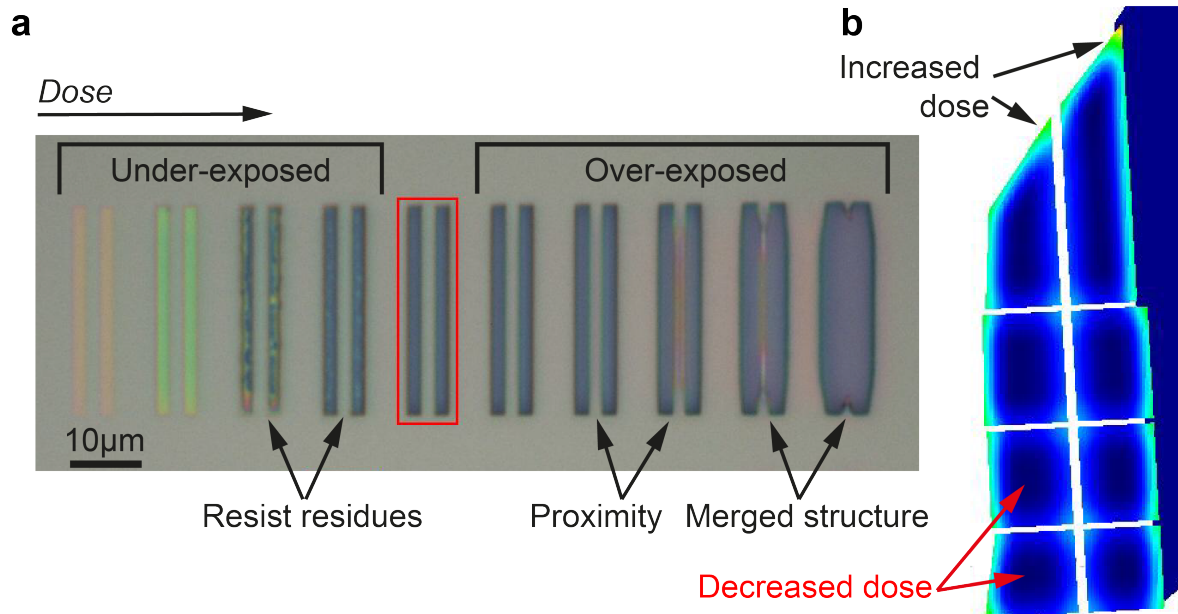
Figure 8.4: Proximity correction. a) Typical "dose test" used to calibrate the exposure of parallel injector and detector contacts in spinvalve devices. The dose increases from left to right. The red rectangle indicates the optimally exposed structure. b) An example of proximity effect correction based on Montecarlo simulations applied to a Hall-bar device. For the darker regions the exposure is reduced to prevent over-exposure. At the corners and edges the dose is increased to compensate for under-exposure.

Figure 8.1(4). The film thickness is controlled by varying the deposition time, while the deposition rate ($>$Å/s) depends on the set current. A lower deposition rate usually ensures more homogeneous films but also more prolonged sample heating. The typical deposition rate used for 50 nm-thick Au contacts was 2 Å/s, while for 40 nm-thick Cobalt the rate was reduced to 1 Å/s.

Depending on the desired metal it might be necessary to use a buffer layer to promote adhesion with the substrate material. Typically a Ti buffer thin-layer (< 2 nm) is used for 50 nm-thick Au contacts on SiO_2 substrates.

8.1.6 Lift-off

Once a continuous metallic film is deposited on the whole sample, the latter is immersed in NEP (1-Ethyl-2-pyrrolidone)-based remover (AR 300-76 by Allresist GmbH) at 60 °C for at least 4 hours. The solvent dissolves the unexposed PMMA removing also the metal that is not in contact with the substrate, Figure 8.1(5). For standard devices with Gold contacts, this is typically the most difficult step of the lithographic process. Indeed, Au films of thickness > 10 nm are pretty robust, and so difficult to be removed. It is thus recommendable to use a two-layer PMMA stack with an appreciable undercut that favors

the rupture of the film, as seen Figure 8.3d.

8.2 Nanostructuring of graphene via reactive io etching (RIE)

8.2.1 Masking

As discussed in the next chapter, one way to enhance the spin-injection efficiency in graphene is by increasing the contact resistance of the device. One way to do that is to reduce the *contact area* by patterning the graphene in narrow stripes (of width of few hundreds of nanometers) [7, 8]. For this, an additional lithographic procedure is carried out previous to the standard device lithography. The PMMA mask is designed so as to open a window over the graphene areas that have to be removed, while leaving the narrow stripe protected, Figure 8.5.
In order to achieve the required accuracy, a single thin film (~ 60 nm) of "hard" 950K PMMA is used;. In addition the Montecarlo-based proximity correction is used to ensure a uniform width along the whole stripe.

8.2.2 Etching

Reactive Ion Etching containing Typical parameters for the patterning of single layer graphene are: Ar at a flow of 100sccm (standard cubic centimeters per minute), O_2 at 11sccm, at an overall pressure of $P = 0.05$ mbar for t=5 seconds at P= 48W.
The starting graphene flake (1) is masked using positive PMMA (2-3) and exposed to reactive ion etching (4) in order to remove part of the flake. After the development (5), only a narrow graphene stripe is left. The adhesion to the SiO_2 substrate is remarkable for stripes with width > 150 nm, enabling further processing (6). Scale: the bottom-right metallic marker is 9 μm wide, the stripe width is 200 nm.

8.3 Deposition of magnetic contacts

The magnetic properties of Cobalt contacts used in spinvalve devices (see Chapters 7) are affected by the Oxygen content and other contaminants [9–13]. The typical Cobalt thicness used in this work is 44±1 nm. In order to maximize the ferromagnet purity, the evaporation is carried out at a residual pressure of $P < 1 \cdot 10^{-7}$ mbar. This high vacuum values are achieved after at least 48 hours of continuous pumping. Interestingly, long pumping times seem to decrease appreciably the contact resistance of graphene devices, likely due to the complete desorption of surface contaminants.
In order to avoid oxidation once the device is exposed to air, a 10 nm-thick Au *capping layer* is added on top of the Cobalt contacts, Figure 8.7a. This latter step, introduces the risk
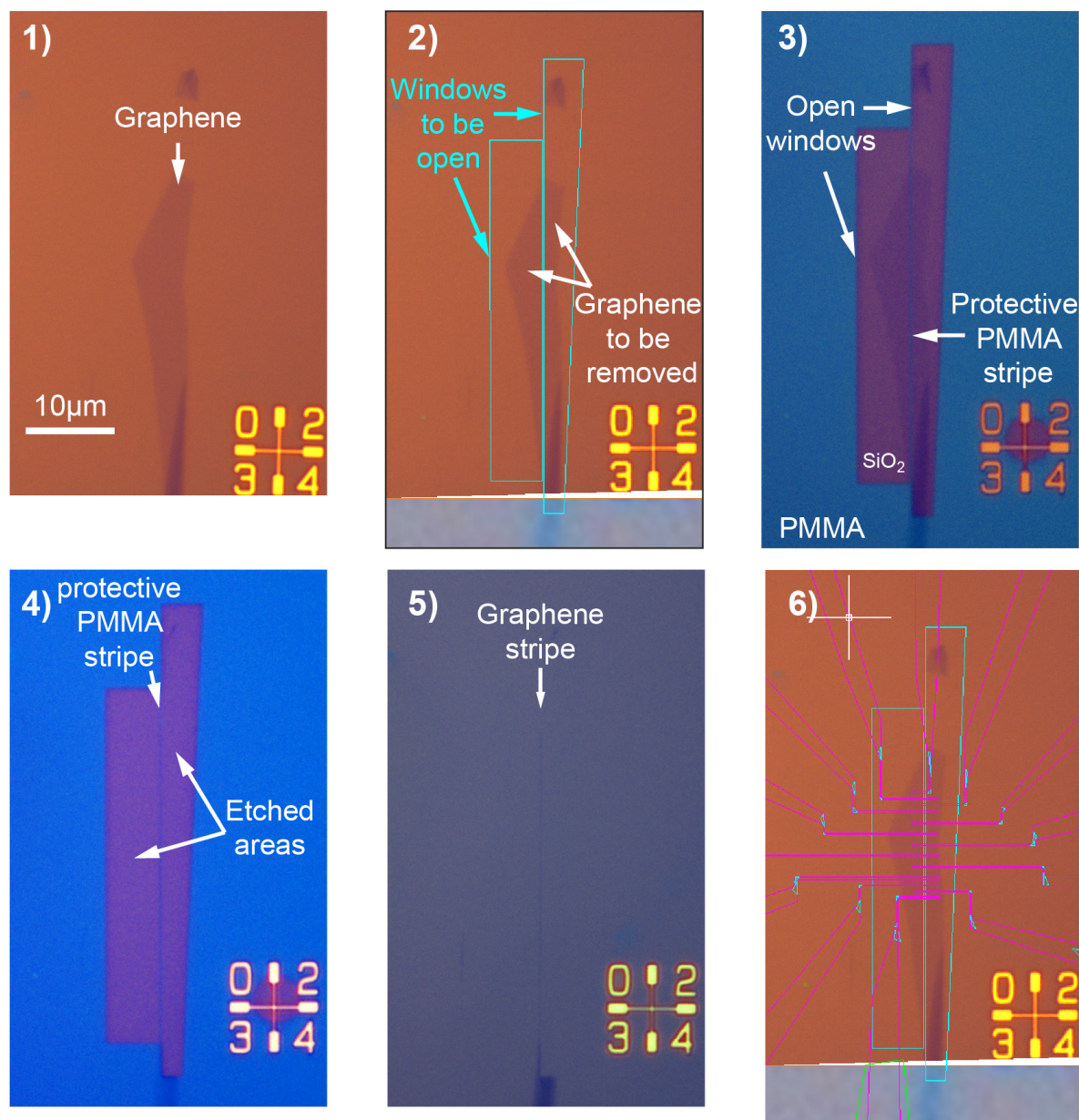
Figure 8.5: Patterning of sub-μm graphene stripes. 1) Starting graphene flake. 2) Auto-CAD Mechanical design of the patterning structure, including a narrow stripe between two large areas that are going to be exposed. 3) After exposure and development, two "windows" are opened in the positive PMMA layer, leaving a narrow PMMA stripe unexposed. 4) Reactive ion etching removes parts of the graphene flake. 5) After the development (5), only the narrow graphene stripe protected by the unexposed PMMA is left. 6) The adhesion to the SiO$_2$ substrate is remarkable for stripes with width > 150 nm, enabling further processing. The stripe width is 200 nm.
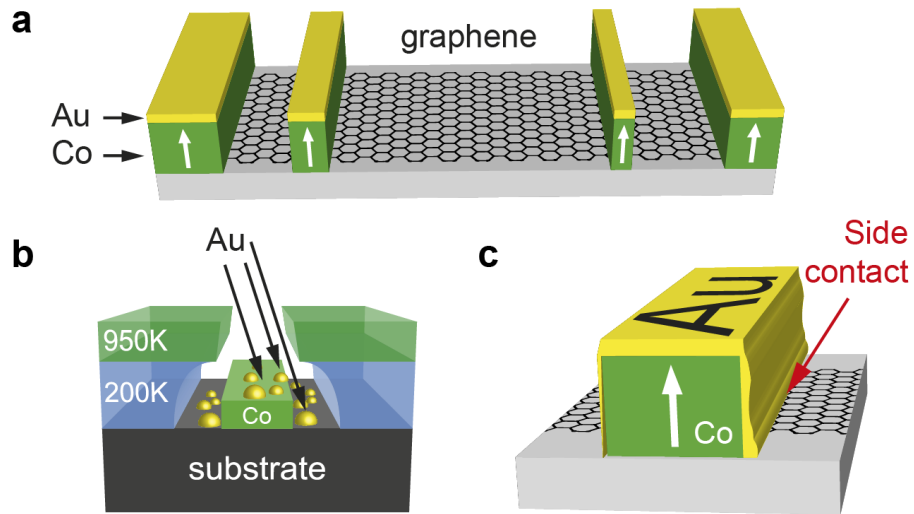
Figure 8.6: Deposition of magnetic contacts for graphene-spinvalve. a) Scheme of a graphene-based spinvalve comprising ferromagnetic Cobalt contacts with a Gold capping layer to prevent oxidation. Non-normal deposition conditions (b) may lead to direct contact between Gold and graphene (c).

of having direct contact between Au and graphene, especially for non-normal deposition conditions, Figure 8.7b,c. To avoid this problem a single layer of hard (950K) PMMA with a maximum thickness of 60 nm has been used instead of the standard 200K/950K (140/60 nm) stack. The use of a single thin resist layer maximizes also the accuracy of the *contacts width*, a very important factor for the spinvalve response. The Co/Au (44/10 nm) films are easily removed during the lift-off overnight.
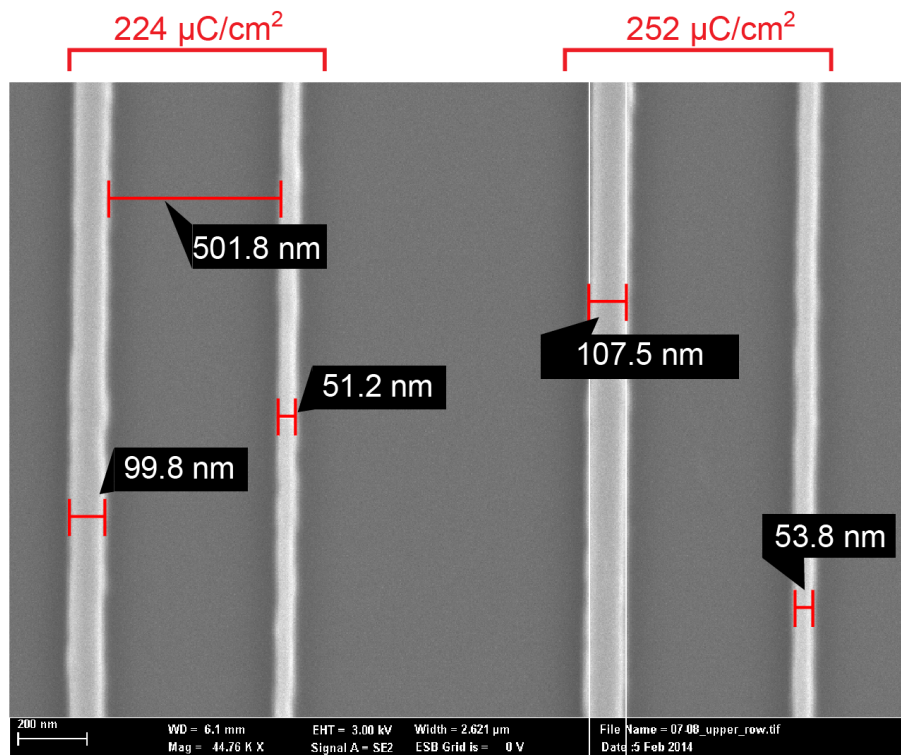
Figure 8.7: SEM image of injector and detector contacts patterned at two different electron doses. The expected contact widths are 100 nm (left) and 50 nm (right). The expected interdistance is 500 nm. The 224 μC/cm^2 dose has been chosen for the fabrication.

Bibliography

[1] Allresist GmbH. AR-P 630-670 series information sheet. URL http://www.allresist.com/ebeamresists-ar-p-631-679/.

[2] Kamp, M., Emmerling, M., Kuhn, S. & Forchel, A. Nanolithography using a 100 kV electron beam lithography system with a Schottky emitter. *Journal of Vacuum Science & Technology B* **17**, 86 (1999).

[3] Mohammad Ali, M., Mustafa, M., Steven K., D. & Stepanova, M. Fundamentals of Electron Beam Exposure and Development. In Maria, S. & Steven, D. (eds.) *Nanofabrication*, chap. 2, 11–41 (Springer, Vienna, 2012).

[4] Brewer, G. *Electron-Beam Technology in Microelectronic Fabrication* (Academic Press, New York, 1980).

[5] Chang, T. H. P. Proximity effect in electron-beam lithography. *Journal of Vacuum Science and Technology* **12**, 1271 (1975).

[6] Mun, L. K., Drouin, D., Lavallée, E. & Beauvais, J. The Impact of Charging on Low-Energy Electron Beam Lithography. *Microscopy and Microanalysis* **10**, 804–809 (2004).

[7] Kimura, T., Otani, Y. & Hamrle, J. Enhancement of spin accumulation in a nonmagnetic layer by reducing junction size. *Phys. Rev. B* **73**, 132405 (2006).

[8] Jo, S., Ki, D.-K., Jeong, D., Lee, H.-J. & Kettemann, S. Spin relaxation properties in graphene due to its linear dispersion. *Phys. Rev. B* **84**, 075453 (2011).

[9] Kim, W., Oh, S.-J. & Nahm, T.-U. Oxidation and Annealing Effect on Cobalt Films on Palladium(111). *Surface Review and Letters* **09**, 931–936 (2002).

[10] Cren, T., Rusponi, S., Weiss, N., Epple, M. & Brune, H. Oxidation induced enhanced magnetic susceptibility of Co Islands on Pt(111). *Journal of Physical Chemistry B* **108**, 14685–14691 (2004).

[11] Tracy, J. B. & Bawendi, M. G. Defects in CoO in oxidized cobalt nanoparticles dominate exchange biasing and exhibit anomalous magnetic properties. *Phys. Rev. B* **74**, 1–11 (2006).

[12] Hill, T., Mozaffari-Afshar, M., Schmidt, J., Risse, T. & Freund, H. J. Changes in the magnetism of small supported cobalt particles during the oxidation process observed by ferromagnetic resonance. *Surface Science* **429**, 246–254 (1999).

[13] Tracy, J. B., Weiss, D. N., Dinega, D. P. & Bawendi, M. G. Exchange biasing and magnetic properties of partially and fully oxidized colloidal cobalt nanoparticles. *Phys. Rev. B* **72**, 1–8 (2005).

Chapter 9

Toward efficient spin-injection in graphene

9.1 Tunneling graphene spin-valve

As introduced in Section 7.1.5, the conductivity mismatch at the ferromagnet/graphene (FM/G) interface is the main factor limiting spin-injection in graphene. One way to overcome this problem is to employ tunneling contacts, with barriers of thickness ≤ 2 nm, that introduce a spin-dependent interface resistance and "*decouple*" the graphene channel from the ferromagnet [1]. Extensive efforts have been devoted to fabricate insulating ultra-thin films on graphene, using a variety of techniques. Successful tunneling spin-injection has been demonstrated for MgO [2] and Al_2O_3 [3] barriers by molecular beam epitaxy and sputtering respectively, while oxidation of ultranthin Al film deposited at liquid nitrogen temperature revealed a limited spin-injection efficiency [4], likely due to film inhomogeneities and presence of pinholes. Here we demonstrate that homogeneous Al_2O_3 tunneling barriers can be fabricated via atomic layer deposition (ALD) using Ti seeding. While the use of Ti seeding is not enough to create closed Al_2O_3 films with thickness < 1 nm, complete oxidation of the Ti seeding prior to ALD is essential to ensure efficient tunneling spin-injection in graphene.

9.1.1 Ultrathin Al_2O_3 films on graphene

Growing homogeneous dielectric Al_2O_3 films (e.g. Al_2O_3, HfO_2) by atomic layer deposition on graphene has proved challenging due to the inertness and hydrophobic nature of the graphene surface. Previous studies [5–8] have shown that, for direct ALD on graphene, film nucleation takes place mainly at the edges, while nucleation in the basal plane is extremely rare in high quality samples. As a consequence, high homogeneity over a technologically relevant length scale of 50 nm is achieved only for rather thick films (> 8 nm) at temperature $T = 200°C$ [5].

Several methods have been developed to enhance film uniformity at lower thicknesses by
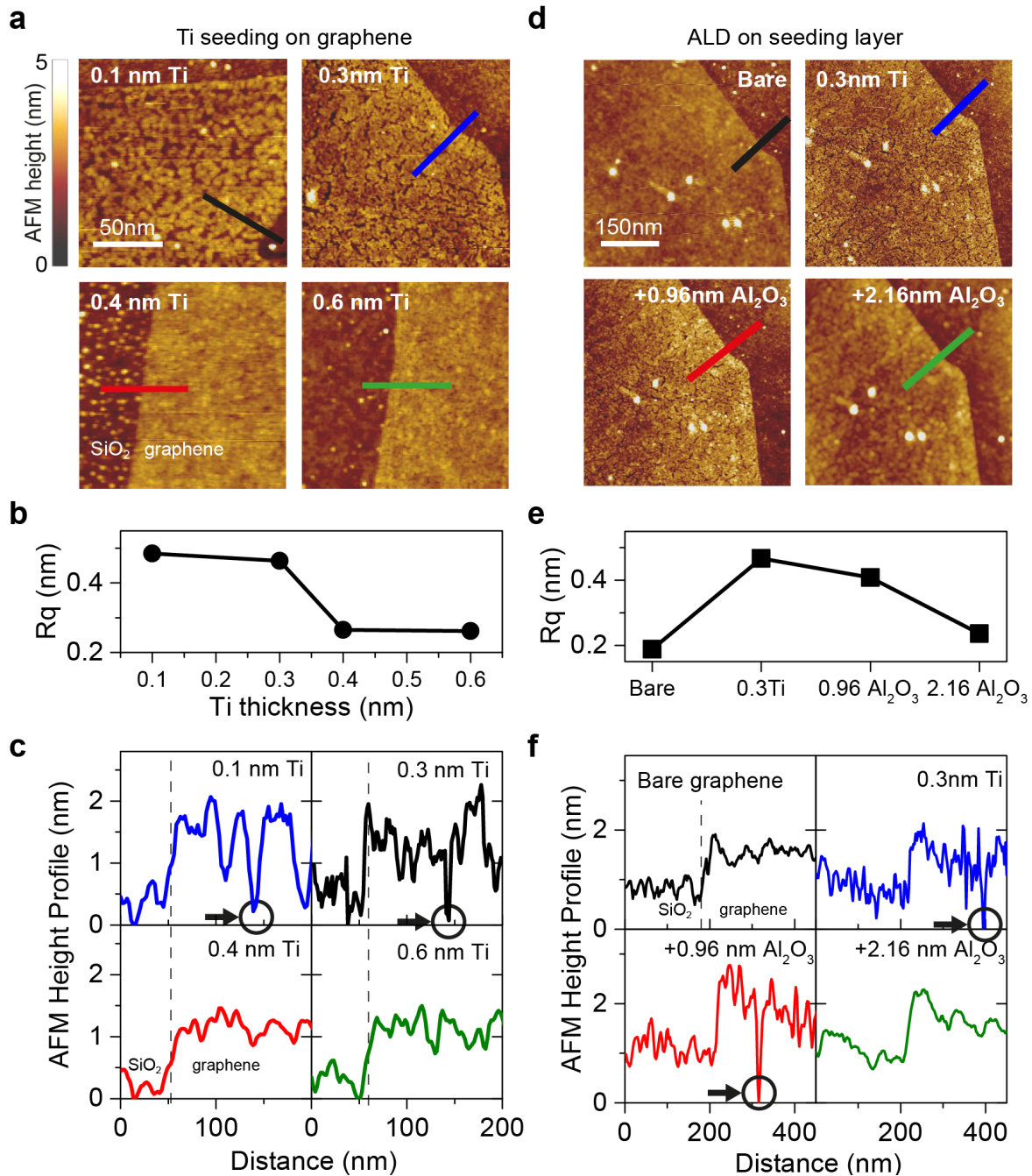
Figure 9.1: AFM topography of Ti seeding (a-c) and Ti/Al_2O_3 (d-f) insulating ultra-thin films on graphene. a) AFM images of graphene after Ti seeding deposition at different thicknesses d_{Ti}. b) Evolution of film roughness R_q as function of the Ti thickness. Ti forms a closed film for $d_{Ti} \geq 0.4$ nm. c) Plot profile for different d_{Ti}. Pinholes are evident for $d_{Ti} < 0.4$ nm (black arrows and circles). d) AFM images of Al_2O_3 on 0.3 nm Ti seeding. e) R_q at different Al_2O_3 thicknesses. The homogeneity of the film improves with Al_2O_3 deposition. f) A closed Al_2O_3 layer is formed for $d_{Al_2O_3} > 0.96$ nm (8 ALD cycles).

inducing nucleation in the graphene basal plane (by increasing the density of nucleation sites). These included ozone (O_2) [7] or NO_2 [9] pre-treatment, low-k polymer buffer layer [10], molecular seeding [8, 11], substrate-induced nucleation [12] and metallic seeding layer [13, 14]. In the latter, Ti seeding shows important improvements in both the crystallinity and the dielectric constant of the Al_2O_3 layers. Nevertheless, tunneling spin-injection in graphene employing such tunneling barrier structure has not been yet reported and only spin-injection experiments using molecular seeding/Al_2O_3 barrier have been attempted [15]. Here we employ the Ti seeding/Al_3O_2 barrier stack to efficiently decouple the graphene spin-transport channel from the ferromagnetic leads and we provide important guidelines for the efficient spin-injection/accumulation in graphene.

Graphene flakes are mechanically exfoliated from HOPG and transferred to highly doped Si substrates with 300 nm-thick thermal SiO_2 layer. A thin Ti film of thickness 0.3-2 nm is deposited by thermal evaporation with deposition rates < 0.1 nm/s, at the residual pressure of $< 10^6$ mbar. The sample is directly transferred to the ALD chamber to avoid oxidation. The thin metal film serves as nucleation layer for the subsequent ALD process. The Al_2O_3 films are deposited using Cambridge Nanotech ALD system with trimethylaluminum (TMA) and H_2O as precursors. The growth was carried out in vacuum at 100 °C with 0.1s/40s and 0.1s/15s pulse/purge time for H_2O and TMA respectively. The resulting growth rate is approximately 0.12-0.16 nm/cycle.

Figure 9.1a shows the topography of graphene flakes probed by atomic force microscopy after the deposition of Ti with thickness t_{Ti} =0.1 - 0.6 nm. The graphene surface roughness for t_{Ti} =0.3 nm is $R_q = 0.44$ nm (Figure 9.1b), more than twice that of pristine graphene (top-left image in Figure 9.1d. For $t_{Ti} \geq 0.4$ nm, R_q drops to 0.27 nm indicating a closed spatially-uniform film. The height profile (Figure 9.1c) evidences the absence of pinholes for $t_{Ti} \geq 0.4$ nm.

To study the influence of Ti seeding on the ALD nucleation a $t_{Ti} = 0.3$ nm is chosen. 8 ALD cycles ($t_{Al_2O_3} = 0.96$ nm) leads to slightly reduced R_q (Figure 9.1d,e) and the height profile confirms the presence of pinholes. Only for $t_{Al_2O_3} > 1.2$ nm (10 cycles) a spatially uniform Al_2O_3 film is created (Figure 9.1d,e,f).

9.1.2 Spin transport with highly decoupled contacts.

Spinvalve devices are fabricated by ebeam lithography using a 950K/200K double layer PMMA stack. A barrier structure of 0.3nm Ti seeding combined with 10 ALD cycles is chosen to ensure the lowest barrier thickness (Figure 9.2a). To make sure that the complete contact area is covered with Ti islands, the deposition is carried out with rotating sample at a tilt angle of $\theta = 20°$ (Figure 9.2a).

To produce a clear spin-valve characteristic (Figure 7.5c), the ferromagnetic electrodes need to have distinct coercive fields H_c^{FM}. To this end [16], the electrodes with different widths w are fabricated. In fact, H_c^{FM} decreases with increasing w [17] because of the different *shape anisotropy*. Typically, an electrode with $w \sim 100$ nm and thickness $t \sim 45$ nm exhibits a coercive field of about 100 mT (the final H_c^{FM} depends also on other geometrical
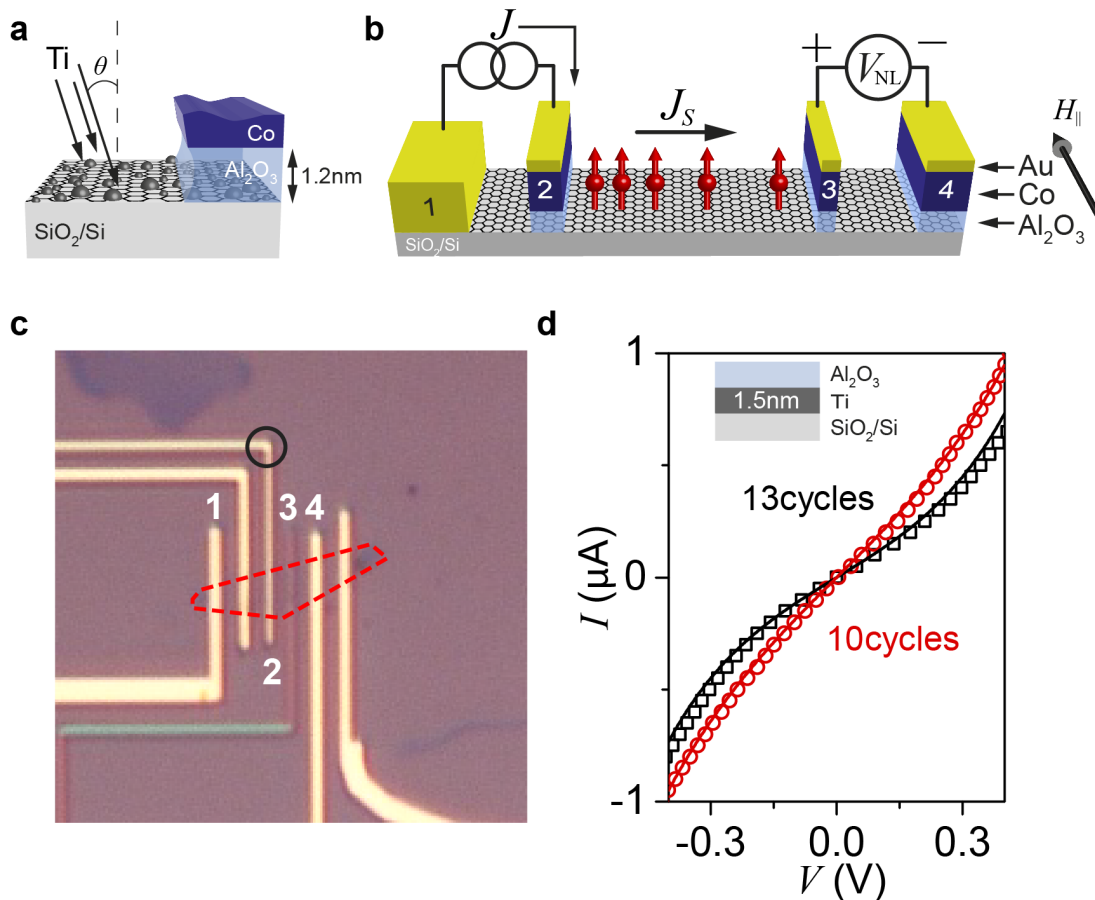
Figure 9.2: Tunneling graphene spinvalve. a) Deposition of Al_2O_3 tunneling contacts with Ti seeding layer (t_{Ti} =0.3 nm) and 10 ALD cycles. b) Scheme of the non-local spinvalve configuration. c) Optical picture of the device. Dashed red curve indicates the graphene flake. Black circle: one of the 90° turns used pin the contact domain structure. Electrodes are equidistant with $L = 0.8 \mu$m. d) I-V curve of a device with a continuous Ti seeding layer ($t_{Ti} = 1.5$ nm). Symbols are experimental data for (red) $t_{Al_2O_3} = 1.2$-1.6 nm (10 ALD cycles) and (black) $t_{Al_2O_3} = 1.8$-2 nm (13 ALD cycles). Solid lines are fits with Simmon's model.

factors). In this way, parallel and anti-parallel configurations of the injector and detector magnetizations are obtained by sweeping the external field $H_{||}$ *along* the contacts long direction.

The ferromagnetic domain structure of the electrode plays an important role in the final spin-injection efficiency. The presence of multiple domains in the FM/graphene junction area can cause simultaneous injection of both spin-up and spin-down species, leading to a decreased net spin-accumulation signal ΔR_{NL}. This is avoided by designing electrodes with large length/width aspect ratio, that maximizes the domains size [16]. In addition, to inhibit domain wall motion, so as to produce a more neat switching characteristics,

each contact is designed with a 90 degree turn before crossing the graphene strip [18] as shown in Figure 9.2c (black circle). Cobalt contacts are deposited by thermal evaporation at a residual pressure of $< 10^7$ mbar. A 10 nm-thick gold capping layer is added to avoid oxidation of the ferromagnetic contacts (Figure 9.2b). The resulting device is shown in Figure 9.2c.

Spin-transport measurements are carried out in a non-local geometry (Figure 9.2b) using the dc polarity inversion method (also called *'Delta method'*) implemented via a dc current source coupled with a low-noise nanovoltmeter (Keithley Delta system [19], with an excitation current of $J = 0.3$ μA. Such a device does not show the expected spinvalve characteristics. This is expected in case of a not oxidized Ti layer. In fact tunneling would occurs mainly towards the metallic Ti and not directly to graphene, both because the Al_2O_3 thickness is lower on top of a Ti island, and because for a 0.3nm-thick seeding the total area covered by Ti is much larger than the uncovered graphene area. This leads to a reduced spin accumulation signal. To verify the oxidation level of the seeding, we fabricated devices with a continuous Ti layer ($t_{Ti} = 1.5$ nm) and measured their tunneling characteristics. Figure 9.2d shows the I-V characteristic for two devices with different Al_2O_3 thickness $t_{Al_2O_3}$ (10 and 13 ALD cycles). The curves are highly non-linear and fitting with the Simmon's tunneling model [20–22] gives effective barrier thicknesses of $t_{Al_2O_3}^{10cycles} = 1.45 \pm 0.03$ nm and $t_{Al_2O_3}^{13cycles} = 1.74 \pm 0.08$ nm. These are in excellent agreement with the thicknesses expected for 10 and 13 ALD cycles respectively, and demonstrate that the seeding layer is not oxidized. In fact, Ti oxidation would lead to an appreciable increase in barrier thickness. An oxidation step previous to the ALD process is then necessary to minimize the spin-relaxation at the contact interface, and consequently enhance the spin-injection efficiency.

Figure 9.3 shows the magnetotransport response of a device with $t_{Ti} = 0.3$ nm and $t_{Al_2O_3} = 0.6$ - 0.8 nm (5 ALD cycles) for which the Ti seeding has been oxidized for 1.5 hours in controlled oxygen atmosphere. Up-sweeping $H_{||}$ from negative to positive values gives rise to the red curve of Figure 9.3. At $H_c^{FM3} = 42 \pm 1$ mT the 140 nm-wide (FM3) electrode flips its magnetization direction as first, resulting in a lowered R_{NL}. This marks the transition from the parallel to the antiparallel magnetization configuration, where FM2 injects *up*-spins in the channel and FM3 probes the consequent depletion of *down*-spins. At $H_c^{FM2} = 75 \pm 1$ mT, the magnetization of FM2 ($w = 90$ nm) flips, restablishing the parallel magnetization configuration (higher R_{NL} value), in which FM2 injects *down*-spins and FM3 probes their accumulation. The fact that the device magnetoresistance (MR) does show two different R_{NL} values for different magnetization configurations demonstrates the effective spin-injection and detection in the graphene channel. Moreover it suggests that the spin-diffusion length of the graphene stripe is larger than the FM2-FM3 interdistance L, i.e. $\lambda_s > L = 0.8\mu$m. A third resistance level is seemingly present at $H_c^{FM2} = 12 \pm 1$ mT, likely indicating the flipping of FM4, suggesting an even larger spin diffusion length, $\lambda_{sf} > 1.6\mu$m

A clear spinvalve behavior is observed at different gate voltages V_{gate} (Figure 9.4a,b). The dependence of the spin-signal on V_{gate} indicates that ΔR_{NL} is maximum at the charge
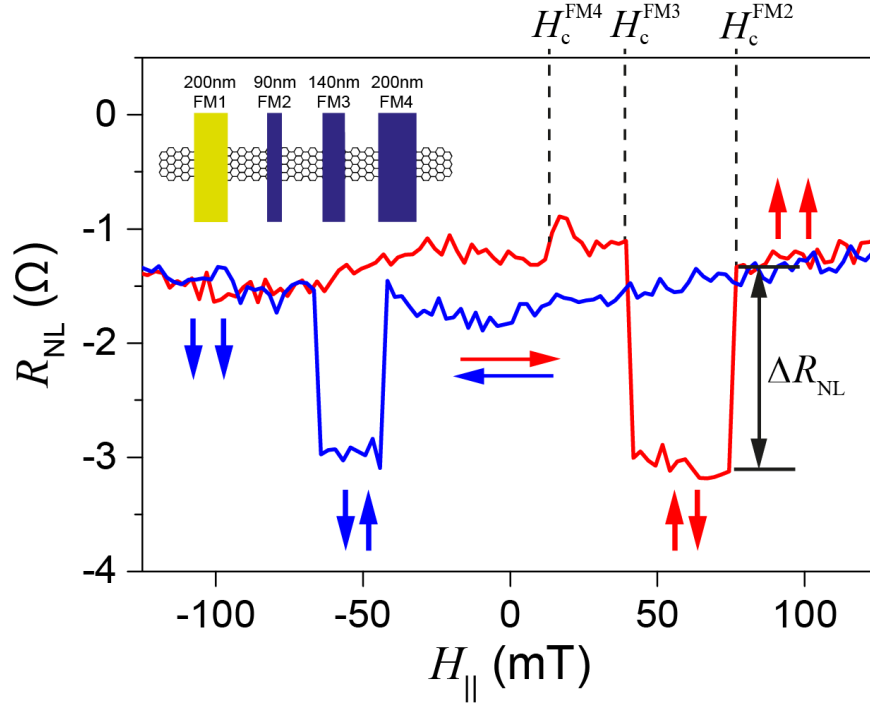
Figure 9.3: Magnetotransport in decoupled graphene spinvalve at $T = 4K$ and $V_{\text{gate}} = +30V$. Inset: scheme of the spinvalve device with different contacts widths.

neutrality point ($V_{gate} = 15.5$ V) (Figure 9.4c). This confirms that the contacts are highly decoupled from the graphene channel [2]. Indeed, for this device a clear spin signal is detected even if the I-V curves of injector and detector are linear and highly resistive, $R^{2P}_{\text{inj}} = 22.1$ kOhm $R^{2P}_{\text{det}} = 12.8$ kOhm (Figure 9.4d).

To conclude the above observations demonstrate that the spin-signal ΔR_{NL} is extremely sensitive on the oxidation level of the seeding, and thus on the actual chemical composition of the barrier film.
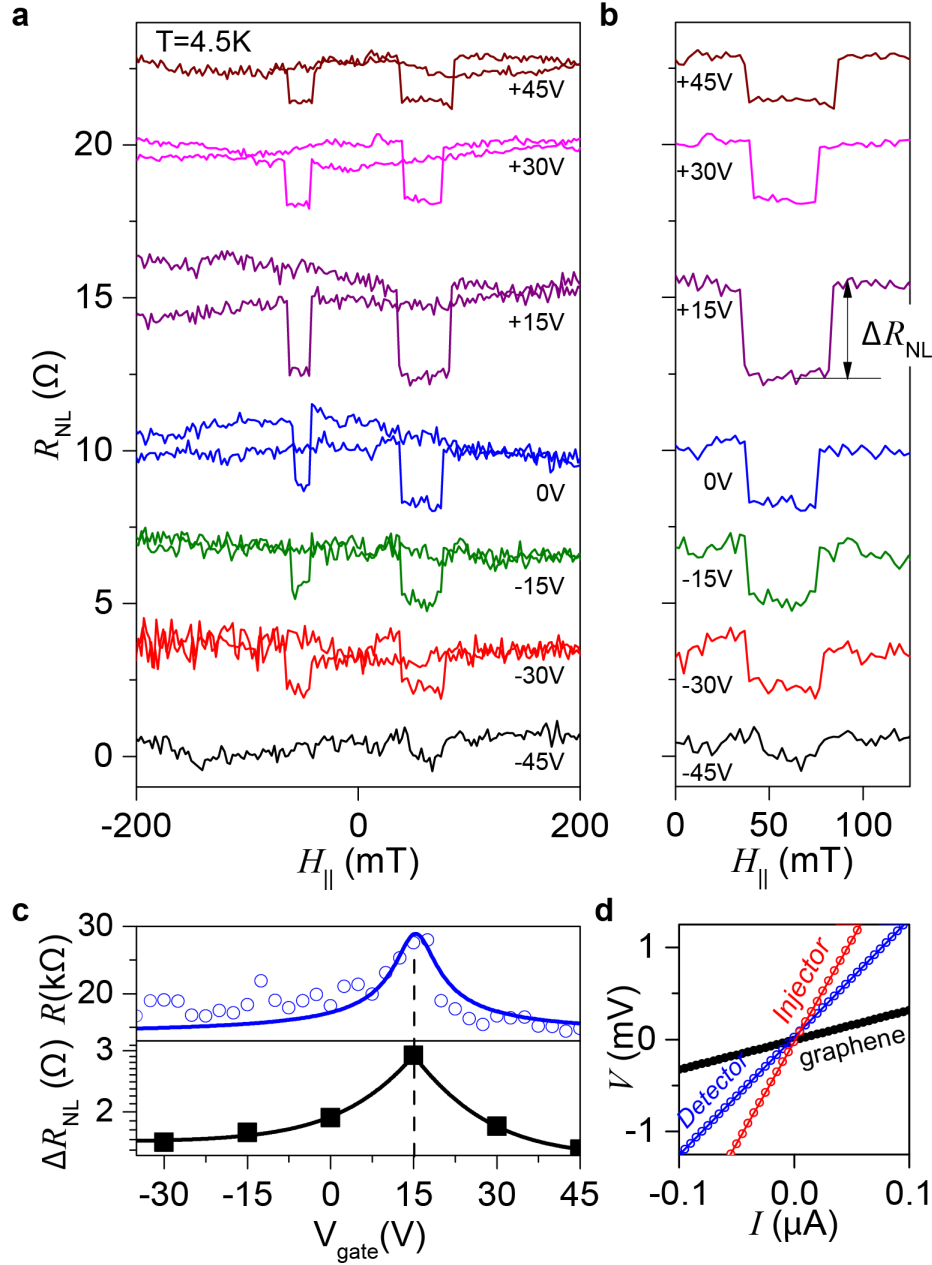
Figure 9.4: Gate dependence of spin-accumulation signal in decoupled graphene spinvalve. a) Spin valve behavior for different gate voltages. b) Zoom-in on ΔR_{NL}. c) comparison between ΔR_{NL} and ρ gate dependences. Blue line: fit with model (2.43). ΔR_{NL} is maximum (3 Ω) at the charge neutrality point ($V_{\mathrm{gate}} = 15.4$ V) demonstrating highly decoupled contacts. d) FM2 injector (red) and FM3 detector (blue) contact I-V curves measured in two-terminal configuration employing a direct Au contact. The graphene contribution (3.2 kOhm) as measured in four-terminal configuration is shown in black. Solid lines are linear fits.

181

9.2 Transparent graphene spinvalve

The observations of the previous section highlight how the performance of graphene spinvalves depends sensibly on the barrier chemical composition, and on the interface quality. The presence of unoxidized seeding material completely hinders the spin-injection in graphene. This not only makes the fabrication and the characterization of the such devices more difficult, but it will hardly allow discriminating the effect of the SMMs functionalization on the channel spin-transport from the effect of the same on the barrier composition, being the functionalization performed via a wet-chemistry approach.
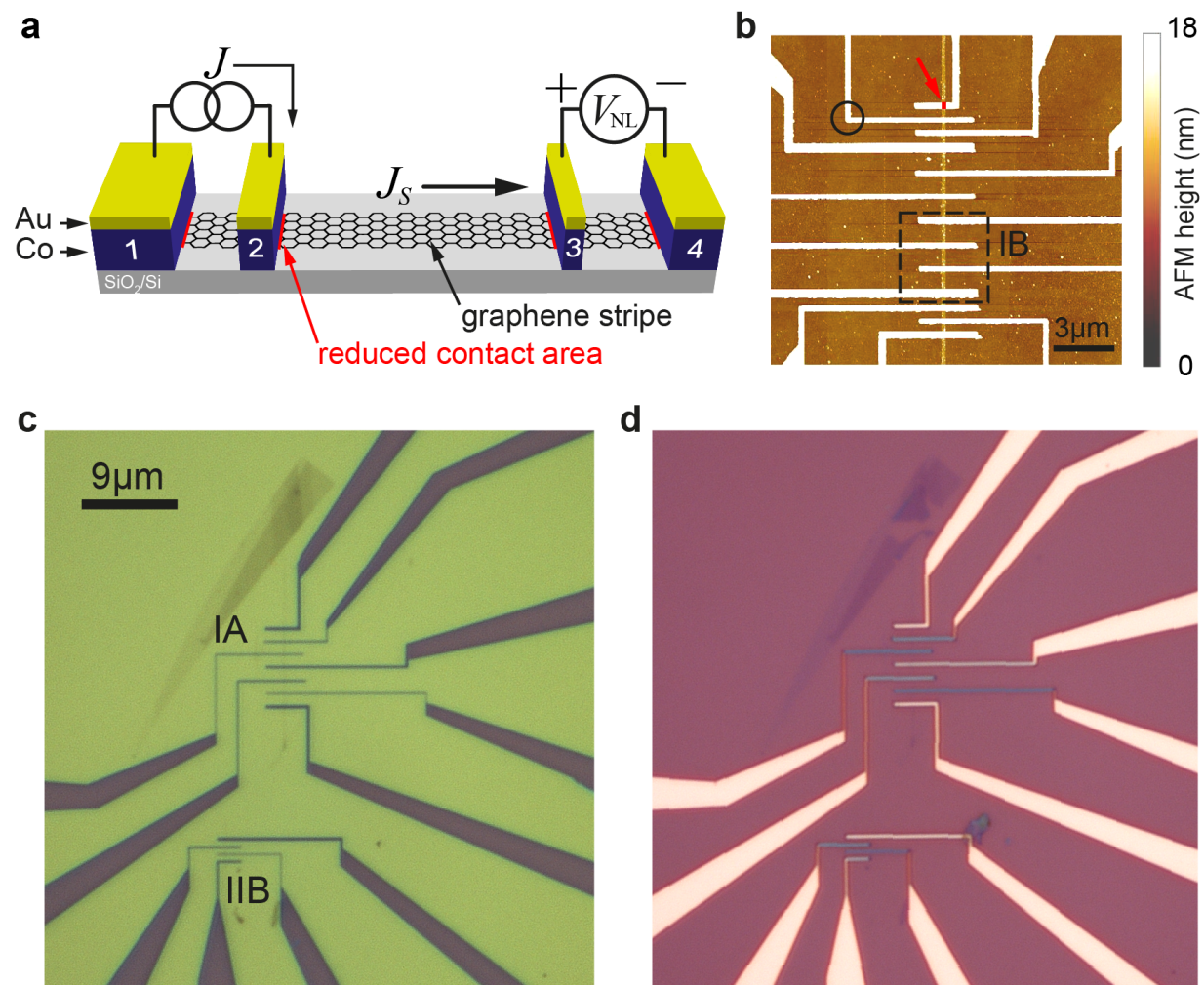
Figure 9.5: a) Scheme of the transparent graphene spinvalve. b) AFM-height image of device IB (dashed black rectangle). Black circle: one of the 90 degree turns inhibiting domain wall motion. The red arrow shows the reduced junction area. b) Optical picture before metal deposition and c) of the completed IA ($W = 300$ nm $L = 1\mu$m) and IIB ($W = 200$ nm $L = 0.5\mu$m) spinvalves.

Another way to overcome the conductivity mismatch problem is to increase the contact resistance by reducing the junction area [23, 24]. To this end, graphene flakes are patterned in narrow stripes of width $W = 200$ and 300 nm, via a combination of ebeam lithography step and reactive ion etching (RIE) micropatterning (see Chapter 8). The graphene stripes are then contacted with a sets of 44 nm-thick Cobalt electrodes capped with 10 nm-think Au. Examples of a final device is shown in Figure 9.5.

Figure 9.5 shows a typical device built for a 200 nm wide graphene stripe. The device design comprises four electrodes sets, each containing 300, 100, 150 and 200 nm-wide equidistant electrodes. The following sections present measurements performed on three different devices which details are reported in Table 9.1.

Device	L	W
IA	1 μm	300 nm
IB	1 μm	200 nm
IIB	0.5 μm	200 nm

Table 9.1: List of the devices described in this chapter.

9.2.1 Effect of rough edges on spin-transport

Figure 9.6a shows the magnetoresistance response of device IB (Figure 9.5b) at $T = 1.6$ K.The non-local voltage V_{NL} is measured while sweeping the magnetic field $H_{\parallel}$ at the constant rate of 20 mT/min. In analogy with the previous section, the measurements are carried out using the polarity inversion method (also called *'Delta method'*) implemented via a dc current source coupled with a low-noise nanovoltmeter (Keithley Delta system [19]. The excitation current used in this case is $|J| = 15\mu$A. To avoid any unwanted charge transport between FM2 and FM4, the nanovoltmeter is used in *float* configuration. Up-sweeping $H_{\parallel}$ from negative to positive values gives rise to the red curve of Figure 9.6a. At $H_{\mathrm{c}}^{\mathrm{FM3}} = +70 \pm 1$ mT the 150nm-wide (FM3) electrode flips its magnetization direction as first, resulting in a negative V_{NL}. This marks the transition from the parallel to the antiparallel magnetization configuration, where FM2 injects *up*-spins in the channel and FM3 probes the consequent depletion of *down*-spin. At $H_{\mathrm{c}}^{\mathrm{FM2}} = +104 \pm 1$ mT, the magnetization of FM2 ($w = 100$nm) flips, restablishing the parallel magnetization configuration (positive value of V_{NL}), in which FM2 injects *down*-spins and FM3 probes their accumulation. The fact that the device magnetorestistance (MR) response does show two different V_{NL} values for different magnetization configurations demonstrates effective spin-injection and detection in the graphene channel. Moreover this observation suggests that the spin-diffusion length of the graphene stripe is larger than the FM2-FM3 interdistance L, i.e. $\lambda_s > L = 1\mu$m.

Figure 9.6b shows a similar spin-transport measurement for device IA ($W = 300$ nm) at $V_{gs} = -10$ V. For this device, four different V_{NL} levels are observed. By up-sweeping $H_{\parallel}$, the electrodes switch their magnetization in the reverse order of their width: FM1, FM4,
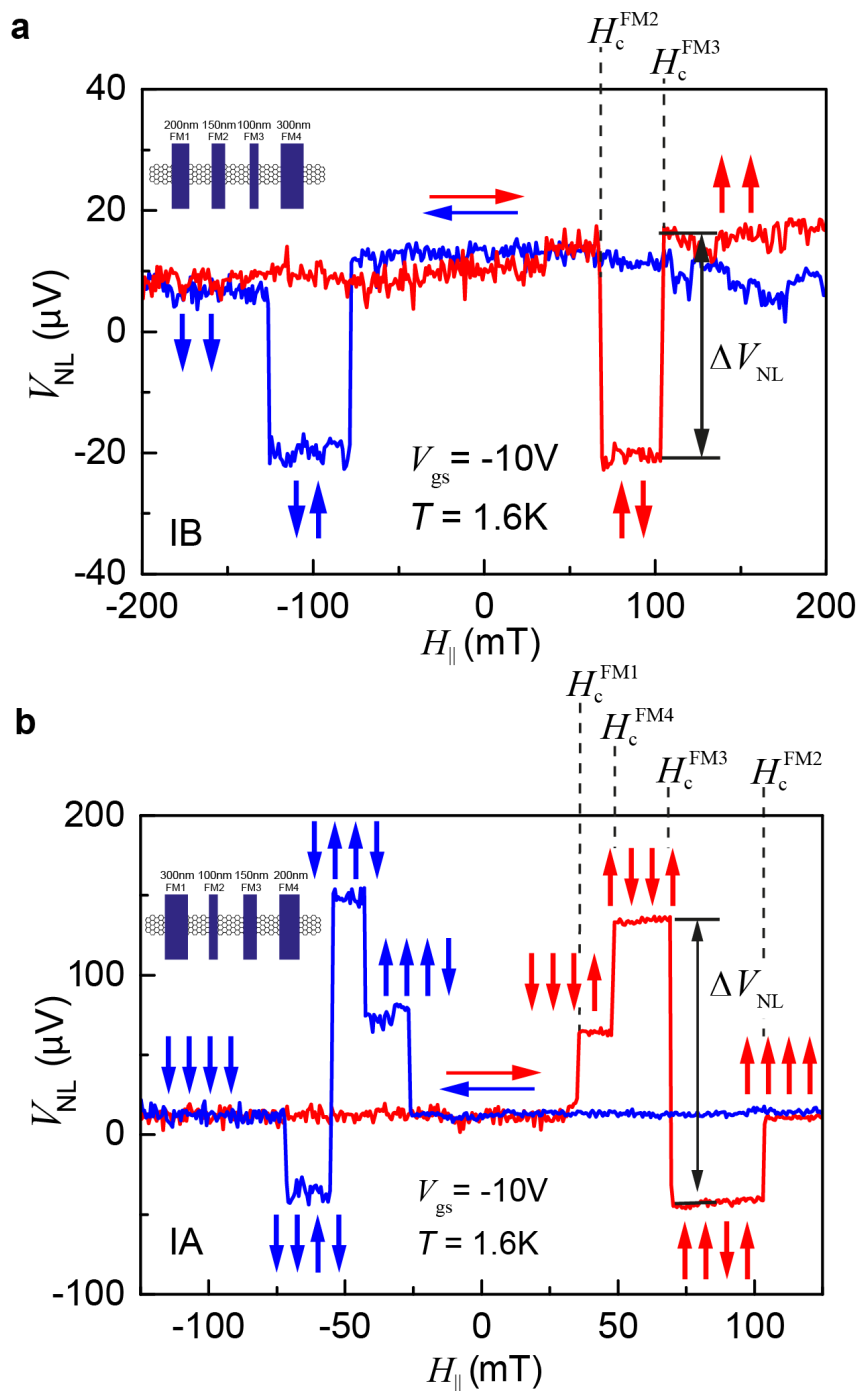
Figure 9.6: Spin-transport in transparent graphene spinvalves at $T = 1.6$ K and $V_{gs} = -10$ V. a) For device IB ($|J| = 15\mu A$) V_{NL} parallel ad antiparallel configurations of injector (FM2) and detector (FM3) contacts are observed. b) For device IA ($|J| = 20\mu A$), four different resistance levels are observed, corresponding to the magnetization-flip of all four electrodes.

FM3, and FM2. Observing four magnetization configurations means that λ_s is at least equal to the FM1-FM3 (or FM4-FM2) distance $\lambda_s > L_{13} = 2\mu$m.

The observation of only two resistance levels for the $W = 200$ nm stripe, suggests a reduced spin-diffusion length λ_s, compared with the $W = 300$ nm case. A possible cause of this enhanced spin-relaxation is spin-flip scattering at the stripe edges. The influence of the edges is confirmed by a reduced mobility μ for the narrower stripe (IB) as extracted from fit of the two-point differential resistance with (2.43) (Figure9.10). Moreover for device IB, the constant contribution ρ_S is more than four times larger. This contribution stems both from the contact resistance R_C (that is expected to be inversely proportional to W), as well as from short-range scatterers. Short-range (inter-valley) nature of the defects at the edges is also confirmed by the appreciable D band in the stripes Raman spectra (Figure 9.7), which becomes more prominent as the W is reduced.

The spin-injection efficiency (i.e. spin polarization P) can be extracted by solving the spin-coupled diffusion equations for spin-up and spin-down electrons (7.9), which in the limit of $R_C >> R_N$ gives [27, 28]:

$$R_{\mathrm{NL}} = \pm \frac{P^2 \lambda_s}{2\sigma W} e^{-L/\lambda_s} \tag{9.1}$$

where P is the spin-injection efficiency, σ is the graphene conductivity and W is the width of the graphene stripe.

The measurements of Figure 9.6 give $R_{\mathrm{NL}} = 2.0 \pm 0.4$ Ω and $R_{\mathrm{NL}} = 9.8 \pm 0.9$ Ω for device IB and IA respectively. Considering that $\sigma = 1.1 \cdot 10^{-4}$ S and $\sigma = 5.3 \cdot 10^{-4}$ S for device IB and IA respectively, and assuming $\lambda_s > 1\mu$m for IB and $\lambda_s > 2\mu$ for AI, Formula (9.1) gives $P = 0.6\%$ and $P = 2.4\%$ (in agreement with other investigations on graphene-spinvalves with transparent contacts [24, 29]), indicating a reduced spin-injection efficiency for the narrower stripe.

The reduction the spin-diffusion length with the W suggests that the defects at the edges induce spin-dependent scattering and contribute to the overall spin-relaxation. Moreover, the fact that spin-flip scattering at the edges impacts on the overall spin-injection efficiency is an important result and further measurements are on the way to better clarify the underlying mechanism.
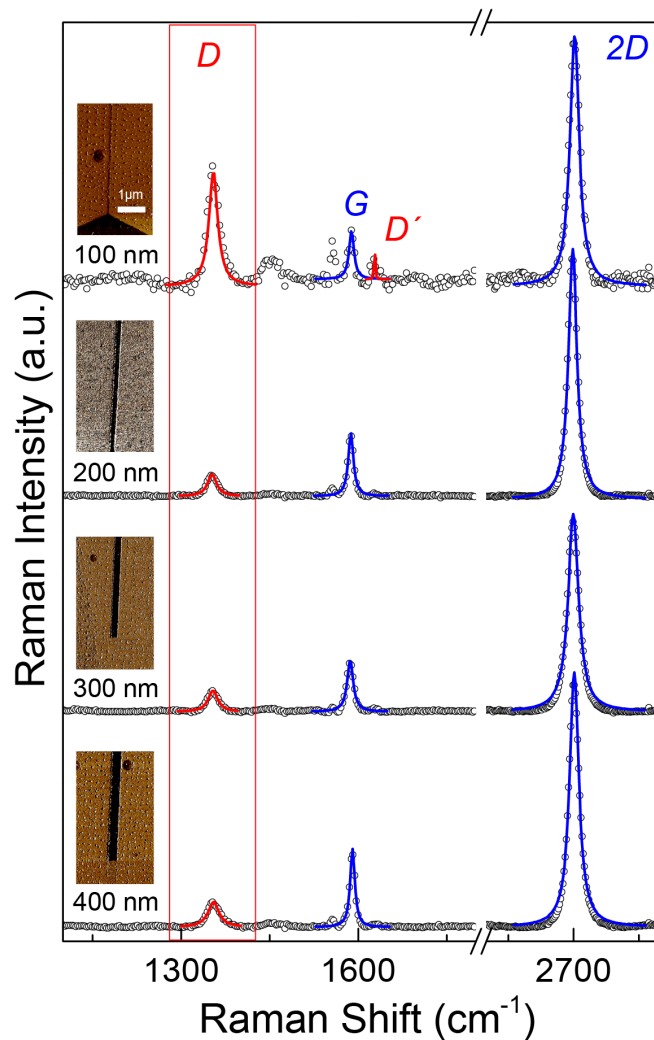
Figure 9.7: Comparison of raman spectra of graphene stripes with different widths. The appreciable D peak indicate presence of intervalley scattering at the edges [25, 26]. As the width is decreased the effect of the edges becomes more pronounced as indicated by the D/G intensity ratio. Lines are fitting with single lorentzian function.

9.2.2 Effect of transparent contacts

To investigate how R_{NL} varies as the Fermi level E_{F} is swept with respect to the charge neutrality point, multiple spin-valve characteristics have been acquired at different gate voltages V_{gs} (Figures 9.8 and 9.9). ΔV_{NL} varies appreciably with gate voltage V_{gs}, (Figure 9.8 and 9.9). In contrast to the decoupled spinvalve of Section 9.1.2, comparison of spin and charge transports (Figure 9.10) reveals a *weaker* spin-signal ΔR_{NL} at the Dirac point, confirming a transparent FM/G interface [30] and an higher coupling to the contact.

It is important to notice that for most devices the ρ vs. V_{gs} curve shows a second maximum (or shoulder) for negative gate voltages, at which ΔR_{NL} in maximum. This is likely a
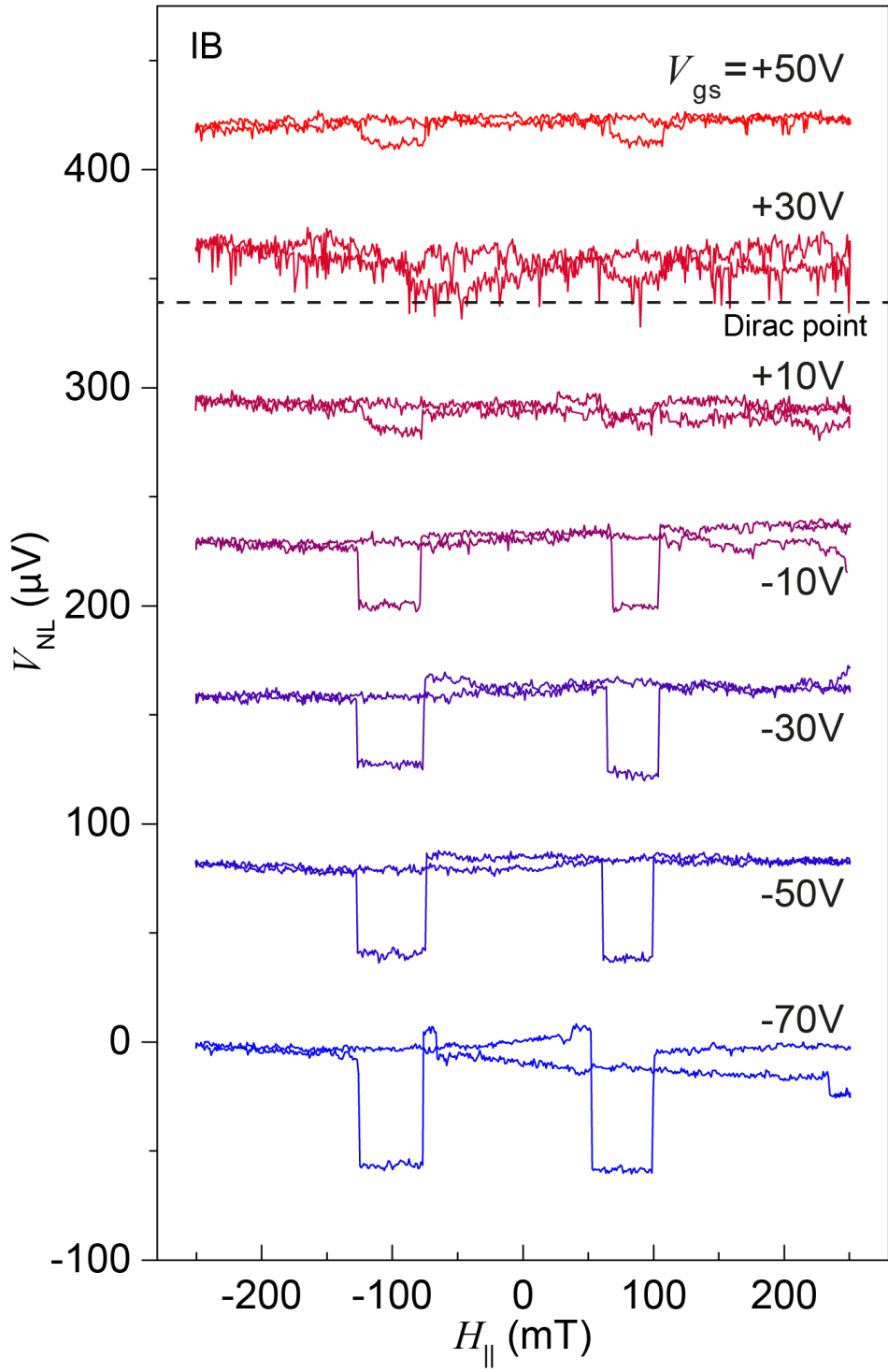
Figure 9.8: Gate dependence of the spin-transport in device IB ($T = 1.6$K and $|J| = 15\mu$A). The non-local signal ΔV_{NL} is minimum for V_{gs} close to the Dirac point.
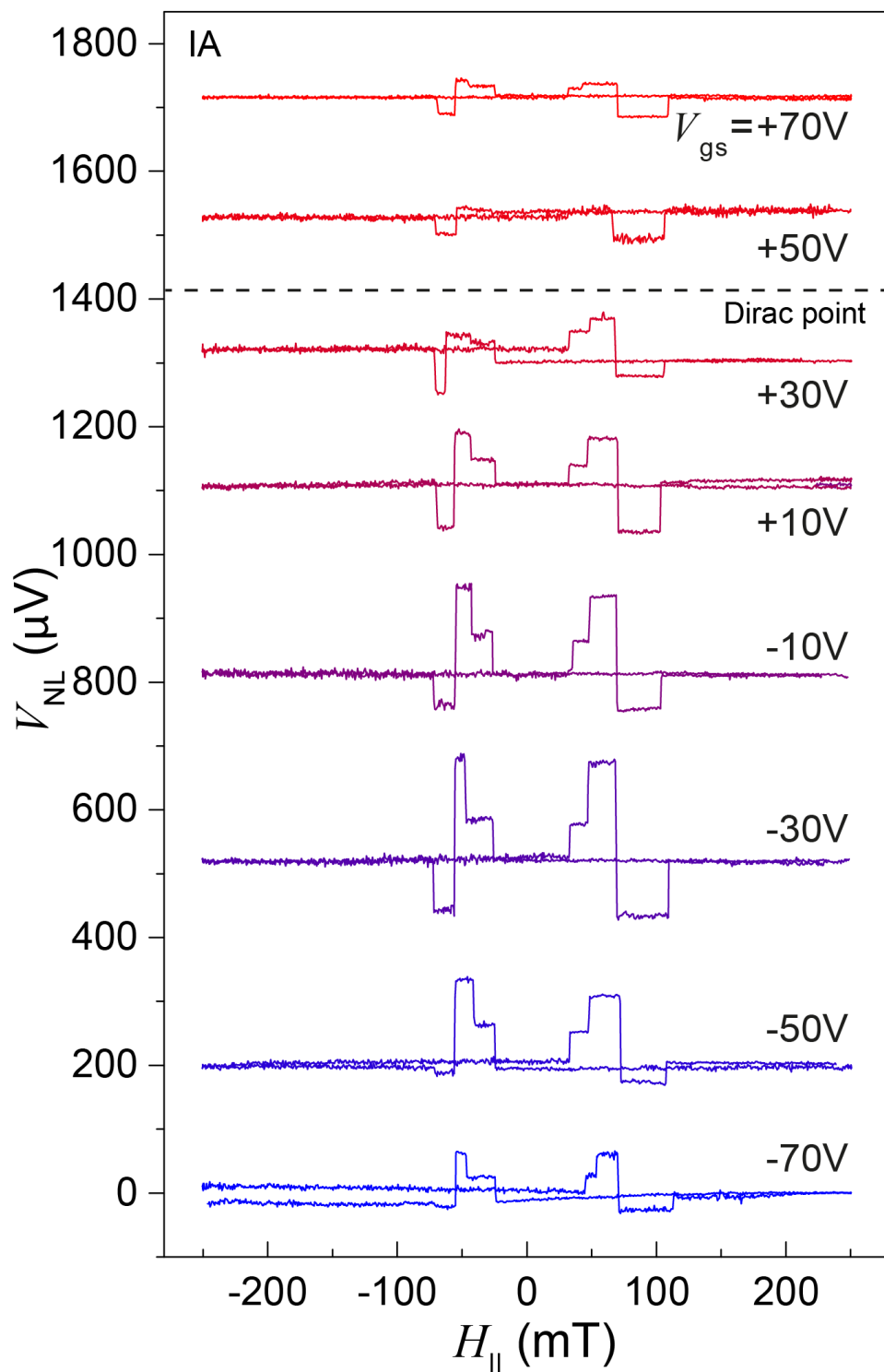
Figure 9.9: Gate dependence of the spin-transport in device IA ($T = 1.6$K and $|J| = 20\mu$A).
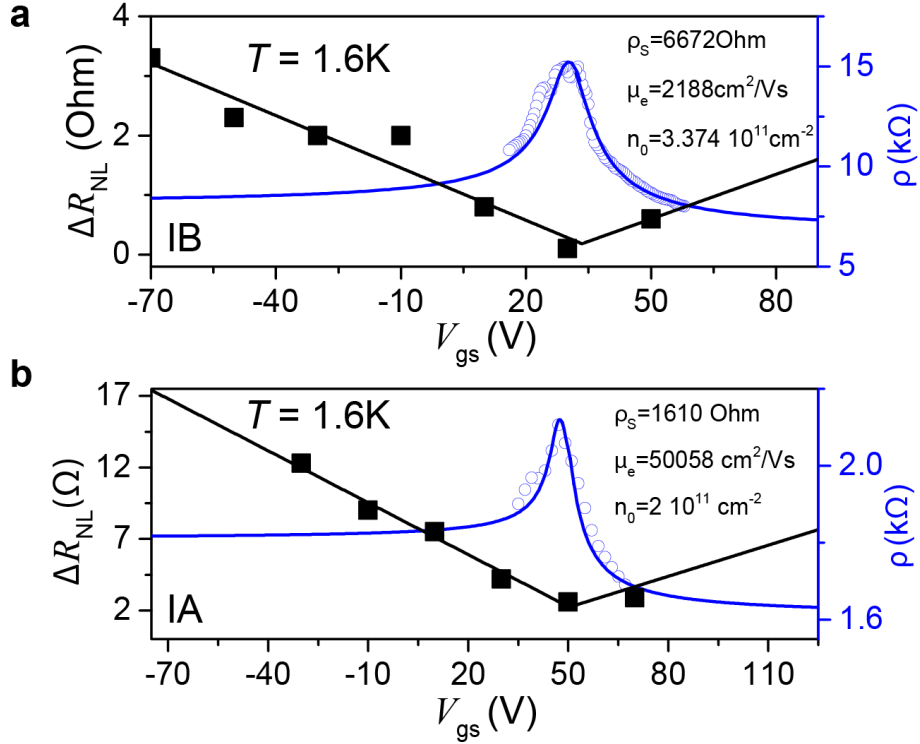
Figure 9.10: Comparison of spin-transport (ΔR_{NL}) and charge transport (ρ)as function of V_{gs} for a) device IB and b) device IA. Black lines are guide to the eyes. Blue lines are fittings with model (2.43). The spin signal is minimum at the Dirac point, indicating transparent FM/G interface.

fingerprint of the direct contact between Cobalt and graphene [31], that, by doping the graphene at the contact areas, shift the charge neutrality point and produces different gate-voltage characteristics [24]. The effect of this will be more evident in spin-precession measurements presented in Subsection (9.3.2).

9.3 Spin-relaxation in graphene

9.3.1 Dependence of spin-signal on inter-electrode distance

The main focus of spin-transport studies is the exact determination of the spin relaxation time τ_s and the spin diffusion length D that characterize the spin relaxation in the material. One way to determine $\lambda_s = \sqrt{D\tau_s}$ is by varying the *injector-detector* spacing L systematically and measure the spin signal ΔR_{NL} at different L. The dependence of ΔR_{NL} on the latter can be modeled using equation (9.1). Obviously this method is time consuming since it requires the fabrication of several devices with different L.

Nevertheless, for measurements where the magnetization switching is observable for all

contacts (Figure 9.6), the above model can be directly employed [28]. Indeed, the four resistance levels $R_1...R_4$ (Figure 9.11a) are due to ferromagnetic electrodes placed at different distances L_{xy} (Figure 9.11b), thus a single measurement provides enough information to be used with Equation (9.1).
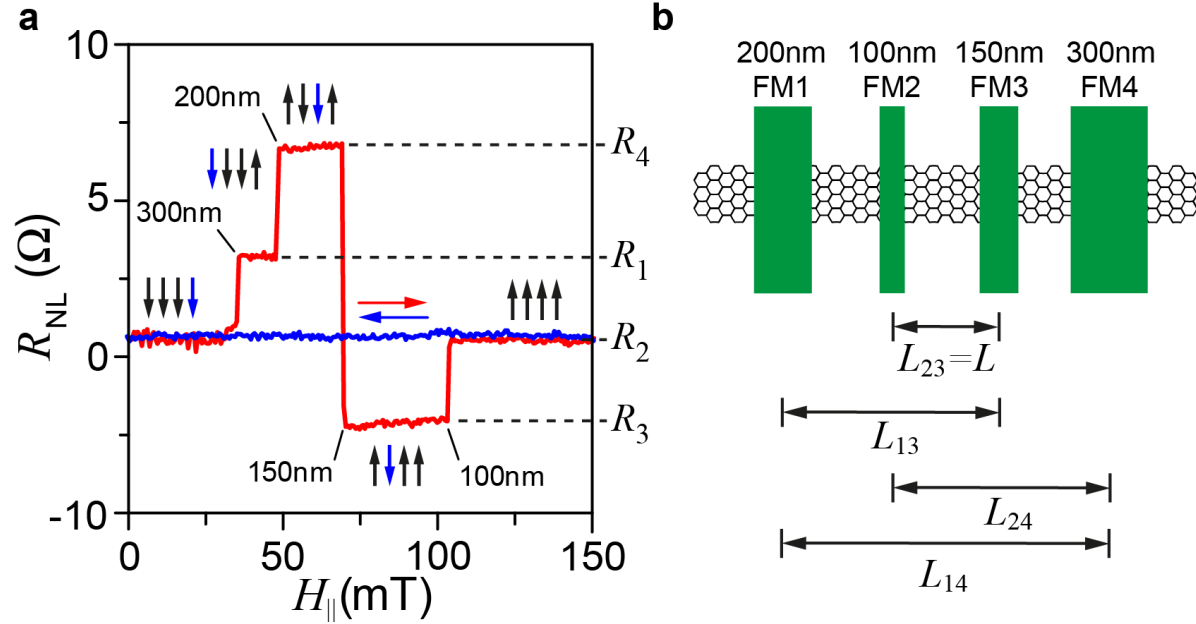

Figure 9.11: Spin-detection for a) parallel and b) anti-parallel configurations. c) Spin-valve behavior, with R_{P} and R_{AP} resistance levels. a) Spin-dependent DOS for a) parallel and b) antiparallel configurations.

This leads to a system of four equations and five unknown:

$$
\begin{aligned}
R_1 &= (+R_{23} + R_{13}) - (+R_{24} + R_{14}) + R_0 \\
R_2 &= (+R_{23} - R_{13}) - (+R_{24} - R_{14}) + R_0 \\
R_3 &= (-R_{23} - R_{13}) - (-R_{24} - R_{14}) + R_0 \\
R_4 &= (+R_{23} + R_{13}) - (-R_{24} - R_{14}) + R_0
\end{aligned}
\tag{9.2}
$$

where R_0 is a gate-dependent background resistance always present in the measurements. Equations (9.3) take into account the fact that the spin accumulation probed by electrode FM3 is the sum of the two spin accumulations of opposite sign produced by the electrodes FM1 and FM2 (negative spin accumulation of FM1 partially cancels the accumulation produced by FM2, see also Figure 7.4b), which decay exponentially over the length L_{13} and L_{23} respectively. The same applies for the spin accumulation probed by FM4. When the electrodes are equally spaced so that $R_{13} = R_{24}$, Equation (9.3) becomes solvable:
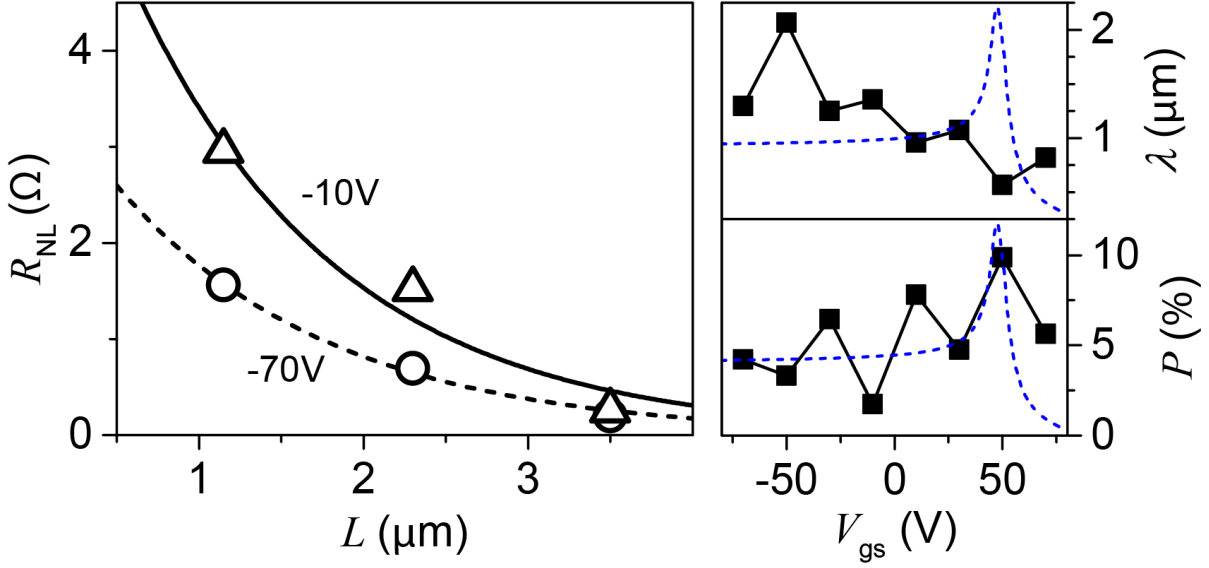
Figure 9.12: Length dependence of the spin signal as extracted from the magnitude of the multiple resistance levels of Figure 9.9.

$$
\begin{aligned}
R_1 &= +R_{23} - R_{14} + R_0 \\
R_2 &= +R_{23} - 2R_{24} + R_{14} + R_0 \\
R_3 &= -R_{23} + R_{14} + R_0 \\
R_4 &= +R_{23} + 2R_{24} + R_{14} + R_0
\end{aligned}
\tag{9.3}
$$

and $\lambda_s = \sqrt{D\tau_s}$ can be extracted.

Fitting with Equation (9.1) (Figure 9.12) affords $P = 4.1 \pm 0.2\%$ and $\lambda_s = 1.36 \pm 0.07$ μm.

9.3.2 Spin-precession measurement: Hanle curve

A more accurate way to determine the spin-diffusion length λ_s, is to directly measure the spin-precession by means of Hanle measurements. Figure 9.13 shows an example set of Hanle curves measured on a IIB device (with $L = 500$ nm and $W = 200$ nm) at T=300 mK for different gate voltages. Fitting with Equation 7.27 provides the values of the spin diffusion constant D and the spin-relaxation time τ_s (Figure 9.14). Interestingly D and τ_s seem to reach a maximum at the second Dirac point induced by Co doping, were also the spin-accumulation signal is maximum. This confirms the high coupling level with the transparent contacts. For devices with small injector-detector interdistance L, like in this case, the strong effect of the transparent contacts on the spin-relaxation is more evident, in fact the spin diffusion length λ_s of the device results to be quite small, lying in the range $\lambda_s = 0.1 - 0.14$ μm. Nevertheless, in this conditions a more sophisticated model for
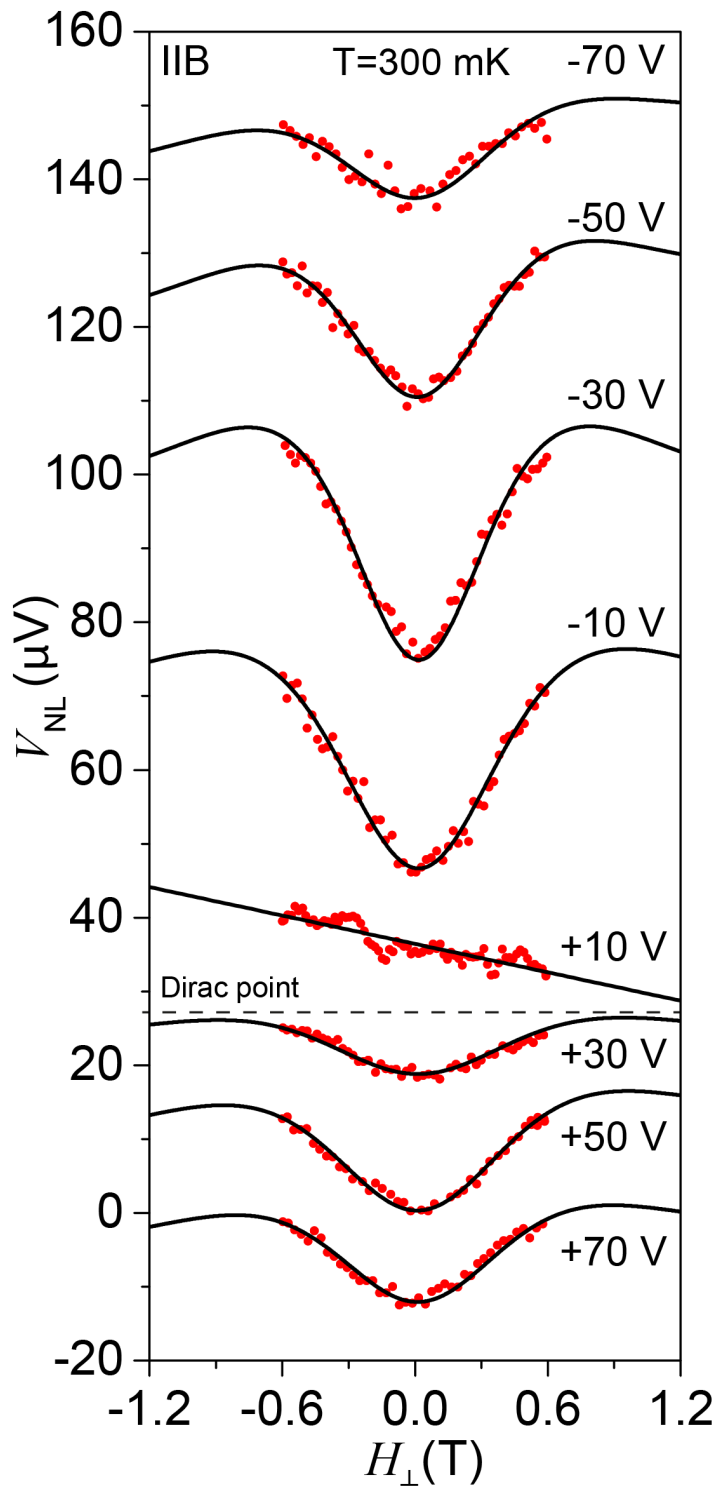
Figure 9.13: Hanle measurements as function of V_{gs} performed on a IIB type device. Black curves are fitting with Equation 7.27. The λ_s of the device is ~ 0.1 μm while $D \sim 1 \cdot 10^{-4}$ m^{2}s^{-1} and $\tau_s \sim 10^{-12}$s.
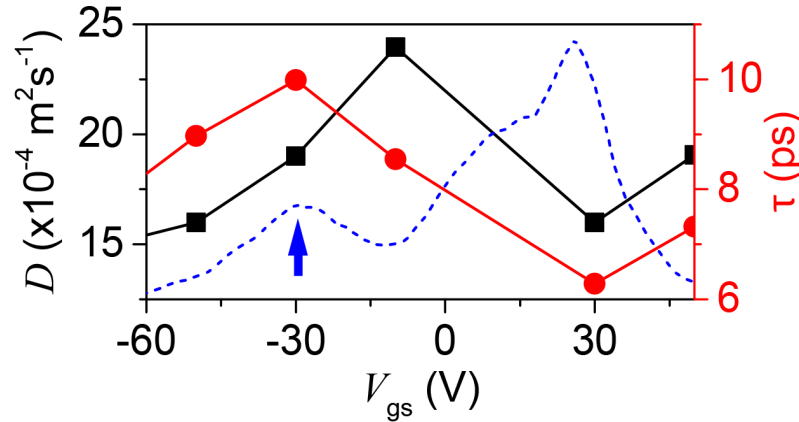
Figure 9.14: Evolution of the spin-diffusion constant D and the spin-relaxation time τ_s with V_{gs}. Both show a minimum at the charge neutrality point, while they are maximum at the second Dirac point induced by doping by the Co contacts.

the spin-precession is necessary in order to account for the effect of high coupling to the contacts.

9.4 Conclusions

To conclude, we presented a new fabrication process for the creation of uniform Al_2O_3 ultra-thin films by atomic layer deposition (ALD) on graphene, to be used as tunneling barriers in spinvalve devices. The uniformity of the films is enhanced by employing a Titanium seed layer that promotes ALD nucleation in the graphene basal plane. Moreover, we demonstrated that the chemical composition of the barrier film is the main factor determining the spin-injection efficiency of the device, even in absence of pinholes. The presence of unoxidized seeding material can hinder the spin-injection in graphene completely, and an additional oxidation step previous to the ALD process is necessary to ensure a fully oxidized barrier stack. While on the one hand, the possibility of using ALD methods greatly simplifies the fabrication of tunneling barriers, the sensibility of the spin-injection on the barrier chemical composition makes this kind of devices non suitable for the study of chemically-functionalized graphene spinvalves, therefore spinvalve devices with ohmic contacts are preferred. To maximize the spin-injection efficiency in transparent spinvalves, the graphene was patterned in narrow stripes so as to reduce the junction size and increase the spin-dependent interface resistance. The patterning is performed by combining electron-beam lithography and reactive ion etching. The design of the final devices involved also the optimization of different factors, such as the ferromagnetic domain size and shape anisotropy, so as to maximize the spin-transport response. Spin-transport in graphene was studied by means of magnetoresistance and Hanle spin-precession measurements. Several factors, such as the width of the graphene stripe and the injector-detector

inter-distance, were found to play an important role in determining the final spin-diffusion length of the devices. The comparison between spin- and charge transports confirms the contact transparency and reveals the doping effect of the ferromagnetic contacts. The design and fabrication process here developed can now be used to study the effect of different chemical functionalizations on the graphene spin-relaxation.

Bibliography

[1] Rashba, E. I. Theory of electrical spin injection: Tunnel contacts as a solution of the conductivity mismatch problem. *Phys. Rev. B* **62**, 16267–16270 (2000).

[2] Han, W. *et al.* Tunneling spin injection into single layer graphene. *Phys. Rev. Lett.* **105**, 167202 (2010).

[3] Dlubak, B. *et al.* Highly efficient spin transport in epitaxial graphene on SiC. *Nat Phys* **8**, 557–561 (2012).

[4] Tombros, N. *et al.* Electronic spin transport and spin precession in single graphene layers at room temperature. *Nature* **448**, 571–574 (2007).

[5] Xie, G. *et al.* Graphene Edge Lithography. *Nano Letters* **0**, null (2012).

[6] Xuan, Y. *et al.* Atomic-layer-deposited nanostructures for graphene-based nanoelectronics. *Applied Physics Letters* **92**, 13101 (2008).

[7] Lee, B. *et al.* Conformal Al2O3 dielectric layer deposited by atomic layer deposition for graphene-based nanoelectronics. *Applied Physics Letters* **92**, 203102 (2008).

[8] Wang, X., Tabakman, S. M. & Dai, H. Atomic Layer Deposition of Metal Oxides on Pristine and Functionalized Graphene. *Journal of the American Chemical Society* **130**, 8152–8153 (2008).

[9] Wang, L. *et al.* Ultrathin oxide films by atomic layer deposition on graphene. *Nano Letters* **12**, 3706–3710 (2012).

[10] Farmer, D. B. *et al.* Utilization of a Buffered Dielectric to Achieve High Field-Effect Carrier Mobility in Graphene Transistors. *Nano Letters* **9**, 4474–4478 (2009).

[11] Sangwan, V. K. *et al.* Quantitatively enhanced reliability and uniformity of high-κ dielectrics on graphene enabled by self-assembled seeding layers. *Nano Letters* **13**, 1162–1167 (2013).

[12] Dlubak, B., Kidambi, P. R., Weatherup, R. S., Hofmann, S. & Robertson, J. Substrate-assisted nucleation of ultra-thin dielectric layers on graphene by atomic layer deposition. *Applied Physics Letters* **100**, 173113 (2012).

[13] Robinson, J. a. *et al.* Epitaxial graphene materials integration: Effects of dielectric overlayers on structural and electronic properties. *ACS Nano* **4**, 2667–2672 (2010).

[14] Fallahazad, B. *et al.* Scaling of Al2O3 dielectric for graphene field-effect transistors-dielectric for graphene field-effect transistors. *Applied Physics Letters* **100**, 93112 (2012).

[15] Yamaguchi, T., Masubuchi, S., Iguchi, K., Moriya, R. & MacHida, T. Tunnel spin injection into graphene using Al2O3 barrier grown by atomic layer deposition on functionalized graphene surface. *Journal of Magnetism and Magnetic Materials* **324**, 849–852 (2012).

[16] Crangle, J. The Magnetic Properties of Solids Ch. 6. Ch. 6 (Edward Arnold, London, 1977).

[17] Jedema, F. J., Nijboer, M. S., Filip, a. T. & van Wees, B. J. Spin injection and spin accumulation in permalloy-copper mesoscopic spin valves. *Journal of Superconductivity* **15**, 8 (2001).

[18] Han, W. *et al.* Spin transport and relaxation in graphene. *Journal of Magnetism and Magnetic Materials* **324**, 369–381 (2012).

[19] http://www.keithley.com/.

[20] Simmons, J. G. Generalized Formula for the Electric Tunnel Effect between Similar Electrodes Separated by a Thin Insulating Film. *Journal of Applied Physics* **34**, 1793–1803 (1963).

[21] Prins, F. *et al.* Room-temperature gating of molecular junctions using few-layer graphene nanogap electrodes. *Nano Letters* **11**, 4607–4611 (2011). arXiv:1110.2335.

[22] Mangin, a., Anthore, a., Della Rocca, M. L., Boulat, E. & Lafarge, P. Reduced work functions in gold electromigrated nanogaps. *Physical Review B - Condensed Matter and Materials Physics* **80**, 1–5 (2009).

[23] Kimura, T., Otani, Y. & Hamrle, J. Enhancement of spin accumulation in a nonmagnetic layer by reducing junction size. *Phys. Rev. B* **73**, 132405 (2006).

[24] Jo, S., Ki, D.-K., Jeong, D., Lee, H.-J. & Kettemann, S. Spin relaxation properties in graphene due to its linear dispersion. *Phys. Rev. B* **84**, 075453 (2011).

[25] Casiraghi, C. *et al.* Raman Spectroscopy of Graphene Edges. *Nano Letters* **9**, 1433–1441 (2009).

[26] Ryu, S., Maultzsch, J., Han, M. Y., Kim, P. & Brus, L. E. Raman spectroscopy of lithographically patterned graphene nanoribbons. *ACS nano* **5**, 4123–30 (2011).

[27] Jedema, F. J. *et al.* Electrical detection of spin precession in a metallic mesoscopic spin valve. *Nature* **416**, 713–716 (2002).

[28] Popinciuc, M. *et al.* Electronic spin transport in graphene field-effect transistors. *Phys. Rev. B* **80**, 214427 (2009).

[29] Han, W. *et al.* Electrical detection of spin precession in single layer graphene spin valves with transparent contacts. *Applied Physics Letters* **94**, 222109 (2009).

[30] Han, W. & Kawakami, R. K. Spin Relaxation in Single-Layer and Bilayer Graphene. *Phys. Rev. Lett.* **107**, 47207 (2011).

[31] Volmer, F. *et al.* Role of MgO barriers for spin and charge transport in Co/MgO/graphene nonlocal spin-valve devices. *Physical Review B* **88**, 161405 (2013).

Chapter 10

Perspectives

This chapter presents the first preliminary spin-transport and spin-precession experiments in graphene spinvalves functionalized with SMMs. The sophisticated mechanisms (spin-injection, -diffusion) underlying the spinvalves function, combined with the rich magnetic behavior of SMMs makes these experiments extremely challenging.

The ultimate goal is to investigate how electronic spins in graphene couple to the spin of SMMs, and to reveal the details of related spin-interactions. The tunable parameters in these experiment are *temperature* and *electrostatic gating*. Varying the temperature across the blocking temperature T_b changes the SMMs magnetic response. The Fe_4Py cluster exhibits a clear transition from paramagnetic to superparamagnetic behaviors at a temperature of about $T_b = 800$ mK (see Chapter 2.2). The presence of Fe_4Py grafted on the graphene surface is thus expected to influence the electron spin in different ways for temperatures above and below T_b. T does not affect spin transport in graphene appreciably. On the contrary, electrostatic gating affects the graphene spin signal ΔR_{NL} substantially (see Chapter 9). At the same time, an external gate electric field strongly influences the magnetic state of SMMs, as demonstrated by transport experiments in molecular nano-junctions [1–3].

10.1 Spin-transport in graphene-SMMs hybrid devices

The spinvalve devices developed in the previous chapters are here used to study the effect of magnetic adsorbates on the graphene spin-injection mechanism (Figure 10.1a). To this end a IIB type device has been functionalized with Fe_4Py by dropcasting, using a $C = 2.5 \cdot 10^{-6}$ M, solution prepared as described Section 4.2, followed by washing with fresh solvent mixture and drying under Ar jet. The functionalization is performed directly on the chip without removing the bonding wires. A shift of the resistivity maximum towards higher gate voltages indicates successful molecular decoration (Figure 10.1b), in agreement with the observations of Section 4.20. After functionalization, the charge neutrality point of the device lies at $V_D = 33.4$ V. The increase in the device mobility after functionalization is likely due to the removal of the resist impurities introduced by the lithographic steps.
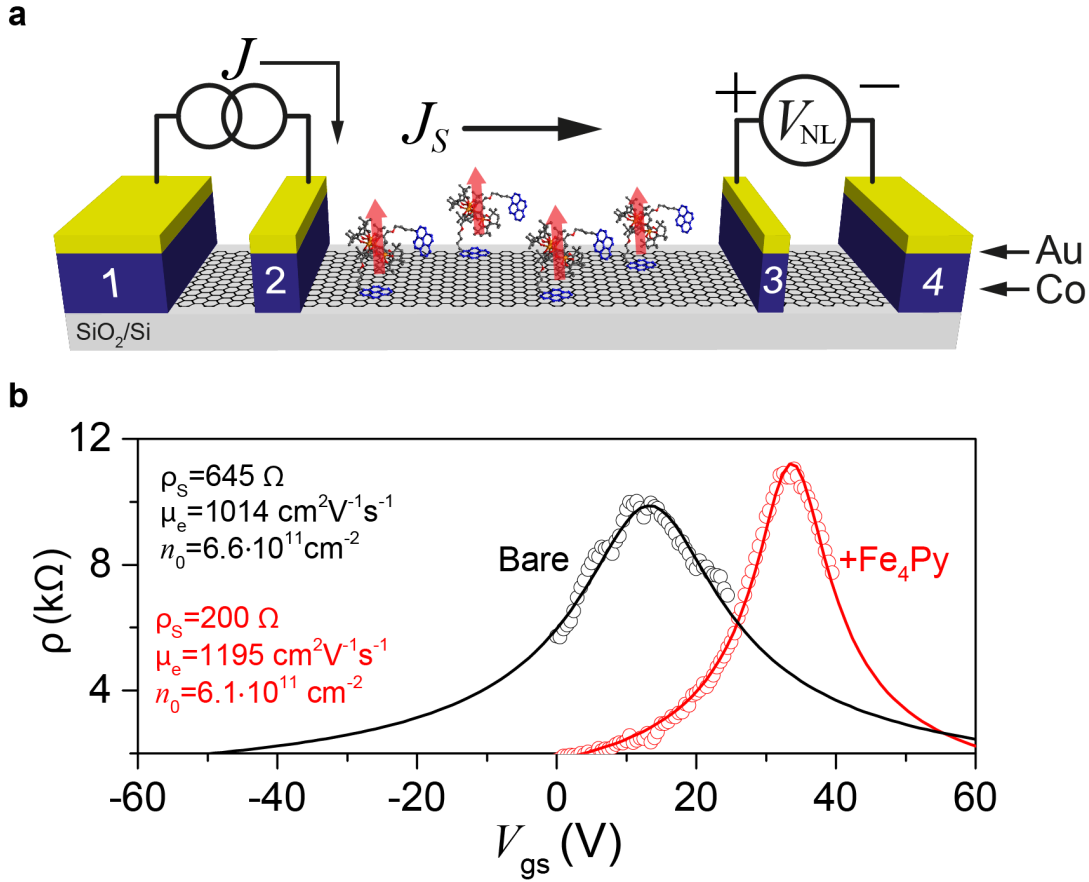
Figure 10.1: SMMs-functionalized graphene spinvalve a) Scheme of transparent spinvalve functionalized with Fe_4Py SMMs. b) ρ vs. V_{gs} measured in four-terminal configuration, before (black) and after (red) functionalization with Fe_4Py ($C = 2.5 \cdot 10^{-6}$ M) at room temperature. The resistivity maximum shifts towards higher gate voltages, in agreement with the characterization of Section 4.20.

Figure 10.2 shows the magneto-transport response of the device after functionalization at $T = 1.6$ K. Even though the spin signal is almost completely suppressed, a weak spin valve characteristics is still visible for gate voltages far from the charge neutrality point ($V_{gs} \ll V_D = 33.4$ V). As expected for transparent contacts, ΔR_{NL} decreases as V_D is approached. Interestingly for $V_{gs} = +30V$ a dip for $H_{||} \approx 0$ is visible. Such a feature was observed for spin-transport experiments in hydrogenated graphene, and is regarded as a fingerprint of paramagnetic adsorbates [?], in addition here shows a hysteresis behavior for up and down $H_{||}$ sweeps. These observations demonstrate that spin-transport is still present after decoration with Fe_4Py, and the device magnetoresistance shows some evidence of the magnetic behavior of the molecular adsorbates at certain gate voltages.
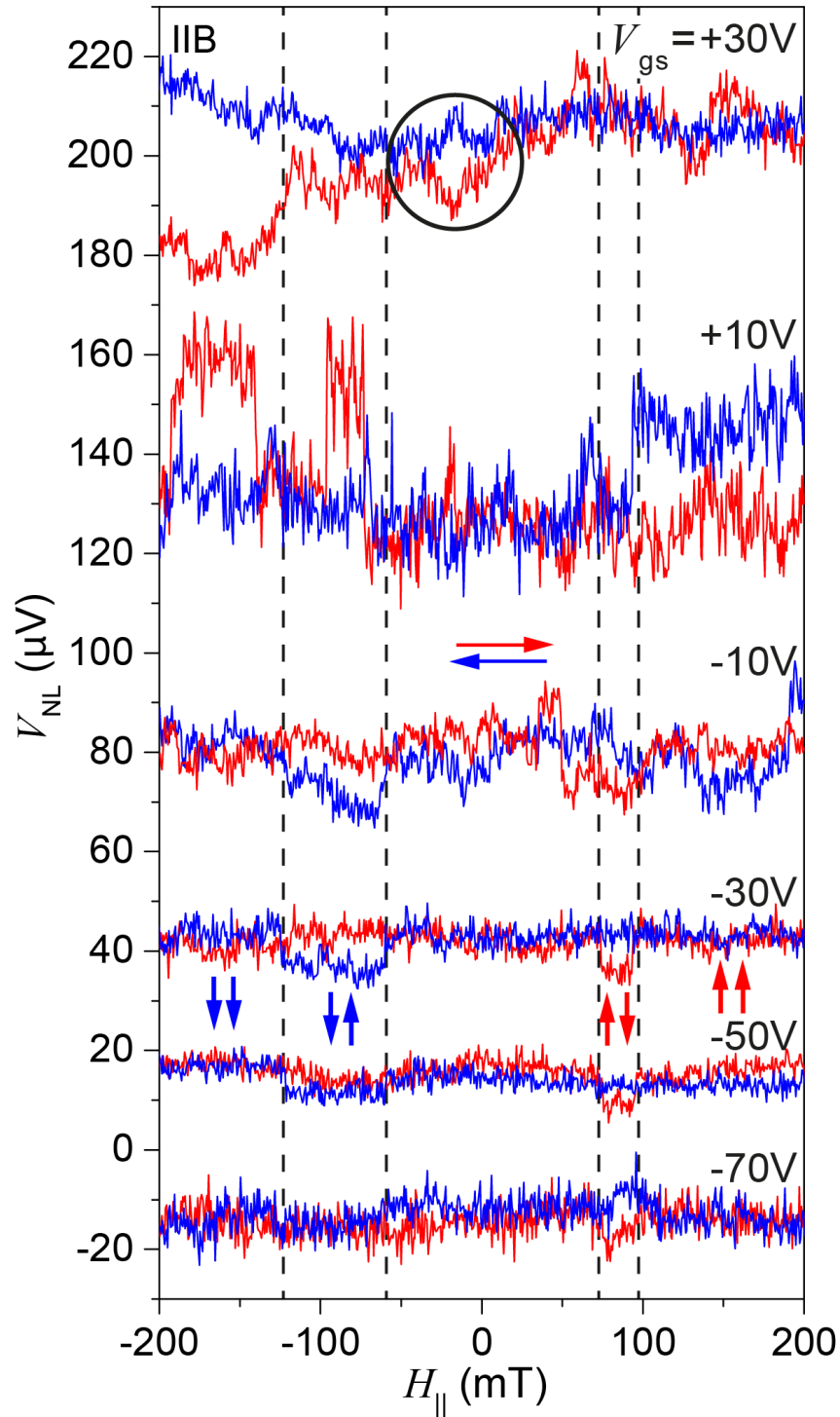
Figure 10.2: SMMs-functionalized graphene spinvalve: gate dependence of magneto-transport at $T = 1.6$ K. The $H_{||}$ sweep-rate is 20 mT/min. The black circle for $V_{gs} = +30$ V highlights a typical fingerprint of paramagnetic adsorbates [?].

10.2 Spin-relaxation in graphene-SMMs hybrid devices

The effect of coupling to the Fe_4Py spins on the spin-relaxation in graphene is studied by means of Hanle spin-precession measurements. The spinvalve is prepared with the injector and detector magnetizations parallel to each other, and lying along the electrodes long direction. The non-local voltage V_{NL} is then acquired while sweeping $H_\perp$ (applied perpendicular to the graphene plane) with excitation current $|J| = 10\mu A$. Figure 10.3 shows spin-precession response measured at $T = 1.6$ K. Both up- and down-sweeps are acquired to reveal any hysteric behavior. The measurements show a very rich behavior, with the shape of the Hanle-curve varying to a great extent as function of the gate voltage V_{gs} (Figure 10.3). Surprisingly for $V_{gs} = -70V$, V_{NL} is minimum at $H_\perp = 0$ in contrast to what expected for parallel injector/detector magnetizations. Fitting with (7.27) provides $\tau_s = 21.4$ ps and $D = 3.3 \cdot 10^{-4}$ m^{2}s^{-1} that yield $\lambda_s = 0.084\mu m$, a slightly reduced values in comparison with the empty device shown in Figurehanlegate. By increasing V_{gs} the shape of the Hanle curve changes drastically. The signal increases as the charge neutrality point is approached, where a more clear Hanle shape is observed. Interestingly the curve seems to undergo an inversion as V_{gs} crosses the charge neutrality point at $V_{gs} = V_D$.

Up and down sweeps overlap at all gate voltages, thus no hysteresis is observed as expected for the *paramagnetic* behavior of Fe_4Py at these temperatures. Hystereretic behavior appears indeed only at lower temperatures ($T = 300$ mK), as an effect of the *superparamagnetism* of Fe_4Py. (Figure 10.4). Interestingly, hysteresis are only observed for V_{gs} close to the Dirac point where the spin signal is minimum (Figure 10.5), suggesting that the sensitivity of the device to the magnetic adsorbates is maximum as the charge neutrality point is approached. A detailed modeling is now necessary to explain the complicated behavior here presented, and to correctly take into account the effect of electrostatic gating on the SMMs magnetic response.
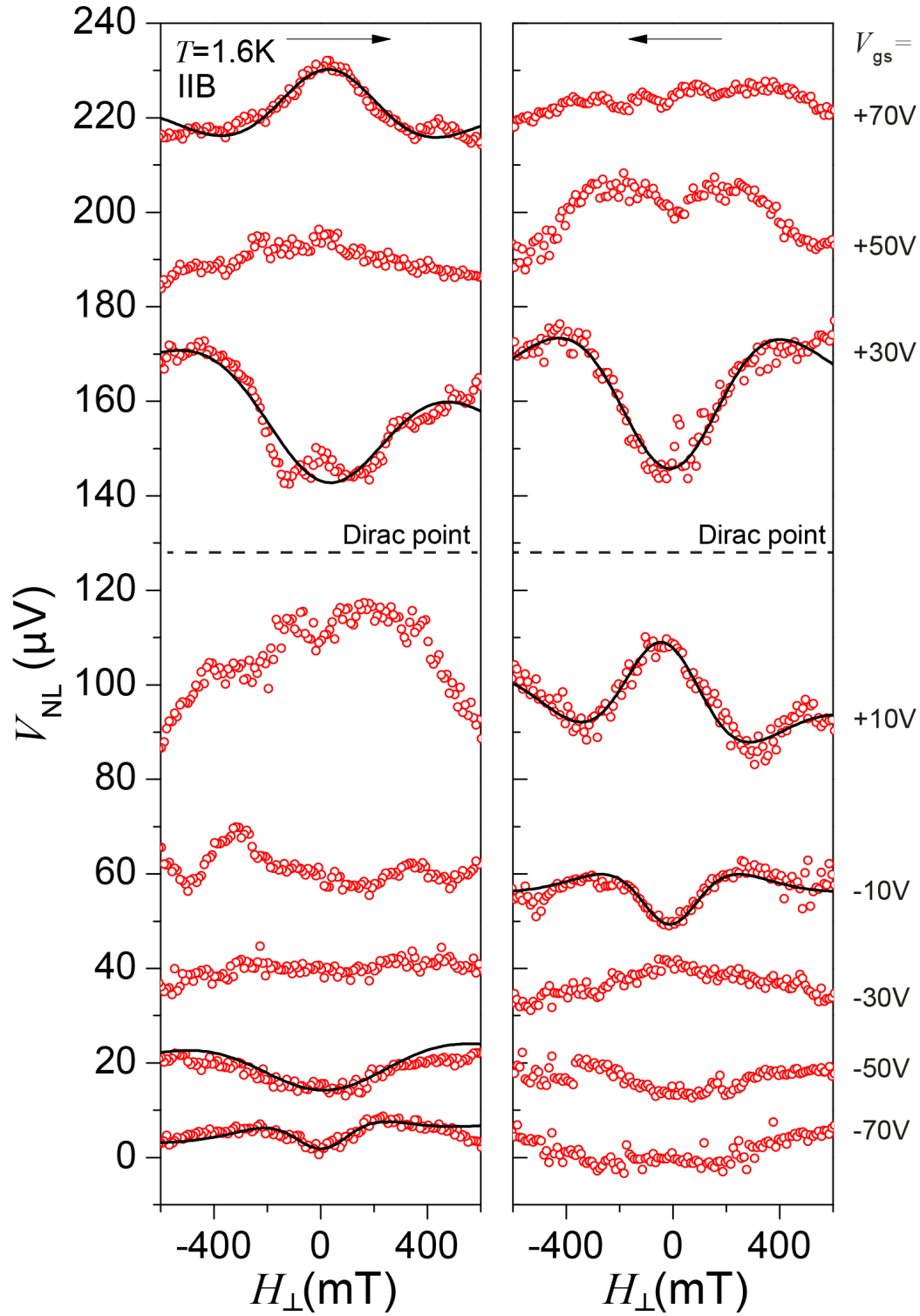
Figure 10.3: SMMs-functionalised graphene spinvalve: Hanle spin-precession for up- (left) and down- (right) magnetic field sweeps at $T = 1.6$ K.
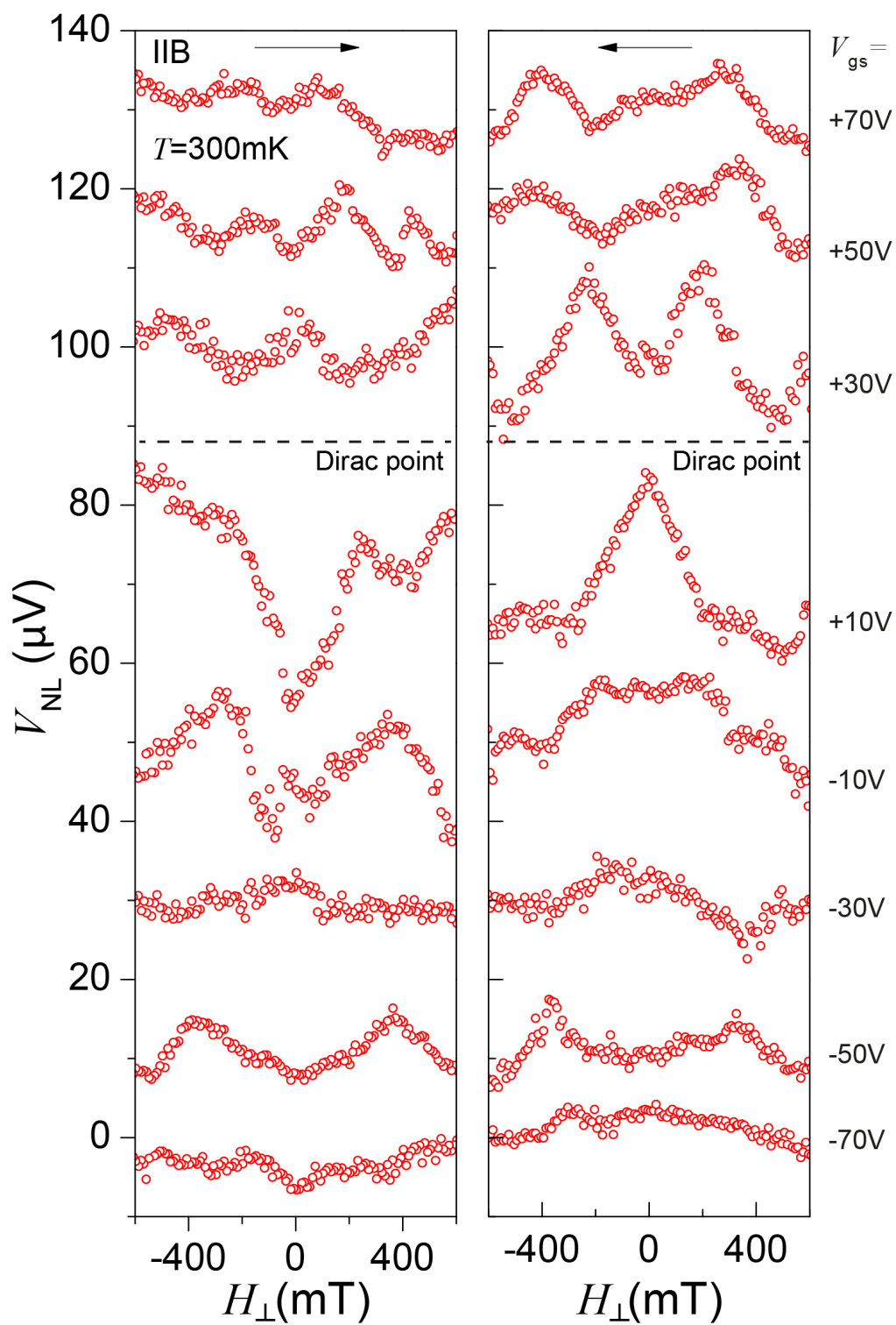
Figure 10.4: SMMs-functionalised graphene spinvalve: Hanle spin-precession for up- (left) and down- (right) magnetic field sweeps at $T = 300$ mK.
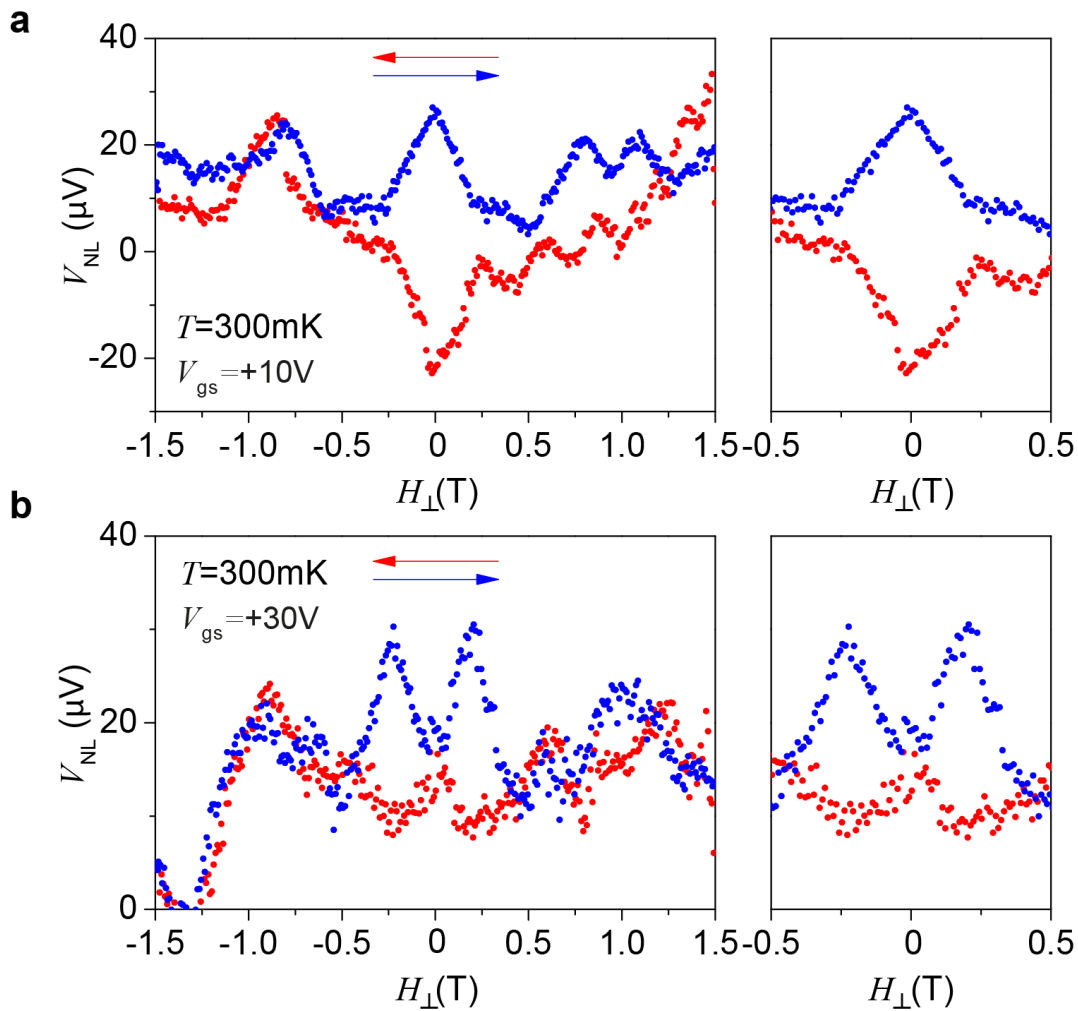
Figure 10.5: Hysteretic behaviour of the Hanle spin-precession curve observed at $T = 300$ mK close to the charge neutrality point. a) $V_{\text{gs}} = +10$ V and b) $V_{\text{gs}} = +30$ V.

Bibliography

[1] Zyazin, A. S. *et al.* Electric Field Controlled Magnetic Anisotropy in a Single Molecule. *Nano Letters* **10**, 3307–3311 (2010).

[2] Zyazin, A. S., van der Zant, H. S. J., Wegewijs, M. R. & Cornia, A. High-spin and magnetic anisotropy signatures in three-terminal transport through a single molecule. *Synthetic Metals* **161**, 591–597 (2011).

[3] Burzurí, E., Zyazin, A. S., Cornia, A., der Zant, H. V. & van der Zant, H. S. J. Direct Observation of Magnetic Anisotropy in an Individual Fe 4 Single-Molecule Magnet. *Physical review letters* **2**, 2–6 (2012).

Chapter 11

Conclusions

This thesis sets the theoretical and experimental basis for the study of spin-relaxation in graphene-based hybrid materials, thus opening the way to the first experimental characterization and the theoretical understanding of graphene-based spintronic devices.

To reach this aim two complementary approaches were followed. In the first, single molecule magnets (SMMs) are used as model spin systems to unveil the detailed interaction between a spin and its environment, by directly looking at their dynamics when placed onto graphene. In the second approach, robust graphene-based spinvalve devices are developed as novel tool to study how molecular spins influence the diffusion of spin-polarized carriers in graphene. Moreover, in the quest for scalable production of high-quality graphene, a novel non-invasive technique based on continuous-wave sub-millimeter spectroscopy is presented as powerful tool for the electrical characterization of large-area graphene.

The SMM $[Fe_4(L)_2(dpm)_6]$ with pyrene grafting groups was employed to embed isolated spins in the graphene environment via wet-chemistry approach. The grafting mechanism was investigated by studying the topography of the molecules bound to high quality graphene flakes. The concentration of the functionalizing solution is found to control the growth mode of molecular islands on the graphene surface. Statistical analysis of the AFM height profile indicates that π-stacking interaction tend to promote the formation of two-dimensional molecular arrangements on the graphene surface. Being three-dimensional growth only possible at high concentrations, proves that the grafting to graphene is stronger than the intramolecular binding. This is confirmed by scaling-analysis that indicates an appreciable surface-diffusion of the adsorbates during the reaction in solution. This opens the way to novel methods for the creation of extended molecular arrangements on graphene. In particular, the synthesis of two-dimension molecular random network is here demonstrated by exposing the functionalized surface to laser light.

The effect of the grafting on the molecular properties is investigated via multiple techniques. Matrix assisted laser desorption ionization mass spectrometry demonstrate the structural robustness of the molecular units, with isotopic patterns that unequivocally indicate an unvaried coordination structure for the molecules magnetic core. The electronic stability of the cluster is confirmed by the position of the Fe_{2p} double peak in the X-ray photoelectron spectra, that matches that of the crystalline compounds and clearly indi-

cate binding to Oxygen. The absence of appreciable charge transfer is also supported by electronic transport measurements on graphene-based field effect transistors functionalized with the SMMs. The position of the Fermi level with respect to the Dirac point (touching point between the conical valence and conduction bands of graphene) is found to be extremely sensitive to the external functionalization. The simple formation of a dipole at the graphene/molecule interface is seen to induce a Fermi level shift of around 30 V. This matches with the energy up-shift and the stiffening of the E_2g mode in the graphene Raman spectra after functionalization.

Magnetization and dc-susceptibility measurements prove that the static magnetic properties of the clusters remain unchanged after the dispersion in solution and the subsequent grafting to graphene, owing to the cluster excellent structural and electronic stability. After subtracting the strong graphene diamagnetic contribution, the χT vs. T curve of the hybrid acquired at 1000 Oe perfectly matches that of the starting crystalline compound, indicating the unvaried nearest neighbor and next nearest neighbor exchange interactions characteristic of the Fe_4 core. Moreover the value of the susceptibility maximum observable at low temperature confirms a spin-ground state $S = 5$. The latter is further confirmed by the saturation value of isothermal magnetization curves acquired at different temperatures. The dynamics of molecular spins in the graphene matrix was studied by means of ac-susceptibility measurements in the broad temperature range $T = 4$ K - 13 mK. Two spin-relaxation regimes were identified: a *classical* (thermal) one, dominating the relaxation at temperatures $T > 0.8$, and a *quantum* one that dominates the relaxation at low temperatures $T < 0.8$. The spin dynamics of the hybrids diverges considerably from that of the pristine crystal compound. A fixed external magnetic field is used to suppress the quantum relaxation channel, so as to study the effect of the graphene environment on classical spin-relaxation mechanism only. The thermal relaxation is found to be mainly determined by interaction of the spins with the graphene phonon bath via *spin-phonon interaction*. By extending the existing theoretical models to the case of a two-dimensional phonon bath, reveals the effect of the phonon-bath dimensionality on the classical spin-relaxation mechanism. The experimental observation are nicely reproduced using the SMM characteristics as extracted from crystal and the graphene sound velocity and without any free fitting parameter.

The quantum relaxation path is studied in absence of external field in the temperature range where the thermal excitation of spin states is negligible. Interaction with graphene enhances the quantum tunneling rate by almost 6 orders of magnitude. Analysis based on a newly developed theoretical model, based on the Stevens' operator equivalents formalism, allows to quantify the contributions of the different fundamental interactions (i.e. hyperfine, dipole-dipole, spin-phonon) to the quantum relaxation. The rate enhancement is explained by introducing in the theory a large perturbative term having a three-fold symmetry that mixes the quantum spin-states differing in m by multiples of 3. This term is likely a fingerprint of the interaction between the spin and graphene charge distribution and is seen to drives the spin dynamics into a *strongly perturbative quantum tunneling regime* predicted by Villain's more than a decade ago, and here observed experimentally for the first time. Being this regime coherent by definition, the influence of graphene carriers

on spin tunneling allows envisaging new schemes for the electrical control of the quantum coherence of spin-states.

The second part of this work is dedicated to the study of spintronic interations between the molecular spins and the spin-polarized massless carriers in graphene.

The challenges in the development of robust graphene-SMMs hybrid spintronic devices are addressed by employing two different strategies. On the one hand, the *conductivity mismatch* between the graphene channel and the ferromagnetic contacts (used as source of spin-polarized carriers) is overcome by integrating ultra-thin Al_2O_3 tunneling barriers at the graphene/ ferromagnet interface. The growth of highly uniform insulating thin-films by atomic layer deposition (ALD) is made possible implementing a Titanium seeding, that promotes Al_2O_3 nucleation in the graphene basal plane. Nevertheless, the spin-injection efficiency is found to be very sensitive to the barrier chemical composition, and the presence of unoxidized Ti island at the interface with graphene is seen to hinder the spin-injection completely. A fully oxidized seeding is the key for the realization of highly decoupled ferromagnetic contact and helps preserving the long spin-diffusion length of graphene. However, being the spin trasport in such devices very sensitive to the barrier composition, such device architecture is incompatible with the study of graphene chemical functionalization that ask for a more robust devices. Efficient spin-injection is achieved in graphene spin-valves with transparent contacts by reducing the contact junction sized so as to enhance the spin-dependent interface resistance. To this end, the graphene flakes are patterned in few hundreds nanometers-wide stripes, via combining ebeam lithography masking and plasma etching. The spin-diffusion length and the spin-injection efficiency are strongly reduced as the stripe width is decreased. This validates theories of spin-flip scattering induced by short-range scatterers at the graphene edges. Presence of short-range scatterers is confirmed by an increase in the constant resistivity contribution in two terminal electronic transport measurements, and further supported by the prominent D band in the Raman spectrum for small-width stripes.

First spin-transport and spin-relaxation experiments in hybrid SMMs-graphene transparent spinvalves reveal a very rich behavior as function of both temperature and electrostatic gating. While clear evidences of interaction with the magnetic adsorbates are observed in both magnetoresistance and Hanle measurements at $T = 1.6$ K. Clear fingerprints of the superparamagnetic SMMs behavior is observed for temperatures below the SMM blocking temperature, as indicated by a clear hysteresis opening. Further experimental investigations and new theoretical modeling are now on the way to further explore the spintronic characteristics of SMM-graphene hybrid devices, and to unravel potential new opportunities for the control of graphene spintronic properties.

Acknowledgments

And here it comes the most read section of any PhD thesis, the Acknowledgments!

My sincere gratitude goes to my supervisor Dr. Lapo Bogani for having complete confidence in me and for giving me total freedom during these years. Thank you for encouraging me in pursuing my own ideas and in developing a broader outlook on everything I do. You taught me how to be an independent scientist and to take full responsibility of my actions. From you I gained a great deal of scientific knowledge and expertise. Thank you sincerely for your esteem and your friendship.

A very special "thank you" goes to Dr. Marko Burghard, for being my "MPI supervisor". Thank you for your patience, understanding and perseverance, and for sharing with me the love for the challenge! I am grateful to you for your constant support, for your sympathy whenever a sample died, and, most importantly, for your esteem and friendship.

I would like to thank Prof. Martin Dressel for welcoming me in his institute and for giving me total freedom to focus on my projects. Thank you for not complaining when I skipped the institute seminar to be at the mpi. Thank you for the having confidence in me, for your patience and support.

My gratitude goes also to Prof. Klaus Kern for welcoming me in his department and for constantly supporting the collaborative work presented in this thesis.

An important thanks to Karin Goß for sharing with me the toughest moments of my PhD and for her friendship in the outside world! Thank you for being always willing to help me. I still would like to see the photo of you with green hair...

Eric Heintze you will always be "our coach". Thank you for your injections of motivation in the toughest of moments, and for your philosophical insights, yes "it's not just a PhD, we are here to stimulate new synapses in the network of science...".

A big thank to Alexander Hoyer for struggling with me in the lab all the time and for being always ready to help and support me and my crazy ideas. I will never forget your: "you know what?, it's a mess...". Hold on Alex you are almost there!

A sincere thanks to Kristina Vaklinova for sharing with me our first office and for helping me whenever I needed it, sorry if I missed some of your cakes, they were always so delicious!

A special thank to Adarsh Sagar, Ravi Shankar Sundaran, Eva Peters, Thomas Defaux for introducing me to the world of nanofabrication and electronic transport measurements,

Declaration

I hereby declare that I have authored this thesis independently and used no other sources and aids than the stated ones.

Christian Cervetti
Stuttgart, July 2015